AD-E500068

IDA PAPER P-1278

A070528

TECHNOLOGY ASSESSMENT OF ADVANCED PROPULSION SYSTEMS FOR SOME CLASSES OF COMBAT VEHICLES

Volume III. Appendices G-M

(12)

Frederick R. Riddell
Donald M. Dix

LEVEL III

September 1978

D D C

RECEIVED

JUN 29 1979

B
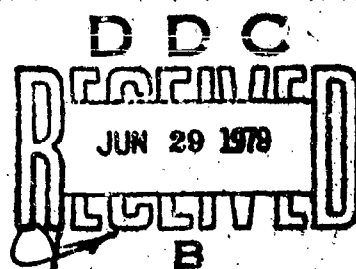
Prepared for

DEFENSE ADVANCED RESEARCH PROJECTS AGENCY

INSTITUTE FOR DEFENSE ANALYSES
SCIENCE AND TECHNOLOGY DIVISION

APPROVED FOR PUBLIC RELEASE; DISTRIBUTION UNLIMITED

UNCLASSIFIED

REPORT DOCUMENTATION PAGE		READ INSTRUCTIONS BEFORE COMPLETING FORM
1. REPORT NUMBER	2. GOVT ACCESSION NO.	3. RECIPIENT'S CATALOG NUMBER
4. TITLE (and Subtitle) Technology Assessment of Advanced Propulsion Systems for Some Classes of Combat Vehicles: Volume III, Appendices G-M		5. TYPE OF REPORT & PERIOD COVERED FINAL
		6. PERFORMING ORG. REPORT NUMBER IDA PAPER P-1278
7. AUTHOR(s) Frederick R. Riddell Donald M. Dix		8. CONTRACT OR GRANT NUMBER(s) DAHC15 73 C 0200
9. PERFORMING ORGANIZATION NAME AND ADDRESS INSTITUTE FOR DEFENSE ANALYSES 400 Army-Navy Drive Arlington, Virginia 22202		10. PROGRAM ELEMENT, PROJECT, TASK AREA & WORK UNIT NUMBERS DARPA Assignment A-40
11. CONTROLLING OFFICE NAME AND ADDRESS Defense Advanced Research Projects Agency 1400 Wilson Boulevard Arlington, Virginia 22209		12. REPORT DATE September 1978
		13. NUMBER OF PAGES 284
14. MONITORING AGENCY NAME & ADDRESS(if different from Controlling Office) N/A		15. SECURITY CLASS. (of this report) UNCLASSIFIED
		15a. DECLASSIFICATION DOWNGRADING SCHEDULE N/A

16. DISTRIBUTION STATEMENT (of this Report)

Approved for public release; distribution unlimited.

17. DISTRIBUTION STATEMENT (of the abstract entered in Block 20, if different from Report)

None

DDC
 RECEIVED
 JUN 29 1979
 B

18. SUPPLEMENTARY NOTES

N/A

19. KEY WORDS (Continue on reverse side if necessary and identify by block number)

propulsion systems; scientific research; engineering development; tanks (combat vehicles); combat vehicles, ground level, mobility, warfare; ships, high velocity; engines, gas-turbine, Stirling cycle, Brayton cycle, Otto cycle; Diesel engines; transmissions (mechanical); transmissions (electrical); transmissions (hydrodynamic); thrusters; vehicle tracks;

20. ABSTRACT (Continue on reverse side if necessary and identify by block number)

This paper presents the results of a study of propulsion systems for surface combat vehicles which is intended to provide information useful to the Defense Advanced Research Projects Agency in identifying high-payoff R&D prospects. The primary purposes of the paper are to: (1) quantify the technological advances needed to make major improvements in appropriate military propulsion systems and indicate relative payoffs; and (2) provide criteria for evaluation of new propulsion system or

DD FORM 1473 JAN 73 EDITION OF 1 NOV 65 IS OBSOLETE

UNCLASSIFIED

19. vehicle wheels; propellers (marine); hydraulic jets

20.

subsystem concepts. The scope of the study is limited to an assessment of propulsion systems for four classes of surface combat vehicles: (1) main battle tanks; (2) light, tracked land combat vehicles; (3) high-mobility land combat vehicles; and (4) high-speed (more than 50 knots) ships. For propulsion subsystems, five engine types (Otto, Diesel, gas turbine, closed Brayton, Stirling), three transmission types (mechanical, hydro-dynamic, electrical), and four thruster types (tracks, wheels, propellers, waterjets) are examined in some detail.

Results are presented in terms of technology goals which are within the bounds of what is judged to be physically possible and which together in relevant sets would have a major impact on the cost or performance of armored land combat vehicles or of high-speed ships. Relative payoffs within each set of goals are also estimated.

This report is in three volumes.

Accession For	
NTIS GRA&I	☑
DDC TAB	☐
Unannounced	☐
Justification	
By	
Distribution/	
Availability Codes	
Dist.	Avail and/or special
A	

IDA PAPER P-1278

TECHNOLOGY ASSESSMENT OF ADVANCED PROPULSION SYSTEMS FOR SOME CLASSES OF COMBAT VEHICLES

Volume III. Appendices G-M

Frederick R. Riddell
Donald M. Dix

September 1978

IDA

INSTITUTE FOR DEFENSE ANALYSES
SCIENCE AND TECHNOLOGY DIVISION
400 Army-Navy Drive, Arlington, Virginia 22202

ACKNOWLEDGMENTS

The authors are indebted to a great number of experts in various aspects of propulsion system technology and its military applications for the contributions they made to this study.

First, there are the individuals who provided analyses of the performance characteristics of specific propulsion system elements and of specific vehicle classes. Their work is the backbone of the study, and their contributions, which are incorporated in the appendices in Volumes II and III, were invaluable. The individual contributors, the fields of their work, and where their contributions appear are as follows:

- E. William Beans, University of Toledo--Otto-cycle engines (Appendix C)
- M.G. Bekker, consultant--thrusters for ground combat vehicles (Appendix J)
- Peter C. Bertelson, consultant--mechanical and hydro-mechanical transmissions (Appendix H)
- A. Douglas Carmichael, MIT--closed Brayton-cycle engines (Appendix F) and thrusters for high-speed oceangoing ships (Appendix K)
- P.C.T. de Boer, Cornell University--Diesel engines (Appendix D)
- B.L. Fletcher, consultant--land combat vehicles (Appendix A)
- James E.A. John, University of Ohio--Otto-cycle engines (Appendix C)
- James L. Kirtley, MIT--electrical transmissions (Appendix I)
- Philip Mandel, MIT--high-speed ships (Appendix B)

iii

- Joseph L. Smith, Jr., MIT--electrical transmissions (Appendix I)
- Graham Walker, University of Calgary--Stirling engines (Appendix G)
- David Gordon Wilson, MIT--open Brayton-cycle engines (Appendix E)

In addition to the specific contributions just cited, these individuals also provided greatly appreciated counsel to the authors throughout the study.

Another group participated in a Steering Committee that was most helpful in providing critical guidance throughout the study and in reviewing the initial draft of this report. Members of the Steering Committee were:

- Carl F. Bachle, consultant
- Arden L. Bement, Defense Advanced Research Projects Agency
- Austin W. Betts, Southwest Research Institute
- Charles H. Church, Headquarters, Department of the Army
- George J. Huebner, Jr. (Chairman), consultant
- E.L. Resler, Jr., Cornell University
- John A. Satkowski, Office of Naval Research
- Edward C. van Reuth, Defense Advanced Research Projects Agency
- Donald D. Weidhuner, consultant.

Thanks are also due to James J. Murray, U.S. Army Research Office, S.J. Deitchman, IDA, and Bernard Palewonsky, consultant, for reviewing the initial draft of this report. Finally, the contribution of Reinald G. Finke and Nancy Fredman at IDA in preparing computer programs is gratefully acknowledged.

ABSTRACT

This paper presents the results of a study of propulsion systems for surface combat vehicles which is intended to provide information useful to the Defense Advanced Research Projects Agency in identifying high-payoff R&D prospects. The primary purposes of the paper are to: (1) quantify the technological advances needed to make major improvements in appropriate military propulsion systems and indicate relative payoffs; and (2) provide criteria for evaluation of new propulsion system or subsystem concepts. The scope of the study is limited to an assessment of propulsion systems for four classes of surface combat vehicles: (1) main battle tanks; (2) light, tracked land combat vehicles; (3) high-mobility land combat vehicles; and (4) high-speed (more than 50 knots) ships. Fc propulsion subsystems, five engine types (Otto, Diesel, gas turbine, closed Brayton, Stirling), three transmission types (mechanical, hydrodynamic, electrical), and four thruster types (tracks, wheels, propellers, waterjets) are examined in some detail.

Results are presented in terms of technology goals which are within the bounds of what is judged to be physically possible and which together in relevant sets would have a major impact on the cost or performance of armored land combat vehicles or of high-speed ships. Relative payoffs within each set of goals are also estimated.

Partial CONTENTS:

vii

APPENDIX G

SIZE AND SPECIFIC FUEL CONSUMPTION RELATIONSHIPS FOR STIRLING ENGINES

Graham Walker

CONTENTS

APPENDIX G
SIZE AND SPECIFIC FUEL CONSUMPTION RELATIONSHIPS FOR STIRLING ENGINES
Graham Walker

A. IDEAL ENGINE PERFORMANCE

1. Ideal Cycles and Mechanical Arrangements

a. **Definition**. A Stirling engine is a heat engine that operates on a closed thermodynamic regenerative cycle in which the flow of working fluid is controlled by volume changes. The working fluid experiences periodic compression at low temperatures and expansion at high temperatures, so there is a net conversion of heat to work. Stirling engines may be rotary or reciprocating machines.

Other machines, with superficial similarity to Stirling engines, operate on a regenerative thermodynamic cycle but are equipped with valves to regulate the flow of working fluid. Such engines may be called Ericsson cycle machines (Appendix E). None of the subsequent discussion relates to this class of engines.

b. **The Ideal Cycle**. The thermodynamic reference cycle of the ideal Stirling engine consists of two isothermal and two constant-volume phases, as shown in pressure-volume and temperature-entropy coordinates in Fig. G-1a. An engine capable of operating on this cycle might conceivably consist of the elements shown in Fig. G-1b, comprising a cylinder containing two opposed pistons and the regenerator. The space between the two pistons is the working space and is divided by the regenerator into two parts, which may be called the expansion space and the compression space. The expansion space is maintained at a high temperature T_h and the compression space is maintained at a low temperature T_c, so that there is a temperature gradient of $T_h - T_c$

across the two transverse faces of the regenerator. The dis-
position of the pistons at the four terminal points of the cycle
and the cyclic piston displacement-time diagram are shown in
Fig. G-1c. It should be noted that in the ideal machine the
pistons have a discontinuous motion and that the expansion space
piston leads the compression space piston by a phase angle α.
If the machine acts as a refrigerator the operational cycle is
precisely similar except that the temperature relation between
the two spaces is reversed.
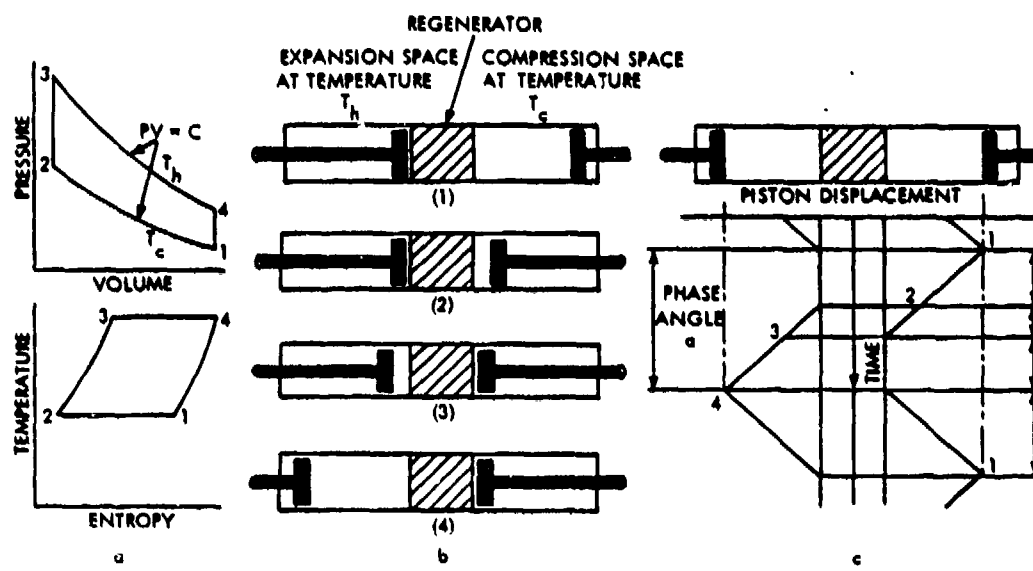
FIGURE G-1. Thermodynamic cycle of the ideal Stirling engine.

c. <u>Practical Cycle</u>. Practical Stirling engines normally
comprise the same basic elements as the ideal engine with the
addition of a heat exchanger at each end of the regenerator. In
most engines the volumes of the compression and expansion spaces
are varied in an approximately sinusoidal manner. This results
in a pressure-volume diagram that is a smooth, continuous en-
velope in which the four phases discussed above are merged.
Since the compression and expansion of the working fluid do not
now take place wholly in one or the other of the two spaces,
three pressure-volume diagrams may actually be drawn: one for

the expansion space, one for the compression space, and one for
the total enclosed volume, which includes the dead space. The
dead space may be defined as that part of the working space not
swept by one of the pistons, and it includes the internal volume
of the heat exchangers, the void volume of the regenerator, and
the volume of associated connecting ducts and ports.

A further important heat exchanger necessary to the system
when utilizing combustion heat is the exhaust-gas heat exchanger.
This may be of the regenerative or recuperative type. It is a
necessary component to extract from the hot combustion gases as
much energy as practicable. Losses to the exhaust in a Stirling
engine are a direct deduction of the energy available for conver-
sion, since the energy of the exhaust bypasses the engine. (In
the case of *internal* combustion engines the exhaust energy has
already passed through the engine conversion system.) As a con-
sequence of this, all the heat rejected from the system, apart
from the exhaust stack loss, must be transferred through the
cooling system. Thus the cooling system for Stirling engines is
approximately twice the capacity of the cooling system of inter-
nal combustion engines of the same power output.

d. <u>Possible Engine Arrangements</u>. All existing designs of
single-cycle reciprocating Stirling engines may be broadly
classified into two groups: (1) two-piston machines and (2)
piston-displacer machines. A further subdivision can be made
in this group between machines in which the piston and dis-
placer operate in a single cylinder and those in which separate
cylinders are provided for the displacer and the piston. An
example of each of these three arrangements is shown in Fig. G-2.
It is now generally recognized that the best possible configura-
tion for engines operating at high speeds and at high-pressure
levels is probably the single-cylinder piston-displacer type.
This arrangement allows for compact design with minimum mechan-
ical and flow losses and can be adequately balanced mechanically.
It is interesting to note that this was the arrangement used in

G-5
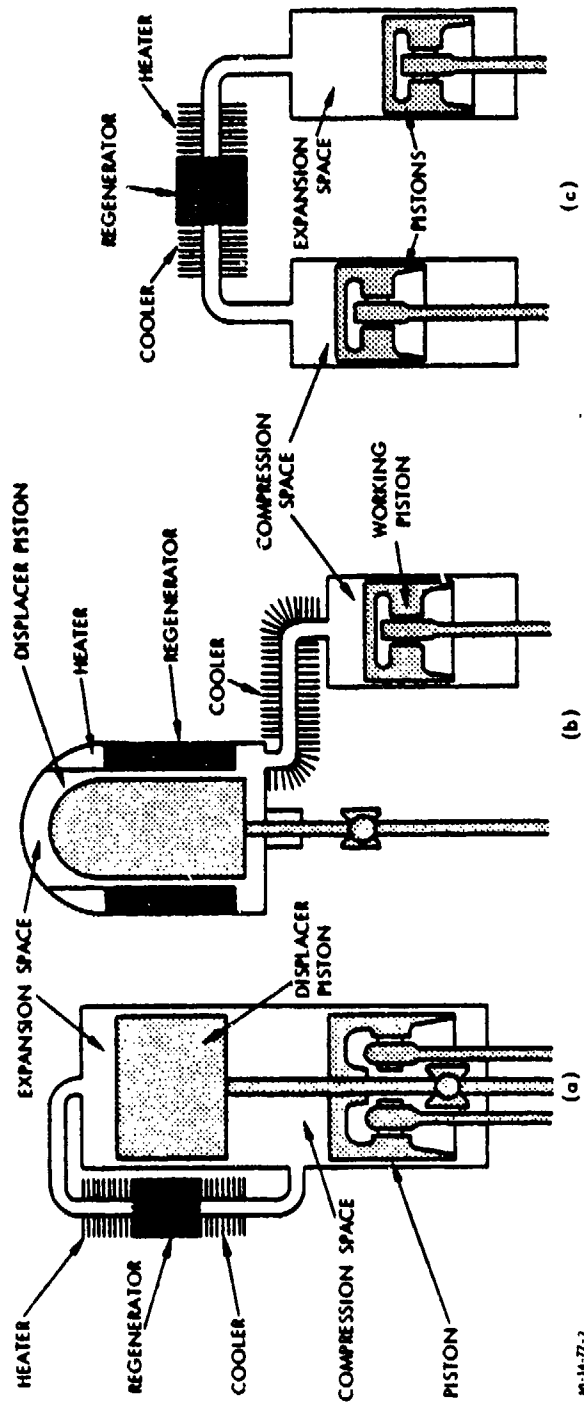
FIGURE G-2. Basic mechanical arrangements for single-cycle Stirling engines. In machines combining a working piston and a displacer piston, which helps to move the gas back and forth between the compression space and the expansion space, the two pistons can be in the same cylinder (a) or in separate cylinders (b). The third basic arrangement (c) is a two-piston Stirling engine.

the original engine built in 1816 by Stirling, who later went on to build engines with separate cylinders for the piston and displacer.

For high-power, multiple-cylinder engines it is possible to mount several single-cycle engines on a common crankshaft. However, the preferred alternative is to use the Rinia arrangement shown in Fig. G-3. This reduces the number of reciprocating elements per cylinder to one, half the number required in the multiple single-cycle case.

2. Ideal Cycle Performance

The cycle performance can be characterized by the thermal efficiency and various measures of specific power output (power output per unit mass flow in the cycle or power output per unit volume), as will be discussed subsequently. For convenience, two ideal cycles are considered here: (1) the ideal Stirling cycle, as depicted in Fig. G-1, and (2) an idealized version of the practical Stirling cycle, which incorporates sinusoidal piston and displacer motion, and inactive internal volumes associated with heat exchangers and clearances, but is ideal in the sense that internal losses are assumed to be absent.

a. **Performance of the Ideal Stirling Cycle.** The thermal efficiency of the ideal Stirling cycle is simply the Carnot efficiency; i.e.,

$$\eta = \frac{T_h - T_c}{T_h} \qquad (G-1)$$

This is due to the isothermal compression and expansion processes, which result in all heat addition at the maximum cycle temperature T_h and all heat rejection at the minimum cycle temperature T_c. Increase in the upper cycle temperature or decrease in the lower cycle temperature will result in an increase in the cycle efficiency as shown in Fig. G-4. Two curves are shown in this figure. One curve shows the effect on cycle efficiency with

G-7

PISTON
HEATER
COOLER
EXPANSION SPACE
REGENERATOR
COMPRESSION SPACE

10-16-77-3
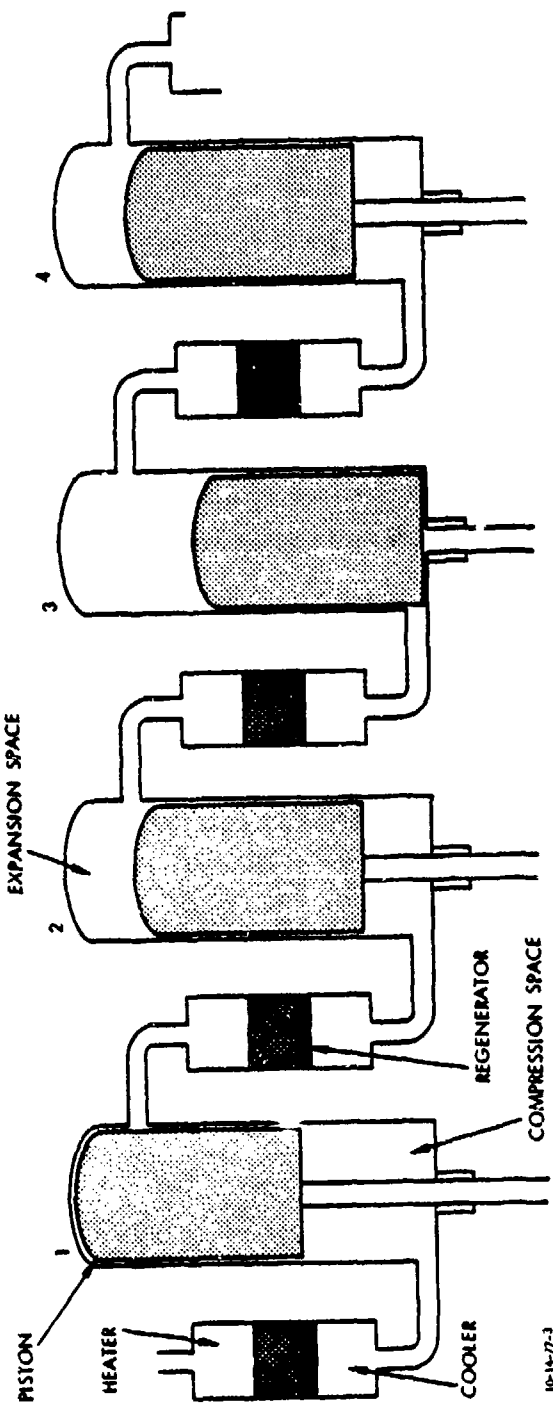
FIGURE G-3. Rinia arrangement of a multicylinder Stirling engine. The arrangement was devised by Herre Rinia of the Philips Research Laboratories in the Netherlands. Adjacent cylinders are interconnected through a regenerator. With this arrangement there is only one reciprocating element per cycle, rather than two elements as in single-cylinder engines.

G-8
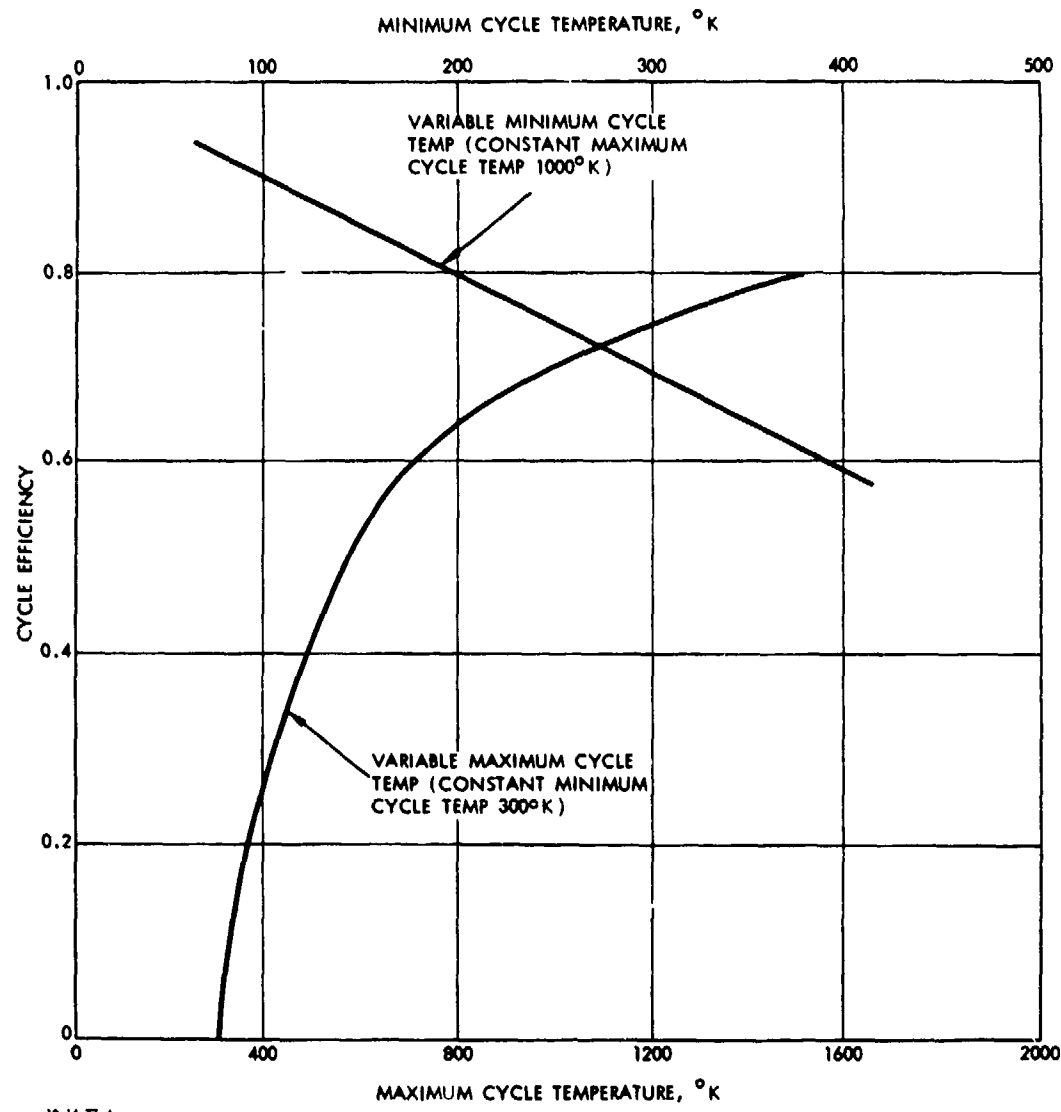
FIGURE G-4. Effect of maximum and minimum cycle temperature on ideal efficiency.

variable minimum cycle temperature and constant maximum cycle
temperature. The other curve shows the effect on cycle effi-
ciency with variable maximum cycle temperature and constant mini-
mum cycle temperature.

The specific power of the ideal Stirling cycle can be ex-
pressed as

$$\frac{P_o}{\dot{m}} = \eta \, \frac{P_{add}}{\dot{m}} \quad , \qquad\qquad (G-2)$$

where

P_o = output power

$\dot{m}$ = cyclic mass flow rate

P_{add} = heat addition rate.

For the ideal cycle, the heat addition rate is

$$P_{add} = \dot{m} \, R \, T_h \, \ln r, \qquad\qquad (G-3)$$

where R is the gas constant and r is the compression ratio
(ratio of maximum to minimum volumes). The power output per
unit volume is obviously proportional to the product of the
density, engine speed, and the power output per unit mass flow
rate.

The basic cycle parameters affecting specific power are
then:
1. Temperature limits of the working fluid
2. Pressure of the working fluid
3. Speed of operation of the engine.

The effect of temperature on engine power output can best
be seen by reference to the pressure-volume and temperature-
entropy diagrams for the ideal Stirling cycle shown in Fig. G-5.
In these diagrams, area 1-2-7-8 represents the energy supplied
to the cycle. Area 3-4-5-6 represents the heat rejected from
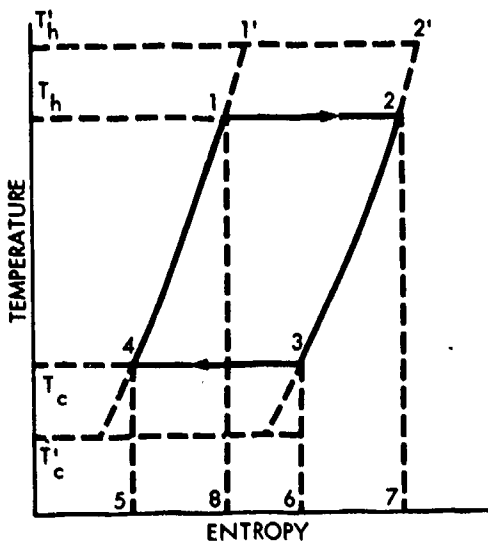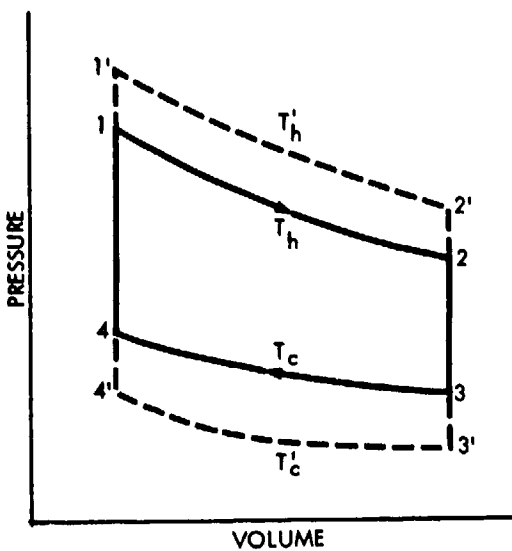
FIGURE G-5. Pressure-volume and temperature-entropy diagrams of ideal Stirling cycle, illustrating effect of variation in cycle temperature limits.

the cycle, and area 1-2-3-4 represents the work output of the cycle. Increase in the upper cycle temperature to the T_h' increases the work output by the area 1-1'-2'-2. Similarly, decrease in the minimum cycle temperature from T_c to T_c' increases the work output by the area 4-3-3'-4'.

Improvements in efficiency and specific output are progressive with separation of the upper and lower cycle temperatures. Practical limits are imposed, however, at the top temperature by the metallurgical limits of the materials used for the heated regions, and at the low temperature by the cooling media available for use in the engine. If a conventional water-cooled radiation system is used, the low-temperature limit is then controlled by the capacity of the radiator cooling system.

Specific power of the engine is related in linear fashion to both the pressure of the working fluid and the speed of operation. Increase in either (or both) causes a corresponding increase in the power output of the engine.

b. __Ideal Performance of a Practical Cycle__. The ideal
performance of a practical cycle, which includes continuous,
rather than discontinuous, motions of the pistons and/or dis-
placers, and which contains appropriate clearance and heat ex-
changer volumes, is influenced by several factors:

1. The ratio of the mean temperature levels in the ex-
    pansion or compression spaces, denoted by τ.
2. The form of the variations in the volumes of the two
    spaces. In most cases, this is nearly simple harmonic.
3. The ratio between the swept volumes in the two spaces,
    denoted by κ.
4. The angular phase displacement by which the expansion
    space leads the compression space, denoted by α.
5. The clearance volume which remains in either space when
    the volume of that space is reduced to a minimum. This
    may frequently be included in:
6. The "dead" volume of the heat-exchanger transfer pas-
    sages and the void volume of the regenerator. This
    may be compared with the maximum volume in the expansion
    space and the ratio denoted by χ.
7. The mean pressure level in the working space p_m.
8. The range and the nature of the variation in pressure
    of the working fluid during the cycle. This depends
    on the temperature and volume variations and so is not
    independent. Often, however, it is comparatively easy
    to measure, and so this becomes an important parameter.
9. The speed of the engine.
10. The physical characteristics of the working fluid.

A theory in which the pistons are assumed to move with
simple harmonic motion, and which indicates the influence of
the above parameters, was developed by Schmidt (Ref. G-1) and
has become the classical analysis of the cycle. The major
assumptions made are that the temperatures of the working fluid
in the compression and expansion spaces remain constant, that

G-12

the regenerative process is perfect, and that there are no internal losses.

The efficiency of cycle remains the Carnot efficiency, again due to the assumptions that all heat addition is accomplished at the maximum cycle temperature, all heat rejection is accomplished at the minimum cycle temperature, and there are no other losses.

The basic equation developed by Schmidt for the work output of a Stirling engine is

$$P = (1-\tau)Q_h = (1-\tau)\pi p_m \frac{V_E \delta \sin \theta}{1+(1-\delta^2)^{\frac{1}{2}}} , \qquad (G-3)$$

where

P = work output per cycle

τ = temperature ratio T_c/T_h

Q_h = heat added per cycle

p_m = mean pressure during cycle

V_E = volume of the expansion space

$\delta = \dfrac{(\tau^2+\kappa^2+2\tau\kappa\cos\alpha)^{\frac{1}{2}}}{\tau+\kappa+[4\kappa\tau/(\tau+1)]}$

$\theta = \tan^{-1}[(\kappa\sin\alpha)/(\tau+\kappa\cos\alpha)]$.

The power output is merely

$$P_o = P \omega, \qquad (G-4)$$

where ω is the cyclic rate.

Equation G-3 expresses the ideal output in terms of the four cycle parameters τ, κ, χ, and α. It is convenient to render this equation nondimensional to examine the influence of these parameters on specific output.

The process to make the power equation nondimensional may be carried out in a number of ways. On a basis of unit mass of working fluid, the power equation becomes

G-13

$$\frac{P}{mRT_c} = \frac{\pi(1-\tau)\delta \sin \theta(1+\delta \cos \theta)}{(1-\delta^2)^{\frac{1}{2}}[1-(1-\delta^2)](\tau+\frac{\kappa}{2}(1+\cos \alpha)+\delta)} \quad . \qquad (G-5)$$

The power equation may also be considered on a basis of some arbitrarily selected pressure and volume. Here the volume V_T used throughout is the sum of the maximum volumes in the expansion and compression spaces. The pressure may have any value, and here the maximum p_{max}, the minimum p_{min}, and the mean p_m cycle pressures have been used. The corresponding equations then become

$$\frac{P}{p_{max}V_T} = \frac{\pi(1-\tau)}{1+\kappa}\left(\frac{1-\delta}{1+\delta}\right)^{\frac{1}{2}}\frac{\delta}{[1+(1-\delta^2)^{\frac{1}{2}}]}\sin \theta \qquad (G-6)$$

$$\frac{P}{p_{min}V_T} = \frac{\pi(1-\tau)}{(1+\kappa)}\left(\frac{1+\delta}{1-\delta}\right)^{\frac{1}{2}}\frac{\delta}{[1+(1-\delta^2)^{\frac{1}{2}}]}\sin \theta \qquad (G-7)$$

$$\frac{P}{p_m V_T} = \frac{\pi(1-\tau)}{(1+\kappa)}\frac{\delta}{[1+(1-\delta^2)^{\frac{1}{2}}]}\sin \theta \quad . \qquad (G-8)$$

Obviously, many thousands of different combinations of the four design parameters τ, κ, χ, α are possible, and the work of optimization has been facilitated by the use of a digital computer. Some characteristic results are given in Fig. G-6. Each of the four separate sets of curves shows the effect on the engine power with variation in one of the design parameters. The values of the other three are fixed as indicated beneath each of the graphs. For reference the pressure ratio is also shown for the four sets of results. This has the unique value for any given combination

$$\frac{p_{max}}{p_{min}} = \frac{1+\delta}{1-\delta} \qquad (G-9)$$

G-14
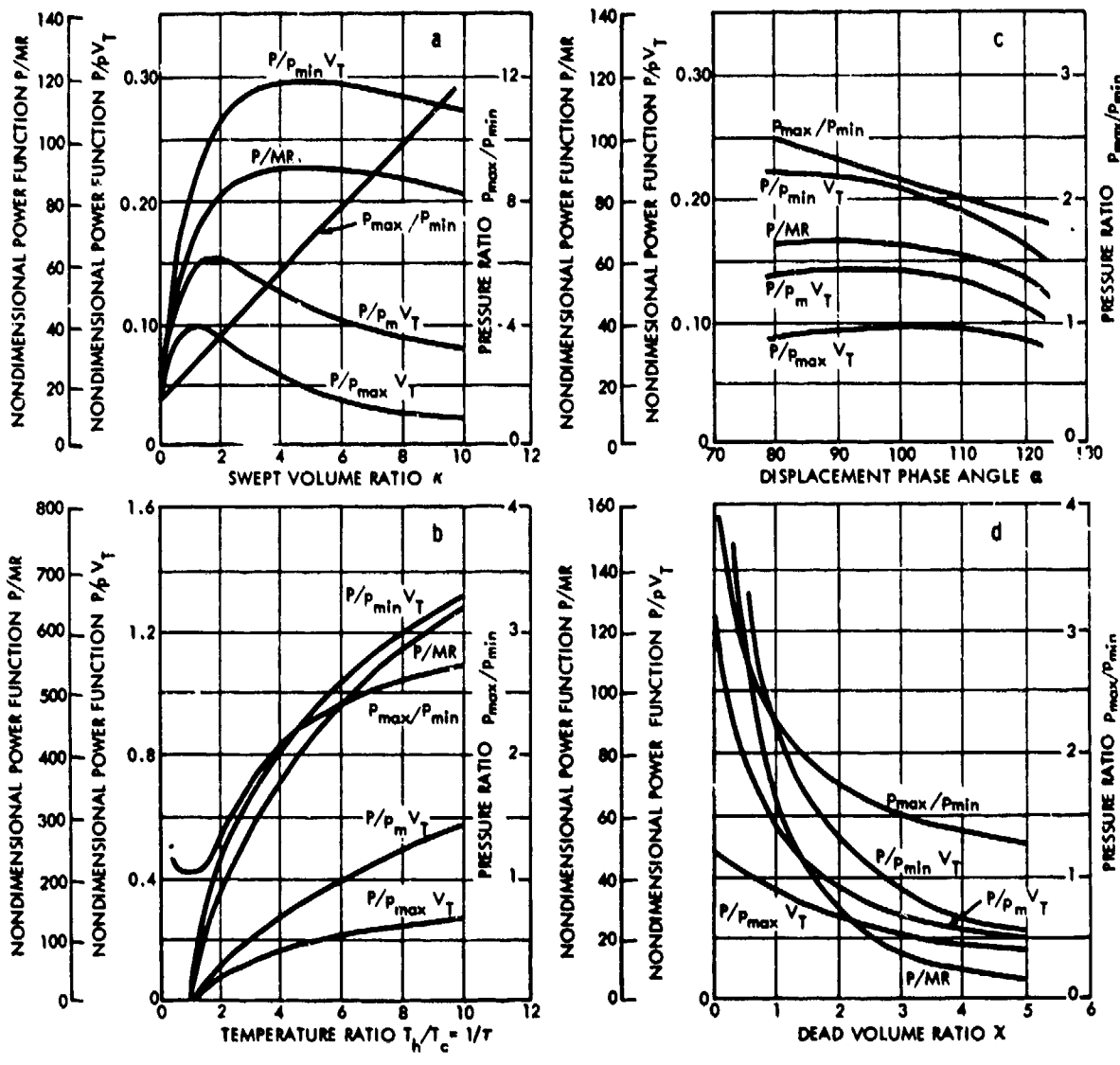
The power has been made nondimensional on four different bases. It should be noted that the optimum value of K or α depends upon the base selected.

a: $T = 0.5$; $\alpha = 90°$; $X = 1.0$ b: $T = 0.5$; $K = 1.0$; $X = 1.0$
c: $K = 1.0$; $\alpha = 90°$; $X = 1.0$ d: $T = 0.5$; $K = 1.0$; $\alpha = 90°$

10-14-77-6

FIGURE G-6.   Variation in the nondimensional power and pressure ratio with change in the four main design parameters according to the Schmidt isothermal analysis.

G-15

Reference to Fig. G-6 shows that the engine power output is not
greatly sensitive to the phase angle α but does tend to reach
a maximum value in the vicinity of 90 deg.

B. RELATIONSHIP OF ACTUAL PERFORMANCE TO IDEAL PERFORMANCE

The subsystems of a Stirling engine include five basic,
internally linked units:

1. Expansion space
2. Heater
3. Regenerator
4. Cooler
5. Compression space.

The working fluid is distributed throughout the five subsystems.
The distribution varies in cyclic fashion as the volumes of the
expansion and compression spaces vary in a cyclic but out-of-
phase fashion. The actual performance of Stirling engines de-
pends upon the detailed behavior of the fluid in the five sub-
systems, and the complexity of this behavior has thus far ham-
pered efforts to associate losses with the individual subsystems
and to quantify their impacts on engine performance. As ex-
amples of the complexities involved, Fig. G-7 shows the cyclic
pressure variations measured in the expansion and compression
spaces of a Stirling engine acting as a refrigerating machine, and
Fig. G-8 shows the variation of mass flow rates in and out of
the compression and expansion spaces of the same machine.

The major factors affecting the actual performance of a
practical Stirling cycle (as opposed to the ideal performance)
are:

1. The nature of the expansion and compression processes.
   At any instant these are probably adiabatic, but the
   issue is complicated by the fact that particular par-
   ticles are generally moving to and from regions at
   different temperature levels

G-16
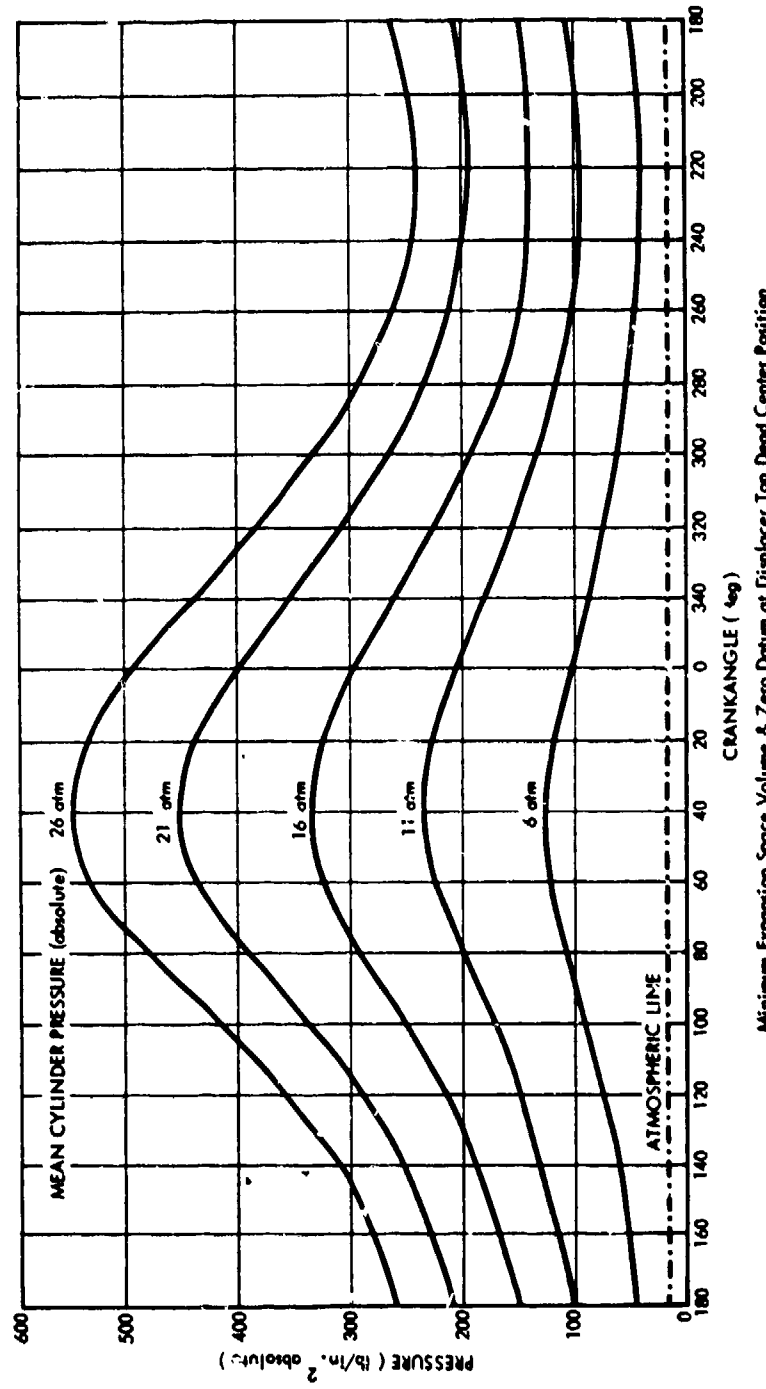
FIGURE G-7. Indicator diagram showing cyclic pressure variation in compression space of gas refrigerating machine running at 1450 rpm and with different mean pressures of the working fluid (hydrogen).
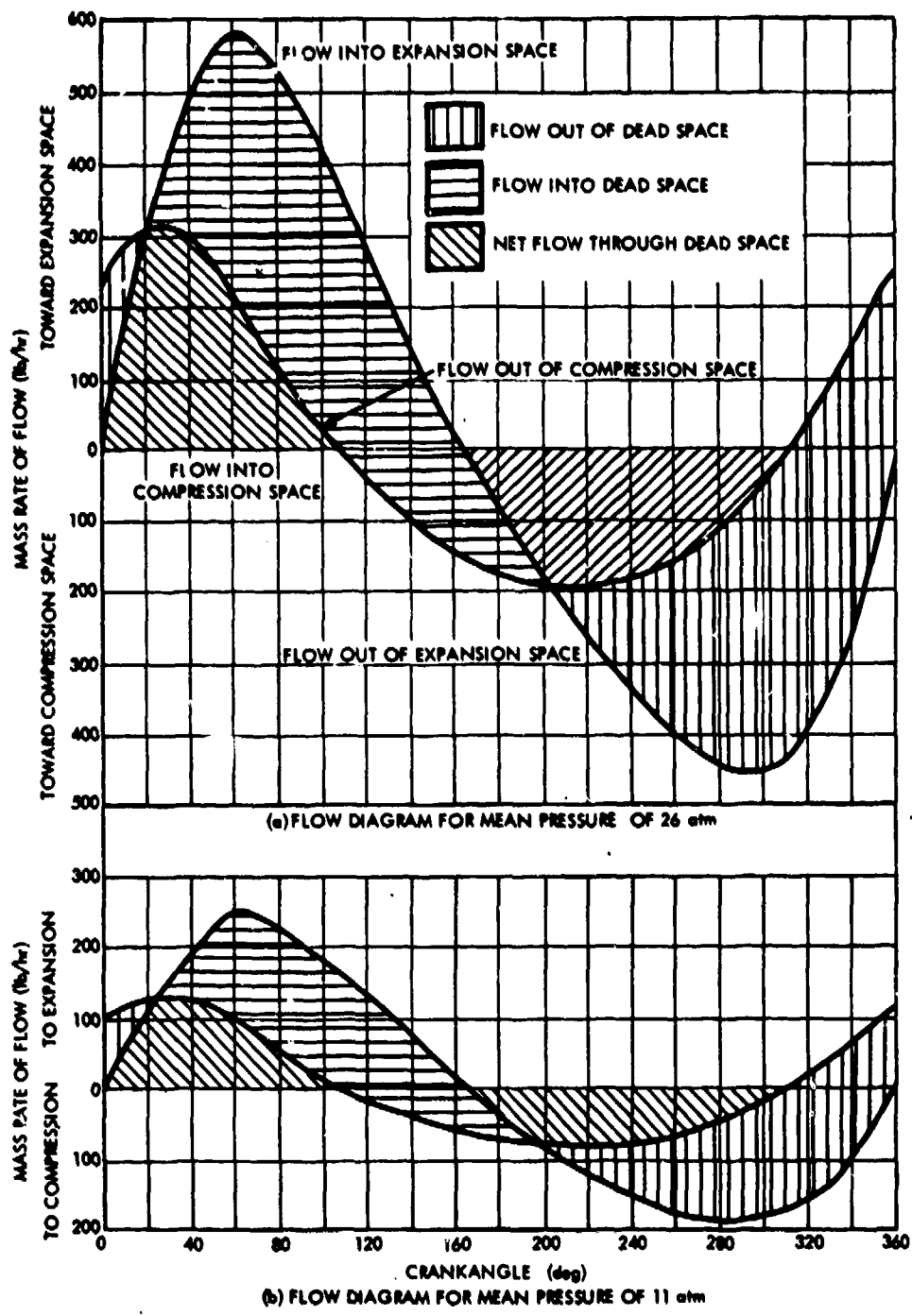
FIGURE G-8. Cyclic mass rate-of-flow diagrams for gas refrigerating machine.

2. The range and the nature of the variation in the temperature in either or both of the working spaces throughout the cycle

3. The heat transfer and flow characteristics of the heat exchangers

4. The effectiveness of the regenerator.

Theoretical efforts subsequent to those of Schmidt have endeavored to account for some of these factors. Other workers, notably Zeuner (Ref. G-2) and Gashof (Ref. G-3), introduced variations of the Schmidt analysis, but the next major contribution to the theory was made by Finkelstein (Ref. G-4). In this analysis it is possible to allow for a variation in the temperature of the working fluid when it is in the two working spaces. The two cases of interest initially are those in which the processes taking place in the expansion and compression spaces are (1) isothermal and (2) adiabatic, but it is possible to allow for any assumed variations between these limits. In the isothermal case, Finkelstein's final equations have closed solutions and can be reduced to a form identical with those of Schmidt, thus tending to confirm the logic of the analysis. Considerable complexity is introduced into the analysis when one allows for the fact that the processes taking place in the expansion and compression spaces may not be isothermal. Thus, the analysis treats nonisothermal compression and expansion processes, but even so a number of assumptions are made. These are summarized below in order to show the extent of unrealism in what is the best available theory at the present time. It is assumed that

1. The regenerative process is perfect

2. The instantaneous pressure is the same throughout the system

3. The working fluid obeys the characteristic equation $PV = RT$

4. There is no leakage and the mass of working fluid remains constant

5. The volume variations in the working space occur sinusoidally
6. The heat exchangers function perfectly
7. The cylinder-wall and piston-head temperatures are constant
8. There is perfect mixing of the cylinder contents
9. The temperature of the working fluid in the ancillary spaces is constant
10. The speed of the machine is constant
11. Steady state conditions are established.

Of these assumptions it is suggested that 1, 2, 3, and 6 are those most worthy of further analytical attention.

Advanced analysis of Stirling engines is invariably accomplished by the operation of computer simulation models that generate specific numerical data rather than the generalized relationships common to other forms of prime mover based on units of mass or volume. Thus, providing such generalized relationships for a Stirling engine would be highly speculative at present, and no attempt to do so is made here.* Experience in the interpretation of the results of computer simulation studies, supported by both experimental and other theoretical work, has, however, permitted the importance of some of the loss mechanisms to be assessed. These losses may be arranged in three groups:

1. Nonisothermal compression and expansion processes
2. Aerodynamic flow friction and mechanical friction losses
3. Imperfect regeneration.

Isothermal compression and expansion processes require infinite rates of heat transfer between the cylinder walls and the working fluid. Clearly this is not attainable in a practicable

---

*[Editor's Note: A crude attempt at portraying the actual performance of Stirling engines in terms of energy transfers and loss characterizations has been made in Annex G1.]

machine operating at some reasonable speed (up to 5000 rpm). Recent studies have been made of the effect in machine performance of zero heat transfer in the cylinders and infinite heat transfer in the heater and cooler units. This is thought to be close to the practical case. The results show that the temperature of the working fluid in the cylinders experiences considerable variation, as shown in the specimen case (Fig. G-9). The result of the temperature variation is to change the mass distribution in the machine and, as a consequence, to reduce very substantially the work *output* from the *expansion* space while the work *input* to the *compression* space remains about the same. The effect, of course, is to reduce the net output from the engine by up to 40%. Other theoretical work supports this evaluation of the magnitude of the losses associated with non-isothermal compression and expansion processes.

In considering the case of a refrigerator, Finkelstein found that the coefficient of performance was reduced from 1 with isothermal processes to 0.543 with adiabatic processes. Later, Stoddard (Ref. G-5) found that the efficiency of an engine was reduced from 50% with isothermal processes to 34.3% with adiabatic processes. The failure of a practical engine to attain isothermal processes of expansion and compression appears to be the prime cause of the relatively disappointing testbed performance of Stirling engines compared with ideal cycles.

The effects of aerodynamic flow losses are illustrated in Fig. G-10. This shows typical work diagrams for a Stirling engine, including diagrams for the expansion space, compression space, and total working space. The diagram for the expansion space is formed by tracing the pressure-volume variations in the expansion space in a clockwise direction. The area of the diagram is positive (output) work. The diagram for the compression space moves in the reverse direction. The area of the diagram is negative (input) work. The difference between these diagrams is net output of the engine.

G-21
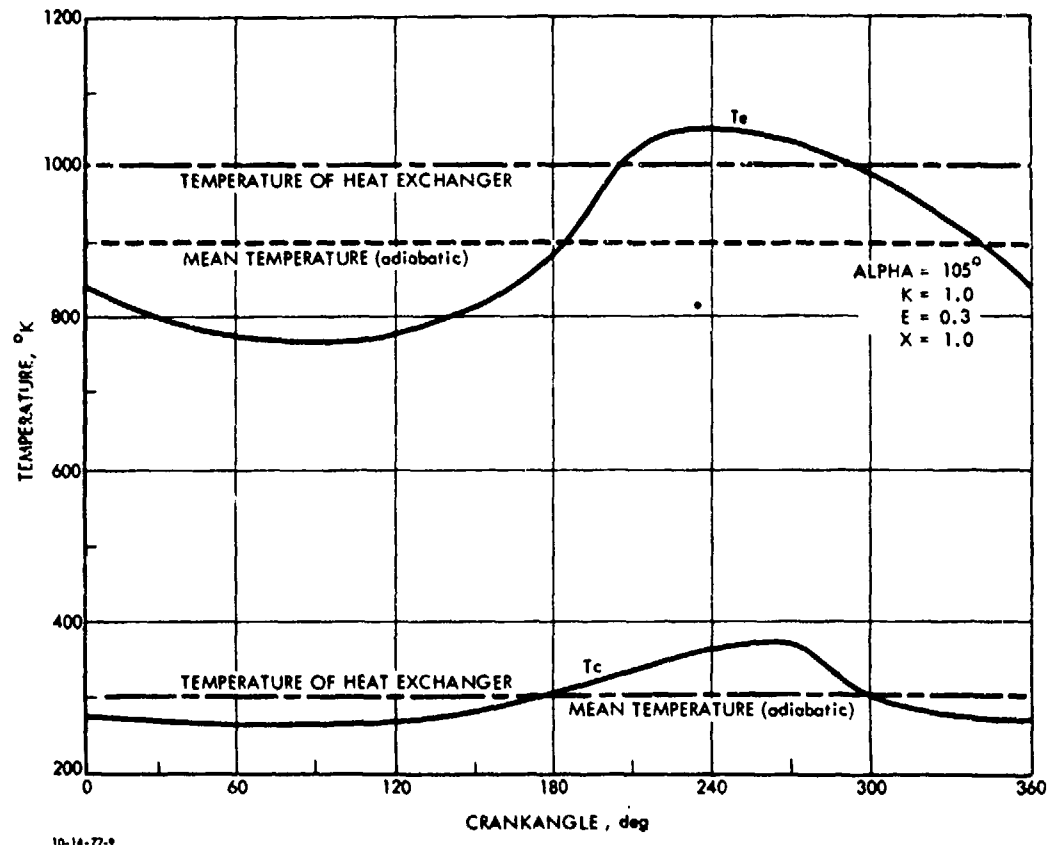
FIGURE G-9. Working fluid temperature versus crankangle for Stirling engine with adiabatic compression and expansion spaces.

G-22
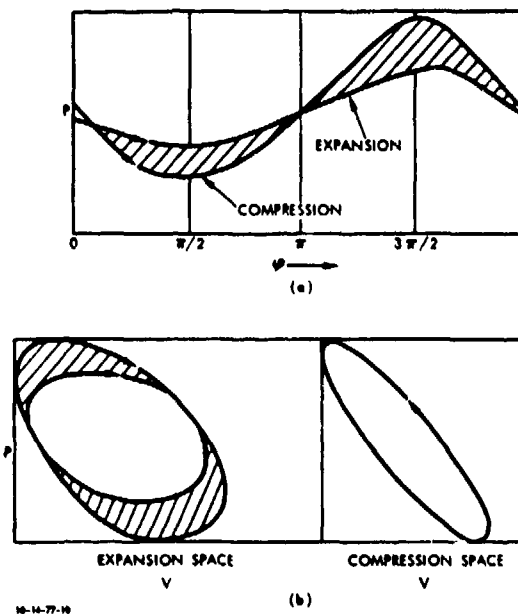
FIGURE G-10.   Effect of aerodynamic flow loss on the work dia-
grams of a Stirling engine.

Aerodynamic friction is manifest principally in the finely
divided metallic matrix of the regenerator and to a lesser extent
in the fine-bore tubes or fin-slots of the heater and cooler.
The effect of the aerodynamic friction is to cause a difference
in pressure between the working fluid in the compression and ex-
pansion spaces. - The range of pressure variation in the compres-
sion space is increased, while the range of pressure variation
in the expansion space is decreased. As shown by the shaded
areas in Fig. G-10, this causes an *increase* in compression work
and a *decrease* in expansion work. Both effects combine to di-
minish the available net engine output.

Mechanical friction in the engine arises from action of
rubbing seals on pistons and rods or from bearing and windage
in the crank mechanism. Typically, in a good engine design 15
to 20% of the available net engine output may be absorbed by
mechanical friction.

Losses due to imperfect regeneration arise from the ex-
istence of finite rates of heat transfer between the working

G-23

fluid and the regenerative matrix material. This causes the regenerator to function less effectively than the ideal case, where infinite rates of heat transfer are assumed. An adequate theory for the operation of a regenerative heat exchanger in a Stirling engine has not yet been developed. Therefore, it is not possible to quantify the effects of imperfect regeneration. Experience has shown that the regenerator is more significant in Stirling engines used as cryogenic cooling engines than in Stirling engines used as prime movers. In advanced engines, however, the regenerator is a key component of the system, and much engineering development effort has been expended in optimizing the balance between better heat transfer and minimizing aerodynamic friction. Much of the best research work on regeneration has been carried out in the research laboratories of Philips in Eindhoven, the Netherlands, and has not been published in the open literature.

C. OVERALL ENGINE CONSIDERATIONS

1. Efficiency and Specific Power of Actual Stirling Engines

There are no Stirling engines in commercial production apart from (1) those produced, mainly by the Philips Company, Eindhoven, for cryogenic refrigerators; (2) demonstration free-piston Stirling engines produced by Sunpower, Inc., Ohio; and (3) laboratory demonstration engines made by Leynold-Heraeus in West Germany.

Very substantial research and development effort on Stirling engines for automotive application has been invested over the past decade by Philips and their licensees, including:

- General Motors, U.S.A., from 1958 to 1970
- United Stirling, Sweden, since 1968
- M.A.N./MWM, West Germany, since 1968
- Ford Motor Co., U.S.A., since 1971.

References G-6 through G-9 summarize the progress of Philips
and their licensees. None of the engines discussed therein can
be considered as production versions of automotive engines. The
general target is to develop power units having compatible effi-
ciencies and specific outputs to internal combustion engines.
Table G-1 is a compilation of data on existing Stirling engines
and is from Ref. G-9.

2. Physical Limits of Performance

At the present stage of experimental development on theore-
tical understanding of Stirling engines, it is not possible to
define the physical limits of subsystem or component performance.

Despite the magnitude and intensity of the Philips effort
over the past 30 years, the total investment in research and
development effort in Stirling engines is virtually negligible
compared with the investment in spark-ignition or compression-
ignition engines. It is likely that a multitude of alternative
concepts and variants await exploration. Two examples of re-
cent innovations include the free-piston Stirling engine devel-
oped by Professor Beale at the University of Ohio and the use of
two-phase/two-component working fluids under investigation at
the University of Calgary. There appear to be many opportunities
in this field for innovations and improvements.

Cost is perhaps the principal impediment to increased appli-
cation of the Stirling engine. The cost arises from the multi-
plicity and the complexity of the heat-exchange equipment. Novel
and innovative approaches to accomplish the necessary heat-trans-
fer functions at significantly lower cost of materials or fabri-
cation would expand the likely range of applications. The de-
velopment of ceramic components may allow the use of higher maxi-
mum temperatures with consequent gains in both thermal efficiency
and specific output. The applications of ceramic units is being
actively pursued by several research and development groups.

TABLE G-1. STIRLING ENGINE CHARACTERISTICS*

Manufacture	Philips 4-215	Philips	United Stirling	GMRL GPU-3	Philips 4-235	Philips 40 hp	United Stirling	MAN-MWM 4-400
Status	Proto (Ford)	Analy. (optimized)	Proto	Proto	Proto	Proto	Analy. phase I	Proto
Type	Two piston	Piston-disp	Two piston	Piston-disp	Piston-disp	Piston-disp	Two piston	Piston-disp
Working fluid	H_2	He	H_2	H_2	He	H_2	H_2	H_e
Max press. $\bar{P}$, psi	2850	3200	2100	1000	3200	2058	2100	1570
No. of cylinders	4	4	4	1	4	1	8	4
Max bhp	170	275	49	11	200	40	200	120
RPM at max power,	4000-4200	1600	3400	3600	3000	1500	2400	1500
Max torque, ft-lbs	300	1287	120	19	253	108	520	475
RPM at max torque	1400	400	955	1200-2400	1000	900	600	700
Gas temp (hot), °F	1300	~1400	1275	1400[a]	1268	1200	1325	1170
Gas temp (cold), °F	175	160	160	180	108	60	160	105
Efficiency at max BHP (%)	24	30	24	25	30	30	30	29
Max efficiency, %	32[b]	43[b]	30	26.5[b]	31	38	35	32
Power at max efficiency, BHP	75	100	35	~7	175 (approx)	23	76	88
RPM at max efficiency	1100-2000	600	2000	1900	1800	725	1200	1000
Weight,[c] lb	750	N/D	N/D	165[d]	1272	N/D	1435	N/D
Dimensions,[c] ft.	N/D	4.9 x 4.3 x 2.2	N/D	1.3 x 1.3 x 2.4[e]	4.1 x 1.7 x 3.6	N/D	3.7 x 2.7 x 3.1	5.0 x 2.3 x 4.3
Applications	Auto	Bus	Auto	EPS	Bus	LRE	Bus, truck	LRE
References	6-6, 13, 22, 27	6-5	6-25, 28	6-3, 26, 38	6-39	6-8, 10	6-25	6-24

[a]Heater tube wall temperature.

[b] ...st brake efficiency accounting for all auxiliaries including cooling fan, combustion blower, and .ter pump, among others.

[c] ...ncludes all auxiliaries except cooling system with fan and transmission.

[d] ...ngine and auxiliaries less electrical power generator.

[e]Engine only.

Abbreviations:
   Proto: operating prototype engine; LRE: Laboratory Research Engine; Analy: computer design projection; N/D: no date; EPS: electric power supply.

*Source: Ref. G-9.

The high-capacity cooling systems required by Stirling engines have spurred the development of improved "folded-front" radiator systems for automotive application. However, this same technology can also be applied directly to water-cooled internal combustion engines, so the unfavorable comparison of Stirling engines to internal combustion engines remains. It is worth noting that the cooling problem disappears in a marine environment. It is likely that Stirling engines may find marine applications where silent operation or the ability to operate on isotope heat or unconventional chemical reaction energy is of value.

To gain a high specific output it has been necessary to use helium or hydrogen as the working fluid at pressures of several thousand pounds per square inch. This has made the seal problem particularly acute. Much internal development on seals has been carried out by Philips and its licensees. A promising approach was the development by Philips of the roll-sock seal (Ref. G-9). This provides a hermetic seal between the high-pressure working fluid and an equally high-pressure hydraulic "reservoir." In this way, the problem of the pneumatic seal is converted into a problem of hydraulic sealing. The viscosity of gas to oil is such that the hydraulic seal is comparatively easy to accomplish. However, the integrity of the roll-sock seal has yet to be adequately demonstrated for the life considered routine for heavy traction motors. Further, the system is relatively complicated and a simpler, more reliable system is preferred.

One possibility still in the early research stage is the use of a working fluid composed of two components, one of which experiences a phase change from liquid to vapor when passing from the cold compression space to the hot expansion space. This has the effect of increasing the virtual compression ratio of the engine. Calculations made using a modified Schmidt analysis indicate that the specific output may be double that attainable with a conventional gaseous working fluid. This work is at a preliminary, laboratory stage of experimentation and has yet to be demonstrated on an operational prototype engine.

The possibilities are so broad and the field is so virtually unexplored, except in certain narrow specialized areas, that excellent opportunities exist for original and innovative contributions to the technology of Stirling engines. It is likely that engines could eventually be developed with efficiencies and specific outputs up to 50% greater than existing prototype units.

3. Advantages and Disadvantages of Stirling Engines

The principal advantages of Stirling engines when used as prime movers generating power from heat supplied are:

1. The peak efficiency and part-load performance are comparable with Diesel engines.
2. The engine can use any source of external heat, in particular, combustion of any fossil fuel.
3. There are no valves or periodic explosions, so the engine operates virtually without noise.
4. The vibration level is very low.
5. The starting torque and torque/speed characteristic is favorable for traction applications.
6. The combustion products are not in contact with the moving parts, so the engine has the potential for long life with minimum wear and virtually zero consumption of lubricating oil.
7. The engine can be used for vehicle braking with negative torques up to 80% of the full-load torque.
8. The engine has a fast response and can accept sudden changes in the load.
9. It is not affected by a dusty or contaminated environment.
10. The engine starts reliably and has the potential for a low maintenance requirement.
11. Combustion takes place externally and continuously in a chamber with heated walls, so the unburned hydrocarbon

content of the exhaust is very low. By recirculation
of a sizeable fraction of the exhaust, the oxides of
nitrogen in the exhaust can be drastically reduced.
In such form the engine can achieve the lowest degree
of air pollution yet demonstrated.

The principal disadvantages of Stirling engines are:

1. That a cooling system is required of approximately
   twice the capacity per horsepower compared with con-
   ventional internal combustion engines.

2. To achieve high efficiencies and specific outputs, it
   is necessary to use helium or hydrogen as the working
   fluid at very high pressures (2 to 4,000 lb/in^2).

3. The multiplicity of heat exchangers increases the cost
   to a value at least twice that of a Diesel engine of
   corresponding power.

REFERENCES, APPENDIX G

G-1. G. Schmidt, "Theorie der Lehmann'schen calorischen Maschine," _Z. Ver. dtsch. Ing._, Vol. 15, No.1, 1871.

G-2. G. Zeuner, _Technische Thermodynamic_, Vol. 1, Leipzig, 1887, pp. 347-357.

G-3. F. Grashof, _Theorie der Kraftmaschinen_, Hamburg, 1890.

G-4. T. Finkelstein, "Generalized Thermodynamic Analysis of Stirling Engines," Annual Meeting of Soc. Automot. Engrs., New York, 1960.

G-5. D. Stoddart, _Generalized Thermodynamic Analysis of Stirling Engines_, Thesis, University of Durham, 1960.

G-6. R. J. Meijer, "Prospects of the Stirling Engine for Vehicular Propulsion," _Philips Technical Review_, Vol. 31, No. 5/6, 1970, pp. 168-185.

G-7. M.A.N.-MWM, Entwicklungsgruppe Stirlingmotor, Augsburg, _Advanced Development on Stirling Engines at MWM_, F. A. Zacharias, undated.

G-8. C.B.S. Alm, S. G. Carlquist, P. F. Kuhlmann, K. H. Silverquist, and F. A. Zacharias, "Environmental Characteristics of Stirling Engines and their Present State of Development in Germany and Sweden," _Proc. CIMAC_, Washington, D.C., March-April 1973.

G-9. Jet Propulsion Laboratory, California Institute of Technology, Pasadena, "The Stirling Automotive Power System," Chapter 6, Vol. 11 of _Should We Have a New Engine -- An Automobile Power Systems Evaluation_, August 1975.

ANNEX G1

PERFORMANCE OF STIRLING ENGINES IN TERMS OF POWER TRANSFER PARAMETERS

CONTENTS

PERFORMANCE OF STIRLING ENGINES IN TERMS
OF POWER TRANSFER PARAMETERS*

A. IDEAL STIRLING CYCLE PERFORMANCE

The performance of the ideal Stirling cycle (isothermal compression and heat rejection, constant-volume regeneration, and isothermal expansion and heat addition) can be characterized in terms of the following power transfer parameters common to all heat engines:

1. The heat addition rate, P_{add}
2. The internal power transfer, P_{int}, consisting of the energy transfer rate to pre-heat-addition processes from processes subsequent to the initiation of heat addition
3. The intermediate power transfer, P_x, consisting of the sum of the energy transfer rates associated with adding or rejecting heat across mechanical surfaces, P_x
4. The energy flow rate associated with the working fluid at the beginning of the cycle, P_1
5. The power output, P_o.

Consider a Stirling cycle with a perfect gas as a working fluid (gas constant, R; specific heats, c_p and c_v; ratio of specific heats, γ), operating between temperatures T_{min} and T_{max}, with a compression ratio (ratio of maximum cycle volume to minimum cycle volume), r, and with a cyclic mass flow rate, $\dot{m}$. The heat addition rate is

*The principal authors of this report (FRR and DMD) bear total responsibility for this annex.

G-33

$$P_{add} = \dot{m} R T_{max} \ln r. \qquad (G1-1)$$

The internal power transfer is the sum of compression power and regenerative heat transfer rate:

$$P_{int} = \dot{m} R T_{min} \ln r + \dot{m} c_v (T_{max} - T_{min}) . \qquad (G1-2)$$

The intermediate power transfer is the sum of the heat addition rate and the heat rejection rate:

$$P_x = P_{add} + R T_{min} \ln r. \qquad (G1-3)$$

The power output is the difference between expansion and compression power:

$$P_o = \dot{m} R (T_{max} - T_{min}) \ln r, \qquad (G1-4)$$

and the "inlet power" is

$$P_i = \dot{m} c_p T_{min} . \qquad (G1-5)$$

The cycle efficiency can be conventionally written as

$$\eta = \frac{P_o}{P_{add}} = 1 - \frac{T_{min}}{T_{max}} , \qquad (G1-6)$$

and, for a typical hydrocarbon fuel the specific fuel consumption is

$$sfc = \frac{0.138}{\eta} \quad lbm/hp\text{-}hr. \qquad (G1-7)$$

The power output can be normalized with respect to the "inlet power" as

$$\frac{P_o}{P_i} = \frac{\gamma-1}{\gamma} \left(\frac{T_{max}}{T_{min}} - 1 \right) \ln r. \qquad (G1-8)$$

G-34

For comparison with other heat engines on the basis used throughout this report, the total internal power transfer per unit power output is

$$\frac{P_{it}}{P_o} = \frac{P_{int} + P_x}{P_o} = \frac{2 + T_{max}/T_{min}}{(T_{max}/T_{min} - 1)\ln r} + \frac{1}{(\gamma - 1)\ln r} , \quad (G1-9)$$

and the normalized heat addition rate is

$$\frac{P_{add}}{P_1} = \frac{\gamma - 1}{\gamma} \frac{T_{max}}{T_{min}} \ln r . \quad (G1-10)$$

Inasmuch as the performance characteristics (sfc and P_o/P_1) depend only upon T_{max}/T_{min} and r, as do the power transfer parameters, it is clear that the former can be expressed in terms of the latter.

The performance characteristics of the ideal Stirling cycle are shown in Fig. G1-1, in terms of sfc and specific power output P_o/P_1, as functions of the total internal power transfer ratio and the temperature ratio. It can be observed that at compression ratios likely to be used in Stirling engines--2 to 4 (see Fig. G-6)--3 to 5 horsepower must be transferred internally per unit output horsepower.

B. IMPACT OF LOSSES ON STIRLING CYCLE PERFORMANCE

As discussed earlier in this appendix, the quantification of the various losses that occur in an actual Stirling engine is a complex matter. In order to gain some appreciation of the impact of the major losses on engine performance, the following assumptions will be made:

1. The compression and expansion processes are adiabatic (and isentropic), rather than isothermal.
2. Heat addition, heat rejection, and regeneration are accomplished at constant volume.

G-35
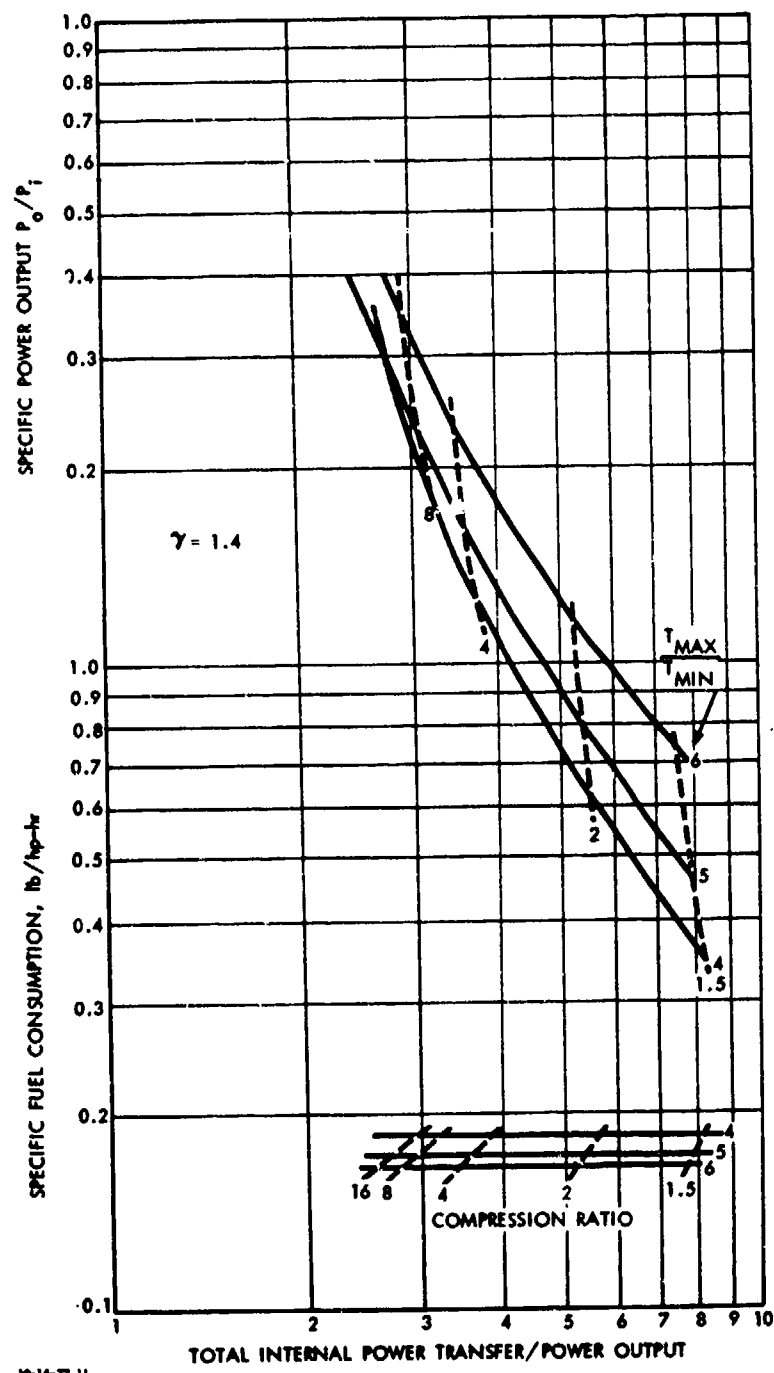
FIGURE G1-1. Performance characteristics of the ideal Stirling engine.

G-36

3. Heater losses can be represented by a heater efficiency

$$\eta_h \equiv \frac{P_{add,c}}{P_{add}} , \qquad\qquad (G1-11)$$

where $P_{add,c}$ is the heat addition rate to the working fluid and P_{add} is the fuel energy consumption rate.

4. The thermal performance of the cooler can be represented by

$$\frac{\Delta T_c}{T_{min}} \equiv \frac{T_1 - T_{min}}{T_{min}} , \qquad\qquad (G1-12)$$

where T_{min} is the available coolant temperature and T_1 is the minimum temperature of the working fluid.

5. Regenerator thermal performance can be represented by an effectiveness

$$\epsilon_r \equiv \frac{T_3 - T_2}{T_4 - T_2} , \qquad\qquad (G1-13)$$

where T_3 is the temperature at the initiation of heat addition, T_2 that after compression, and T_4 that at the end of expansion.

6. The effects of all frictional losses (both internal and external to the cylinders) can be represented by an efficiency

$$\eta_f \equiv \frac{P_o}{P_{o,c}} , \qquad\qquad (G1-14)$$

where $P_{o,c}$ is the power extracted from the working fluid in the absence of frictional losses and P_o is the power output of the engine.

The effect of these assumptions is to produce an approximation to the cycle which actually occurs in a Stirling engine as shown in Fig. G1-2. Obviously, the approximation is rather severe compared to the classical Stirling cycle, and better approximations could undoubtedly be made. It is felt, however, that

10-14-77-12
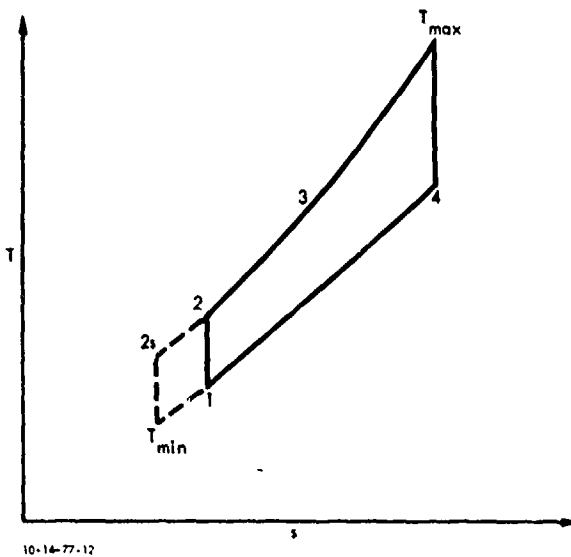
FIGURE G1-2.   An approximation to the thermodynamic cycle in an
              actual Stirling engine.

this approximation yields reasonably simple representations of
the major losses.

The thermal efficiency of the engine can be written as

$$\eta = \eta_h \, \eta_f \, \eta_c \, ,$$ (G1-15)

where η_c is the efficiency of the cycle shown in Fig. G1-2.
Similarly, the engine power output is

$$P_o = \eta_f \, P_{o,c} \, ,$$ (G1-16)

where $P_{o,c}$ is the power output which would be obtained from the
cycle.

Although the cycle efficiency and power output can be de-
termined in a straightforward way, it is convenient to isolate
the impacts of the individual losses in the following way. The
cycle efficiency can be written as

G-38

$$\eta_c \equiv \frac{P_{o,c}}{P_{add,c}} = \frac{P_{o,cs} - P_{loss}}{P_{add,cs} + P_{add,loss}} , \qquad (G1\text{-}17)$$

where $P_{o,cs}$ is the power output in the absence of losses, P_{loss} is the loss of power output due directly to losses, $P_{add,cs}$ is the heat addition rate in the absence of losses, and $P_{add,loss}$ is the increased heat addition due directly to losses. Assuming the impact of losses is small, this can be written as

$$\eta_c = \eta_{cs} - \frac{P_{loss}}{P_{add,cs}} - \frac{P_{add,loss}}{P_{add,cs}} , \qquad (G1\text{-}18)$$

where η_{cs} is the efficiency of the cycle in the absence of the losses. In the present case, the only loss which directly detracts from cycle power output is that associated with the cooler:

$$P_{loss} = \left(\frac{\Delta T}{T_{min}}\right) P_{cool,s} \equiv \left(\frac{\Delta T}{T_{min}}\right) \dot{m} \ c_v \ (T_{25} - T_{min}). \quad (G1\text{-}19)$$

Similarly, the only loss which affects cycle heat addition is that due to the regenerator:

$$P_{add,loss} = (1-\epsilon) P_{reg,s} \equiv (1-\epsilon) \dot{m} \ c_v \ (T_4 - T_2) . \qquad (G1\text{-}20)$$

In a general way, then, the impact of losses on cycle efficiency depends upon both the loss factor and the amount of power transferred in the process; i.e.,

$$\eta_c = \eta_{cs} - \left(\frac{\Delta T}{T_{min}}\right) \frac{P_{cool,s}}{P_{add,cs}} - (1-\epsilon) \frac{P_{reg,s}}{P_{add,cs}} . \qquad (G1\text{-}21)$$

G-39

Similarly, the specific power output can be written as

$$\frac{P_{o,c}}{P_i} = \frac{P_{o,cs}}{P_i} - \left(\frac{\Delta T}{T_{min}}\right)\left(\frac{P_{cool,s}}{P_{add,cs}}\right)\left(\frac{P_{add,cs}}{P_i}\right) \ . \qquad (G1-22)$$

By rather straightforward manipulation, the cycle efficiency and specific power output can be expressed in terms of the temperature ratio T_{max}/T_{min} and the compression ratio r as

$$\eta_c = 1 - r^{\gamma-1}\frac{T_{min}}{T_{max}} - \left(\frac{\Delta T}{T_{min}}\right)r^{\gamma-1}\frac{T_{min}}{T_{max}} - (1-\varepsilon)\left[\frac{\dfrac{1}{r^{\gamma-1}}\dfrac{T_{max}}{T_{min}} - r^{\gamma-1}}{\dfrac{1}{r^{\gamma-1}}\dfrac{T_{max}}{T_{min}}(r^{\gamma-1}-1)}\right]$$

$$(G1-23)$$

and

$$\frac{P_o}{P_i} = \frac{1}{\gamma}\left\{\frac{T_{max}}{T_{min}}\left(1 - \frac{1}{r^{\gamma-1}}\right) - \left(1 + \frac{\Delta T}{T_{min}}\right)(r^{\gamma-1}-1)\right\}\eta_f \ . \qquad (G1-24)$$

Noting that

$$P_{add,c} = \dot{m}\,c_v\,(T_{max} - T_3)$$

$$P_{int} = \dot{m}\,c_v\,(T_3 - T_1)$$

$$P_x = P_{add,c} + (1-\eta_c)\,P_{add,c} \ ,$$

one can also write the relevant power transfer parameters in the same terms:

$$\frac{P_{add}}{P_i} = \frac{1}{\gamma\eta_h}\left\{\frac{1}{r^{\gamma-1}}\frac{T_{max}}{T_{min}}(r^{\gamma-1}-1) + (1-\varepsilon)\left(\frac{1}{r^{\gamma-1}}\frac{T_{max}}{T_{min}} - r^{\gamma-1}\right)\right\}$$

$$(G1-25)$$

G-40

$$\frac{P_1}{P_0} = \frac{1}{(P_0/P_1)} \left[\frac{1}{\gamma} \left(\frac{T_{max}}{T_{min}} - 1 - \frac{\Delta T}{T_{min}} \right) + (1-\eta_c)\eta_h \frac{P_{add}}{P_1} \right]$$

(G-1-26)

Again, the performance characteristics can be determined as functions of the power transfer parameters.

The performance characteristics of this approximation to the cycle in Stirling engines are shown in Fig. G1-3 for a working fluid with $\gamma = 1.4$ and loss factors of $\eta_h = 0.9$, $\Delta T_c/T_{min} = 0.04$, $\epsilon_r = 0.90$, and $\eta_f = 0.80$, all of which seem reasonably consistent with current state-of-the-art values. It may be observed that the optimum compression ratio, for minimum sfc, is in the range of 3 to 4, which seems to be the range in which Stirling engines currently operate. The minimum sfc for $T_{max}/T_{min} = 4$ is in the vicinity of 0.37, which seems not inconsistent with current state-of-the-art values (somewhat higher sfc at somewhat lower temperature ratio). The losses obviously have a large impact, roughly doubling the sfc from the Carnot value.

The impact of the individual losses on performance characteristics is shown in Fig. G1-4 for $T_{max}/T_{min} = 4$. The origin of the minimum in sfc is apparently a balance between regenerator losses and nonisothermal losses, both of which can become extremely large, but at opposite ends of the compression ratio scale. The dominant losses are as previously discussed in this appendix—nonisothermality, imperfect regeneration, and friction, with heater losses a lesser, but important, contributor.
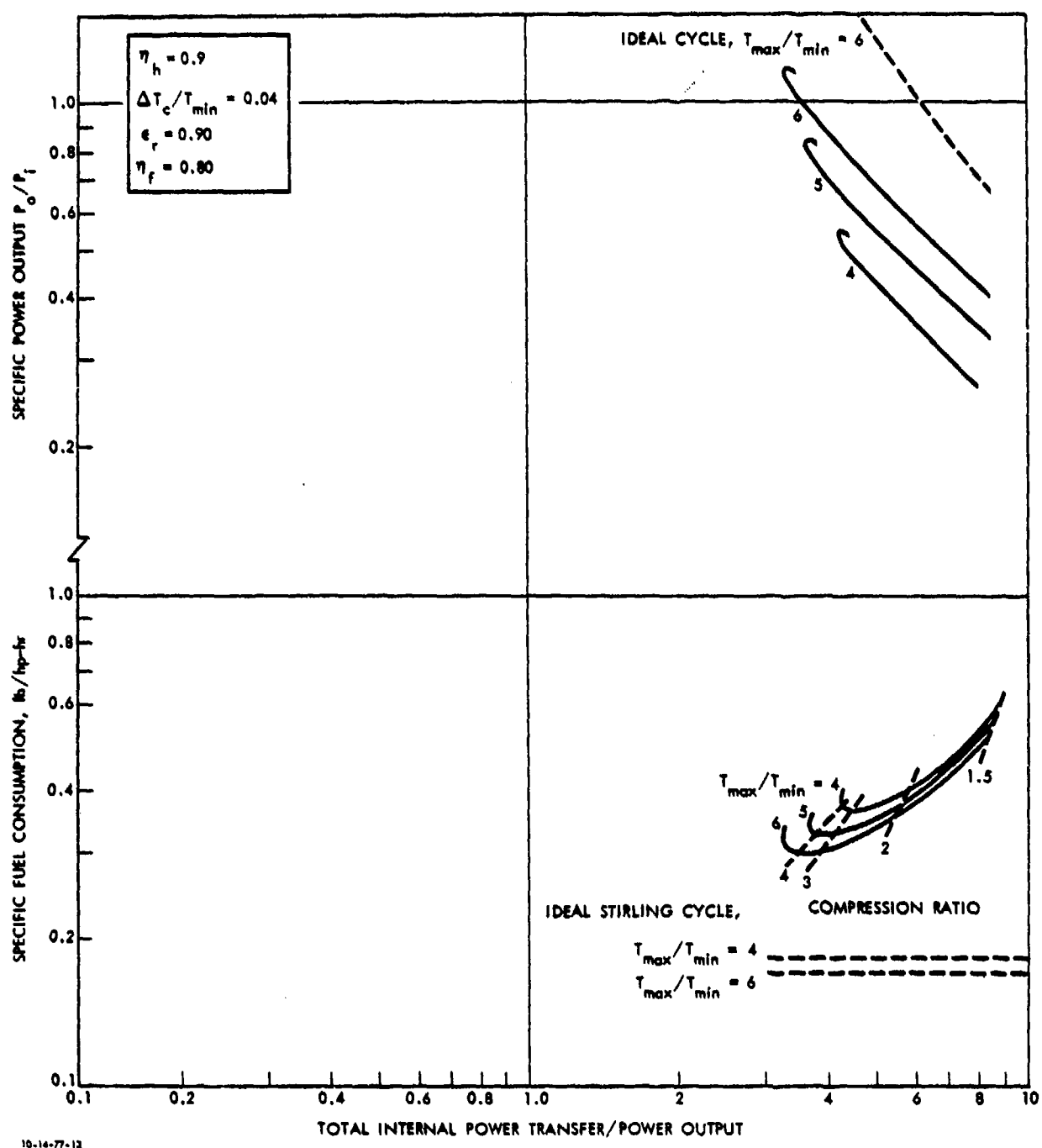
FIGURE G1-3. Performance characteristics of an approximation to an actual Stirling engine.
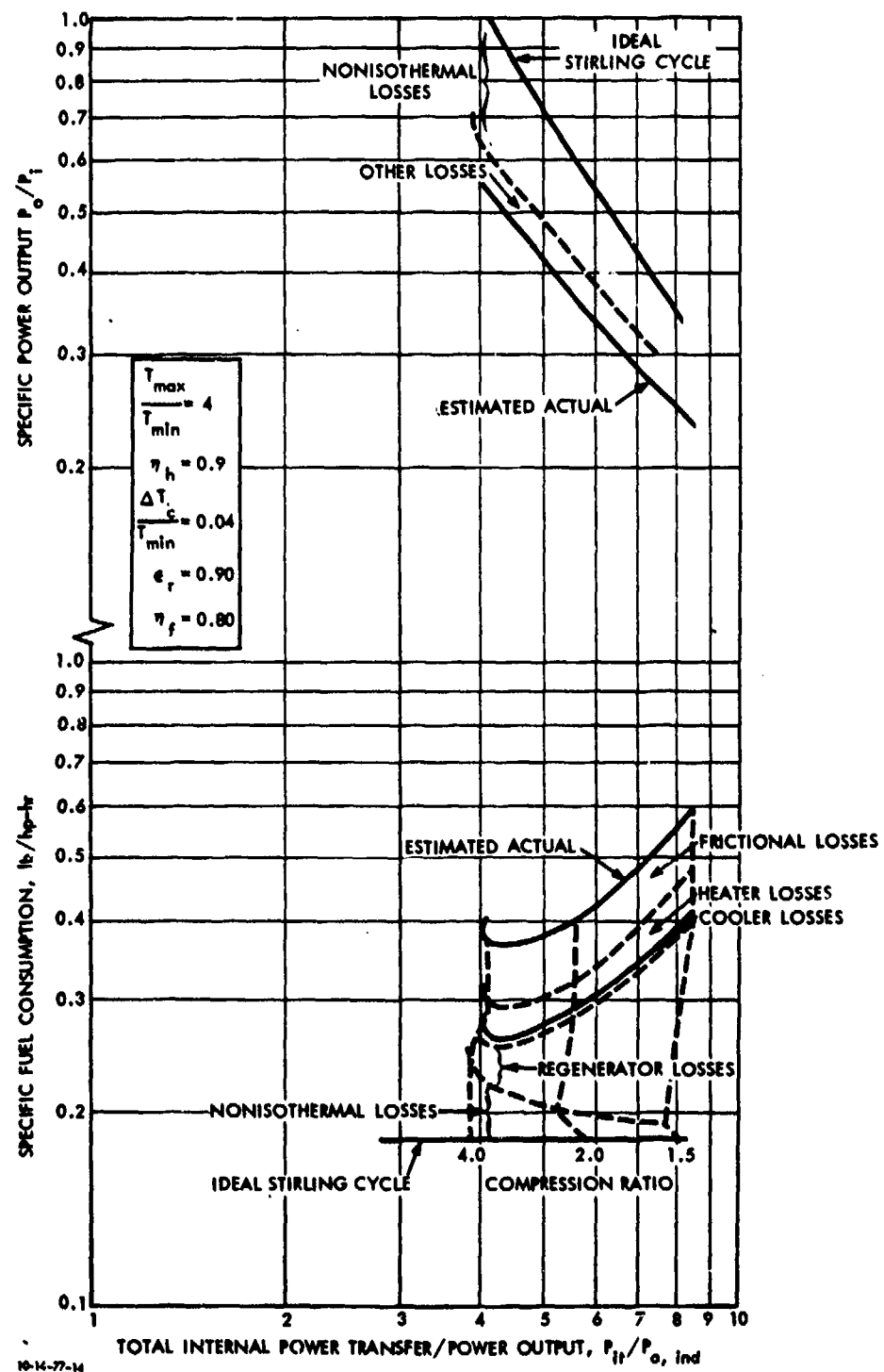
FIGURE G1-4. Impact of individual losses on approximate Stirling engine performance.

GLOSSARY, APPENDIX G

c_p Specific heat at constant pressure of the working fluid

c_v Specific heat at constant volume of the working fluid

$\dot{m}$ Cyclic mass flow rate

P Work output per cycle

P_{add} Rate of heat addition to the engine

$P_{add,c}$ Rate of heat addition to the working fluid

$P_{add,cs}$ Rate of heat addition in the absence of losses

$P_{add,loss}$ Increment in heat addition rate due to losses

$P_{cool,s}$ Heat-transfer rate in cooler in the absence of losses

P_i Rate of energy transport associated with the working fluid, $\dot{m}c_p T_{min}$

P_{int} Internal power transfer; the energy transfer rate to the working fluid before heat addition from the working fluid subsequent to the initiation of heat addition.

P_{it} Total internal power transfer, $P_o + P_x$

P_{loss} Losses in power output

p_m Mean pressure of the working fluid

p_{max} Maximum pressure of the working fluid

p_{min} Minimum pressure of the working fluid

P_o Power output of an engine
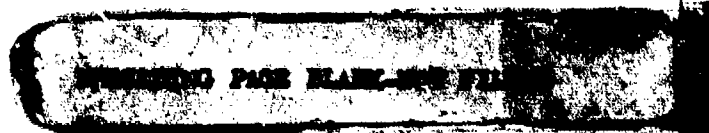
Symbol	Description
$P_{o,c}$	Power output of a cycle
$P_{o,cs}$	Power output of a cycle without losses
$P_{o,ind}$	Power output of an engine in the absence of frictional losses
$P_{reg,s}$	Heat-transfer rate in an ideal regenerator
P_x	Intermediate power transfer; the sum of the heat-transfer rates in the heater and cooler
Q_h	Heat addition per cycle
r	Compression ratio; ratio of maximum working fluid volume to minimum working fluid volume
R	Gas constant of working fluid
sfc	Specific fuel consumption, fuel flow rate per unit power output, lb/hp-hr
T	Temperature of the working fluid
T_c	Minimum temperature of working fluid in cycle
T_h, T_{max}	Maximum temperature of working fluid in cycle
T_{min}	Minimum temperature available for the cooler
V	Volume
V_E	Maximum volume of the expansion space
V_T	Sum of the maximum volumes of compression and expansion spaces
α	Angular phase displacement by which expansion space volume leads compression space volume
γ	Ratio of specific heats of the working fluid
ε	A function defined in Eq. G-3
ϵ, ϵ_r	Regenerator heat-transfer effectiveness
η	Thermodynamic efficiency, work output/heat input
η_c	Thermodynamic efficiency of the cycle

η_{cs} Thermodynamic efficiency of the cycle in the absence of losses

η_f Mechanical efficiency; ratio of actual power output to power output in the absence of frictional losses.

η_h Heater efficiency; ratio of heat input to heater to heat input to working fluid.

θ A parameter defined in Eq. G-3

κ Ratio of swept volume of expansion space to that of compression space

τ Ratio of mean expansion space temperature to mean compression space temperature

χ Ratio of "dead volume" to maximum volume of the expansion space

ω Angular speed

APPENDIX H

MECHANICAL AND FLUID MECHANICAL TRANSMISSIONS FOR PROPULSION OF LAND COMBAT VEHICLES AND HIGH-SPEED SHIPS

P. C. Bertelson

CONTENTS

APPENDIX H
MECHANICAL AND FLUID MECHANICAL TRANSMISSIONS FOR PROPULSION OF LAND COMBAT VEHICLES AND HIGH-SPEED SHIPS
by
P.C. Bertelson

A. INTRODUCTION

A transmission is defined in this study as the subsystem that transfers power from the engine output shafts to the thruster input shafts.* There are two basic functions, the first to reduce rpm (or increase torque) to meet thruster requirements, and the second to distribute power from the engine location to the thruster location. With regard to rpm reduction the requirement may be a fixed reduction ratio, as in a conventional ship, or a wide range of reduction ratios, as in a tank. With regard to distribution of power the requirement may be from one or two parallel inputs along a straight line to a single thruster, as in a conventional ship, or from a single input to two outputs with 90° turns, as in a tank. Even more complex power distribution systems may be required, as, for example, in six- or eight-wheel drives for land vehicles.

The point is that even in its basic functions the transmission characteristics are closely linked to the particular application in mind. Further, there are additional functions that transmissions perform, such as reversing, braking and disconnecting, which are also determined by the application. For these reasons the following sections are restricted to

---

*Note that this is a broader definition than commonly used for "transmission" in the automotive industry. It includes, for example, the final drive on a tank.

discussion of the specific applications of interest in this
study--land combat vehicles and high-speed ships.

B. TRANSMISSIONS FOR LAND COMBAT VEHICLES

1. Background

A previous IDA investigation showed that advanced power
plants for ships had reached the point where the prime mover
was smaller and/or lighter than the "transmission" or main
reduction gear, so that the latter may be considered as a poten-
tially fruitful area for substantial improvement through the ap-
plication of more modern technology. In a remarkably parallel
manner it appears that, with the latest diesel and turbine tank
engines, transmissions of modern tanks are tending to dominate
the weight, volume, and cost impact of the propulsion system on
these vehicles. That is to say, in the advanced MBTs the trans-
mission requires as much weight and armored volume as the engine
does, or more.

The goal of this discussion is therefore to identify the
physical basis for greater energy efficiency and reduced size
in tracked-combat-vehicle transmissions. Tank transmissions
will be considered first as typical of this application.

2. Current Attainment and Functions

At the end of World War II, the U.S. Army began the develop-
ment of the first power shift ("automatic" in lay terms) trans-
mission for track-laying vehicles. The hydrodynamic unit in this
transmission was the CD850 from Detroit Diesel Allison which
was used successively in the M47, M48, and M60 tanks (Ref. H-1).
In the -6 version, this hydrodynamic unit, apparently a military
equivalent of the GM "Hydra-matic" used in passenger cars,
weighed 3185 lb and took up 35 cubic feet in the armored hull--
all this for 650 hp transmitted through it.

Though this scheme sufficed for a variety of other vehicles over a thirty-year period, a comparable new family, the X1100 series, is being developed for 1500-hp power plants. The new transmission is better in its functional performance, i.e., fully automatic, four speeds forward and two in reverse, with torque converter which can be locked out. There are, also, significant improvements in specific weight and specific volume. At the same time the efficiency of the hydrodynamic unit was improved slightly to about 81% under high-load conditions.

Our purpose here is to assess what further size and efficiency improvements may be possible. In doing this, it should be kept in mind that the necessary functions of a transmission for a land combat vehicle are:

1. Speed-reducing to increase engine torque
2. Changing rotation direction for reverse travel
3. Disconnecting the engine (for starting) from the power train
4. Providing vehicle brake capability
5. Dividing engine power between two tread sprockets, variably so that steering is effected.

The power takeoff from the transmission is probably incidental, but a further function of the transmission is not: the X1100 is to be built to match the AVCR-1360 diesel, the AVDS-1790 diesel, and the AGT-1500 gas turbine.

3. Transmission Characteristics

When gears are involved, the old rule of 1% per mesh is a good estimate for the energy loss to be expected (Ref. H-2). If the losses were of this order, there would be little need for the discussion. However, ordinary parallel-axis gears cannot be shifted while transmitting appreciable torques. Thus gear-shifting, by coordinating throttle and clutch actuation, allows a vehicle to adjust its traction to the terrain and speed desired. But gear-shifting takes some skill, it may take great effort with large engines, and in muddy or other areas the momentary loss of torque can limit vehicle mobility. Hence the military adoption of planetary or continuous-mesh gearing systems which effect ratio changes by applying successive clutches or brake bands while engine torque continues to be applied. This, for land vehicles, is invariably associated with the use of a hydrodynamic unit. The reason apparently is to optimize cross-country mobility (where large and frequent torque changes are required) without requiring high driving skills.

The earliest popular hydrodynamic unit was the fluid coupling. It was introduced in passenger cars more than 40 years ago, but it is not used in modern civilian vehicles. The efficiency is simply the slip ratio, the fractional output shaft speed relative to the speed of the engine. This is beautifully discussed as a design report in a paper by Qualman and Egbert (Ref. H-3). As they mention, it is simply a starting device which also isolates vibration and shock. At idle, slip is essentially total and efficiency zero. At 1600 rpm, depending on the design, efficiency might reach 75%.

One also should realize that the fluid coupling takes the place in weight and volume of the flywheel and clutch in engines without fluid couplings, and the coupling can mount the ring gear for the starter pinion. By almost trivial design change, as detailed in the above reference, one can make the efficiency of

H-6

a fluid coupling higher. Very slight diameter increases decrease slip and hence increase efficiency. But of course starting becomes harder and creep a larger problem.*

A second type of hydrodynamic coupling is the torque converter, which always has three or more independently movable rotating elements. As described in two excellent references (Refs. H-4, H-5), it increases torque--like a gear--at low speeds where fluid couplings only slip. This torque multiplication decreases with speed (sometimes as much as 4:1, but usually not much more than 2:1) and operates over the top half of engine speed ranges. Being variable in their torque multiplication, torque converters are well suited for vehicles but hard to analyze. They also provide disconnect capability for starting and act as flywheels to smooth the torque from internal combustion engines.

4. Potential for Improved Transmission Characteristics

a. General Considerations. The discussion above has centered on the hydrodynamic unit that includes both a fluid torque converter and gearing to provide multiple speed reduction. In a tracked vehicle there is also a final drive that splits the power output from the hydrodynamic unit, turns it 90 degrees, and delivers it to the sprockets that drive each track. When the engine is a turbine, there is an extra reduction gear at the input to match engine rpm to the input of the hydrodynamic unit. All these elements are part of the transmission of a land combat vehicle.

To consider the potential for improvement, it is convenient to separate the hydrodynamic unit from the input and output gearing, the latter being treated as purely mechanical elements with fixed reduction ratios.

---

*If efficiency is of prime importance, a topic to be considered is the split-torque coupling which cuts all coupling losses, typically by a factor of 3. This is detailed also in Ref. H-3, page 193.

b. **Characteristics of Mechanical Transmissions.** There
are a number of empirical formulae for estimating gear weights.
One in common use is the Dudley formula

$$W_g = C_1 \frac{Q^n}{K} \quad ,$$

where W_g = weight of gears

K = the gear loading factor

Q = torque factor

C_1 and n are empirical constants depending on the type of
gears, and n is approximately unity for lightweight gears.
The torque factor Q is given by

$$Q = \frac{shp}{rpm} \frac{(R + 1)^3}{R} \quad ,$$

where shp is shaft horsepower, rpm is shaft rpm, and R is reduc-
tion ratio. Q is thus proportional to torque for a fixed reduc-
tion ratio; and from the equation for W_g, gear weight is nearly
proportional to torque and inversely proportional to the gear
loading factor. This formulation is adequate for simple gear
systems and was used to calculate gear weight for any mechan-
ical elements associated with the transmission subsystems.

The efficiency of mechanical transmissions can be con-
sidered independent of the weight. The rule of thumb for well-
designed gears is a loss of 1% per gear mesh. This allows easy
estimation of the efficiency of mechanical transmissions, which
can be seen to be very high.

The weight of shafting, the other element of mechanical
transmissions, depends on the torque and the length of the shaft
and can be easily calculated. For short runs, losses in the
shafting can be considered to be negligibly small.

In summary, mechanical transmission elements do not show an efficiency/weight tradeoff in design in the same way as engines or electromechanical converters. The losses in purely mechanical transmissions are typically as low as 3-4%, so there is little scope for major improvements in efficiency. Improvements in specific weight may be expected as material properties are improved. In the long run it is estimated that a 40% reduction in specific weight may be possible.

c. **Characteristics of the Hydrodynamic Unit.** The hydrodynamic unit consists of a fluid torque converter together with gearing which can deliver power to the final drive through a range of rpm. The major losses in this unit occur in transferring energy into and out of the fluid, and these losses are quite size dependent. The efficiency of torque converters has been the subject of enormous effort, so far as passenger cars are concerned. It is interesting to see that there has been an evolution in twenty or thirty years. One can secure torque multiplication with gears or with turbine and reactor blades. The (1957) Chevrolet Turboglide used a complex, five-element converter with a pump, three turbines, and a stator (Ref. H-6). It weighed 93 lb less than the industry average and was "shiftless," since successive turbines were acting through roller clutches. Nevertheless, passenger cars today use only the simplest three-element torque converter. The simpler converters are probably more efficient. This is deduced from Ref. H-7, which compares a variety of multi-turbine torque converters, the best of which show 85% as maximum efficiency.

Since the hydrodynamic unit in a tank must deliver maximum power for slope climbing at low output rpm, the efficiency that is attainable is somewhat lower than in automobiles. In the latest tank units (e.g., the X1100) efficiencies of 81% are reported. It is estimated that three-quarters of the losses occur in the fluid torque converter, which is typically one-third the total weight of the unit. The other two-thirds of

weight is in structure and mechanical gearing, which contributes 25% of the losses. As noted above, the mechanical gearing losses can be considered independent of the specific weight. In the fluid torque converter, however, there is a sharp increase in losses if the unit is made too small. Combining the behavior of these two elements gives efficiency/specific weight characteristics for the hydrodynamic unit as a whole.

Using the X200/1100 series as representative of current technology (see Annex H-1), the current and potential design tradeoff curves of efficiency and specific weight are estimated to be as shown in Fig. H-1. The potential limit was based on reducing the losses in the fluid-mechanical elements by one-third at constant weight, and the weight of the mechanical elements by 40% at fixed efficiency.

A similar situation with regard to the distribution of weight and losses occurs in hydromechanical transmissions. That is, by weight the larger part of the system is mechanical, and the smaller part involves fluid-mechanical energy transfer. One can expect weight reduction largely in the mechanical part and efficiency improvement largely in the fluid-mechanical part. Thus, the potential effects of technology advances are similar to those shown in Fig. H-1.

C. TRANSMISSIONS FOR HIGH-SPEED OCEANGOING SHIPS

1. Background

The physics of vehicles moving against fluid resistance-- ships and aircraft--requires that they be propelled by accelerating adjacent fluid streams that are large by velocity changes that are relatively small. For ships this means that propellers should be large and slow-turning. This is opposite to the prime-mover trend toward high speeds of rotation for minimum power-plant specific weight.

It was for this reason that gears were used to reconcile the high speeds of turbines with the low speeds needed by pro-
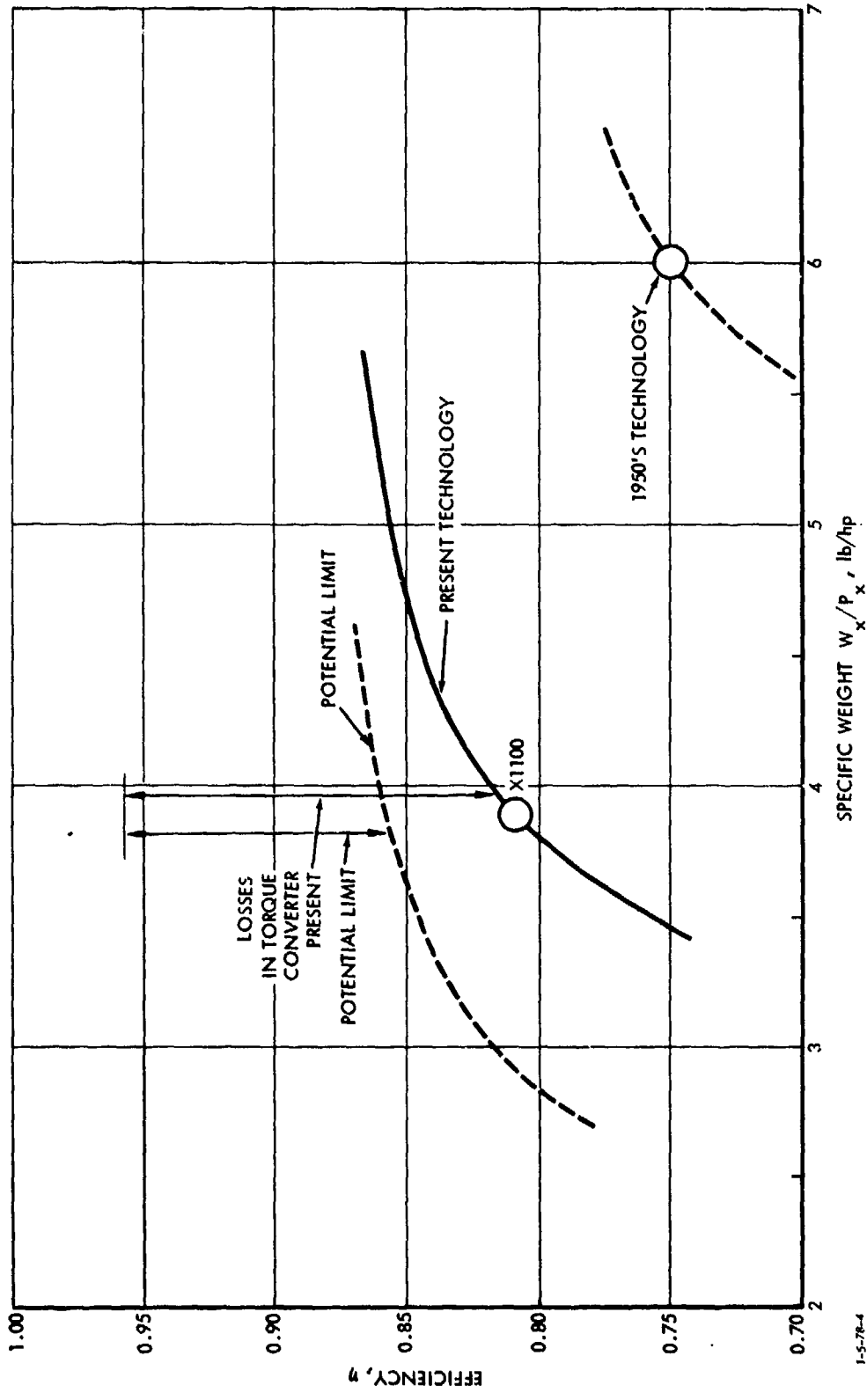
FIGURE H-1. Efficiency and specific weight characteristics of a hydrodynamic transmission unit for an MBT.

1-5-78-4

pellers. From the first application in 1910 (by Sir Charles
Parsons in the *S.S. Vespasian*), there were nearly 600 instal-
lations eight years later. And there were no failures (Ref.
H-8).

These natural couplings of steam turbines with speed-
reducing gears relied entirely on single reductions with ratios
less than 10:1, since higher ratios in a single mesh compromise
tooth strength. Just before World War II, the U.S. Navy scored
a major advance with the development of a compact double-reduction-
gear design. This was copied by other navies after this war and
was recognized as the economic way to minimum-size, minimum-
weight merchant marine plants larger than 25,000 hp per engine
(Ref. H-9).

A purpose of this study is to identify technology advances
that would support military vehicles with superior capability.
For high-speed ships, lighter-weight power plants are an in-
disputable goal. Since reduction gears in modern warships tend
to be heavier than main propulsion engines (Ref. H-10), there
may be greater potential for weight reduction here than in the
main engines.

2. Current Attainment and Functions

Weight, volume, cost, and reliability are the essential
criteria for evaluating improvements in transmissions for ships.
In contrast to prime movers, efficiency, internal power transfer,
sfc, and temperature are not relevant to usual reduction gears
where the losses are but a few percent. Efficiency *may* be
relevant in assessing advanced types of reduction devices to
be mentioned later.

The examination of attainment in reduction gears must
recognize that this power-plant subsystem has three functions
in usual ships:

H-12

1. *Speed-reducing* (or impedance-matching) between engine and propeller
2. *Reversing* shaft direction, sometimes, as for backing a vessel with diesel or gas turbine engines
3. *Combining* shaft inputs from two engines or two shafts of a double-casing turbine.

Some of this is a good deal more than merely gear design. The gear is strongly influenced by the necessity of clutches, the adjacent space required for steam condensers, ducting, etc. It may also be influenced by the requirement for ballast mass in the bottom portion of an engine room. Hence it is not surprising that reduction gears are typically designed by the firms who make main engines. For instance, there is logic—following aircraft practice—in making the reduction gear the mounting and the foundation for the main engines (Ref. H-9), or, as in minesweepers which follow automotive practice, mounting the gears on a main engine. Similarly, the use of contra-rotating propellers (for greater efficiency) essentially dictates the use of planetary reduction gears, which are half the weight of parallel-axis gears but unsuited to inputs from two engines. For these reasons, the transmission system is inextricably linked with the rest of a marine power plant.

3. Transmission Characteristics

The current reduction gears in the U.S. Navy are apparently much like the designs originated prior to World War II. In essence, the now-conventional DTALT (dual-tandem-articulated-locked-train) gearing reduces loading of the turbine input gear by sharing, equally, this torque between two driven pinions. This cuts the expected input pinion face width in half for the same stress level. Each of the primary reduction gears also divides its torque so that the final drive gear is driven by four pinions with a considerable reduction in the sizes of the gears involved. This is the technology introduced 40 years ago. With minor increases in the stress levels and in the degree

of sound isolation, it is the technology of present U.S. warships.

The quantitative basis for this capability is indicated by several figures that reflect the attainment of post-World War II construction (Ref. H-10). This data (Fig. H-2) shows the specific weight in pounds per shaft horsepower for 2 DEs, 5 DDs, 2 CVAs, and 12 auxiliaries. The warships with speeds above 30 knots have lighter gears partly because they use higher shaft speeds than the auxiliaries.

Theoretically, reduction gears must be larger for larger reduction ratios. Thus, in Fig. H-3 the same data was plotted a little more tightly as a function of the reduction effected in each mesh. The data collect somewhat better, and the auxiliaries-- the vessels using slower maximum shaft speeds--seem to be designed at the same levels of technology.

A third plot (Fig. H-4) shows the torque per unit reduction gear weight for these vessels and a number of submarines. The latter might be expected to be designed more elaborately to minimize sound transmissions, but no details of this are available.

Because these data suggested that projections and future performance be inferred merely as an extrapolation of past practice, without relation to design variables or the materials of construction, the application was examined in greater analytical detail.

4. Potential for Improved Transmission Characteristics

a. For a Conventional High-Speed Ship.* The different areas where current industrial technology may be used to improve the characteristics of conventional reduction gears are as follows:

_____
*I.e., a ship using a conventional hull (but perhaps modified in shape to optimize high-speed drag) and a supercavitating propeller.

H-14
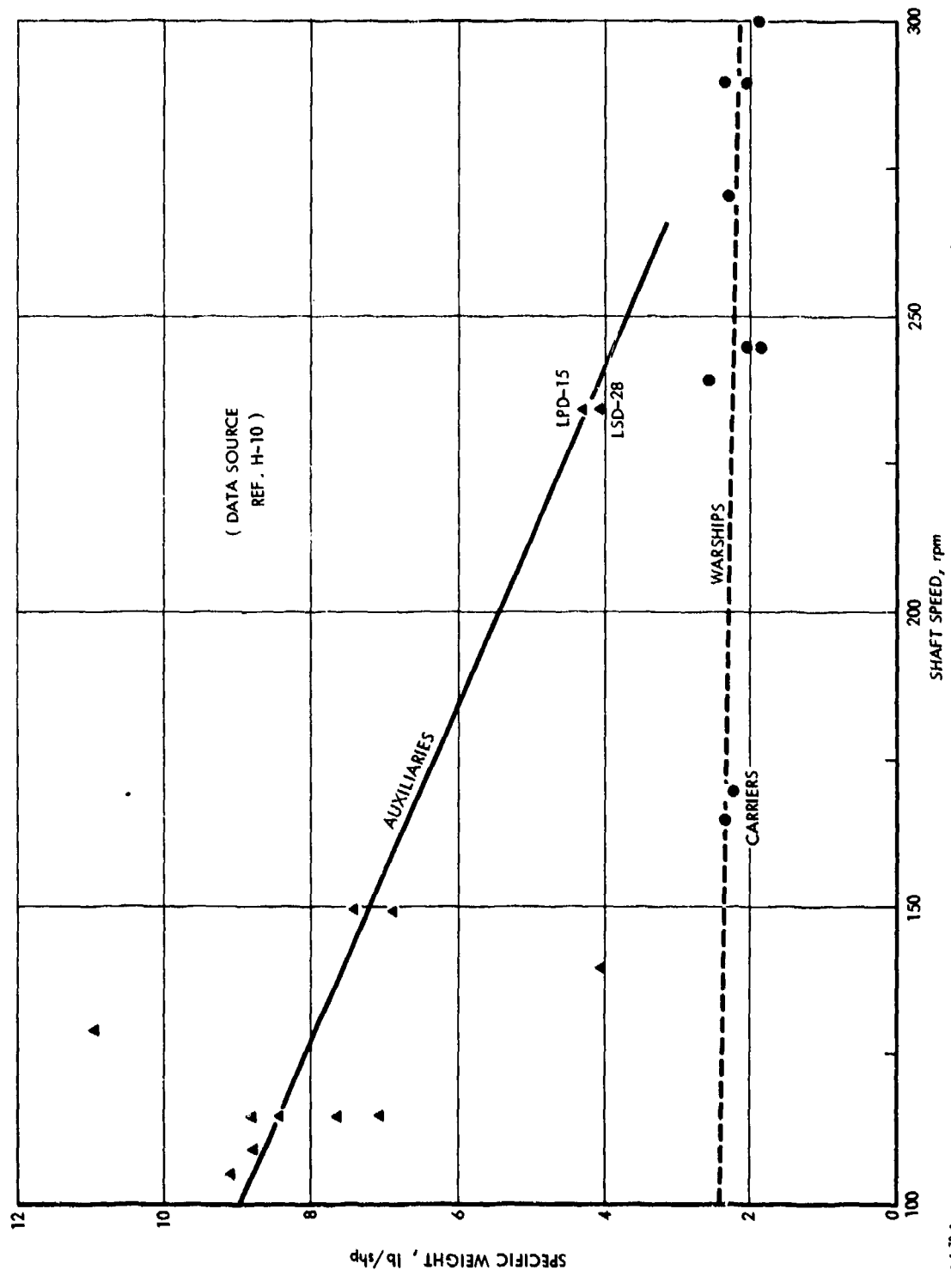
FIGURE H-2. Trends in reduction gear specific weight versus shaft speed.

H-15
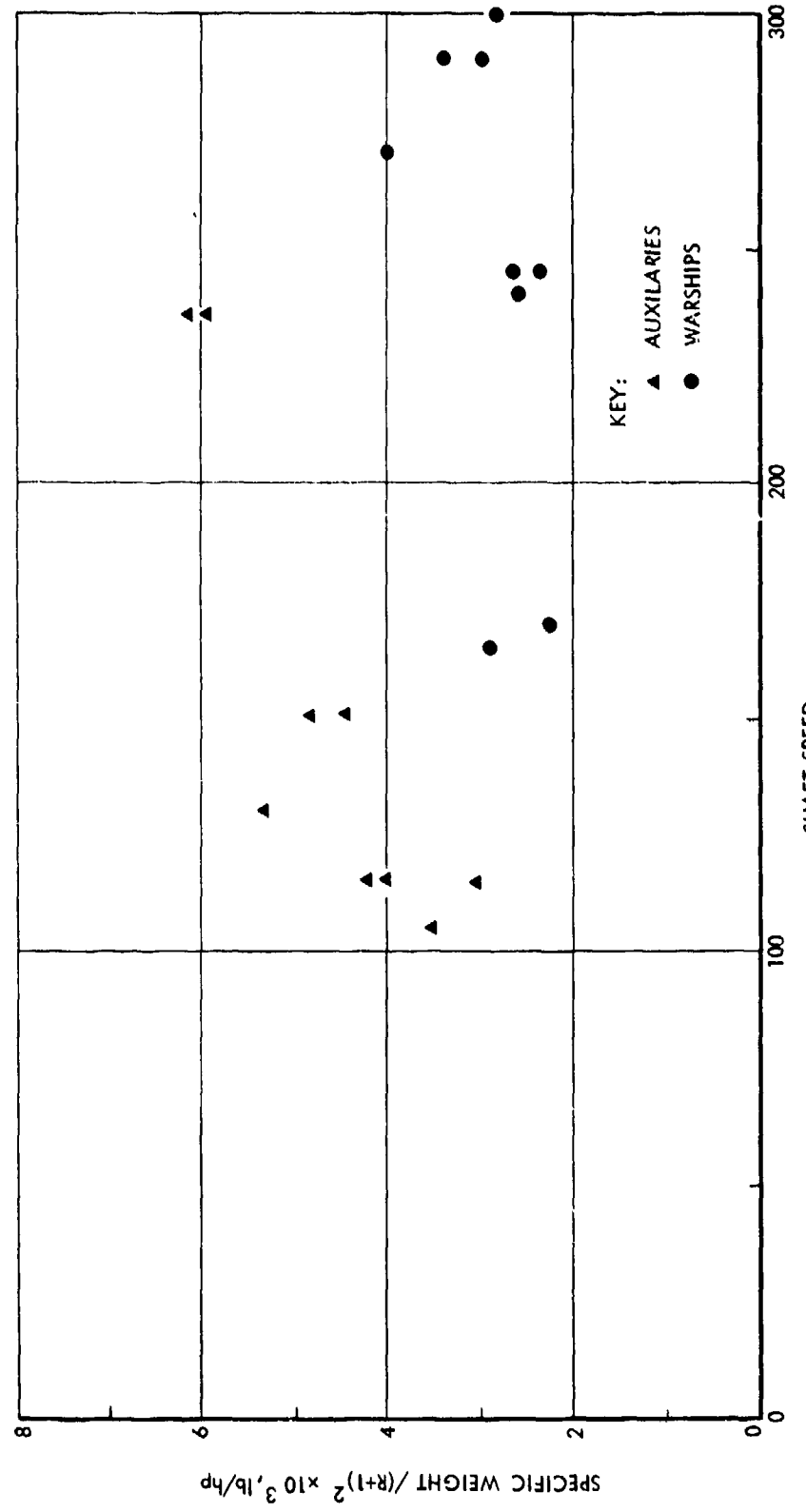
FIGURE H-3. Reduction gear weight (corrected for reduction ratio) versus shaft speed.

1-5-78-6

H-16
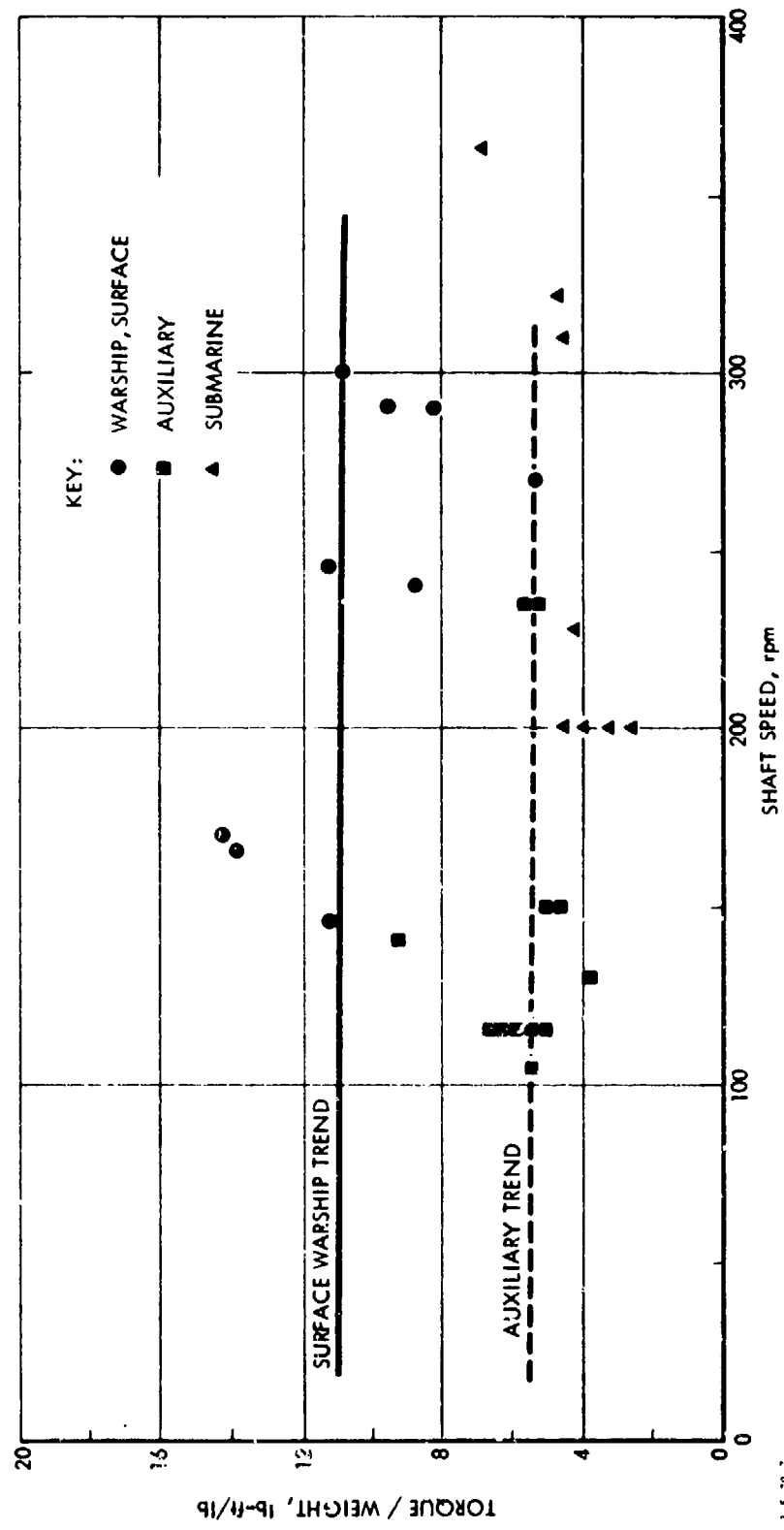
FIGURE H-4. Torque per unit weight versus output speed.

H-17

1. Single helical gears are the rule in all land vehicle applications and have been for at least a generation. The use of double helical gears requires a clearance gap that is 22% of the gear-tooth width. Additionally, the lower helix angles used with single helical gears save another 10-12% of the working gear face width. This in turn reduces the axial thrust of such gears to manageable amounts.

2. Gears for ships, like gears for land vehicles, can be case-hardened. They *should* be case-hardened to double their fatigue strength. In automobiles, case-hardened gears are used because they are less expensive, but in ships they should support reduction gears roughly half as heavy as present gears. •

3. Planetary reduction gears offer a large weight and volume saving where there is no necessity to combine multiple turbine inputs.

4. Journal bearings for reduction gears are designed for pressures of 500 psi and less. For machinery that stops and starts far more frequently, journal bearings of unlimited life and at higher temperatures are successfully applied at double and triple these working pressures. This might allow savings in size.

5. There has been the most tentative Naval interest in controllable-pitch propellers. These are inherently reversible. A completely different approach is the roller transmission. This was suggested to the Navy by Hewko and others at New Departure Division of General Motors. There is a 24-dB reduction in noise when a single planetary roller reduction is used instead of a conventional geared planetary (Ref. H-11). Some of the most insightful researchers insist, on the other hand, that if one is to use rollers in a so-called traction transmission where one has to drive through a film of oil, it may be better to use tapered rollers or

cones. This gives one the capability for an infinitely variable (or IV) transmission. Noise would be less than with gears, and size/weight may be comparable to current gears (Refs. H-12, H-13).

6. The life of gears is limited by the bending strength of gear teeth, or by the fatigue of the surfaces of gear teeth. It has been thought that this fatigue is mitigated by extreme-pressure lubricants that are chemically attached to the metal. It now appears that under extreme pressure, above 100,000 psi, oil congeals so as to limit the hydrostatic pressures that can separate grain boundaries of a metal. Accordingly, the synthetic lubricants from one firm (Monsanto) have been designed to become glassy solids at these very great pressures. Such materials may promote longer life in highly loaded gear systems just as they have tripled the life of ball bearings that are limited by surface fatigue (Ref. H-14).

b. **For an SES.** The favored design for an oceangoing SES uses a waterjet thruster in which the pump is placed immediately adjacent to the engine. The transmission is then essentially a simple reduction gear, since the reversing and distribution functions are eliminated. It is assumed that the input power would be from a single engine, and that hence a simple planetary gear can be used. The weight of such a gear can be calculated by using the Dudley formula discussed in this appendix in Subsection B-4-a on mechanical transmissions.

H-19

REFERENCES, APPENDIX H

H-1. J.W. Schmidt and G.L. Hadley, The New X1100 Automatic Transmissions for the XM1 Tank, SAE 770339, 4 March 1977.

H-2. V.M. Faries, Design of Machine Elements, Macmillan Co., New York, 1946, p. 239.

H-3. J.W. Qualman and E.L. Egbert, "Fluid Couplings," Design Practices-Passenger Car Automatic Transmissions, 2nd Ed., SAE, Inc., New York 10001.

H-4. J.W. Qualman and E.L. Egbert, "New Type of Three Member Hydrodynamic Unit,", Design Practices-Passenger Car Automatic Transmissions, 2nd. Ed., SAE, Inc., New York 10001.

H-5. V.J. Jandasek, "Design of Single Stage, Three-Element Torque Converter," Design Practices-Passenger Car Automatic Transmissions, 2nd Ed., SAE, Inc., New York 10001.

H-6. F.J. Winchell, W.D. Route, and O.K. Kelley, The Chevrolet Turboglide Transmission, SAE Annual Meeting Paper, January 1957.

H-7. F.H. Walker, "Multiturbine Torque Converters," Design Practices-Passenger Car Automatic Transmissions, 2nd Ed., SAE, Inc., New York 10001.

H-8. H.P. Tostevin, "Experience and Practice in Mechanical Reduction Gears in Warships," Trans. R.I.M.A., Vol. LXII, 1920, p. 129.

H-9. E.C. Rohde and H.C.K. Spears, "Steam Propulsion Systems for Modern Ships," Soc. Naval Architects and Marine Engineers Proceedings, No. 22, 1968.

H-10. G.C. Sharp, Inc., An Algorithm for Scaling Power Plants, Reports 7871 and 788, 1973.

H-11. L. Hewko, "Planetary Friction Drive Quietly Outperforms Gears," Product Engineering, 23 October 1967, p. 39.

H-12. C.E. Kraus, "Traction Drives," _Power Transmission Design_,
       March, May and July 19

H-13. "Toric Transmission Smoothes Vehicles Power," _Product
       Engineering_, 2 June 1969.

H-14. R.L. Green and F.L. Langenfeld, "Lubricants for Traction
       Drives," _Machine Design_, 2 May 1974, p. 108.

ANNEX H1

SERIES HYDROSTATIC TRANSMISSION*
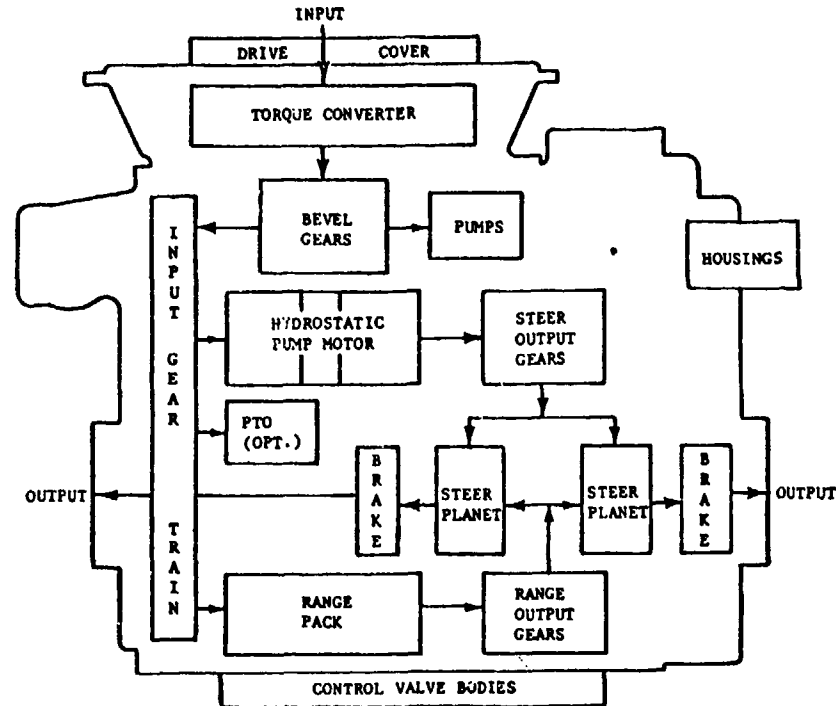
TYPICAL WEIGHT DISTRIBUTION

Fluid-Mechanical Energy-Transfer Elements:		Mechanical Energy-Transfer Elements:	
Drive cover & converter	11%	Bevel gears	4%
Pumps, flow valves & filter	3	Input gear train	3
Hydrostatic unit & controls	11	Range pack	14
Control valve bodies	6	Range output gear	3
Total	31%	Steer planet & brakes	15
		Steer output gears	3
		Housings	24
		Miscellaneous hardware	3
		Total	69%

*Source: Detroit Diesel Allison, Division of General Motors.
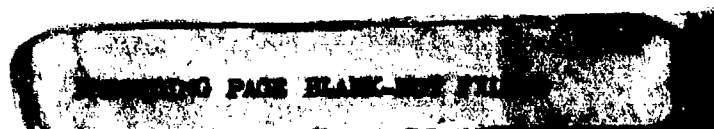
APPENDIX J

ASSESSMENT OF THE TECHNOLOGY OF ELECTRIC TRANSMISSION SUBSYSTEMS FOR SURFACE VEHICLES

Joseph L. Smith, Jr.
James L. Kirtley
Joseph Gerstman
Frank C. Rumore

CONTENTS

GLOSSARY OF SYMBOLS

A	Cross section of conductor
a_i	Empirical constants $i = 1, 2, 3,$ etc.
B_c	Saturation flux density in magnetic material
B_s	Usable magnetic flux density
$\left.\begin{array}{l}B_x \\ B_y\end{array}\right\}$	x and y components of magnetic flux density
c	Specific heat of coolant
d	Density
D	Diameter
E_o	Insulating strength of dielectric
f	Fraction of magnetic teeth in winding region
F	Fanning friction factor
g	Air-gap dimension
G	Mass velocity (velocity x fluid density)
h	Heat transfer coefficient
h_o	Total height of machine
H_m	Magnetic flux density in superconducting windings
$\left.\begin{array}{l}H_x \\ H_y\end{array}\right\}$	x and y components of H
J	Current

J_c	Usable conductor current density
J_m	Maximum usable current density
J_s	Peak usable current density in winding region
J_z	z component of J
j	$\sqrt{-1}$
j_o	Superficial current density
j_c^+	Dimensionless superficial current density j_o
j_e^+	Dimensionless temperature-limited j_o
j_h^+	Dimensionless heat-transfer-coefficient-limited j_o
$\underline{J}_s$	Complex amplitude of J_s
$\left.\begin{array}{c} \underline{J}_1 \\ \underline{J}_2 \end{array}\right\}$	Complex amplitude of J_s in windings 1 and 2
k	Wavenumber based on pole pitch (in electromechanical calculations)
k	Thermal conductivity (in heat transfer calculations)
$\overline{K}$	Surface current density
$\underline{K}$	Complex amplitude of $\overline{K}$
K	Magnitude of current density
K_R	Surface current density in rotor
K_S	Surface current density in stator
K_a	Armature reaction
$\left.\begin{array}{c} K_1 \\ K_2 \end{array}\right\}$	Surface current density in windings 1 and 2

L	Length
M	Mass
n	Rotational speed (rpm)
N	Number of poles
p	Pressure
Δp	Maximum allowable coolant pressure drop
P	Power
P_d	Power dissipated
Pr	Prandtl Number (coolant)
q	Volumetric energy dissipation rate (J^2/γ)
R	Radius
t	Winding thickness (depth)
T	Temperature
T_1	Inlet temperature
T_o	Final temperature
ΔT_o	Allowable temperature difference between conductor and coolant
T_h	$(T_1$ - coolant temperature)
u	Relative velocity of rotor and stator
v	Voltage
V	Volume
V_{act}	Volume of active components
V_{rot}	Volume of rotor
X	Radius ratio
α	Machine aspect ratio

β	Ratio B_s/B_c
γ	Electrical conductivity
δ	Relative phase angle
η	Efficienty
μ	Magnetic permeability
ρ_o	Apparent resistivity of coils (based on gross coil and tooth volume)
ρ_c	Resistivity of conductor
ρ_e	Resistivity of copper
σ	Magnetic shear stress
σ_r	Rotor surface traction
σ_s	Stator surface traction
$\langle\sigma_{xy}\rangle$	Spatial average of magnetic shear stress
ω	Electrical frequency
ω_m	Mechanical frequency
$*$	Complex conjugate operator

APPENDIX J

ASSESSMENT OF THE TECHNOLOGY OF ELECTRIC
TRANSMISSION SUBSYSTEMS FOR SURFACE VEHICLES

Joseph L. Smith, Jr.
James L. Kirtley
Joseph Gerstman
Frank C. Rumore

A. INTRODUCTION

Electric transmission subsystems may be used in a wide
variety of surface vehicles to transmit power from one or more
prime movers to one or several propulsion, suspension (lift),
and auxiliary subsystems. Electric transmissions are generally
characterized as having excellent power control capability,
operational flexibility, and design flexibility, especially
in the location of major power train components. On the other
hand, electric transmissions are generally considered to be
heavy, bulky, and expensive compared to direct mechanical
drives. Present designs that provide full control of torque
over the rated range of speed are especially heavy, bulky, and
expensive.

The first objective of this appendix is to develop a
general description (analytical model) of an electric trans-
mission subsystem so that the complete range of existing
equipment and potential equipment can be considered on a common
basis. This analytical model will define general design and
performance parameters and allow fundamental physical limits to
be established for these parameters, independent, insofar as
possible, of the specific details of the system.

J-7

The second objective of this appendix is to establish the current state of technology and to express it in terms of parameters and physical limits developed from the general analytical model. Potential for improvement of current technology will be indicated by differences between the theoretical limits and current practice. The improvements in overall system performance that can be expected as a result of approaching these physical limits will be discussed, but the specific means for approaching the limits requires invention, analysis, and development that are well beyond the scope of this appendix.

B. DEFINITION OF ELECTRIC TRANSMISSION SUBSYSTEM MODEL

An electric drive transmission is defined as the electromechanical system which connects one or more rotating input shafts to one or more rotating output shafts. In surface vehicle applications, on-board prime movers drive the input shafts that turn electric generators. The electric power from these generators is fed through appropriate switch-gear and wiring to various electric motors that turn the output shafts of the transmission. Control of speed or torque, and thus of power, is achieved by electric power conditioning equipment which may be part of the motors and generators or in completely separate components. Power conditioning may be as simple as a field rheostat for a DC machine or as complex as a solid-state cycloconverter.

The objective of the analytical model for the transmission is to describe the transmission in a way that will exhibit the common functions and common features of the widest variety of electromechanical transmission systems. Analysis of these common functions will provide a set of fundamental parameters that can be used to assess physical limits on these transmissions.

The functional model for analysis of the transmission is shown in Fig. J-1. The three basic functions are:

J-8

1. Electromechanical conversion
2. Current switching
3. Electric power distribution.

In the transmission the input mechanical power produces electric power (currents and voltages) in the input electromechanical converters. The input converters are connected to the electric bus by input current switching systems, which match the currents and voltages of the converter to the common voltage and frequency of the bus. The bus transmits and distributes the electric power to the output current switching systems. Here, the voltage and frequency of the bus are matched to the currents and voltages required for the conductors of the output electromechanical converter. In general, output (and/or input) power is controlled by the timing and sequence of individual switching actions within the current switching systems.
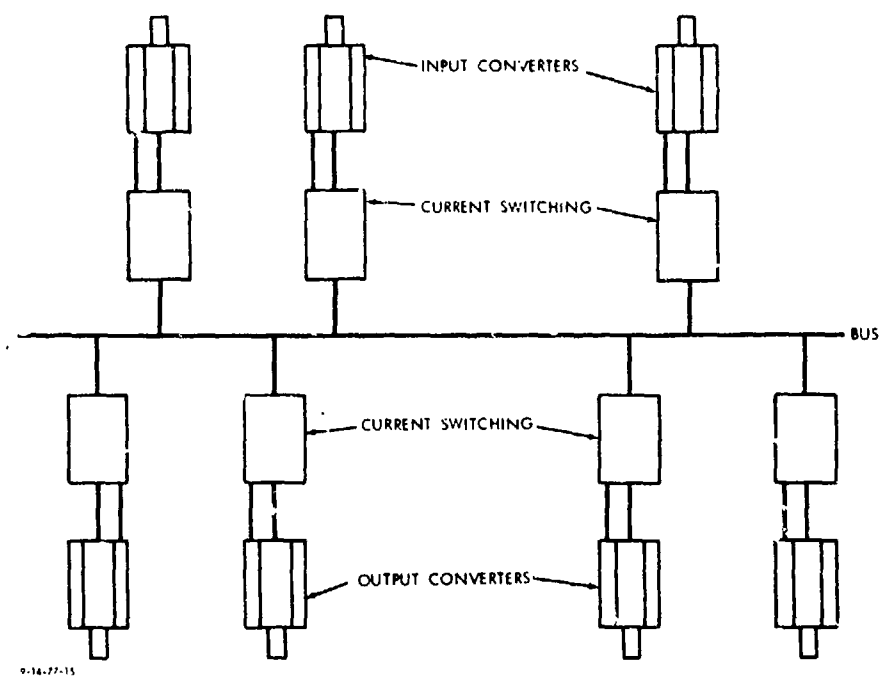

FIGURE J-1. Electric transmission schematic.

J-9

Electromechanical conversion in the input converter is
from mechanical power to electrical power, while conversion in
the output converters is from electrical power to mechanical
shaft power by the same, but inverted, process. Conversion in
this sense is the major function of electric generators and
motors. However, conventional machines include all or a part
of the current switching function, which is considered sepa-
rately in this analytical model. For example, the function of
the commutator in a DC machine is clearly to be included in
the model as a part of the current switching function rather
than as a part of the electromechanical conversion. The
excitation system and the slip rings of a synchronous machine
are also considered current switching rather than conversion.
The induction motor has a close integration of current switching
function and conversion function that must be conceptually
separated when applying the basic transmission model developed
here. In the induction motor the transformer action that
induces the current in the squirrel-cage rotor is a current-
switching function according to the model, while the interaction
that produces the mechanical torque on the rotor is the conver-
sion function.

With the switching function separated, the electro-
mechanical conversion reduces to the magnetic interaction
between a current sheet in the stator interacting with a
current sheet in the rotor in the presence of magnetic material
in both the rotor and stator. The current sheets interact with
the magnetic material and with each other and produce a force
between the rotor and stator. This force, together with the
relative velocity between rotor and stator, provides the
mechanical power, while the currents together with the voltages
induced by the relative velocity provide the electrical power.

In the following, we shall consider first the power
distribution function, then the current switching function,
and finally the power conversion process itself.

J-10

C. BUS AND ELECTRICAL CONDUCTORS

Electrical conductors will connect the electromechanical energy converters to each other and to the switching apparatus. It is of interest first to consider the case where an optimum transmission voltage can be selected. As it turns out, in this case these conductors will not constitute a major part of total system weight.

An analysis* is carried out in Annex J1 in which the optimum conductor radius, transmission voltage, and resulting power transmission density are determined. For round conductors with cylindrical insulation, the voltage corresponding to optimum transmission is

$$v = 0.43 \ E_o^{2/3} \ P^{1/3} \ J_c^{-1/3} \quad , \qquad (J-1)$$

and the optimum power transmission density is

$$\frac{P}{A} = 0.15 \ J_c^{2/3} \ E_o^{2/3} \ P^{1/3}. \qquad (J-2)$$

These relationships are shown in Figs. J-2 and J-3. It is clear that, for reasonable values of J_c and E_o and for reasonable transmission length, the weight and volume occupied by conductors and insulation will be small compared with the weight and volume occupied by electromechanical converters, if transmission voltage can be selected to be near optimum.

This condition will not, of course, be satisfied for systems involving some types of converters. In particular, DC machines may not be operable at voltages anywhere near optimum for the transmission system. Acyclic machines are extreme examples of this and can demand extremely heavy conductors at high power levels.

The weight and volume of conductors in this case is dependent on the I^2R losses that can be tolerated.

*Symbols for this analysis are defined at the end of Section C.
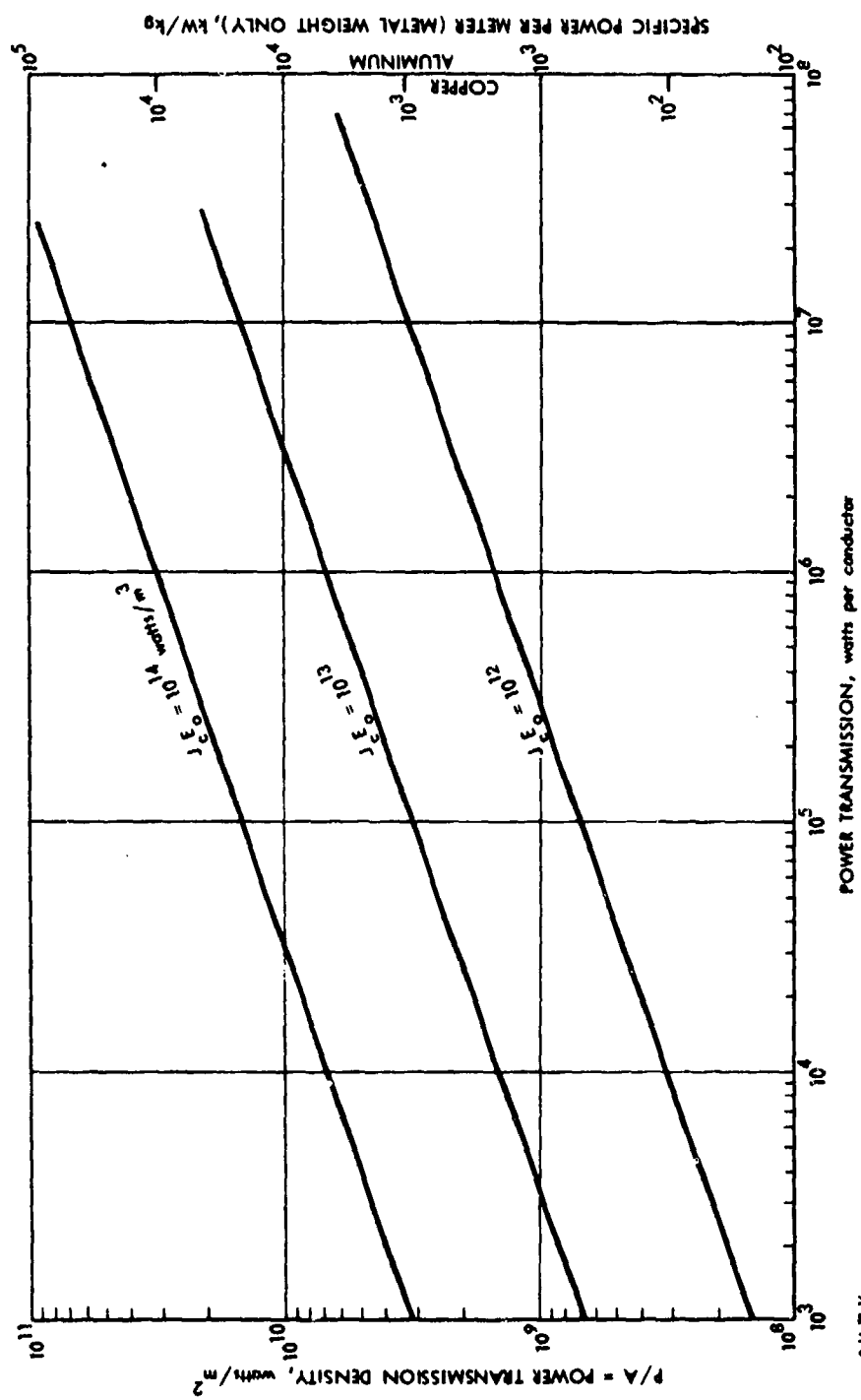
FIGURE J-2. Optimum voltage power transmission density.
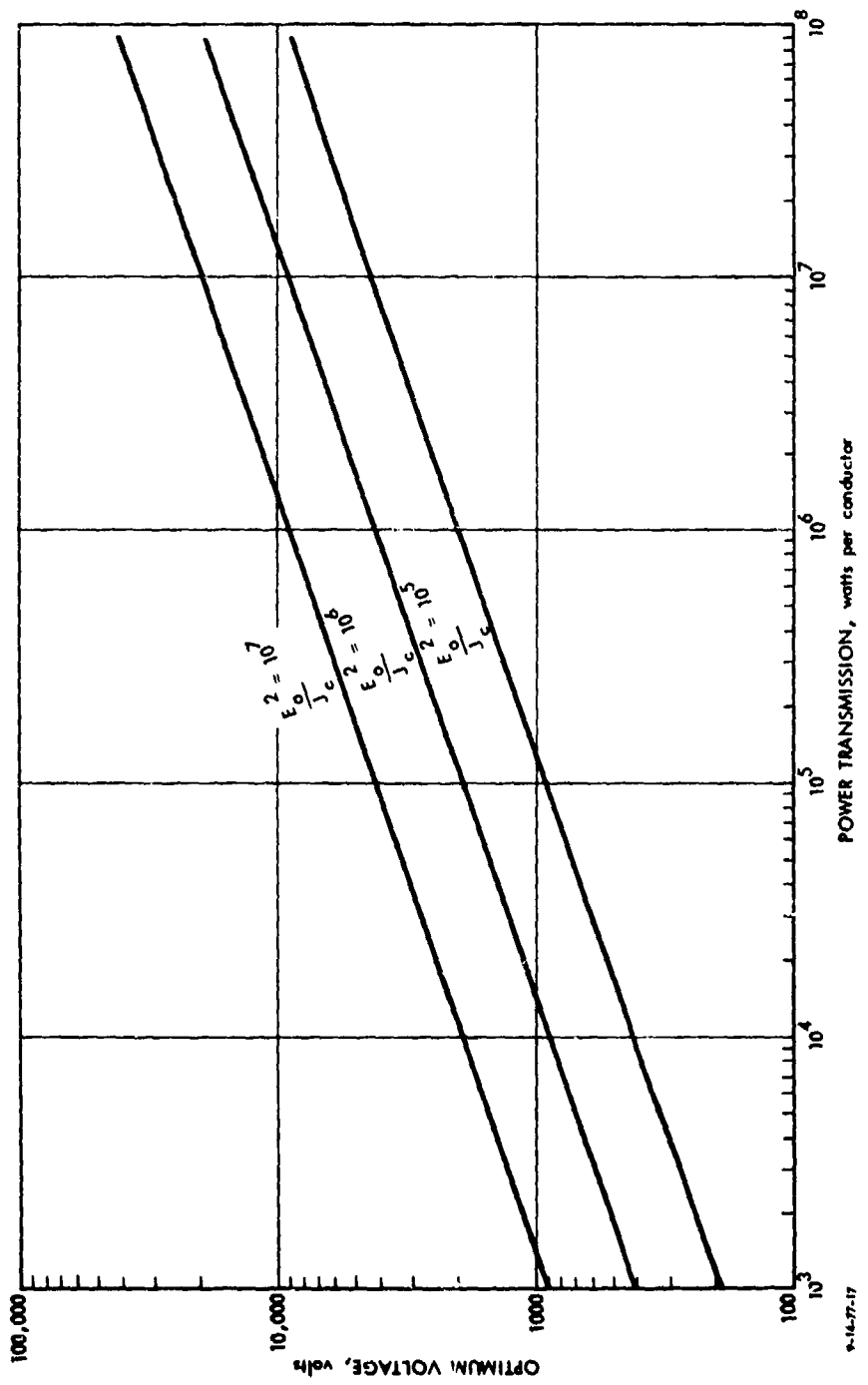
FIGURE J-3. Optimum transmission voltage.

$$1 - \eta = \frac{P_{loss}}{P_{trans}} = \frac{J\rho_c L}{v} = \frac{P}{A} \frac{\rho_c L}{v^2} \quad ,$$

which gives

$$\frac{\text{power transmitted}}{\text{conductor weight}} = \frac{v^2(1-\eta)}{L^2 d_c \rho_c} \qquad (J-3)$$

Equation J-3 is plotted in Fig. J-4 for aluminum. For copper, the specific power is half that of aluminum.

The symbols used in this section are:

A   Cross section of conductor

E_o Insulating strength of dielectric

J_c Current density

P   Power per conductor

v   Transmission voltage

ρ_c Resistivity of conductor

d_c Density of conductor

D. SWITCHING APPARATUS

Between the prime-mover converters (generators) and propulsion converters (motors) there may be control apparatus. In many systems this control apparatus must handle full system power, and in a fairly sophisticated way.

The control apparatus will consist of mechanical switches and semiconductor components. As the demand for sophisticated power handling increases, so will the use of semiconductors, especially for controlled rectifiers.

It is particularly difficult to pin down an ultimate limit on the power density capabilities of equipment containing semiconductor devices. This is because the power handling capability of a given device may be quite high. This is particularly

J-14
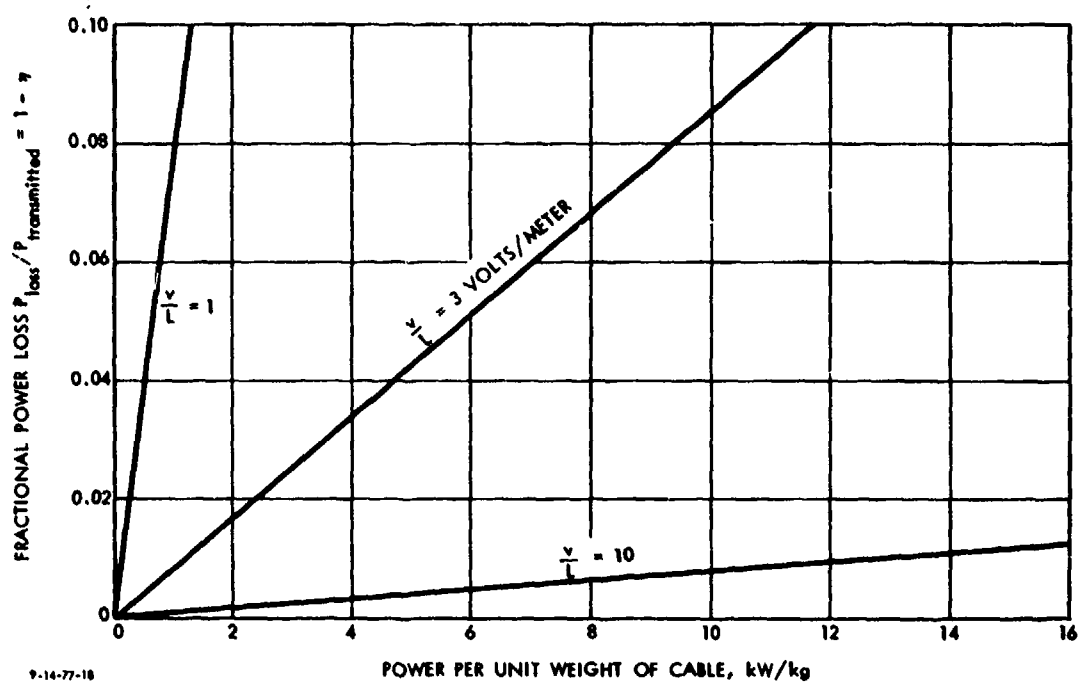
FIGURE J-4.   Power per unit weight of aluminum cable for low-
voltage transmission.

true of large thyristors. For example, a type C701 thyristor is 1 in. thick and has a diameter of 3 in. It is rated at 1800 volts and 1250 amperes, giving it a power handling capability of over 1 MW and a power density of better than 10^9 W/m^3.

Obviously, if this were the limit on power density for large switching apparatus using semiconductors, such apparatus would be a small part of the weight of an electric transmission. Present-day apparatus using semiconductors is substantially heavier. In fact, the devices handling actual power constitute only a small part of the switching equipment in which they are used.

Two classes of components seem to make up the major part of the weight of switching apparatus. These are heat sinking components for removing heat from the semiconductors, and energy storage elements used for filtering, snubbing, and commutation.

Heat-sinking components are so large because relatively crude means are still used to cool semiconducting devices. Air-cooled heat sinks pressed against the flat surfaces of thyristor cases are still common and are referred to as highly advanced means of cooling. The effects of using a better coolant (oil in this case) are apparent from Table J-1. Still further improvements are to be expected from more advanced cooling techniques such as direct, internal cooling.

The need for energy storage in equipment such as inverters is not well understood. Further work in this area is required before the ultimate limits on such apparatus are determined.

There are classes of apparatus that require minimal energy storage. The line-commutated cycloconverter is an example of such apparatus. So is the simple controlled rectifier. It is expected that equipment using these classes of apparatus will yield the most compact switching apparatus for the transmission subsystem.

J-16

TABLE J-1. SIZE AND WEIGHT OF MOBILE POWER
ELECTRONICS REPORTED IN THE LITERATURE

	P, kW	M, kg	V, m³	ρ, kg/m³	P/V, W/m³	P/M, kW/kg	Ref.
AIR COOLED:							
Chopper	960	3770	--	--	--	0.255	J-6
Inverter	150	--	1.06	--	1.42×10^5	--	J-22
Inverter	300	--	2.38	--	1.26×10^5	--	J-22
Cycloinverter	362	907	--	--	--	0.40	J-25
Inverter	240	800	--	--	--	0.30	J-26
Cycloconverter	60	31	--	--	--	1.46	J-27
FORCE COOLED: Rectifiers							
Forced-Air	150	52	0.058	897	2.59×10^6	2.88	J-15
Oil-Cooled:							
Controlled	7480	980	0.82	1195	9.12×10^6	7.63	J-15
Controlled	1300	600	0.48	1257	2.73×10^6	2.16	J-15
Controlled	1520	600	--	--	--	2.53	J-16
Uncontrolled	2240	200	0.36	561	6.29×10^6	11.20	J-15

E. ELECTROMECHANICAL CONVERTERS

1. Introduction

In this section we consider the weight and efficiency of motors and generators, which are the most important parts (at least in terms of weight) of electric transmissions. Since motors and generators are physically similar, they will be considered together.

Four physical configurations are considered in the following manner:

1. A basic idealized model consists of two current sheets with relative motion: a narrow air gap and a magnetic-flux return path. This simple model is used to obtain the limits to the operation of an electric machine in the most general terms.

2. An idealized model of the tooth-and-slot region of most machines is used to determine the magnetic limits to current conduction. This model, which recognizes the anisoptropic nature of the teeth, provides an understanding of the fundamental nature of the "reactance limit" of AC machines and shows that this limit applies to all machines.

3. A double-sided air-gap-winding machine geometry is used to investigate the effects of employing this geometry to eliminate certain of the magnetic limits uncovered in the tooth-and-slot model. While we cannot claim this to be the ultimate machine, it does illustrate the possible effects of a major advance in the technology.

4. A brief look at air-core geometry is intended to give some indication of the effects of the use of superconducting technology on electric machines.

At appropriate points in the development, existing technology is compared with the results of the analysis.

2. Basic Model of an Electromechanical Energy Converter

For the purposes of this analysis a rectilinear model will be assumed. This corresponds to a rotating machine "rolled out flat" and is a particularly good approximation for machines with a large number of pole pairs and with a narrow air gap.

The model is illustrated in Fig. J-5. The electromechanical interaction is between two current sheets that are disposed on either side of a narrow "air gap", which is simply a space between two regions of magnetic material. The regions of magnetic material must have a certain thickness away from the air gap in order to carry the flux that crosses the air gap.
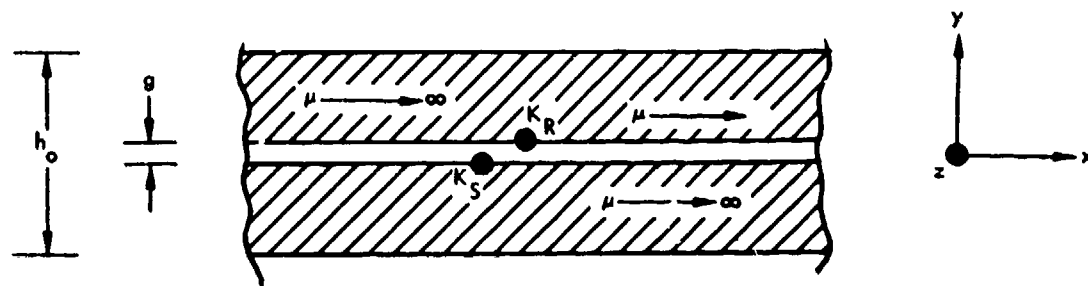
9-14-77-19

FIGURE J-5. Basic electromechanical converter model.

There is relative motion between the two sides of the converter. This is manifest as a motion of the material carrying one or both of the currents. From some frame of reference, however, both current distributions must be stationary, and of course this is the frame that is used for the analysis. Energy conversion is the product of shear force between the two sheets and relative velocity.

J-19

In this analysis, e will assume that the direction of current variation is the same as the direction of motion (at right angles to the direction of current flow). This corresponds to the geometry of conventional AC or DC machines. Another possibility is the acyclic or homopolar geometry, in which the current does not vary in the direction of motion but rather varies in the direction of current flow. Physically, this means that the current must cross the air gap periodically. It is not difficult to show that the two cases are equivalent in terms of efficiency and power density. For an illustration of the relationship between the two geometries, see Fig. J-6.

Figure J-6a shows the conventional machine geometry. Load current and exciting current both flow in the same windings, on either side of the air gap. The magnetic field lines "wrap around" the load-carrying conductors, and magnetic field lines in the core iron run generally in the same direction as the motion of the machine.

Figure J-6b shows the equivalent situation in a homopolar machine. In this machine, a separate winding produces excitation, through currents that run parallel to the motion and at right angles to the load current. Load currents on the two sides of the air gap essentially cancel, as far as the magnetic circuit is concerned, producing only a "kink" in magnetic field in the relative motion gap.

In the homopolar geometry, magnetic field lines wrap around the excitation winding (which must be periodic with the same pole length as the load windings). Thus magnetic flux is carried in a direction parallel to the load current and at right angles to motion.

It is important to note that the most important features of the two configurations are the same. True load currents in both geometries cancel: load current on one side of the air gap is just opposite to that on the other side. Magnetic field must

J-20
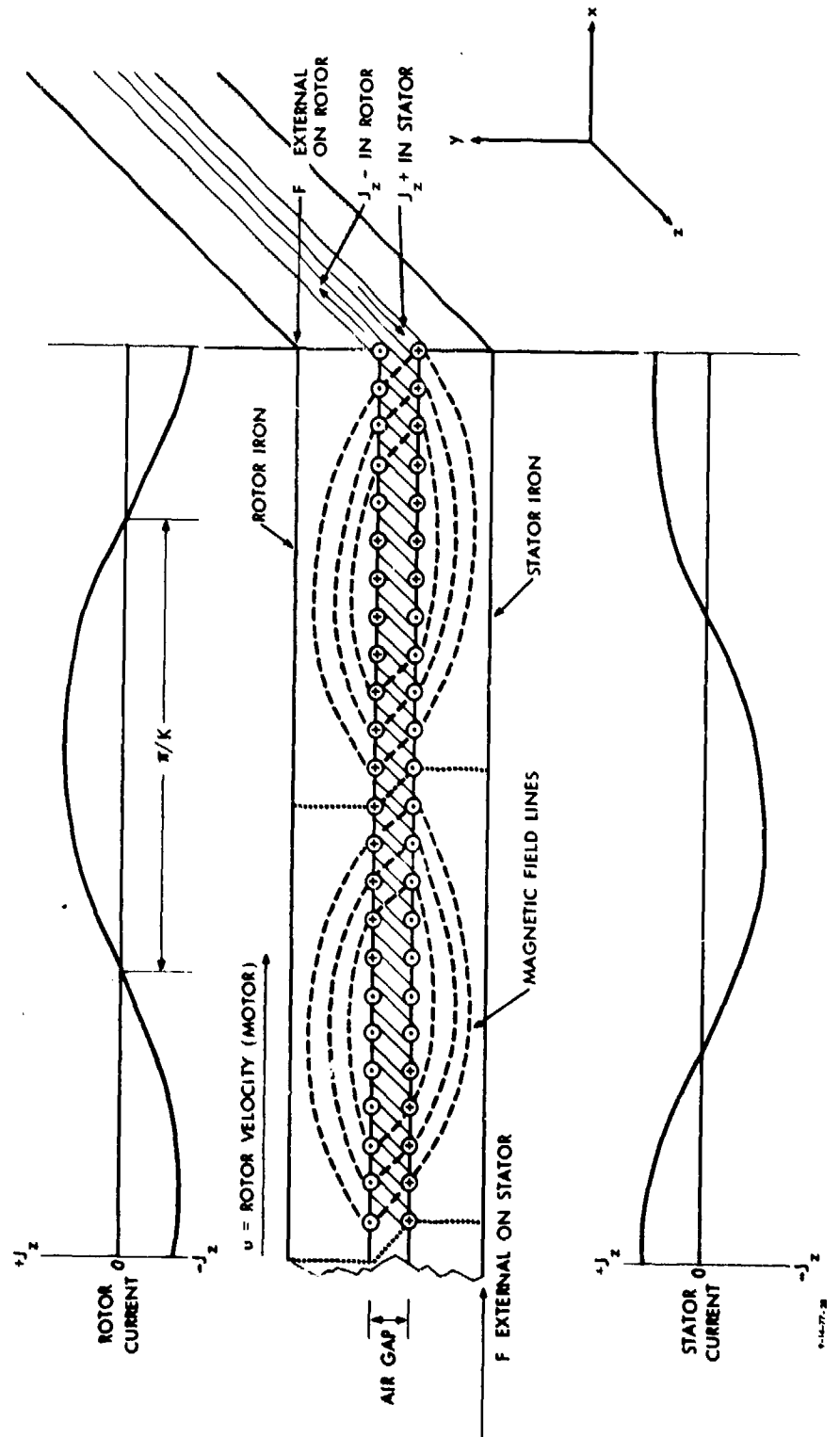
FIGURE J-6a. Normal converter configuration.

J-21
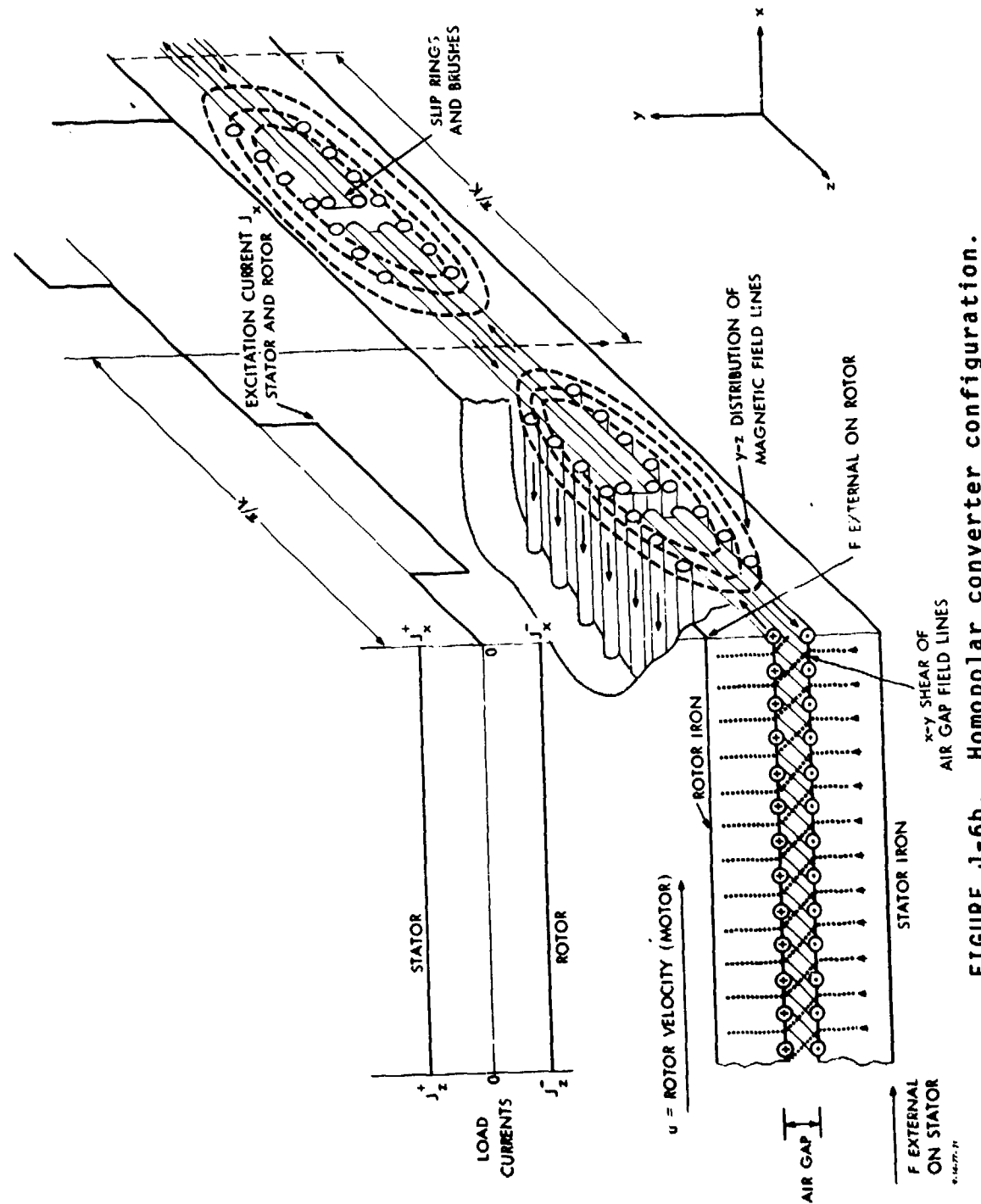
FIGURE J-6b. Homopolar converter configuration.

J-22

be carried by a magnetic circuit, and the flux capability of this circuit is proportional to pole length, even if the poles are arranged axially rather than circumferentially.

Throughout this analysis the two parts of the machine are denoted as "rotor" and "stator" for convenience, although these notations are arbitrary.

The analysis of the basic geometry of Fig. J-5 geometry carried out in Annex J2 shows that maximum power density (power per unit of active volume) is given by

$$\frac{P}{V} = \frac{B_s^2}{4\mu_o} \ uk \ \frac{\mu_o K_S}{B_s} \ . \tag{J-4}$$

Here, the dimensionless group $\mu_o K_S/B_s$ is the specific armature reaction. The product uk is electrical frequency, ω (radians/second). The results of Eq. J-4 are plotted in Fig. J-7.

Power loss per unit of power converted is given by

$$1 - \eta = \frac{\mu_o K_S'}{B_s} \left[\frac{1}{\mu_o \gamma_S u} + \frac{1}{\mu_o \gamma_R u} \right] \ . \tag{J-5}$$

Note that loss in efficiency is directly proportional to specific reaction and inversely proportional to speed, as we might expect. This result is plotted in Fig. J-8, assuming $\gamma_R = \gamma_S$.

As is apparent from Eqs. J-4 and J-5, the limitations on machine performance are characterized by:

- Usable magnetic flux density B_s
- Electrical frequency ω = uk
- Armature reaction $K_a = \mu_o K_S/B_s$
- Relative velocity u
- Surface conductivites γ_R and γ_S .
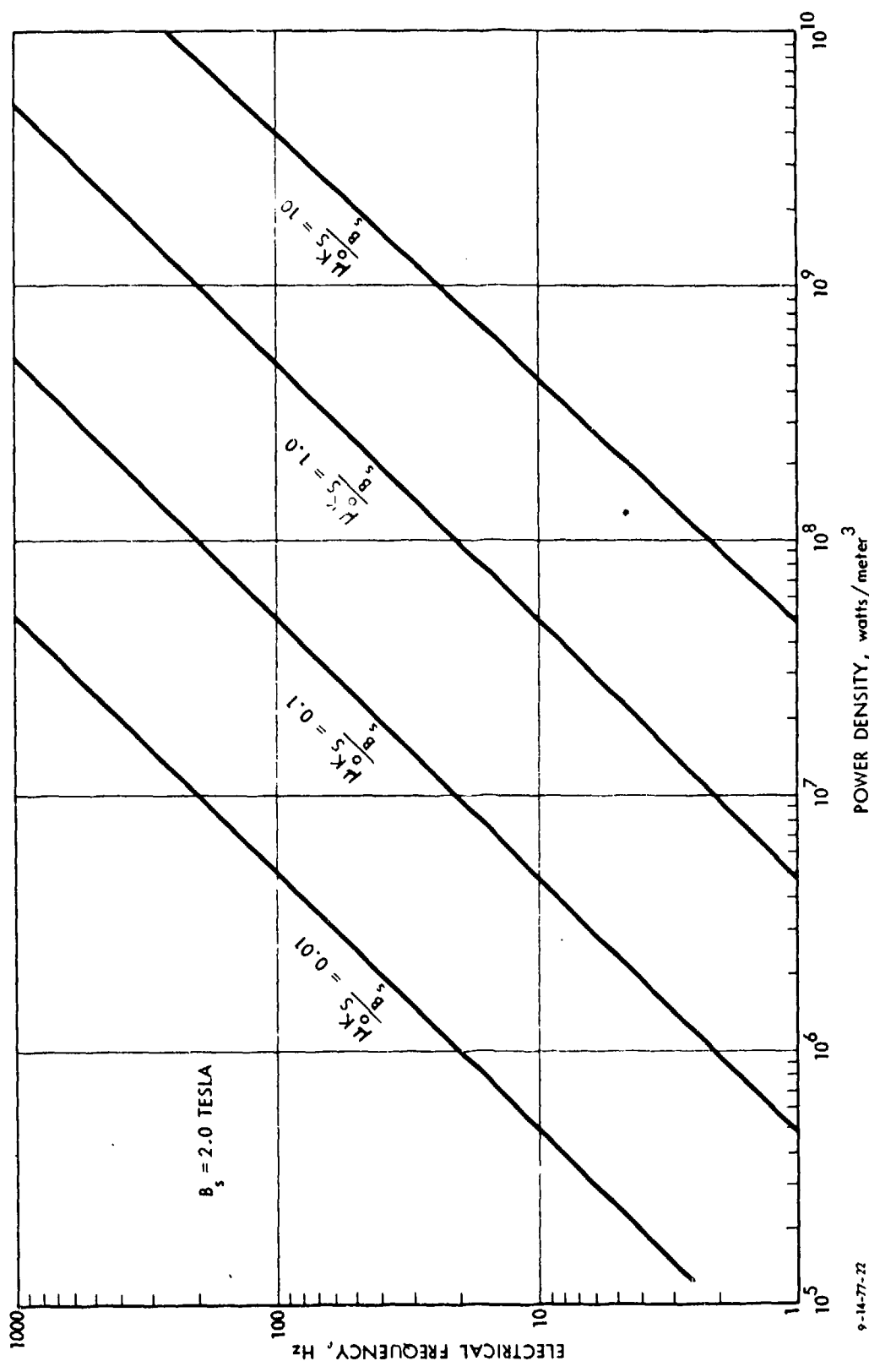
FIGURE J-7. Power density of the basic, idealized electromechanical energy converter.
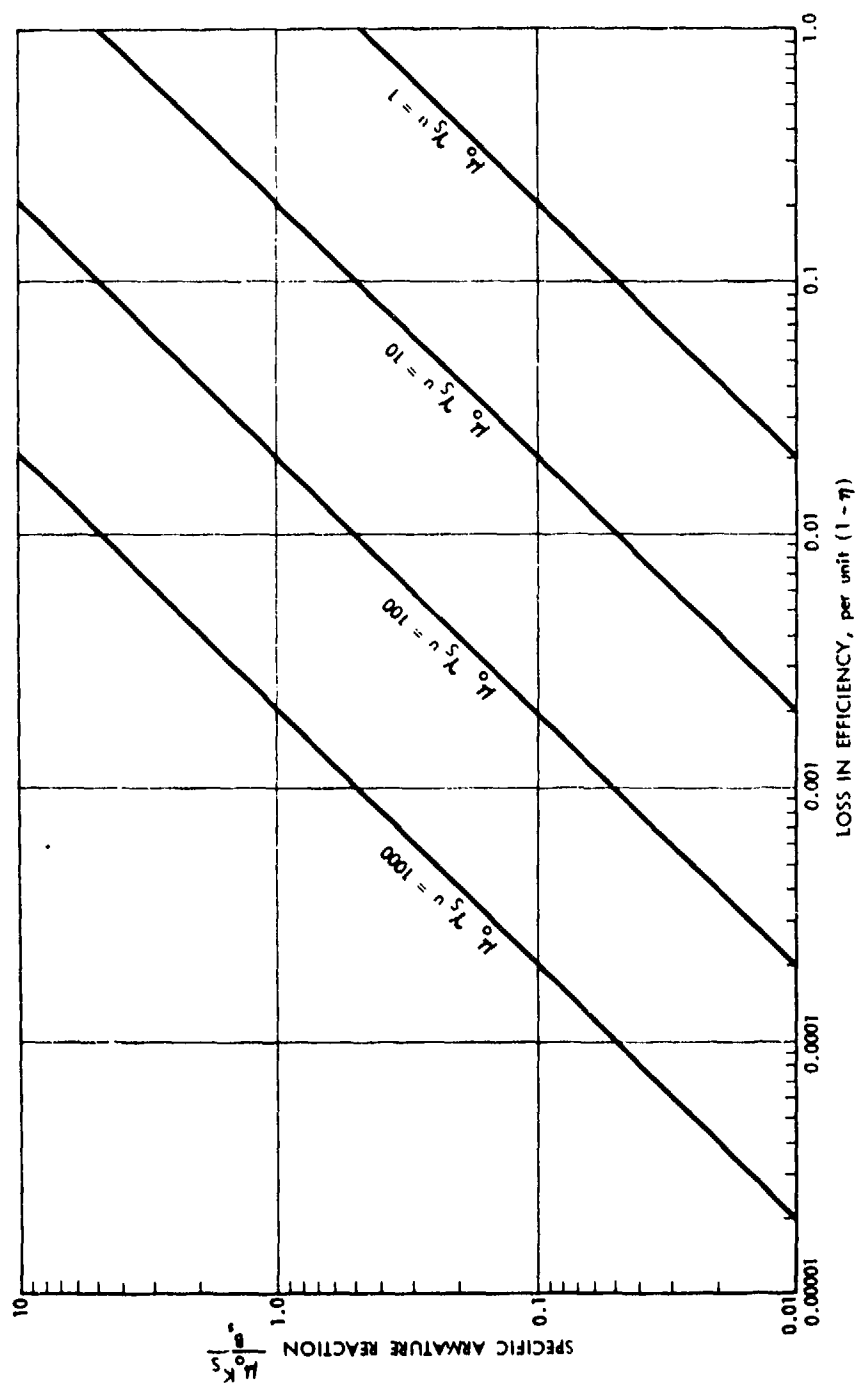
FIGURE J-8. Electrical efficiency: effect of armature reaction.

J-25

It is apparent that power density and efficiency trade off through armature reaction K_a. It will be shown in the next sections that the tradeoff includes electrical frequency also.

Magnetic flux density is limited by the saturation flux density of iron, at least in machines with iron magnetic circuits. This limit is about two tesla.

Relative velocity u may be limited by specific application (that is, by shaft speed and machine diameter), or it may be limited by centrifugal force in very large or high-angular-speed machines.

Allowable armature reaction and surface conductivity are both affected by the thickness of the current-carrying layers. There are definite limits on these layers, and these are developed in the next section.

3. Tooth-and-Slot Region Model, Winding Region Limits

The most common form of electric machine construction involves putting the electrical conductors in slots in the surface of the iron magnetic core. The iron intervening between slots is called "teeth". The teeth affect magnetic field handling capability in two ways. First, since the teeth cover only about half of the air-gap area, they reduce radial air-gap flux density by one-half. Second, currents in the slots between the teeth produce "leakage" flux that circulates through the teeth and core together with azimuthal air-gap flux that also circulates through the teeth and core. The azimuthal air-gap flux density is produced by the load currents and is required for the magnetic shear in the air gap, but the associated leakage flux does not contribute to the interaction. Thus the design should minimize the leakage flux for the given azimuthal flux density in the air gap.

Saturation in the teeth comes about in two ways. First, the azimuthal flux density in the air gap and across the tips

J-26

of the teeth adds vectorially to the main radial air-gap flux
density and serves to reduce the maximum level of air-gap flux
density. The second limitation is due to leakage flux circu-
lating in the teeth and core. This flux has a maximum at the
tooth bottoms and in the core.

As is shown in Annex J2, the limiting values of power
density are approximately

$$\frac{P}{V} \leq \frac{B_c^2}{4\mu_o} \quad \frac{uk}{2} \sqrt{\frac{\mu_o J_m}{\sqrt{2}\ k\ B_c}} \qquad (J-6)$$

(base of tooth and core limit)

$$\frac{P}{V} \leq \frac{B_c^2}{4\mu_o} \quad uk \quad \frac{1}{2\sqrt{2}} \quad . \qquad (J-7)$$

(tooth tip limit)

Actually, these limits are somewhat optimistic, since they con-
sider only core-back volume.

The limiting value of efficiency is affected by flux limi-
tation also. Power loss is approximately

$$1 - \eta = 2\sqrt{2} \quad \frac{\mu_o J_m}{k\ B_c} \quad \frac{ku}{\mu_o \gamma u^2} \quad . \qquad (J-8)$$

4. Symmetrical Air-Gap-Winding Machine

To investigate the effects of a major advance in machine
technology, an advanced configuration has been postulated and
evaluated. This configuration has two air-gap windings disposed
in the space between two magnetic "back-iron" elements (Fig. J-9).
It is assumed that the current distributions are identical but
displaced by a phase angle, and that the physical gap between

J-27

them is small. The peak magnetic field at the surface of each
magnetic element is equal to saturation flux density, and the
iron is fully utilized. Under these assumptions, power per
unit of active volume is

$$\frac{P}{V} = \frac{B_c}{4} \quad ku \quad F(kt,\delta) \quad , \qquad (J\text{-}9)$$

per-unit dissipation is

$$1 - \eta = \frac{2kt}{\mu_o \gamma tu} \quad E(kt,\delta) \quad , \qquad (J\text{-}10)$$

and peak current density in the two windings is

$$J_s = k \frac{B_c}{\mu_o} \quad \alpha(kt,\delta) \quad \cdot \qquad (J\text{-}11)$$

The parameters F, E, and α are tabulated in Annex J2.
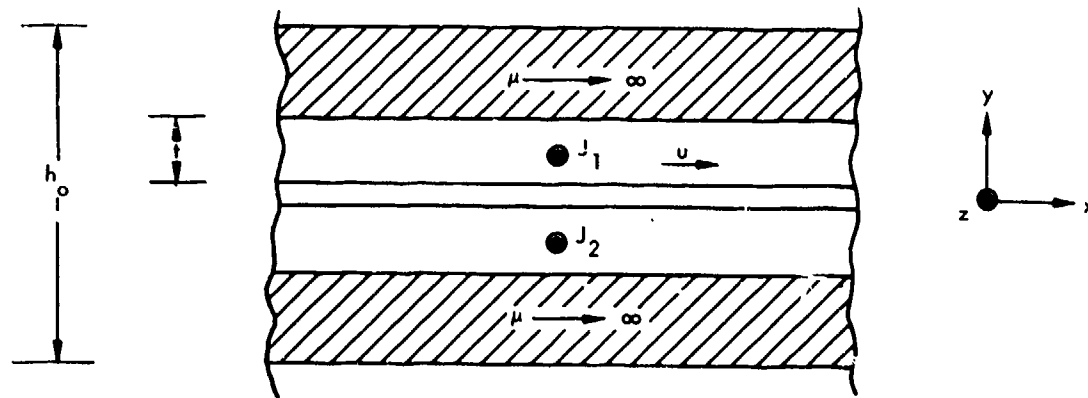
v-14-/7-21

FIGURE J-9.   Symmetrical air-gap-winding machine.

It is quite difficult to see just what significance these expressions have. It is clear from looking at the tabulated parameters that somewhat higher power densities than are possible with toothed machines can be obtained with this geometry, but it is not clear which of these would be acceptable from a viewpoint of efficiency or current density.

It is possible to eliminate k from Eq. J-9 and either Eq. J-10 or J-11, using Eq. J-11 or J-10. The result is:

$$\frac{P}{V} = \frac{B_c^2}{4\mu_o} \frac{(1-\eta)}{2} \mu_o \gamma u^2 P_1(kt,\delta) \tag{J-12}$$

$$J_s = \frac{(1-\eta)}{2} B_c \gamma u C_1(kt,\delta) \tag{J-13}$$

or

$$\frac{P}{V} = \frac{B_c J_s}{4} u P_2(kt,\delta) \tag{J-14}$$

$$(1-\eta) = \frac{J_s}{B_c} \frac{2}{\gamma u} E_2(kt,\delta) \quad . \tag{J-15}$$

The coefficients P_1, C_1, P_2, and E_2 are tabulated in Annex J2. From examining these tables, we see that we can define two machines that are "optimum" in one sense. There is a set of values of kt and δ for which P_1 is a maximum, denoting a geometry that maximizes the ratio between power density and efficiency. Similarly, there is a set of values of kt and δ that miximizes the ratio between power density and current density. Power density and current density are plotted versus efficiency in Figs. J-10 and J-11 for the machine of case 1: the machine that maximizes the ratio of power density to efficiency. Power density versus current density and efficiency versus current density are plotted in Figs. J-12 and J-13 for
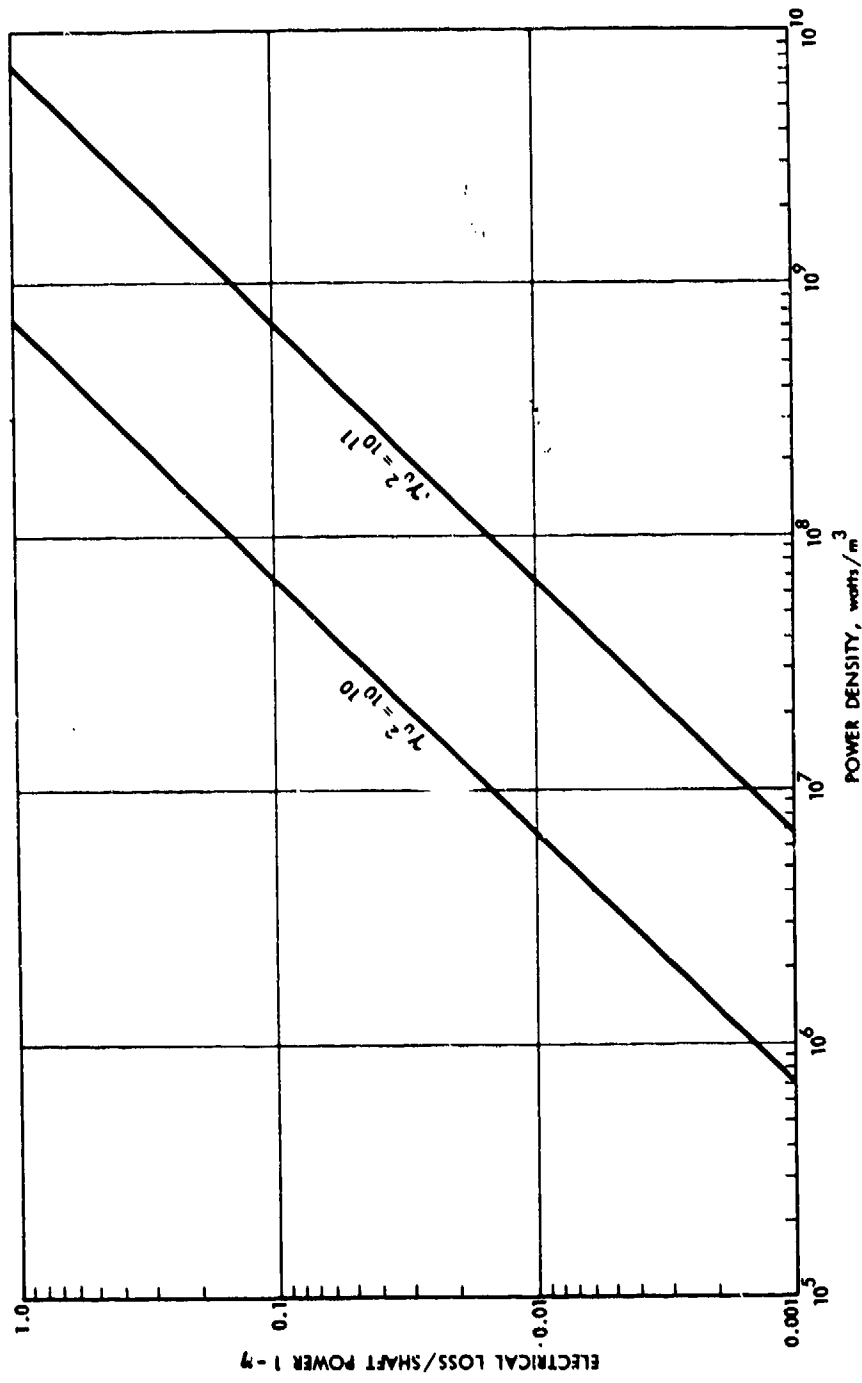
FIGURE J-10. Power density versus efficiency: air-gap case 1.

J-30
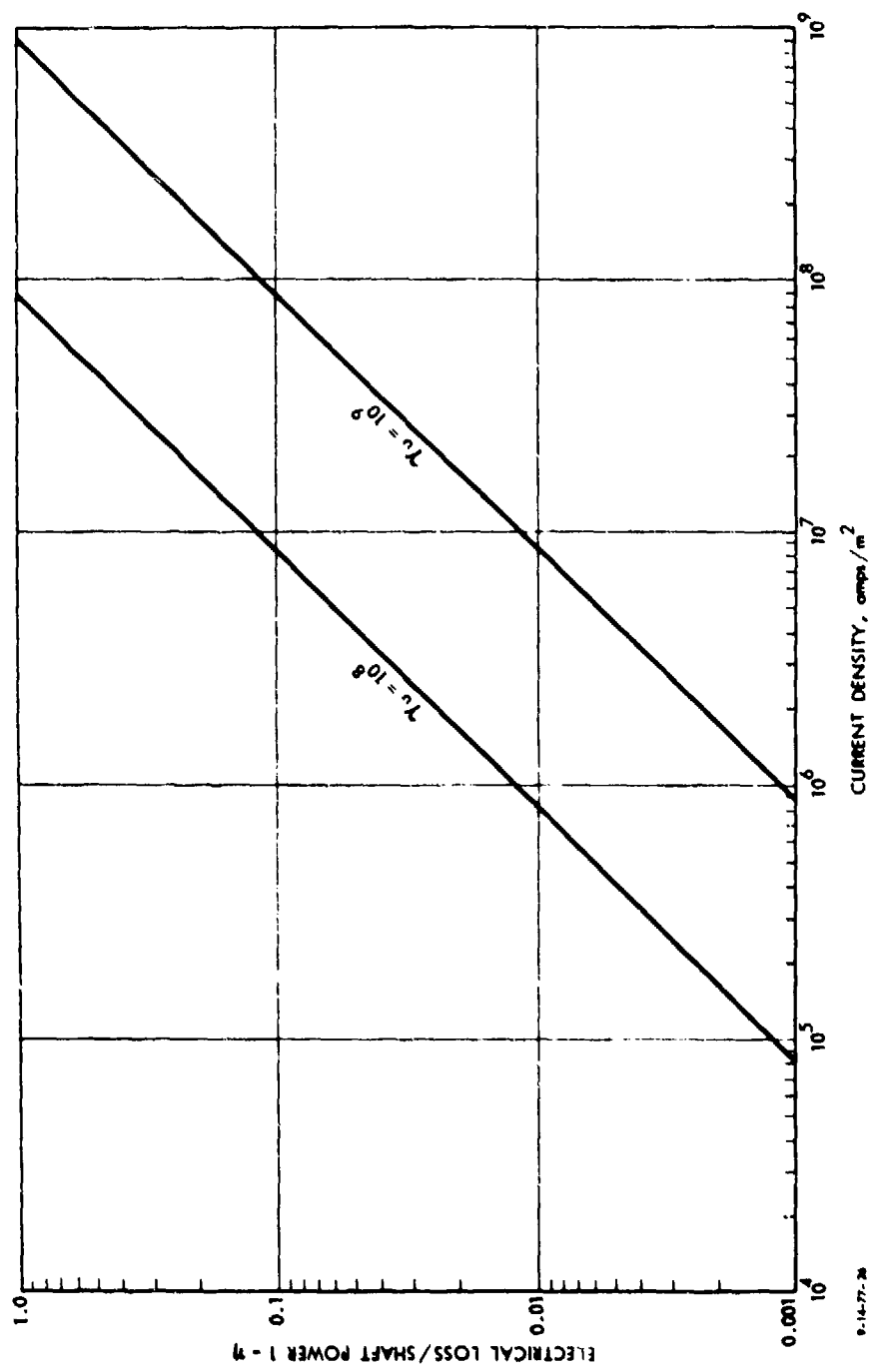
FIGURE J-11. Current density versus efficiency: case 1.

J-31
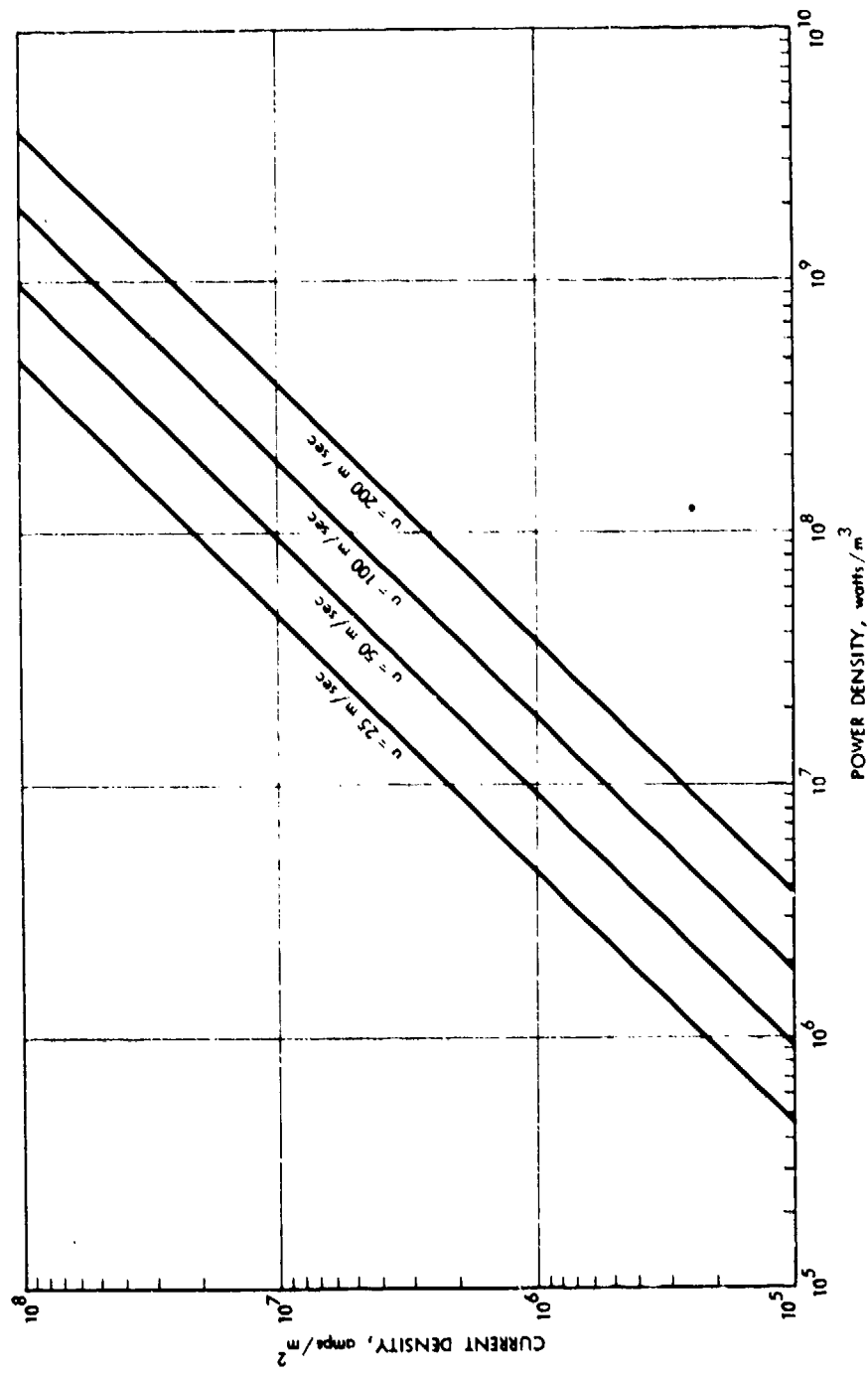
FIGURE J-12. Power density versus current density, case 1.
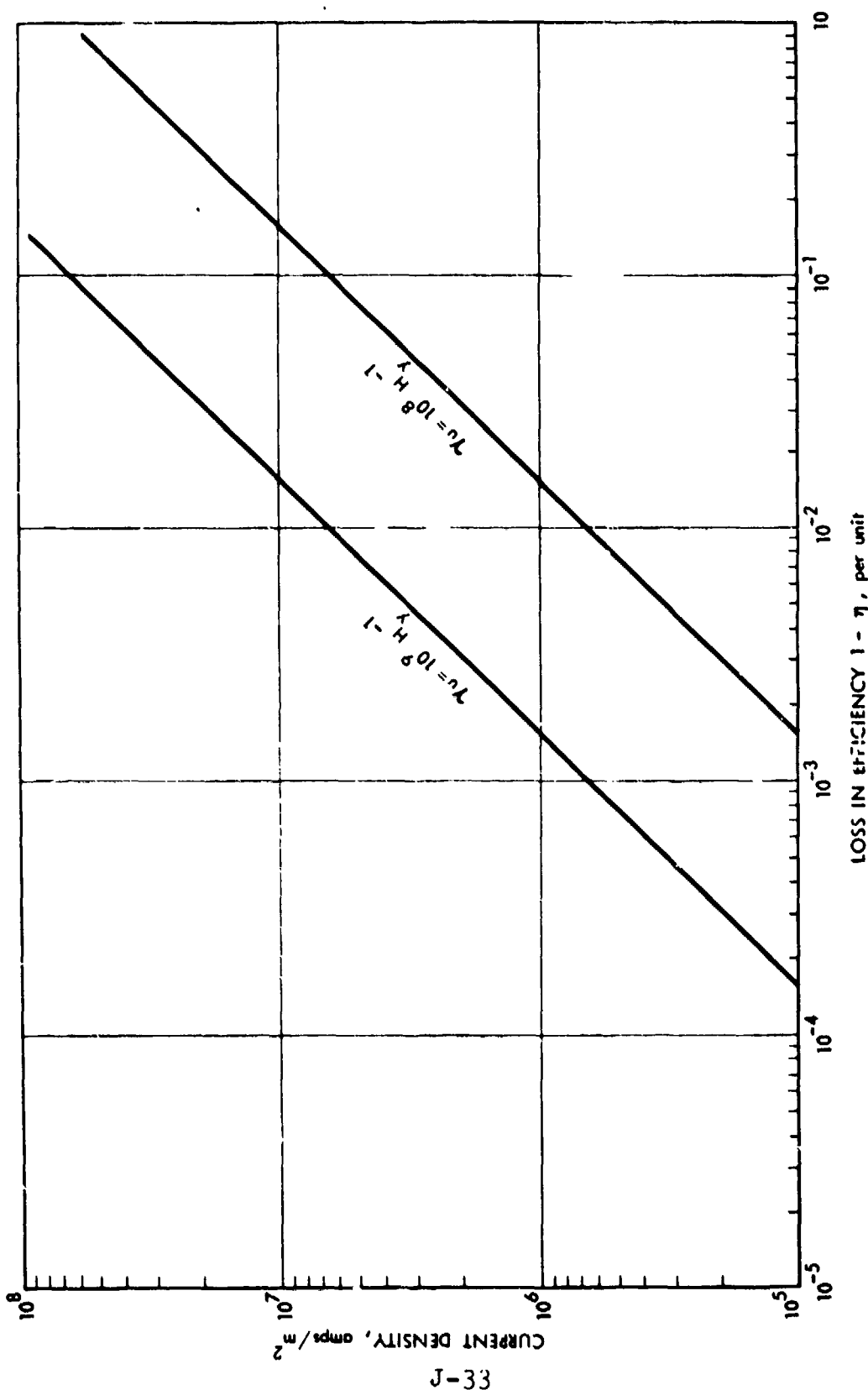
FIGURE J-13. Efficiency versus current density, case 2.

9-14-77-28

J-33

the machine of case 2: the geometry that maximizes the ratio between power density and current density.

Finally, a comparison of these two machines and a third case has been made. The third-case machine was chosen with kt = 1.0, δ = 90 deg. This is the normalized thickness that maximizes power density for a fixed-boundary magnetic field at δ = 90 deg.

By examining Figs. J-14 and J-15, it is possible to see that:

1. These machines appear to have somewhat higher power densities than are possible in machines with teeth.

2. Efficiencies are marginal or not acceptable for all machines that do not have very high surface speed and long pole pitch. Thus, this class of machine is useful only for high-speed, high-power machines.

Plotted also in Fig. J-14 are examples of machines currently available. These are generally quite far from limiting power density.

5. Effects of Air-Core Geometry and Superconducting Windings

What follows is a more-or-less qualitative discussion of the effects of the use of superconducting windings in air-core geometry. Due to time limitations, this discussion has not been fully developed.

Consider the model of an air-core machine shown in Annex J2, Fig. J2-4. The current-carrying members are thin sheets situated close together. The boundaries of the machine are diamagnetic surfaces that represent conductive, eddy-current shields.

A limit for the power density of this type of machine is derived in Annex J2 and is plotted in Fig. J-16. As can be seen, the power density can be substantially larger in this geometry, largely because magnetic fields need not be limited by iron

J-34
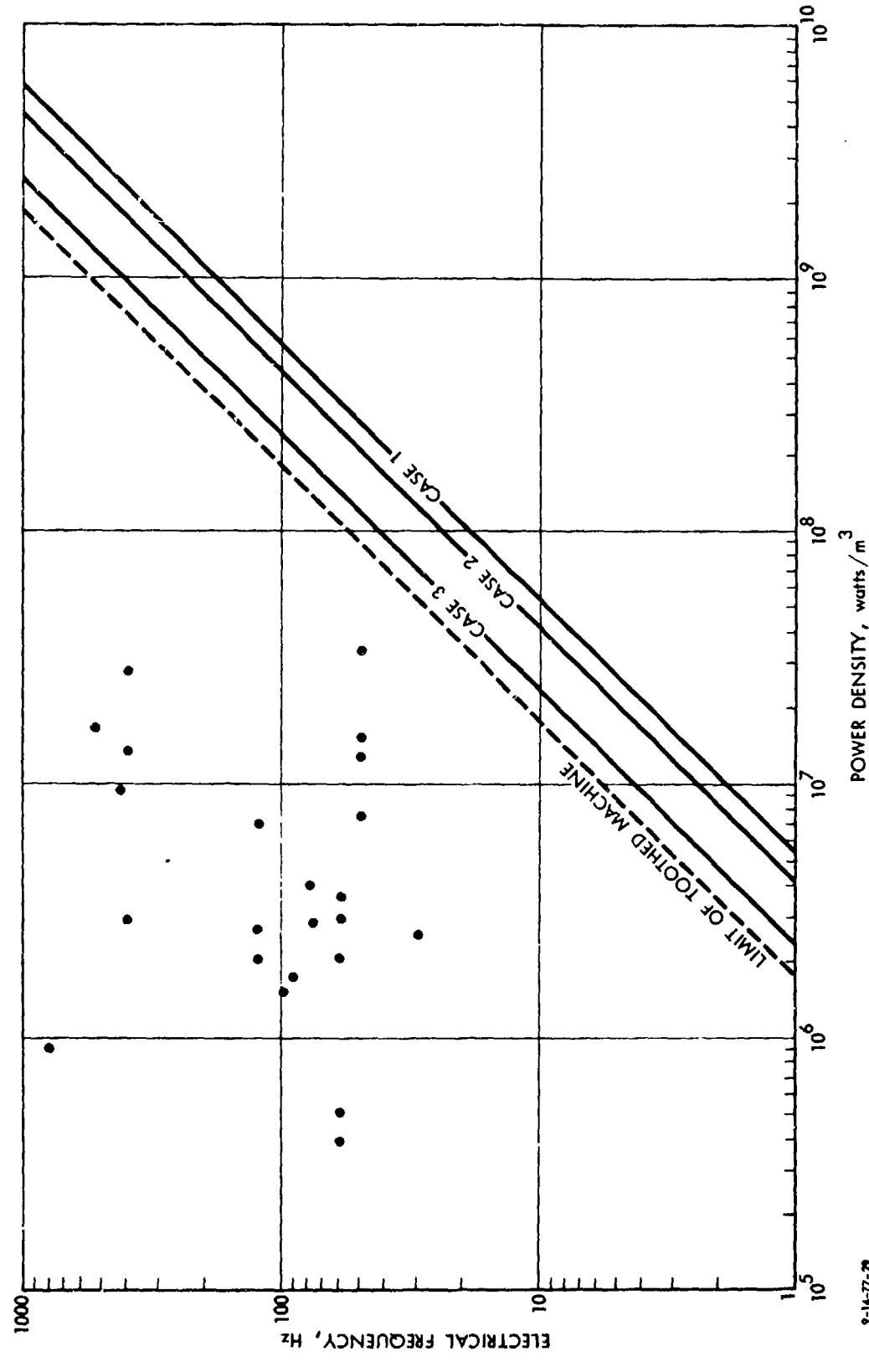
FIGURE J-14. Comparison of machines, power density.

J-35
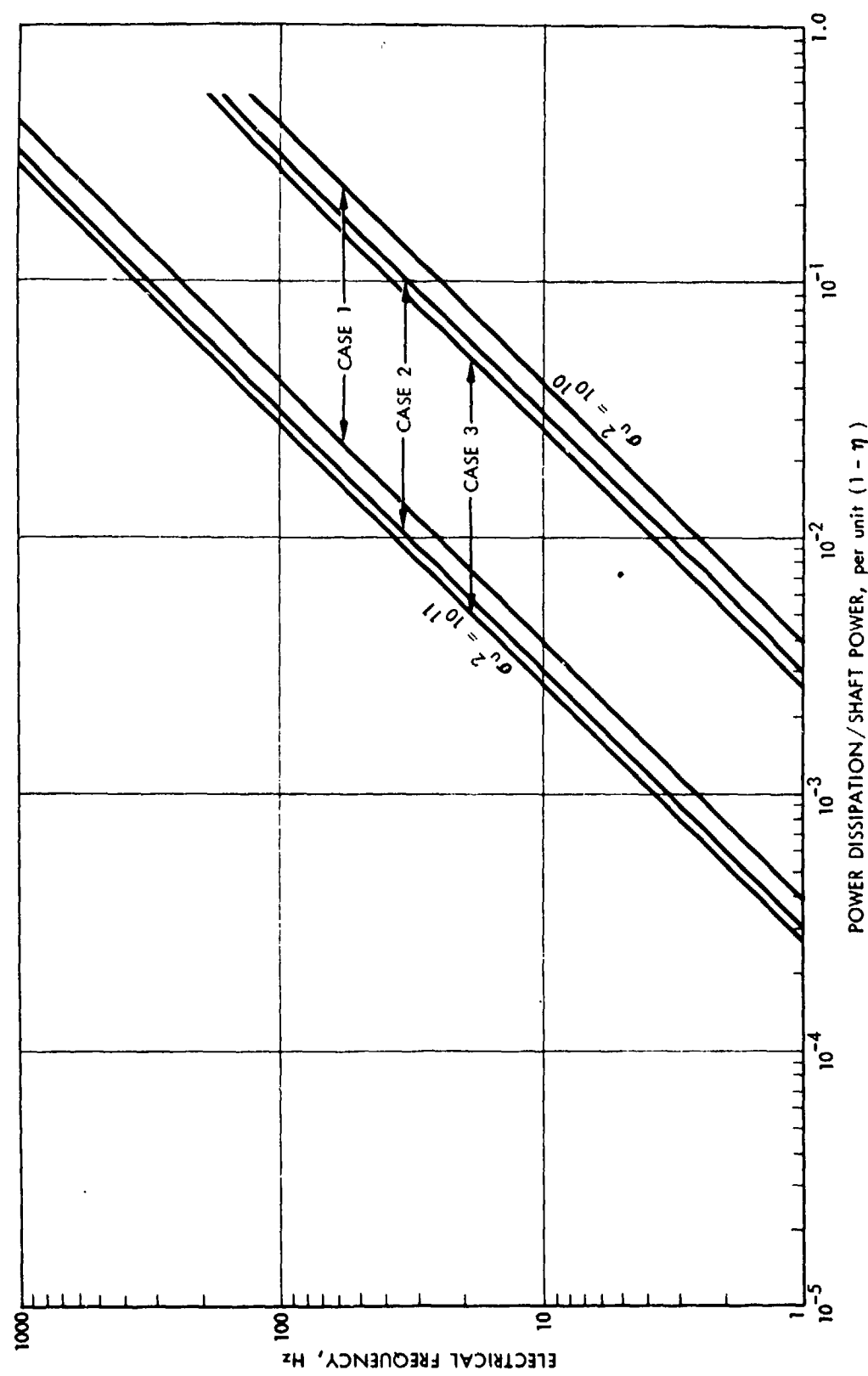
FIGURE J-15. Comparison of machines, efficiency.

POWER DISSIPATION/SHAFT POWER, per unit $(1 - \eta)$

ELECTRICAL FREQUENCY, Hz

9-14-77-30

J-36
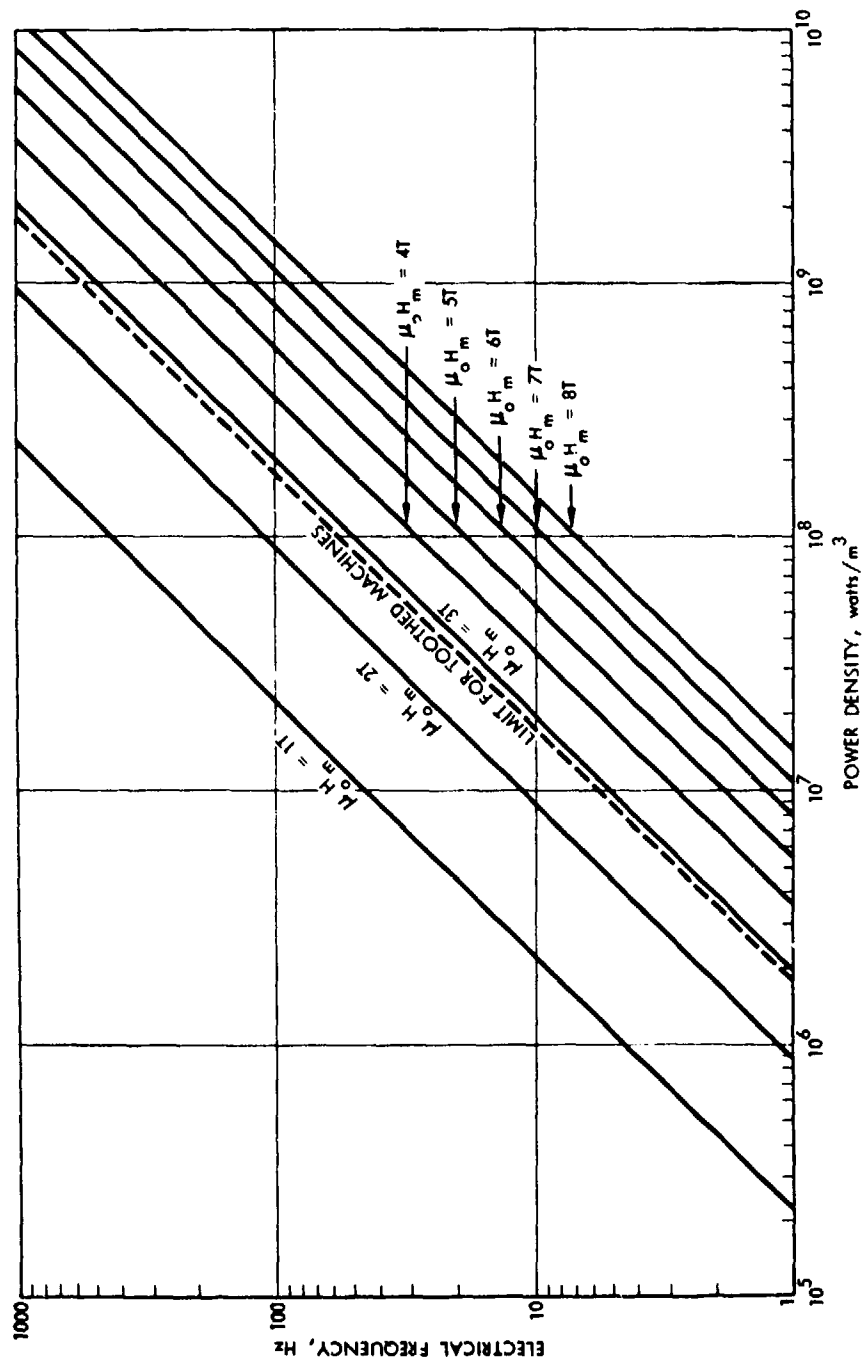
FIGURE J-16. Air-core machine power density.

J-37

saturation. We expect that flux densities on the order of 6 to 8 T should be achievable with the classes of superconducting materials presently available.

Further, Fig. J-16 does not tell the whole story. The volume of a machine with an iron magnetic circuit is filled with heavy material. The air-core machine is largely empty of material. (It *is* full of magnetic field, however.) Thus, Fig. J-16 strongly understates the difference between iron- and air-core machines with respect to power-to-weight ratio. In addition, air-core superconducting machines will have substantial efficiency advantages, particularly in the middle sizes. In such machines all of the excitation and compensation current would be supplied by lossless conductors. We have not attempted to quantify this effect here.

Table J-2 contains a summary of a comparison between various conventional and superconducting machine designs in large ratings. This table and Fig. J-17 were put together for another purpose and consequently are in a different form from other data here. The possibility of improving shear interaction, and hence power density, is apparent.

6. <u>Symbols Used in Section E</u>

The symbols used in Section E include the following:

B_c . Saturation flux density in magnetic material

B_s Usable magnetic flux density

H_m Magnetic field limitation of superconducting windings

J_m Maximum current density in slots

J_s Peak usable current density in the winding region

k Wavenumber corresponding to pole pitch

K_S, K_R Stator and rotor surface current density: current density times winding thickness

P Power

t Winding thickness

TABLE J-2. COMPARISON OF MAGNETIC SHEAR STRESS LEVELS FOR VARIOUS SUPERCONDUCTING (SC) AND CONVENTIONAL (CONV) ELECTRIC MACHINES*

Machine	Power Rating P, kW	Mechanical Freq. ω_m, Radians/sec	Rotor Diameter D, in.	Rotor Length L, in.	Magnetic Shear Stress σ_m, psi
1. Avco SC, Operating	8	1257	2.18	4.49	1.68
2. First MIT SC, Operating	80	377	5.75	4.5	7.76
3. USSR SC, Operating	62	314	5.51	9.84	3.72
4. USSR SC, Operating	1×10^3	157	20.3	21.4	4.07
5. Second MIT SC, Operating	2×10^3	377	8.0	24.0	19.47
6. Westinghouse SC, Operating	5×10^3	377	10.2	17.6	40.81
6'. Projected Capability of Item 6 with Modification	1.5×10^4	377	10.2	17.6	147
7. Westinghouse SC, Ship Drive Design	3×10^4	18.85	87.25	27.0	43.4
8. MIT SC Design from Thesis	3×10^4	12.57	143.04	20.0	31.0
9. IRD SC Paper Design	5×10^5	377	41.3	145.0	36.29
10. MIT SC Paper Design	1×10^6	377	35.2	123.3	97.7
11. General Electric SC Paper Design	2×10^6	377	43.0	117.5	98
12. MIT SC IEEE Paper Design	1×10^6	377	21.6	130.0	246.4
13. General Electric CONV Ship Drive	3×10^4	12.57	240	48	4.86
14. Westinghouse Airborne SC, Operating	5×10^3	1257	10	10.5	20.38
15. Various CONV Alternators, Operating Mostly on American Electric Power System:					
(1964)	3×10^5	377	37	200	16.4
(1953)	4.4×10^4	377	29	125	6.26
(1953)	1.12×10^5	188.5	54	167	6.87
(1953)	1.47×10^5	377	38	180	8.45
(1953)	1.25×10^5	188.5	56	150	8.00
(1970)	8.0×10^5	377	44.5	290	20.82
(1970)	8.0×10^5	377	43	245	26.4
	1.30×10^5	377	40	179	6.79

*From MIT summer course 6.50S, 1974, Smith, Thullen, Keim, and Kirtley.
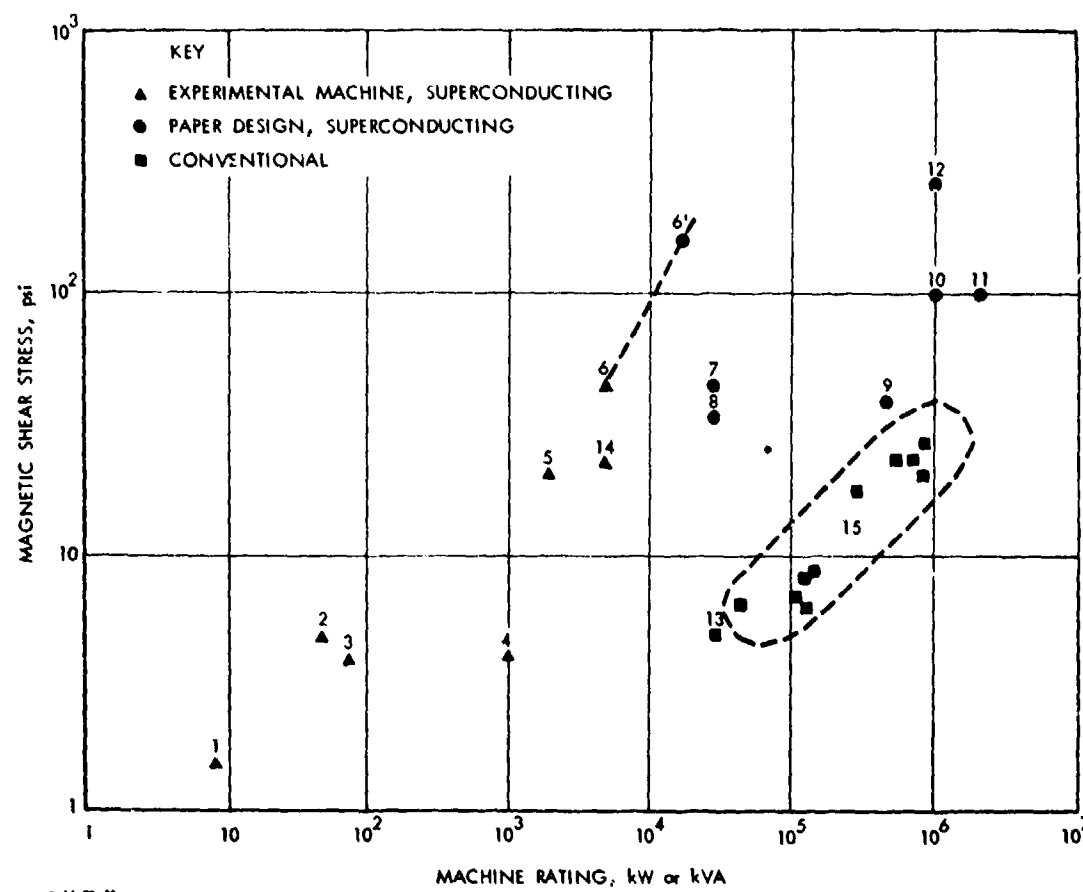
FIGURE J-17. Magnetic shear stress versus machine rating.
(Data points are keyed to Table J-2.)

J-40

u	Relative velocity
V	Volume of active elements of the power converter
δ	Relative phase angle
η	Efficiency
γ	Conductivity
γ_S, γ_R	Stator and rotor surface conductivity: conductivity times winding thickness
ω	Electrical frequency.

F. THERMAL LIMITS

Thermal limits for current-carrying conductors are set by three primary energy transport mechanisms: (1) thermal conduction within the electrical conductor, (2) heat transfer from the surface of the conductor to a cooling medium, and (3) energy transfer from the cooling medium to an eventual heat sink, which is usually accomplished through transport of the cooling medium itself, i.e., forced-convection cooling. Thus the thermal limit is generally composed of a conduction limit, a (surface) heat transfer limit, and an enthalpy transport (or First Law) limit. Since the thermal limit is manifested by a peak conductor temperature rise above the coolant temperature, these three limits combine as energy transfer resistances in series, each with its own temperature rise, the sum of which must equal the maximum allowable conductor rise.

The model for analyzing the thermal limits in electric transmission subsystems comprises a cylindrical conductor of radius R_o and length L, with a coaxial cooling channel of radius R_1. The outer surface at R_o is assumed to be adiabatic, and any axial conduction is neglected. This model may be extended to a conductor with multiple cooling channels by equating R_o to the per-unit radius, as

$$\pi R_o^2 = \text{(total cross section/number of channels)}. \qquad (J-16)$$

The volumetric energy dissipation rate is equal to

J-41

$$q = j^2 \rho_e \quad , \tag{J-17}$$

where j is the current density and ρ_e is the electrical resistivity. Since, in general, the specific current-carrying capacity is of primary interest, we define the superficial current density j_o so that

$$j_o \, R_o^2 \equiv j \, (R_o^2 - R_i^2) \tag{J-18}$$

or, defining the radius ratio X as

$$X \equiv R_i/R_o = (\text{void fraction})^{1/2} \quad , \tag{J-19}$$

we have

$$j_o = j \, (1 - X^2) \quad . \tag{J-20}$$

In the remainder of this section, each of the three thermal limits will be evaluated individually, and then the combined limit will be determined.

1. **Conduction Limit**

For steady-state conduction within a cylindrical conductor with boundary conditions of no heat flux at $r = R_o$ and $T = T_i$ at $r = R_i$, the temperature distribution is given by

$$T - T_i = \frac{j^2 \rho_e R_o^2}{4k} \left[\frac{R_i^2 - r^2}{R_o^2} + 2\ell n(r/R_i) \right] , \tag{J-21}$$

where k is the thermal conductivity. Solving for the maximum temperature T_m, which occurs at $r = R_o$, and replacing j by $j_o/(1 - X^2)$, we have

$$T_m - T_i = \frac{j_o^2 \rho_e R_o^2}{4k} (X^2 - 1 - 2\ell n X) / (1 - X^2)^2 \quad . \tag{J-22}$$

J-42

We define ΔT_c to be

$$\Delta T_c \equiv T_m - T_1 \quad , \tag{J-23}$$

and we define a dimensionless superficial current density J_c^+ so that

$$J_c^{+2} \equiv \frac{J_o^2 \rho_e R_o^2}{4k\Delta T_c} = (1-X^2)^2 / (X^2 - 1 - 2\ell nX) \quad . \tag{J-24}$$

Examination of Eq. J-24 reveals that the maximum value of J_c^+ occurs at $X = 1$, or at 100% void fraction. This of course implies infinite dissipation. Also, J_o varies inversely as R_o and is obviously independent of conductor length.

2. Convective Heat Transfer Limit

Determination of the convective heat transfer limit assumes that the maximum coolant velocity is determined by a maximum allowable coolant pressure drop ΔP. The cooling medium is assumed to be pressurezed water with no boiling taking place, so that incompressibility can be assumed. For a given R_1 and L, the pressure-drop limitation fixes the coolant velocity, so that the convective heat transfer coefficient (HTC) can be expressed in terms of ΔP, R_1, and L. Once the HTC is determined, the volumetric energy dissipation rate $J_o^2 \rho_e$ can be related to the rate of heat removal at $r = R_1$. The details of the analysis are given in Annex J3. The resulting expression for J_h^+, the dimensionless HTC-limited superficial current density, is given by

$$J_h^{+2} \equiv \frac{J_o^2 \rho_e R_o^2}{4k\Delta T_h} = (1-X^2) \, X^{3/2} \left[\frac{F d_w \Delta P R_o^3 C^2}{16 k^2 Pr^{4/3} L} \right]^{1/2} \quad , \tag{J-25}$$

where

T_h = (T_i - coolant temperature)

F = Fanning friction factor

d_w = Coolant density

c = Coolant specific heat

P_r = Coolant Prandtl number.

Examination of Eq. J-25 shows that the maximum superficial current density for a given ΔT_h occurs at $X = (3/7)^{1/2} = 0.655$, or at 43% void fraction. The superficial current density j_o is weakly dependent on R_o and L, varying as $(R_o L)^{-1/4}$.

3. First Law Limit

As with the HTC limit, it is assumed that the maximum coolant flow rate is limited by a maximum allowable pressure drop. If the current density is uniform along the conductor, then the maximum conductor temperature will occur at the coolant exit, where the coolant temperature will be a maximum. Derivation of the coolant temperature rise ΔT_e follows along similar lines as for ΔT_h and is given in Annex J3. The dimensionless superficial current density j_e^+ is given by

$$j_e^{+2} \equiv \frac{j_e^2 \rho_e R_o^2}{4k\Delta T_e} = (1-X^2) \; X^{5/2} \left[\frac{d_w \Delta P R_o^5 c^2}{16k^2 F L^3} \right]^{1/2} \; . \qquad (J-26)$$

Here the maximum value of j_e occurs at $X = (5/9)^{1/2} = 0.754$, or at 55% void fraction. It too is weakly dependent on R_o, varying as $R_o^{1/4}$, and it varies as $L^{-3/4}$.

The values of j_c^+, j_h^+, and j_e^+ are plotted versus X for three values of L and R_o in Figs. J-18 through J-20 for the case of a copper conductor cooled with water flowing at a 100-psi (690 kPa) pressure drop. These examples show that for small R_o (e.g., 3 mm) the current density is First Law limited at long conductor lengths (e.g., 3 m), but becomes HTC limited

J-44
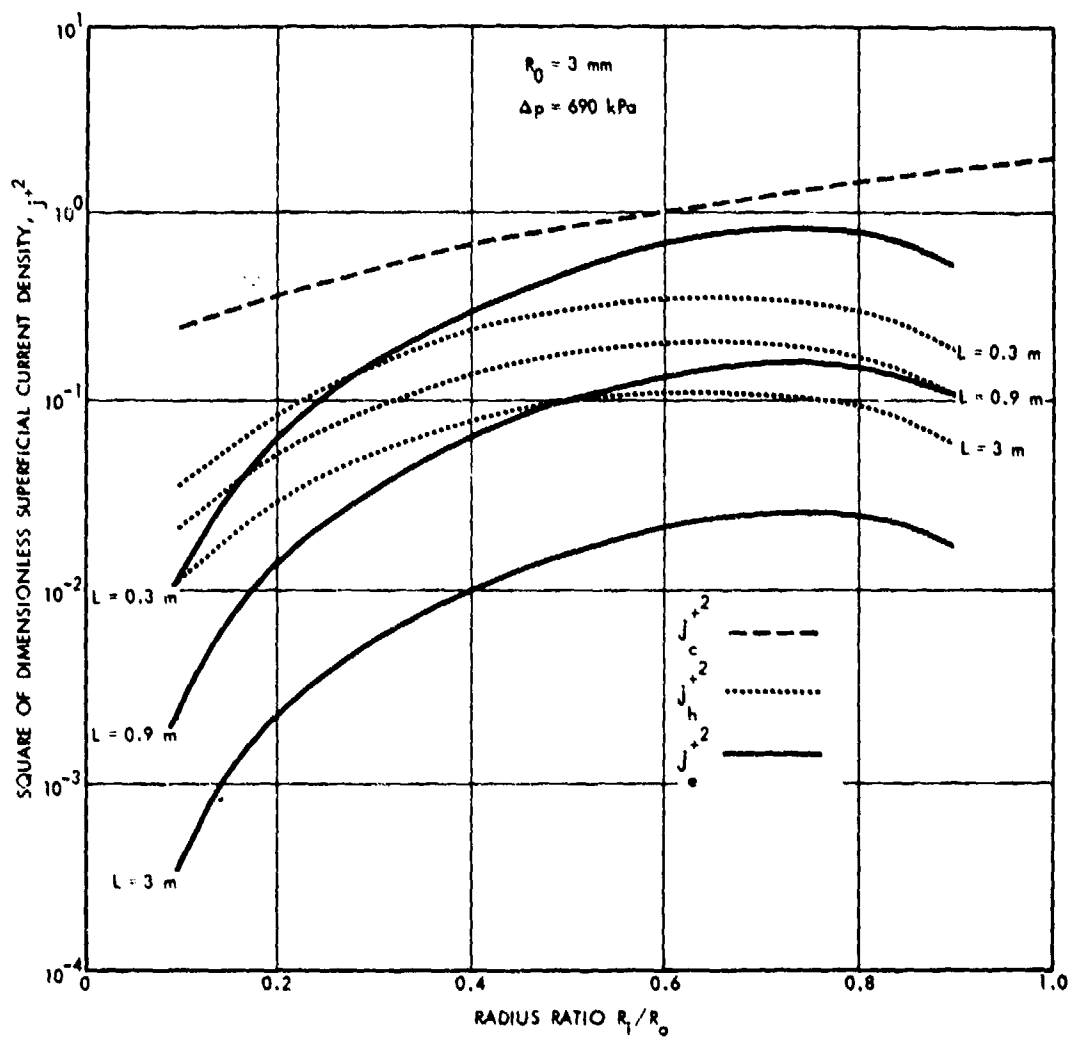
FIGURE J-18. Thermal limits of current density for water-cooled copper, R_0 = 3mm.

9-14-77-33
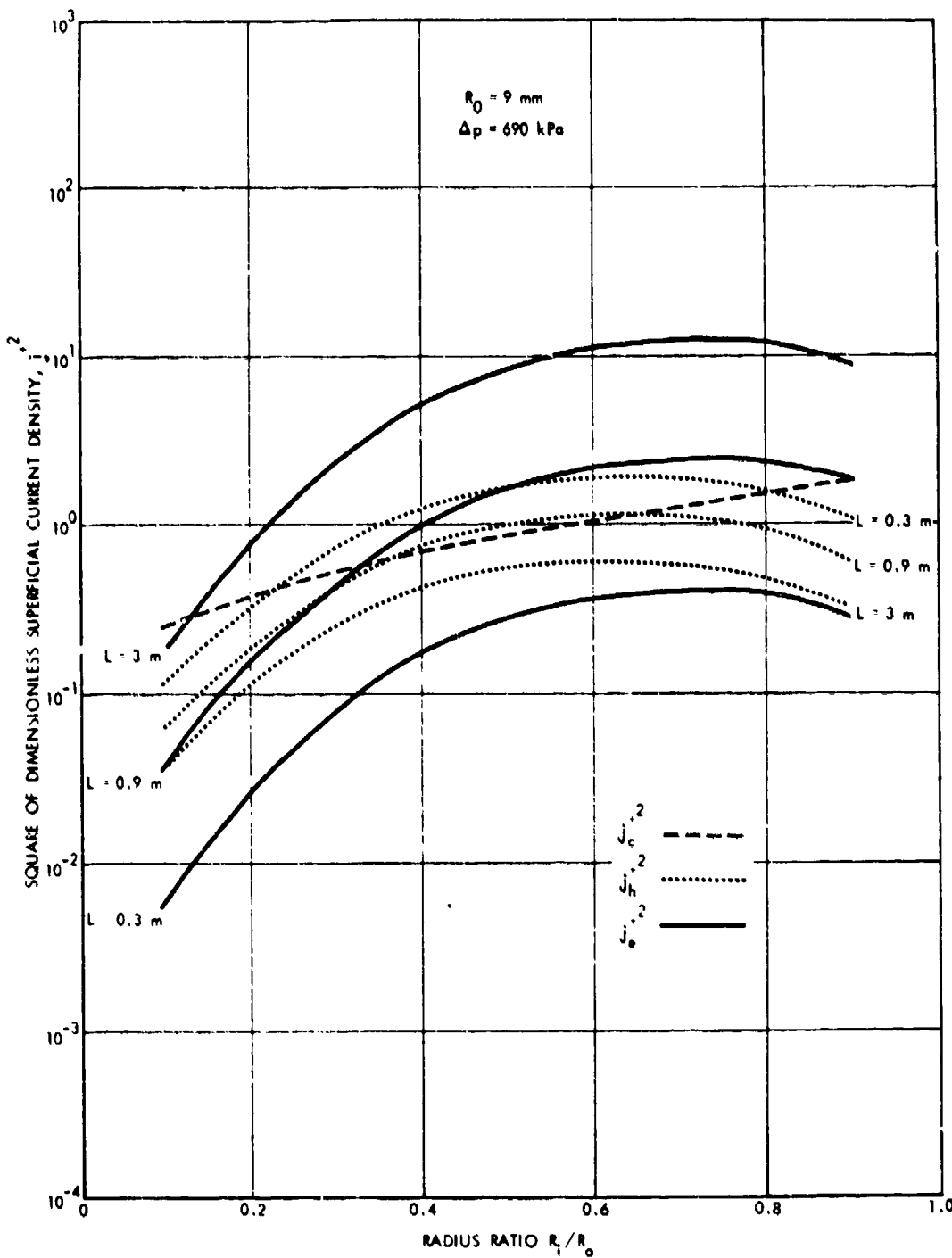
FIGURE J-19. Thermal limits of current density for water-cooled copper, $R_0 = 9$ mm.

J-46
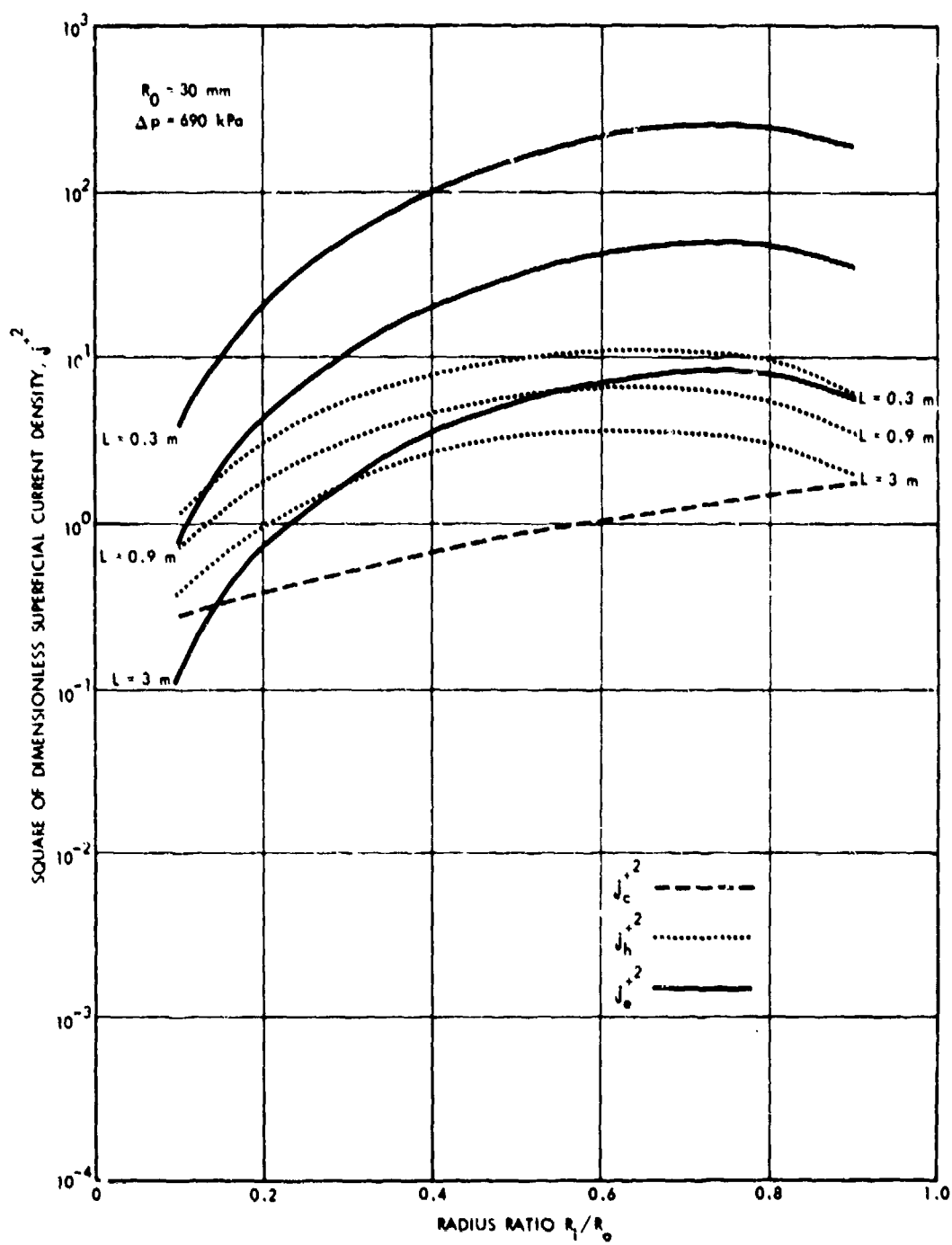
FIGURE J-20. Thermal limits of current density for water-cooled copper, R_0 = 30 mm.

J-47

at shorter lengths (e.g., 0.3 m). For somewhat larger R_o (e.g., 9 mm), all three energy transfer mechanisms are equally limiting except for short lengths of the order of 0.3 m, in which case the First Law is no longer limiting. For larger conductors of the order of 30 mm, the current density is clearly conduction limited except for very long lengths.

4. Overall Thermal Limit

As stated above, the three dissipative energy transfer mechanisms operate in the form of series thermal resistances. Therefore the available conductor temperature rise must be distributed among all three at any given set of conditions. The curves of Figs. J-18 through J-20 show that the maximum value of J_o is relatively insensitive to the value of radius ratio (or void fraction) except for extreme values of X. Thus, if a reasonable void fraction of, say, 50% (X = 0.7) is selected, then for every value of conductor length there will be a value of R_o that will maximize the allowable current density J_o.

If the allowable conductor temperature rise over coolant inlet temperature amounts to ΔT_o, then ΔT_o is equal to

$$\Delta T_o = \Delta T_c + \Delta T_h + \Delta T_e \quad . \qquad (J-27)$$

Substituting Equations J-24, J-25, and J-26 for the individual ΔT's, we have

$$\Delta T_o = J_o^2 \ (R_o^2 K_c + R_o^{1/2} \ L^{1/2} \ K_h + R_o^{-1/2} \ L^{3/2} \ K_c) \ , \qquad (J-28)$$

where:

J-48

$$K_c = \left[\frac{\rho_e}{4k}\right] (X^2 - 1 - 2\ell nX)(1-X^2)^{-2}$$

$$K_h = \left[\frac{Pr^{4/3}\rho_e^2}{Fd_w \Delta PC^2}\right]^{1/2} (1-X^2)^{-1} X^{-3/2} \qquad (J-29)$$

$$K_e = \left[\frac{F\rho_e^2}{d_w \Delta PC^2}\right]^{1/2} (1-X^2)^{-1} X^{-5/2} .$$

Differentiating Eq. J-28 with respect to R_o to find the value of R_o which minimizes ΔT_o, we find

$$R_o = (L/R_o)^{3/2} K_e/4K_c - (L/R_o)^{1/2} K_h/4K_c . \qquad (J-30)$$

For the case of a copper conductor cooled with water flowing at a pressure drop of 100 psi (690 kPa), the K's have a value of (see Annex J3 for details):

$$K_c = 1.44 \times 10^{-11} \quad C\text{-}m^2/A^2$$

$$K_h = 1.59 \times 10^{-14} \quad C\text{-}m^3/A^2 \qquad (J-31)$$

$$K_e = 6.81 \times 10^{-17} \quad C\text{-}m^3/A^2 .$$

Thus the optimum value of R_o is

$$R_o = 1.18 \times 10^{-6}(L/R_o)^{1/2} [(L/R_o) - 233] . \qquad (J-32)$$

This relationship between R_o and L, as well as the resulting $j_{o,m}$ is shown in Fig. J-21. It is seen that for any

J-49
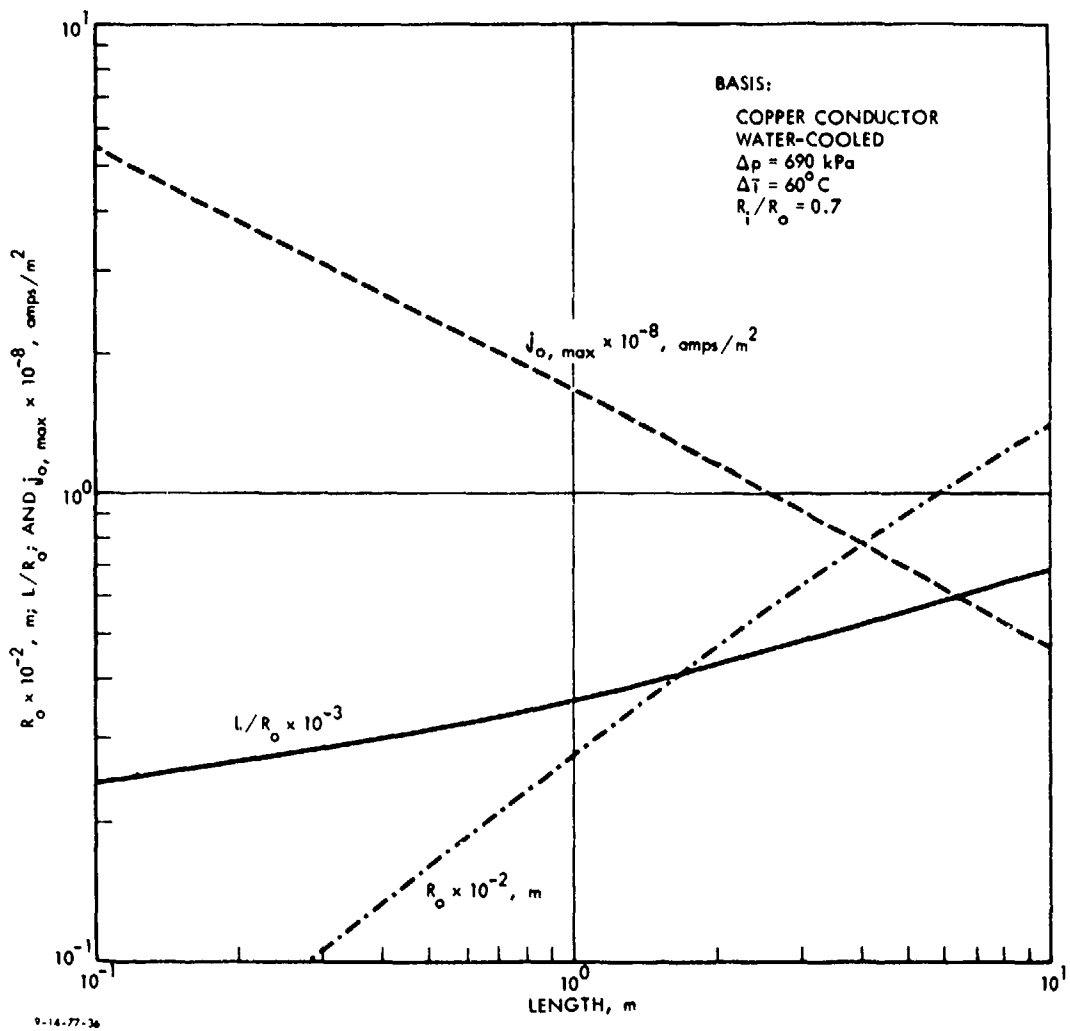
FIGURE J-21. Optimum conductor size for maximum current density. Conductor radius R_0, length-to-radius ratio L/R_0, and maximum current density $j_{o,max}$ versus conductor length L.

J-50

conductor length from zero to the order of 10 meters, the
value of L/R_o remains within the relatively narrow range of
233 to 700. Also, for conductors longer than about 2 meters,
the allowable superficial current density is in the range of
0.5×10^8 to 1.0×10^8 A/m^2 for a ΔT_o of $60^\circ C$.

G. SCALING LAWS FOR ELECTRIC MACHINES

The study and assessment of propulsion systems that employ
electric machines requires a relatively simple description of
the size, weight, and efficiency of the machines.

An empirical relation that is generally accepted for rough
estimates for commercially designed electric machines is

$$D^2 L = a_2 \left(\frac{P}{n} \right)^{0.65} , \qquad (J-33)$$

where D = rotor diameter

L = rotor active length

P = power output

n = rotational speed (rpm)

a_2 = an empirical constant.

The constant a_2 has different values for different classes
of machines, ranging from a low value for aircraft machines to
a high value for heavy-duty conservatively rated industrial
machines.

The objective of this section is to arrange the fundamen-
tal relations which establish the limits on machine performance
into a form similar to the empirical relation (Eq. J-33). To
do this, a number of reasonable assumptions will be made of the
relative geometry of practical electric machines.

The first step is to cast Eq. J-33 into a format that is
more directly related to machine performance in a propulsion
system: power output per unit volume. If Eq. J-33 is solved

for power, the result is

$$P = n \left(\frac{D^2L}{a_2} \right)^{1.54} . \tag{J-34}$$

Rotor volume is

$$V_{rot} = \frac{\pi}{4} D^2 L , \tag{J-35}$$

so that power per unit volume of rotor is

$$\frac{P}{V_{rot}} = \frac{4}{\pi} n \left(D^2 L \right)^{0.54} \left(\frac{1}{a_2} \right)^{1.54} . \tag{J-36}$$

We can also express this as the magnetic shear stress σ at the surface of the rotor, since torque is given by

$$\text{Torque} = \frac{\sigma \pi D^2 L}{2} . \tag{J-37}$$

Torque, of course, also power-divided by angular velocity:

$$\text{Torque} = P \cdot \frac{60}{2\pi n} . \tag{J-38}$$

Solving for magnetic shear stress, we obtain

$$\sigma = \frac{60}{\pi^2} \left(D^2 L \right)^{0.54} \left(\frac{1}{a_2} \right)^{1.54} . \tag{J-39}$$

The next step is to cast the basic relations of Section E of this appendix into a format that gives the limits on power density in terms of the system power and efficiency. To do this we start with Eqs. J-4 and J-5 of Section E:

J-52

$$\frac{P}{V_{act}} = \omega \frac{B_s K_s}{4} = uk \frac{B_s K_s}{4} \qquad \text{(J-40)}$$

$$1 - \eta = \frac{K_s}{B_s} \left[\frac{2}{\gamma_s u}\right], \qquad \text{(J-41)}$$

where P = power

V_{act} = volume of active components

ω = electrical frequency

u = relative velocity of rotor and stator

k = interaction wavenumber = π/pole pitch

B_s = peak air-gap flux density

K_s = peak surface current density

η = efficiency

γ_s = surface conductivity.

In Eq. J-41 (from Eq. J-5), the dissipations in the rotor and stator windings have been taken to be equal, and the dissipation associated with exciting the radial air-gap flux has been neglected.

We assume that the pole pitch is proportional to the machine active length:

$$\frac{\pi}{k} = \frac{L}{\alpha} \qquad \text{(J-42)}$$

where π/k = pole pitch

L = active length

α = machine aspect ratio.

Further, we assume that winding thickness is also proportional to pole pitch:

J-53

$$t = a_3 \frac{\pi}{k} \quad . \tag{J-43}$$

Now the relative velocity is

$$u = \frac{\omega}{k} = \frac{\omega L}{\pi \alpha} \quad .$$

Then Eq. J-41 becomes

$$K_s = (1 - \eta) B_s \gamma_s \frac{\omega L}{2 \pi \alpha} \quad . \tag{J-44}$$

Since the winding thickness is proportional to pole pitch, the surface conductivity is given by

$$\gamma_s = \frac{a_3 \pi}{\rho_0 k} = \frac{a_3 L}{\rho_0 \alpha} \quad , \tag{J-45}$$

where ρ_0 is the apparent resistivity of the coils based on gross coil and tooth volume.

Using Eq. J-44 and J-45 in Eq. J-40, we have

$$\frac{P}{V_{act}} = \frac{1}{8 \pi \alpha^2} \frac{(1 - \eta) k_t}{\rho_0} B_s^2 \omega^2 L^2 \quad . \tag{J-46}$$

Equation J2-15 of Annex J2 gives the thickness of the active elements:

$$h_0 = \frac{2}{k} \frac{B_s}{B_c} = \frac{2}{\pi} \frac{L}{\alpha} \frac{B_s}{B_c} \quad ,$$

where B_s = air-gap magnetic flux density

B_c = core magnetic flux density.

J-54

We will denote the ratio of these two flux densities by

$$\beta = B_s/B_c \quad .$$

Then the active volume of the machine is

$$V_{act} = L \cdot \frac{L}{\alpha} \cdot \frac{2}{\pi} \frac{L}{\alpha} \beta N = \frac{2}{\pi} \frac{\beta}{\alpha^2} L^3 N \quad , \qquad (J\text{-}47)$$

where N is the number of poles.

From Eq. J-46 and J-47, we obtain

$$P = \frac{1}{4\pi^2} \frac{\beta}{\alpha^4} \frac{(1 - \eta)a_3}{\rho_o} B_s^2 \omega^2 L^5 N \quad . \qquad (J\text{-}48)$$

Now, solving Eq. J-45 for L, we have

$$L = \left[\frac{4\pi^2 \alpha^4 \rho_o P}{(1 - \eta)a_3 \, B_s^2 \omega^2 N} \right]^{1/5} \quad . \qquad (J\text{-}49)$$

Then, using Eq. J-49 in Eq. J-46, we obtain power density in terms of power level:

$$\left(\frac{P}{V_{act}}\right) = \frac{(4\pi^2)^{2/5}}{8\pi} \frac{1}{\alpha^{2/5}\beta^{2/5}} \frac{(1 - \eta)^{3/5}a_3^{3/5}}{\rho_o^{3/5}} (\omega B_s)^{6/5} \left(\frac{P}{N}\right)^{2/5} . \quad (J\text{-}50)$$

In the discussion to this point the machine has been considered in terms of a linear air-gap geometry developed on a plane. The circular motor has the air gap wrapped into a circle of diameter D, so that

J-55

$$N \frac{\pi}{k} = \pi D \qquad (J\text{-}51)$$

or

$$N = \frac{\pi D \alpha}{L} \quad . \qquad (J\text{-}52)$$

The rotor volume is then

$$V_{rot} = \frac{\pi}{4} D^2 L \quad , \qquad (J\text{-}53)$$

whereas the active volume is

$$V_{act} = \frac{2\beta}{\pi \alpha^2} L^2 N = \frac{2\beta}{\alpha} DL^2 \quad . \qquad (J\text{-}54)$$

Then the ratio between V_{act} and V_{rot} is

$$\frac{V_{act}}{V_{rot}} = \frac{8\beta}{N} \quad . \qquad (J\text{-}55)$$

Then Eq. J-50 becomes

$$\left(\frac{P}{V_{rot}}\right) = \frac{4^{2/5}}{\pi^{1/5}} \frac{\beta^{3/5}}{\alpha^{2/5}} \left[\frac{(1-\eta)a_3}{\rho_o}\right]^{3/5} (\omega B_s)^{6/5} \left(\frac{P}{N}\right)^{2/5} \frac{1}{N} \quad . \qquad (J\text{-}56)$$

In terms of rotational speed in revolutions per minute, where

$$\omega = \frac{N\pi}{60} n \quad , \qquad .$$

we obtain

J-56

$$\left(\frac{P}{V_{act}}\right) = \frac{(4\pi^2)^{2/5}}{8\pi} \left(\frac{\pi}{60}\right)^{6/5} \frac{1}{\alpha^{2/5}\beta^{2/5}} \left[\frac{(1-n)a_3}{\rho_0}\right]^{3/5} n^{6/5} B_s^{6/5} \left(\frac{P}{N}\right)^{2/5} N^{6/5}$$

(J-57)

$$\left(\frac{P}{V_{rot}}\right) = \frac{4^{2/5}}{\pi^{1/5}} \left(\frac{\pi}{60}\right)^{6/5} \frac{\beta^{3/5}}{\alpha^{2/5}} \left[\frac{(1-n)a_3}{\rho_0}\right]^{3/5} n^{6/5} B_s^{6/5} \left(\frac{P}{N}\right)^{2/5} N^{1/5} \quad .$$

(J-58)

Finally, casting this in terms of core flux density, so that

$$B_s = \beta B_c \quad ,$$

we have

$$\left(\frac{P}{V_{act}}\right) = \frac{(4\pi^2)^{2/5}}{8\pi} \left(\frac{\pi}{60}\right)^{6/5} \frac{\beta^{4/5}}{\alpha^{2/5}} \left[\frac{(1-n)a_3}{\rho_0}\right]^{3/5} n^{6/5} B_s^{6/5} \left(\frac{P}{N}\right)^{2/5} N^{6/5}$$

(J-59)

$$\left(\frac{P}{V_{rot}}\right) = \frac{4^{2/5}}{\pi^{1/5}} \left(\frac{\pi}{60}\right)^{6/5} \frac{\beta^{9/5}}{\alpha^{2/5}} \left[\frac{(1-n)a_3}{\rho_0}\right]^{3/5} n^{6/5} B_s^{6/5} \left(\frac{P}{N}\right)^{2/5} N^{1/5} \quad .$$

(J-60)

Equation J-60 is of the form

$$D^2 L \sim \frac{P^{3/5} N^{1/5}}{B_s^{6/5} n^{6/5} (1-n)^{3/5}} \quad .$$

(J-61)

If we take $(P/n)^{3/5} \approx (P/n)^{0.6}$ and compare Eq. J-61 to the empirical result in Eq. J-33, then

J-57

$$a_2 \sim \frac{N^{1/5}}{B_s^{6/5} \, n^{3/5} (1 - \eta)^{3/5}} \tag{J-62}$$

if we replace mechanical frequency n by electrical frequency
$\omega = Nn$. Then we have

$$a_2 \sim \frac{N^{4/5}}{B_s^{6/5} \, \omega^{3/5} (1 - \eta)^{3/5}} \tag{J-63}$$

Thus the condition for the empirical relationship of Eq. J-33
to be true is that the expressions for a_2 in Eq. J-62 or J-63
be constant.

H. SUMMARY, CONCLUSIONS, AND RECOMMENDATIONS

1. General Conclusions

This study has shown that electric transmissions can be
functionally modeled in a general way as an assembly of electro-
mechanical converters, current switching systems, and an elec-
trical power transmission system and bus.

The power distribution bus is not a significant part of
the size, weight, or inefficiency of the electric transmission
system unless the system voltage is far from optimum in terms
of bus requirements, due to the different requirements of the
electromechanical converters. Current switching systems tend
to be a substantial part of the weight of transmission systems
using present-day designs. Substantial improvements may be
achieved before physical limits are reached.

Size, weight, and losses are most significant in the
electromechanical converters. Although the most advanced of
high-performance electric machines approach physical limits of

J-58

performance, machines for most applications could be improved substantially before physical limits are reached.

2. Limiting Parameters

The limiting parameters for the electric power bus are electric stress level in the insulation and current density, as determined by the relative importance of weight, efficiency, and thermal limits. There is an optimum bus voltage for minimum weight depending on stress level, current density, and power. For voltages very much smaller than this level, insulation thickness is negligible, and power density is directly proportional to voltage.

The physical parameters that limit the power density of semiconducting power-switching systems are current density in the semiconducting elements as limited by the cooling of these elements, packaging efficiency, and energy storage per unit of energy transfer as dictated by filtering, snubbing, and commutation of the semiconducting switches.

The limiting parameters for the electromechanical converters are surface speed, effective surface conductivity, converter electrical frequency or equivalent frequency, and the limiting ratio of reaction flux density to the saturation flux density of magnetic material. This is equivalent to the ratio of azimuthal to radial flux density in the air gap. The equivalent electrical frequency for a conventionally commutated DC machine is defined as the rotational speed times the number of pole pairs. In a homopolar/acyclic machine the equivalent electrical frequency is the air-gap surface speed divided by the pole pitch, i.e., the wavelength of the periodicity of the magnetic field in the direction orthogonal to the surface speed.

More specifically for machines with slots and teeth of magnetic material, two limitations are imposed by saturation of the teeth. Saturation at the tooth tip limits the reaction

J-59

flux density (azimuthal) to be equal to radial flux density in the air gap; both are equal to 35% of the saturation flux density of the magnetic material. Saturation at the base of the teeth imposes a limit on the reaction flux density that depends on current density in the windings and on pole pitch. A toothed machine of optimum design operates at both limits.

The same basic parameters may be used to set the physical limits on machines with air-gap windings (no teeth). These limits include parameters reflecting winding geometry, including the ratio of winding thickness to wavelength.

The physical limits for iron-free machines can be expressed in terms of these same parameters, but with a conductor field limit in place of a magnetic saturation limit.

Thermal limits on current density in conductors can be expressed in terms of cooling length, allowable temperature rise, conductor and coolant thermal properties, and conductor resistivity. The power density of transmission lines, electromechanical converters, and switching apparatus may be constrained by these thermal limits, but other limits may require lower current densities.

3. Comparison with Current Technology

Current practice limits electric stress to about 2×10^6 volts/meter for good quality insulation intended for long life, high reliability, and relatively severe mechanical duty, up to 10^7 volts/meter for the most highly stressed insulation used in power cables. These limits provide power per unit area high enough that transmission bus size and weight are comparatively negligible for reasonable power transmission distances, as long as voltages are near optimum. Cooling for semiconductors is currently limited by conduction within the device, contact resistance of the clamp-on heat sink, and heat-sink effectiveness. Heat sinks cooled with oil show substantial improvements

in power density. Direct internal water cooling of these
devices should be able to give power density improvements com-
parable with directly water-cooled high-power vacuum tubes.

Design of the converter and switching system should be
considered together to provide a system with minimum require-
ments for energy storage components. For example, by using
line commutation in the manner employed in a line-commutated
inverter, the required energy storage can be within the elec-
tromechanical converter. The extent to which this can be done
requires further investigation; however, the potential seems to
be very large because of the high power density available in
existing semiconducting devices (approaching 10^9 W/m^3). To
realize the full benefit, advanced packaging and layout and the
use of miniaturized signal-level electronics will be required.

In the electromechanical converter, surface speed is
determined by application requirements or by centrifugal stress
limitations. High-speed machines employing high-strength
materials operate at surface speeds on the order of 200 m/sec.
Surface conductivity and frequency are both affected by a
tradeoff between power density and efficiency. Small machines,
which are constrained to small pole pitches, have low surface
conductivity because the winding depth is limited by tooth
saturation to a fraction of the pole pitch. The use of high
current density allows higher surface current density within
the tooth flux limitation, at the expense of reduced surface
conductivity and thus reduced efficiency. High frequency re-
sults in high power density at the expense of short pole pitch
and low winding thickness, and hence low surface conductivity
and low efficiency. Large, high-surface-speed machines with
long pole pitch can have high power density at extremely high
efficiency. Large, high-performance machines come within a
factor of about three of the ultimate power-density and

J-61

frequency limit for machines with slots and teeth. Good industrial practice comes within a factor of between 10 and 20 of this limit. High-frequency machines (400-800 Hz) come within a factor of 20-50. Low-power and low-speed machines are as much as a factor of 100-200 from the ultimate limit.

The use of air-gap windings removes the tooth-saturation limits, and allows power density to be extended about a factor of 2.5, if efficiency remains acceptable. Acceptable efficiency can be achieved in large machines with high surface velocities.

A major limitation in all machines using an iron core is the limitation on air-gap magnetic shear stress imposed by saturation of the iron. The use of superconducting windings in iron-free machines can extend the limit on magnetic shear by a factor perhaps as large as ten to twelve. Further, superconducting machines will not be efficiency limited in short-pole-pitch configuration, although short pole pitch may result in somewhat lower power density, because of winding thickness limitations.

4. Recommendations

1. A program of study is recommended on the energy storage requirements for switching systems to define minimum requirements.

2. A program is recommended to fully develop a general field theory of fully compensated electromechanical converters, in order to completely describe all machines on a common basis.

3. Equipment development is recommended to achieve better cooling of semiconducting devices by direct internal liquid cooling.

4. A program is recommended to develop the integration of semiconducting switching devices within electromechanical converters, so as to realize the full potential

J-62

of the converters over a wide range of applications.

5. A machine development program is recommended with the objective of achieving machines operating at the tooth saturation limits, core flux limits, and/or superconductor field limits. Except in turbine generators, there is potential for development of higher power density and efficiency in electromechanical converters by using copper and iron. There is a possibility for the development of improved power density and efficiency through the use of superconducting windings, particularly in large, high-power machines.

ANNEX J1

OPTIMUM CONDUCTOR SIZE

ANNEX J1

OPTIMUM CONDUCTOR SIZE

Consider a round cylindrical conductor, insulated by a cylinder of dielectric material with insulating strength E_o. Maximum voltage capability is

$$v = E_o \, R_1 \, \ell n \, \frac{R_o}{R_1} \quad . \tag{J1-1}$$

Current-carrying capability is

$$I = \Pi \, R_1^2 \, J_c \quad . \tag{J1-2}$$

Total volume per unit length is

$$A = \Pi \, R_o^2 \quad . \tag{J1-3}$$

Power carried per unit area is

$$\frac{P}{A} = J_c E_o R_1 \left(\frac{R_1}{R_o}\right)^2 \ell n \, \frac{R_o}{R_1} \quad . \tag{J1-4}$$

This has its maximum when

$$\frac{R_o}{R_1} = 1.65 \;, \; \ell n \, \frac{R_o}{R_1} = 1/2 \quad . \tag{J1-5}$$

J-67

Thus maximum power density is

$$\frac{P}{A} = 0.18 \ J_c E_o R_i \ .$$

(J1-6)

Now, inverting Eq. J1-2,

$$R_i = \sqrt{\frac{I}{\Pi J_c}} \ ,$$

(J1-7)

inserting it into Eq. J1-1, and using Eq. J1-5, we obtain

$$v = E_o \sqrt{\frac{I}{\Pi J_c}} \ .$$

(J1-8)

Total power is found to be

$$P = \frac{\Pi J_c E_o}{2} \ R_i^3 \ .$$

(J1-9)

Now if Eq. J1-9 is solved for R_i and used in Eq. J1-6, maximum power density is found as a function of total power:

$$\frac{P}{A} = 0.15 \ J_c^{2/3} E_o^{2/3} P^{1/3} \ .$$

(J1-10)

Similarly, optimum transmission voltage is found by using this expression for R_i in Eq. J1-1:

$$v = \left(\frac{E_o}{2}\right)\left(\frac{2}{\pi} \ \frac{P}{J_c E_o}\right)^{1/3} \ ,$$

(J1-11)

which becomes Eq. J-1 of Section C of Appendix J.

Glossary of Symbols for Annex J1

E_o	Insulating strength of dielectrics
J_c	Usable conductor current density, amperes/meter^2
I	Current, amperes
P	Power, watts
R_i	Conductor radius, meters
R_o	Insulation outer radius, meters
v	Voltage, volts

ANNEX J2

DEVELOPMENT OF THE ELECTROMECHANICAL ENERGY CONVERTER

CONTENTS

ANNEX J2

DEVELOPMENT OF THE ELECTROMECHANICAL ENERGY CONVERTER

A. BASIC MODEL

The flat model considered here is pictured in Fig. J-5 in Section E of Appendix J. The stator and rotor currents are represented by flat, thin current sheets of the form:

$$\overline{K}_R = \overline{1}_z \ R_e \left[\underline{K}_R \ e^{-jkx} \right] \quad . \tag{J2-1}$$

$$\overline{K}_S = \overline{1}_z \ R_e \left[\underline{K}_S \ e^{-jkx} \right] \quad . \tag{J2-2}$$

The magnetic field crossing the air gap is

$$H_y = R_e \left[j \ \frac{\underline{K}_e + \underline{K}_S}{kg} \ e^{-jkx} \right] \quad . \tag{J2-3}$$

This is, of course, of the form:

$$\mu_o H_y = R_e \left[\underline{B}_s \ e^{-jkx} \right] \quad . \tag{J2-4}$$

We will use Eq. J2-4 here because the magnetic surfaces will limit the magnitude of the magnetic field.

Shear traction is given by the component of the Maxwell stress tensor, acting of the surface normal and in the direction of motion:

J-73

$$\sigma_{xy} = \mu_o \, H_x \, H_y \quad . \tag{J2-5}$$

The spatial average value of this is

$$\langle \sigma_{xy} \rangle = \frac{1}{2} \, R_e \left[\mu_o \, H_x \, H_y^* \right] \quad . \tag{J2-6}$$

If we evaluate Eq. J2-6 just above the surface of the stator, we obtain

$$\langle \sigma_{xy} \rangle = - \frac{1}{2} \, R_e \left[B_s^* \, K_S \right] \quad . \tag{J2-7}$$

Now if total current $\underline{K}_S + \underline{K}_R$ and stator current $\underline{K}_S$ are separated by a phase angle, we have

$$\underline{K}_S = K_S \, e^{j\theta}$$

$$\underline{K}_R = K_R \, e^{j(\theta+\delta)} \quad . \tag{J2-8}$$

Where θ is arbitrary, shear stress is obtained as

$$\langle \sigma_{xy} \rangle = \frac{B_s \, K_S}{2} \sin \delta \quad . \tag{J2-9}$$

A comparison of Eqs. J2-4 and J2-3 yields an expression for rotor current density:

$$\underline{K}_R = \frac{g \, k \, B_s}{\mu_o} \, e^{j\delta} - \underline{K}_S \quad . \tag{J2-10}$$

J-74

By using the definitions in Eq. J2-8, the magnitude of $\underline{K}_R$ is found to be

$$K_R = \left[\left(\frac{g\,k\,B_S}{\mu_O} \cos \delta - K_S \right)^2 + \left(\frac{g\,k\,B_S}{\mu_O} \sin \delta \right)^2 \right]^{1/2} . \quad \text{(J2-11)}$$

In this development we are employing the notion of a fully compensated machine. In such a machine K_R is adjusted to keep magnetic field constant. This guarantees that the magnetic circuit can be fully utilized. Examples of machines that operate this way are DC motors with pole-face compensation, acyclic motors, and synchronous generators with voltage regulation.

At the phase angle for maximum shear, we have

$$\langle \sigma_{xy} \rangle_{max} = \frac{B_S\,K_S}{2} \quad \text{(J2-12)}$$

$$K_R^2 = K_S^2 + \left[\frac{g\,k\,B_S}{\mu_O} \right]^2 \quad \text{(J2-13)}$$

Now, to determine machine volume, we must determine how thick the magnetic slabs must be to carry the air-gap flux. To do this, we equate flux carried in the slab cross section with flux crossing the air gap over one-half pole pitch:

$$\int_0^{\frac{\Pi}{2k}} B_S \cos kx \, dx = dB_c$$

$$d = \frac{B_S}{B_c} \, \frac{1}{k} \quad . \quad \text{(J2-14)}$$

J-75

Since there are two slabs, the total height of the machine is

$$h = \frac{2}{k} \frac{B_s}{B_c} \quad . \tag{J2-15}$$

Now we may calculate power density. If $B_s = B_j$ (as it will be for the flat-slab model), we obtain

$$\frac{P}{V} = \frac{\langle \sigma_{xy} \rangle u}{2/k}$$

or, at maximum thrust,

$$\frac{P}{V} = \frac{B_s K_S u k}{4} \quad . \tag{J2-16}$$

Equation J-4 in Section E of Appendix J is a straight-forward manipulation of Eq. J2-16.

Power dissipated per unit area is

$$P_d = \frac{K_S^2}{2\gamma_S} + \frac{K_R^2}{2\gamma_R} \quad . \tag{J2-17}$$

At maximum thrust, this is

$$P_d = \frac{K_S^2}{2\gamma_S} + \frac{K_S^2}{2\gamma_R} + \left[\frac{g \, k \, B_s}{\mu_o} \right]^2 \frac{1}{2\gamma_R} \quad . \tag{J2-18}$$

In all cases, we will ignore the last term in Eq. J2-18. This is because it is invariably small in any reasonably loaded machine. This term represents the energy required to produce the magnetic flux density across the air gap. It is, of course,

not the total "field" or "excitation" energy as these are commonly defined, for these contain, in addition, the energy required to compensate, or balance, the reaction current.

Loss in efficiency is then written as

$$\frac{P_d}{P} = 1 - \eta = \frac{\mu_0 K_S}{B_s} \left[\frac{1}{\mu_0 \gamma_S u} + \frac{1}{\mu_0 \gamma_R u} \right] . \qquad (J2\text{-}19)$$

B. ANISOTROPIC WINDING REGION MODEL

Figure J2-1 shows the geometry described here. The region containing teeth and slots with conductors is presumed to have

permeability in the y-direction $\mu_y \to \infty$

permeability in the x-direction $\mu_x = \dfrac{\mu_0}{1-f}$. $\qquad (J2\text{-}20)$

Now, if there is a current distribution in the anisotropic slot region

$$J_z = R_e \left[\underline{J}_s \ e^{-jkx} \right] , \qquad (J2\text{-}21)$$

the x-directed magnetic flux is

$$B_x = - \frac{\mu_0}{1-f} R_e \left\{ \underline{J}_s \ e^{-jkx} \right\} y . \qquad (J2\text{-}22)$$

In particular, right at the top of the teeth, we have

$$B_x \ (y=t_s) = - \frac{\mu_0 \ t_s}{1-f} R_e \left\{ J_s \ e^{-jkx} \right\} . \qquad (J2\text{-}23)$$

Now, if we use Gauss' law on Eq. J2-22, we find that

J-77
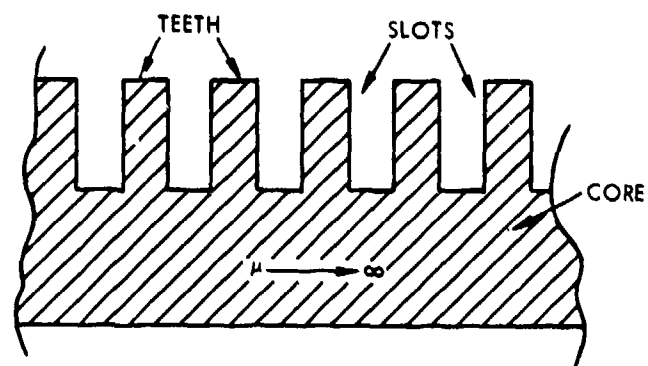
9-14-77-37

FIGURE J2-1a.   Tooth + slot + core magnetic circuit.
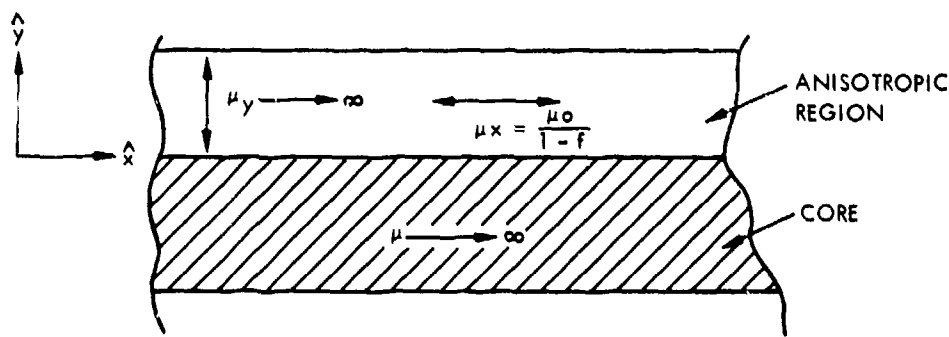
9-14-77-38

FIGURE J2-1b.   Anisotropic equivalent to tooth + slot region.

$$\frac{\partial B_y}{\partial y} = - R_e \left\{ j \ \frac{\mu_o k}{1-f} \ y J_s \ e^{-jkx} \right\} \quad . \qquad (J2-24)$$

Then, if the air-gap field is

$$B_y \ (y=t_s) = R_e \left[\underline{B}_s \ e^{-jkx} \right] \quad , \qquad (J2-25)$$

we may integrate Eq. J2-24 to find the y-directed flux density

$$B_y \ (y) = B_y \ (y=t_s) - \int_y^{ts} \frac{\partial B_y}{\partial y} \ dy \quad .$$

This turns out to be

$$B_y = R_e \left[\left\{ \underline{B}_s + jk \ \frac{\mu_o J_s}{1-f} \ \frac{t_s^2 - y^2}{2} \right\} e^{-jkx} \right] \quad . \qquad (J2-26)$$

In particular, at the tooth root it is

$$B_y \ (0) = R_e \left[\left\{ \underline{B}_s + jk \ \frac{\mu_o J_s t_s^2}{2(1-f)} \right\} e^{-jkx} \right] \quad . \qquad (J2-27)$$

Now we must consider the limits imposed by flux densities at the two locations. Since maximum slot current density is given by

$$J_m = \frac{J_s}{1 - f} \quad , \qquad (J2-28)$$

the x-directed flux at the tooth tips is

$$B_x = - R_e \left\{ \mu_0 \ J_m \ t_s \ e^{-jkx} \right\} \quad . \qquad (J2-29)$$

The flux limitation is established by the vectorial addition of B_x and B_y:

$$B_y = R_e \left[\frac{B_s}{f} \ e^{-jkx} \right] \quad . \qquad (J2-30)$$

Thus we find that

$$B_c^2 = \left(\frac{B_s}{f} \right)^2 + \left(\mu_0 \ J_m \ t_s \right)^2 \quad . \qquad (J2-31)$$

This expresses the limitation that total flux density in the tooth tips must not exceed saturation flux level.

Now, maximum shear stress is

$$\langle \sigma_{xy} \rangle = \frac{B_s}{2} \ J_m \ t_s \ (1 - f) \quad . \qquad (J2-32)$$

Using the definition

$$\mu_0 \ J_m \ t_s = \xi \ B_c \quad , \qquad (J2-33)$$

we may rewrite Eq. J2-32 as

$$\langle \sigma_{xy} \rangle = \frac{B_c^2}{2\mu_0} \ f(1-f) \ \xi \sqrt{1 - \xi^2} \quad . \qquad (J2-34)$$

This has a maximum value when

J-80

$$f = \frac{1}{2}$$

$$\xi = \frac{1}{\sqrt{2}} \quad , \tag{J2-35}$$

and then we have

$$\mu_o \, J_m \, t_s = \frac{B_c}{\sqrt{2}}$$

$$B_s = \frac{B_c}{2\sqrt{2}} \tag{J2-36}$$

$$\mu_o \, K_S = \frac{B_c}{2\sqrt{2}} \quad .$$

Thus the maximum value for shear stress is

$$\langle \sigma_{xy} \rangle = \frac{B_c^2}{16 \, \mu_o} \tag{J2-37}$$

For this limit, machine height is

$$j_o = \frac{2}{k} \, \frac{B_s}{B_c} = \frac{1}{\sqrt{2} \, k} \quad , \tag{J2-38}$$

and Eq. J-7 in Section E of Appendix J follows directly.

To obtain the limitation pertaining to the tooth root, see that the maximum-field addition analogous to Eq. J2-31 is

J-81

$$B_c^2 = \left(\frac{B_s}{f}\right)^2 + \left(\frac{\mu_o \, J_s \, k \, t_s^2}{2f \, (1 - f)}\right)^2 \quad . \tag{J2-39}$$

Now, by making the definition

$$\frac{\mu_o \, J_m \, k \, t_s^2}{2} = \xi \, B_c \quad , \tag{J2-40}$$

shear stress is found to be

$$\langle \sigma_{xy} \rangle = \frac{B_s \, J_m \, t_s \, (1-f)}{2} \quad , \tag{J2-41}$$

which is rewritten using Eqs. J2-39 and J2-40 as

$$\langle \sigma_{xy} \rangle = \frac{B_c^2}{2\mu_o} \, f \, (1 - f) \, \frac{2\xi}{k \, t_s} \sqrt{1 - \xi^2} \quad , \tag{J2-42}$$

which has a maximum, as before, when $f = \frac{1}{2}$ and $\xi = \frac{1}{\sqrt{2}}$, and thus we find that

$$\frac{\mu_o \, J_m \, k \, t_s^2}{2} = \frac{B_c}{\sqrt{2}} \quad . \tag{J2-43}$$

This results in a maximum value for t_s when

$$t_s \leq \sqrt{\frac{\sqrt{2} \, B_c}{\mu_o \, J_m \, k}} \tag{J2-44}$$

and a maximum for shear stress when

J-82

$$\langle \sigma_{xy} \rangle = \frac{B_c^2}{8 \mu_o} \sqrt{\frac{\mu_o J_m}{\sqrt{2} \, k \, B_c}} \quad . \tag{J2-45}$$

For the tooth root limit, we then have

$$h = \frac{2}{k} \cdot f = \frac{1}{k} \tag{J2-46}$$

because the teeth are running at maximum flux density.

Thus, power density is as given by Eq. J-6 in Section E of Appendix J.

C. AIR-GAP MODEL

The geometry of a symmetrical air-gap-winding machine is shown in Fig. J-8 in Section E of Appendix J. Analysis of this geometry consists of finding the magnetic fields produced by the two current distributions and then evaluating the Maxwell stress tensor at the interface. Through some manipulation it is possible to do this holding magnetic flux density constant at the two magnetic surfaces.

The magnetic field analysis proceeds in building-block fashion. First, the field of a thin current sheet is determined, and then the field of a thick current distribution is found by integrating over its thickness.

1. Field Distribution of a Thin, Sinusoidally Distributed Current Sheet between Two Magnetic Planes

Figure J2-2 shows the geometry and coordinate system. The current sheet at position $y = \xi$ has the value:

$$\overline{K} = \overline{I}_z \, R_e \left[\underline{K} \, e^{-jkx} \right] \quad . \tag{J2-47}$$

J-83
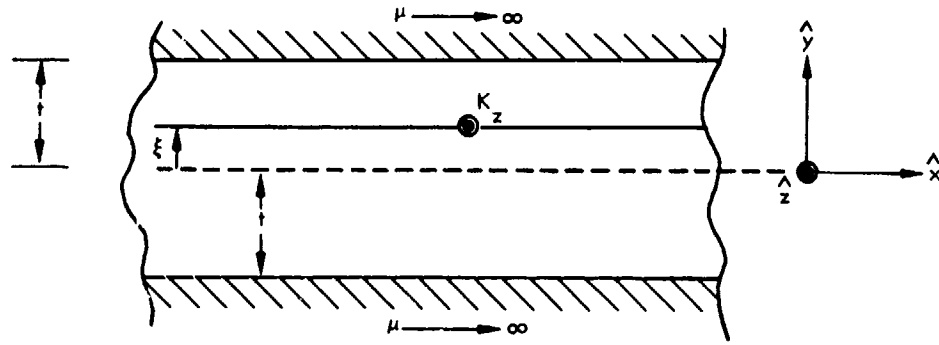
9-14-77-39

FIGURE J2-2. Building-block magnetic field problem.

The fields "above" and "below" the current sheet, $(y > \xi)$
and $(y < \xi)$, must satisfy Ampere's law and Gauss' law (that is,
they must be curl- and divergence-free). By direct substitution
into Maxwell's equations, it is possible to verify that the
following form for the fields satisfies these conditions:

- Above the sheet:

$$H_{x_+} = R_e \left[(A_+ \, e^{ky} + B_+ \, e^{-ky}) \, e^{-jkx} \right]$$

$$H_{y_+} = R_e \left[j(A_+ \, e^{ky} - B_+ \, e^{-ky}) \, e^{-jkx} \right]$$

- Below the sheet:

$$H_{x_-} = R_e \left[(A_- \, e^{ky} + B_- \, e^{-ky}) \, e^{-jkx} \right]$$

$$H_{y_-} = R_e \left[j(A_- \, e^{ky} - B_- \, e^{-ky}) \, e^{-jkx} \right] . \qquad (J2-48)$$

J-84

The boundary conditions that these fields must satisfy are:

$$H_{x_+} \ (y=t) \ = \ 0$$

$$H_{x_-} \ (y=t) \ = \ 0$$

$$H_{y_+} \ (y=\xi) \ = \ H_{y_-} \ (y=\xi)$$

$$H_{x_+} \ (y=\xi) - H_{y_-} \ (y=\xi) \ = \ - \ K_z \quad . \qquad (J2\text{-}49)$$

Substitution of Eq. J2-48) into Eq. J2-49) and some manipulation leads to expressions for the fields:

$$H_{x_+} = R_e \left[- \ \underline{K} \ \frac{\cosh \ k(\xi+t)}{\sinh \ 2kt} \ \sinh \ k(t-y) \ e^{-jkx} \right]$$

$$H_{x_-} = R_e \left[\underline{K} \ \frac{\cosh \ k(\xi-t)}{\sinh \ 2kt} \ \sinh \ k(t+y) \ e^{-jkx} \right]$$

$$H_{y_+} = R_e \left[j \ \underline{K} \ \frac{\cosh \ k(\xi+t)}{\sinh \ 2kt} \ \cosh \ k(t-y) \ e^{-jkx} \right] \qquad (J2\text{-}50)$$

$$H_{y_-} = R_e \left[j \ \underline{K} \ \frac{\cosh \ k(\xi-t)}{\sinh \ 2kt} \ \cosh \ k(t+y) \ e^{-jkx} \right] \quad .$$

2. Field of a Thick Current Distribution

Figure J2-3 shows the situation. The current distribution is

$$\overline{J} = \overline{1}_z \ R_e \left[\underline{J} \ e^{-jkx} \right] \qquad 0 < y < t \quad . \qquad (J2\text{-}51)$$
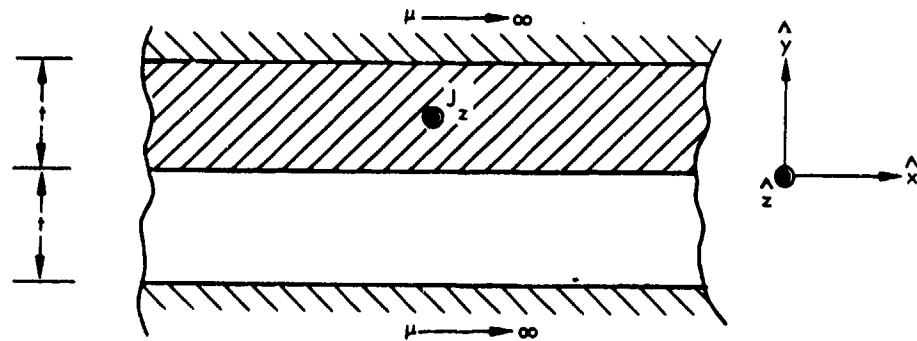
FIGURE J2-3. Model for thick current sheet magnetic field problem.

The magnetic fields in this system are found by considering the current distribution to be a series of thin sheets, and integrating the contributions. Thus, for $y < 0$, we obtain

$$H_{x_-} = R_e \left[\int_0^t J_o \, \frac{\sinh k(t+y)}{\sinh 2kt} \cosh k(t-\xi) \, d\xi \, e^{-jkx} \right]$$

$$H_{y_-} = R_e \left[\int_0^t J \, \underline{J} \, \frac{\cosh k(t+y)}{\sinh 2kt} \cosh k(t-\xi) \, d\xi \, e^{-jkx} \right] .$$

(J2-52)

For $y > 0$, two integrals are required:

$$H_{x_+} = R_e \left[\int_0^y - J \, \frac{\sinh k(t-y)}{\sinh 2kt} \cosh k(t+\xi) \, d\xi \, e^{-jkx} \right.$$

$$\left. + \int_y^t \underline{J} \, \frac{\sinh k(t+y)}{\sinh 2kt} \cosh k(t-\xi) \, d\xi \, e^{-jkx} \right]$$

J-86

$$H_{y_+} = R_e \left[\int_0^y j\, \underline{J}\, \frac{\cosh k(t-y)}{\sinh 2kt} \cosh k(\xi+t)\, d\xi\, e^{-jkx} \right.$$

$$\left. + \int_y^t j\, \underline{J}\, \frac{\cosh k(t+y)}{\sinh 2kt} \cosh k(\xi-t)\, d\xi\, e^{-jkx} \right]. \quad (J2\text{-}53)$$

These are evaluated as:

$$H_{x_-} = R_e \left[\frac{\underline{J}}{k} \frac{\sinh k(t+y)}{\sinh 2kt} \sinh kt\, e^{-jkx} \right]$$

$$H_{y_-} = R_e \left[j\, \frac{\underline{J}}{k} \frac{\cosh k(t+y)}{\sinh 2kt} \sinh kt\, e^{-jkx} \right]$$

$$H_{x_+} = R_e \left[\frac{\underline{J}}{k} \frac{\sinh k(t-y)}{\sinh 2kt} \sinh kt\, e^{-jkx} \right]$$

$$H_{y_+} = R_e \left[j\, \frac{\underline{J}}{k} \left(1 - \frac{\sinh kt\, \cosh k(t-y)}{\sinh 2kt} \right) e^{-jkx} \right].$$

$$(J2\text{-}54)$$

3. Iron-Core, Air-Gap-Winding Machine

The fields of a thick winding have been derived. The machine has the current densities:

$$0 < y < t \qquad \overline{J} = \overline{I}_z\, R_e \left[\underline{J}_1\, e^{-jkx} \right]$$

$$-t < y < 0 \qquad \overline{J} = \overline{I}_z\, R_e \left[\underline{J}_2\, e^{-jkx} \right]. \qquad (J2\text{-}55)$$

J-87

The complex amplitudes of the magnetic fields produced by these currents are:

$$\underline{H}_y \ (y=t) = j \ \frac{\underline{J}_1}{k} \left(1 - \frac{\sinh kt}{\sinh 2kt}\right) + j \ \frac{\underline{J}_2}{k} \ \frac{\sinh kt}{\sinh 2kt}$$

$$\underline{H}_y \ (y=-t) = j \ \frac{\underline{J}_1}{k} \ \frac{\sinh kt}{\sinh 2kt} + j \ \frac{\underline{J}_2}{k} \left(1 - \frac{\sinh kt}{\sinh 2kt}\right)$$

$$\underline{H}_y \ (y=0) = j \ \frac{\underline{J}_1 + \underline{J}_2}{2k}$$

$$\underline{H}_x \ (y=0) = \frac{\underline{J}_1 - \underline{J}_2}{k} \ \frac{\sinh^2 kt}{\sinh 2kt} \ .$$

(J2-56)

Magnetic shear stress at $y = 0$ is

$$\langle \sigma_{xy} \rangle = \frac{\mu_o}{2} \ R_e \left[H_x \ H_y^* \right]$$

or

$$\langle \sigma_{xy} \rangle = \frac{\mu_o}{2} \ R_e \left[- j \ \frac{(\underline{J}_1 - \underline{J}_2)(\underline{J}_1^* + \underline{J}_2^*)}{2k^2} \ \frac{\sinh^2 kt}{\sinh 2kt} \right] \ .$$

(J2-57)

Now, if the currents are of equal magnitude but are separated by a phase shift, we have

$$\underline{J}_1 = J_s \ e^{j(\delta+\theta)}$$

$$\underline{J}_2 = J_s \ e^{j\theta} \ ,$$

(J2-58)

J-88

and then we find that

$$\langle \sigma_{xy} \rangle = \frac{\mu_o}{2k^2} \frac{\sinh^2 kt}{\sinh 2kt} J_s^2 \sin \delta \quad . \tag{J2-59}$$

Under the conditions of Eq. J2-58, the magnitude of magnetic field at the boundaries is

$$|H_{y+} (y=t)| = \frac{J_s}{k} A (kt,\delta) \quad , \tag{J2-60}$$

where

$$A^2 (kt,\delta) = \left[\left(1 - \frac{\sinh kt}{\sinh 2kt} \right) \cos \delta + \frac{\sinh kt}{\sinh 2kt} \right]^2$$

$$+ \left[\left(1 - \frac{\sinh kt}{\sinh 2kt} \right) \sin \delta \right]^2 \quad . \tag{J2-61}$$

Now, we may use Eq. J2-60 to determine current density to fix magnetic flux density at the boundaries to saturation level:

$$J_s = \frac{k B_c}{A \mu_o} \quad . \tag{J2-62}$$

Under this condition, shear stress becomes

$$\langle \sigma_{xy} \rangle = \frac{B_c^2}{2 \mu_o} \frac{\sinh^2 kt \sin \delta}{\sinh 2kt A^2} \quad . \tag{J2-63}$$

Machine volume per unit area is

$$V = 2 \left(t + \frac{1}{k} \right) = \frac{2}{k} (1 + kt) \quad , \tag{J2-64}$$

J-89

so that power density is

$$\frac{P}{V} = \frac{B_c}{2 \mu_o} \frac{\sinh^2 kt \sin \delta}{\sinh 2kt \, A^2} u \frac{k}{2} \frac{1}{1 + kt} \quad . \qquad (J2-65)$$

This is somewhat more conveniently rewritten as

$$\frac{P}{V} = \frac{B_c^2}{4 \mu_o} ku \cdot F (kt, \delta) \quad , \qquad (J2-66)$$

where

$$F (kt, \delta) = \frac{\sinh^2 kt \sin \delta}{A^2 (1+kt) \sinh 2kt} \quad . \qquad (J2-67)$$

Power dissipated in the two sheets is

$$P_d = \frac{J_s^2}{2\gamma} \cdot 2t = \frac{t}{\gamma} \frac{k^2 B_c^2}{\mu_o^2 A^2} \quad , \qquad (J2-68)$$

and thus loss in efficiency is

$$1 - \eta = \frac{2k^2 t}{\mu_o \gamma u} \cdot \frac{\sinh 2kt}{\sinh^2 kt \sin \delta} \quad . \qquad (J2-69)$$

This is more conveniently written as

$$1 - \eta = \frac{2kt}{\mu_o \gamma ut} E (kt, \delta) \quad . \qquad (J2-70)$$

To complete this, current is found to be

$$J_s = k \frac{B_c}{\mu_o} \alpha (kt, \delta) \quad . \qquad\qquad (J2\text{-}71)$$

The dimensionless parameters F, E, and $\alpha = 1/A$ are tabulated in Table J2-1.

TABLE J2-1. COEFFICIENTS FOR THREE AIR-GAP MACHINES

Coefficient*	Case 1	Case 2	Case 3
kt	0.5	0.8	1.0
δ	145	125	90
F	1.039	0.7389	0.4518
E	3.774	2.935	2.626
α	3.128	1.953	1.334
P_1	0.1377	0.1259	0.0861
C_1	0.8289	0.6655	0.5080
P_2	0.3322	0.3783	0.3387
E_2	1.607	1.503	1.969

_____

*See text for coefficient definitions.

It is possible to reduce the number of equations to be considered at one time by using Eq. J2-69 to eliminate k from Eqs. J2-66 and J2-71, or by using Eq. J2-71 to eliminate k from Eqs. J2-69 and J2-66. The results are Eqs. J-12 through J-15, in which the coefficients are:

$$P_1 (kt, \delta) = \frac{F (kt, \delta)}{E (kt, \delta)}$$

$$C_1 (kt, \delta) = \frac{\alpha (kt, \delta)}{E (kt, \delta)}$$

$$P_2 (kt,\delta) = \frac{F (kt,\delta)}{\alpha (kt,\delta)}$$

$$E_2 (kt,\delta) = \frac{E (kt,\delta)}{\alpha (kt,\delta)} \tag{J2-72}$$

These coefficients are all tabulated in Table J2-1.

D. AIR-CORE MODEL

Consider the geometry shown in Fig. J2-4. Two thin current sheets are situated in a space between perfectly diamagnetic boundaries. The current sheets carry current distributions of the form

$$\overline{K}_1 = \overline{I}_z \, R_e \left[\underline{K}_1 \, e^{-jkx} \right]$$

$$\overline{K}_2 = \overline{I}_z \, R_e \left[\underline{K}_2 \, e^{-jkx} \right] \quad . \tag{J2-73}$$
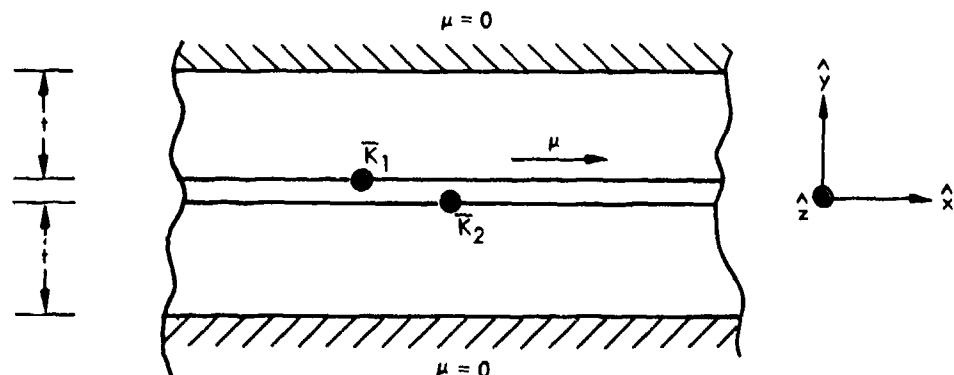
9-14-77-41

FIGURE J2-4. Air-core geometry.

J-92

If the sheets are close together, the fields in between
are

$$H_x = R_e \left[\frac{\underline{K}_1 - \underline{K}_2}{2} \, e^{-jkx} \right]$$

$$H_y = R_e \left[j \, \frac{\underline{K}_1 + \underline{K}_2}{2} \, \tanh kt \, e^{-jkx} \right] \quad . \qquad (J2\text{-}74)$$

If the two current sheets are of equal magnitude but
different phase, we have

$$\underline{K}_1 = K \, e^{j(\delta+\theta)}$$

$$\underline{K}_2 = K \, e^{j\theta} \quad .$$

Traction between the sheets is

$$\langle \sigma_{xy} \rangle = \frac{\mu_o}{4} \, K^2 \, \tanh kt \, \sin \delta \quad . \qquad (J2\text{-}75)$$

Maximum traction occurs when $\sin \delta = 1$. Power per unit volume
is then:

$$\frac{P}{V} = \frac{\mu_o}{4} \, K^2 \, \tanh kt \cdot \frac{u}{2t}$$

$$\frac{P}{V} = \frac{\mu_o}{8} \, K^2 \, k \, u \cdot \frac{\tanh kt}{kt} \quad . \qquad (J2\text{-}76)$$

This has its maximum relative to kt when $kt = 1.2$.

Maximum field intensity will be

J-93

$$H_m \approx \sqrt{2} \; K \quad ,$$

so that power per unit volume may be written as

$$\frac{P}{V} = \frac{\mu_O \; H_m^2}{4} \; uktx \cdot 174 \quad . \qquad (J2\text{-}77)$$

ANNEX J3

DERIVATION OF THERMAL LIMITS

CONTENTS

ANNEX J3

DERIVATION OF THERMAL LIMITS

A. CONVECTIVE HEAT TRANSFER LIMIT

The frictional pressure drop for a fluid flowing at a mass velocity G (velocity times fluid density) through a tube of length L and radius R_1 is

$$\Delta P = FLG^2 / d_w R_1 \quad . \tag{J3-1}$$

The heat transfer coefficient h can be expressed in terms of the mass velocity as

$$h = J_{HTC} G c Pr^{-2/3} \quad , \tag{J3-2}$$

where J_{HTC} is the Colburn "j" factor. However, Reynolds analogy between heat and momentum transfer shows that, for skin friction losses,

$$F = 2 J_{HTC} \quad . \tag{J3-3}$$

Thus, we may replace J_{HTC} by F/2 in Eq. J3-2, which, combined with Eq. J3-1, gives

$$h = \left[\frac{F d_w \Delta P c^2 R_1}{4 L Pr^{4/3}} \right]^{1/2} \tag{J3-4}$$

By equating the volumetric heat dissipation rate to the surface heat transfer rate, we get

J-97

$$J^2 \rho_e \pi (R_o^2 - R_i^2) = 2\pi R_i \Delta T_h \left[\frac{F d_w \Delta P c^2 R_1}{4 L P r^{4/3}} \right]^{1/2} , \quad (J3-5)$$

which reduces to Eq. J-25 in Section F of Appendix J after replacing j by $j_o/(1 - X^2)$, and R_1 by $R_c X$.

B. FIRST LAW LIMIT

The first law of thermodynamics requires that the heat transferred to the coolant equal the enthalpy flux, or

$$J^2 \rho_e \pi (R_o^2 - R_i^2) = \pi R_i^2 G c (T_{out} - T_{in})/L . \quad (J3-6)$$

Substituting Eq. J3-1 for the mass velocity, we get

$$J^2 \rho_e (R_o^2 - R_i^2) = \left[\frac{d_w \Delta P c^2 R_i^5 \Delta T^2}{F L^3} \right]^{1/2} , \quad (J3-7)$$

which reduces to Eq. J-26 in Section F of Appendix J when j is replaced by $j_o/(1 - X^2)$ and R_1 is replaced by $R_o X$.

C. BASIS FOR CALCULATIONS

For the case of a copper conductor cooled by water flowing with a pressure drop of 100 psi (690 kPa), the following properties were used:

k = thermal conductivity of copper = 379 W/m-$^\circ$K

ρ_e = electrical resistivity of copper = 2.8 x 10^{-8} V-m/A

Pr = water Prandtl number = 1

d_w = water density = 960 kg/m^3

c = water specific heat = 4187 J/kg-$^\circ$K

F = fanning friction factor = 0.003

The values for K_c, K_h and K_e as defined by Eq. J-29 in Section F of Appendix J are:

$$K_c = (\rho_e/4k) \quad (X^2-1-2\ln(X)) \ (1-X^2)^{-2} \tag{J3-8}$$

$$= (2.8 \cdot 10^{-8}/(4 \cdot 379)) \cdot (0.7^2-1-2 \cdot \ln(0.7)) \cdot (1-0.7^2)^{-2}$$

$$= 1.44 \cdot 10^{-11}$$

$$K_h = \left[\frac{Pr^{4/3}\rho_e^2}{Fd_w\Delta Pc^2}\right]^{1/2} \quad (1 - X^2)^{-1}X^{-3/2} \tag{J3-9}$$

$$= (1 \cdot (2.8 \cdot 10^{-8})^2/(0.003 \cdot 960 \cdot 690 \cdot 10^3 \cdot 4187^2))^{1/2}$$

$$\cdot (1 - 0.7^2)^{-1} \cdot (0.7)^{-3/2} = 1.59 \cdot 10^{-14}$$

$$K_e = \left[\frac{F\rho_e^2}{d_w\Delta Pc^2}\right]^{1/2} \quad (1 - X^2)^{-1} \ X^{-5/2} \quad \cdot$$

$$= (0.003 \cdot (2.8 \cdot 10^{-8})^2/ (960 \cdot 690 \cdot 10^3 \cdot 4187^2))^{1/2}$$

$$\cdot (1 - 0.7^2)^{-1} \cdot (0.7)^{-5/2} = 6.81 \cdot 10^{-17} \tag{J3-10}$$

ANNEX J4

STATE-OF-THE-ART DATA

The tabulations in this section contain the pertinent
data on the state of the art of electric power conversion sub-
systems used in this study. Reference sources are listed
following the tabulations.

CURRENT COMPONENT STATE OF THE ART

Type/Application	Power, kW	Speed, rpm	Freq., Hz	Effic., %	Mass, kg	Vol., m³	Power/Vol, W/m³	Power/Mass, kW/kg	Ref.
MOTORS AND GENERATORS:									
Turbogenerator	750000	3000	50	98.97	400000	50.1	1.5×10^7	1.8	J-1
DC Aircraft Generator	11	8000	-	77	28	-	-	0.4	J-2
DC Traction Motor	304	3100	-	93	1840	-	-	0.17	J-2
DC Locomotive Motor	1140	1880	-	93.5	3600	-	-	0.31	J-2
AC Locomotive Motor	1140	2360	-	-	3160	-	-	0.36	J-2
DC Torpedo Motor	22	7100	-	85.5	20	-	-	1.19	J-2
MIT Motor-40 Pole	21	5000	1670	78	38	-	-	0.55	J-2
GM 4-Pole AC Motor, Oil Filled	67	13000	430	89	59	0.02	3.2×10^6	1.1	J-5
Induction Motors	4500	3600	60	-	12700	-	-	0.35	J-3
	4500	1800	60	-	10200	-	-	0.44	J-3
	3000	1800	60	-	8900	-	-	0.34	J-3
	2200	1800	60	-	6000	-	-	0.37	J-3
	1500	1800	60	-	3700	-	-	0.40	J-3
	750	3600	60	-	2250	-	-	0.33	J-3
	450	3600	60	-	1450	-	-	0.31	J-3
	300	3600	60	-	1200	-	-	0.25	J-3
	225	1800	60	-	800	-	-	0.28	J-3
	19	1800	60	89	-	0.047	4.0×10^5	-	J-4
DC Traction Motor	1300	-	-	-	3750	-	-	0.34	J-8
4-Pole Induction Traction Motor	1500	2360	79	-	3150	-	-	0.48	J-9

J-103

CURRENT COMPONENT STATE OF THE ART (Contd.)

Type/Application	Power, kW	Speed, rpm	Freq., Hz	Effic., %	Mass, kg	Vol., m^3	Power/Vol., W/m^3	Power/Mass, kW/kg	Ref.
MOTORS AND GENERATORS (Contd.):									
8-Pole DC Traction Motor	900	1880	-	-	3650	-	-	0.25	J-9
TEFC DC Motor	98	1500	-	-	1160	-	-	0.08	J-10
Spray Oil-Cooled Aircraft Generator	60	12000	-	-	-	-	-	3.3	J-11*
Aircraft Generator (Concorde)	63	8000	-	-	-	-	-	1.58	J-11*
4-Pole DC Motor	72	3000	-	-	380	-	-	0.19	J-12
Railroad Traction Motor - 10-Pole	1113	-	-	-	3680	-	-	0.30	J-13
Railroad Traction Motor DC, 8-Pole	380	1390	-	-	1765	-	-	0.21	J-16
Railroad Traction Motor - 8-Pole	1287	1161	-	-	3750	-	-	0.34	J-19
Ship Drive Motor	30000	120	60	-	-	50	5.0x10^5	-	J-21
Bus Traction Motor	90	2250	-	-	605	-	-	0.15	J-23
4-Pole DC Series Tank Drive Motor	184	3700	-	-	220	-	-	0.84	J-23
Tank Alternator (Plus Rectifiers)	119	10000	-	-	131	-	-	0.91	J-23
Westinghouse SEGMAG Homopolar Motor	2240	3600	-	96.5	-	-	-	-	J-24
AC Traction Motor - 2-Pole	224	1800	30	-	726	-	-	0.31	J-25
AC Traction Motor (Geared)	111	12000	400	-	311	-	-	0.36	J-26
Turbogenerator	60000	3000	50	-	128000	-	-	0.47	J-28
Turbogenerator	200000	3000	50	-	223000	-	-	0.9	J-28
Turbogenerator	660000	3000	50	-	432000	-	-	1.53	J-28

*Asterisk denotes kVA rather than kW.

J-104

CURRENT COMPONENT STATE OF THE ART (Contd.)

Type/Application	Power, kW	Speed, rpm	Freq., Hz	Effic. %	Mass, kg	Vol., m³	Power/Vol, W/m³	Power/Mass, kW/kg	Ref.
MOTORS AND GENERATORS (Contd.):									
Aircraft Alternator	76	12000	-	-	19	-	-	4.0	J-29*
4-Pole Propulsion Motor (ASEA)	52	2730	-	-	250	-	-	0.21	J-29
AC Aircraft Generator	60	-	400	-	20	-	-	3.0	J-30*
Permanent Magnet ($SnCO_5$) Generator	60	8000	400	-	20	-	-	3.0	J-31
Induction Wheel-Motor, Cycloconverter-powered, Oil Cooled	38	24000	800	87	340	0.053	7.2×10^5	0.11	J-32
Railway Traction Motor	1240	-	17	-	3880	1.0	1.2×10^6	0.32	J-33
Army Truck Drive Generator	108	7100	-	-	184	0.084	1.2×10^6	0.59	J-34*
Army Truck Wheel Motor	150	16000	533	93	76	0.017	8.9×10^6	2.0	J-34
Army Truck Frequency Converter	66	-	-	-	45	0.041	1.6×10^6	1.47	J-34*
Army Truck Frequency Converter	-	-	-	-	14	-	-	4.7	J-34*

Type/Application	Power, kW	Mass, kg	Vol., m³	Power/Vol, W/m³	Power/Mass, kW/kg	Ref.	Comments
ELECTRONICS & MISCELLANEOUS SYSTEMS							
GM Vehicle Controller	93	98	-	-	-	J-5	
GM Electric Drive	93	250	-	-	0.37	J-5	Total system weight
DC Chopper	960	3770	-	-	0.25	J-6	
Controlled Rectifier & DC Motor	2096	36000	-	-	0.06	J-7	Total system weight
Controlled Rectifier & DC Motor	5400	46000	-	-	0.12	J-8	Total system weight

*Asterisk denotes kVA rather than kW.

CURRENT COMPONENT STATE OF THE ART (Contd.)

Type/Application	Power, kW	Mass, kg	Vol., m³	Power/Vol, W/m³	Power/Mass, kW/kg	Ref.	Comments
ELECTRONICS & MISCELLANEOUS SYSTEMS (Contd.):							
Electric Locomotive	465	15000	-	-	0.03	J-14	Weight of "Electrical Part"
Oil-Filled Controlled Rectifier	7480	980	0.82	9.2×10^6	7.6	J-15	
Oil-Filled Controlled Rectifier	1300	600	0.48	2.7×10^6	2.2	J-15	
Oil-Filled Uncontrolled Rectifier	2240	200	0.36	6.3×10^6	11.2	J-15	
Oil-Filled Uncontrolled Rectifier, Forced Air	150	52	0.058	2.6×10^6	2.9	J-15	
Oil-Filled Uncontrolled Rectifier, Nat. Conv.	60	52	0.058	1.0×10^6	1.2	J-15	
Thyristor Locomotive, 4 Motors	1520	23000	-	-	0.065	J-16	Total system weight
Rectifier, Oil-Cooled	1520	600	-	-	2.5	J-16	
Thyristor Chopper	850	3770	-	-	0.23	J-17	97.4% efficiency
Rail Vehicle Drive	1048	16000	-	-	0.065	J-18	Total "electrical part"
Rail Vehicle Drive	2096	32000	-	-	0.065	J-18	Total "electrical part"
Rail Vehicle Drive with 4 Motors	320	8000	-	-	0.04	J-20	Total "electrical part"
Self-Commutated Inverter	150	-	1.06	1.4×10^5	-	J-22*	
Self-Commutated Inverter	300	-	2.37	1.3×10^5	-	J-22*	
Bosch Electric Car Drive	44	65	-	-	0.68	J-23	Complete drive-converter and motor
Allis Drive System for BARTD	362	5960	-	-	0.06	J-25	Total system weight, 83% efficiency

*Asterisk denotes kVA rather than kW.

CURRENT COMPONENT STATE OF THE ART (Contd.)

Type/Application	Power, kW	Mass, kg	Vol., m^3	$\dfrac{Power}{Vol}$, W/m^3	$\dfrac{Power}{Mass}$, kW/kg	Ref.	Comments
ELECTRONICS & MISCELLANEOUS SYSTEMS (Contd.):							
Allis "Power Electronics Box"	362+	900	-	-	0.4	J-25	
Garrett DC-AC Inverter (BARTD)	240	800	-	-	0.3	J-26	
Cycloconverter (Estimated)	13400	2300 to 400	4.8	2.8×10^6	3.4-5.8	J-27	

REFERENCES, APPENDIX J

J-1. V.P. Anempodistor, *Problems in the Design and Development of 750 MW Turbogenerators*, The Macmillan Company, New York, 1963.

J-2. *Proc. Second International Electric Vehicle Symposium*, Atlantic City, N.J., November 8-10, 1971.

J-3. General Electric Company, *Custom 800 Induction and Synchronous Motors 250 HP and Larger*, data recorded for dropproof induction motors.

J-4. Century Electric Division, Gould, Inc., Sheet E-20, November 17, 1975.

J-5. P.D. Agarwal, "The G.M. High-Performance Induction Motor Drive System," *IEEE Trans. Power Apparatus and Systems*, Vol. PAS-88, No. 2, February 1969.

J-6. T. Shimizu, "Thyristor-Scherbius System Efficient for Motor Speed Control," *Toshiba Review*, No. 63, November 1971, pp. 13-18.

J-7. J.C. Schaffner, *Brown Boveri Review*, Vol. 62, December 1975, p. 542.

J-8. F. Kuehrer, *Brown Boveri Review*, Vol. 62, December 1975, p. 550.

J-9. H. Largiader, *Brown Boveri Review*, Vol. 57, No. 4, April 1970, p. 152.

J-10. E. Beier, *Siemens Review*, Vol. 22, No. 10, 1974, pp. 464-466.

J-11. P.G. Sperling, "Advances in the Construction of Three-Phase Electrical Machines for Aircraft and Land Vehicles," *Siemens Review*, 1971?, pp. 526-531.

J-12. E. Beier and W. Schuler, "Converter-Fed Enclosed-Ventilated D.C. Motors for a Torque Range from 75 to 450 Nm," *Siemens Review*, Vol. XLI, No. 10, 1974, pp. 459-463.

J-13. M.A. Borel and C. Florin, "Class Re $4/4^{II}$ High-Power Locomotives for Swiss Federal Railways," _Brown Boveri Review_, Vol. 57, No. 10, October 1970, pp. 398-409.

J-14. A. Jaeger, "Thyristorized Control System for a Two-Frequency Shunting Locomotive of Swiss Federal Railways," _Brown Boveri Review_, Vol. 57, No. 10, October 1970, pp. 410-418.

J-15. X. Vogel, "Oil-Cooled Traction Converters," _Brown Boveri Review_, 1974?

J-16. W.U. Bohli, "Ge $4/4^{II}$ Thyristor Locomotives Nos. 611 to 620 of Raetian Railways," _Brown Boveri Review_, Vol. 60, No. 12, December 1973, pp. 526-538.

J-17. T. Jinzenji, "Thyristor Chopper Controller for Suburban Railcars," _Toshiba Review_, 1974 or 1975?

J-18. J.C. Schaffner, A. Bautz, and P. Vilpert, "New Suburban Motor-Coach Compositions, Class RABDe 8/16, of the Swiss Federal Railways," _Brown Boveri Review_, 1975?

J-19. F. Kuehrer, "Bo'Bo' Thyristor Locomotives, Class 1044, of the Austrian Federal Railways," _Brown Boveri Review_, 1974?

J-20. U. Baechler, "Type Bo'Bo' + 2'2' Electric Motorcoach Compositions No. 41 to 52 of Class Be 4/8 for Suburban Services on the Solothurn-Zollikofen-Bern (SZB) and Vereinigte Bern-Worb (VBW) Railways," _Brown Boveri Review_, 1974?

J-21. Department of Mechanical Engineering, Massachusetts Institute of Technology, S.M. Thesis, J. Minervini, February 1974.

J-22. _Electrical Variable Speed Drives_, IEEE Conference Publication 93, 1972.

J-23. Defense Intelligence Agency, _Electric Vehicle Research, Development and Technology--Foreign_, June 1975 (NTIS AD-A011 129).

J-24. C.J. Mole, _Design and Development of a Segmented Magnet Homopolar Torque Converter_, ARPA Contract DAHC-15-72-C-0229.

J-25. Louis Allis Company, _Performance Demonstration of the Alternating Current Propulsion System for the San Francisco Bay Area Rapid Transit District_.

J-26. Garrett AiResearch, _A-C Propulsion System for BARTD Rail Car Application_.

J-27. D.L. Greene, "Superconducting Electrical Machines for Ship Propulsion," _Marine Technology_, April 1971.

J-28. A. Frankl, "Large Turbine Generators" Survey of Progress," _Proc. IEEE_, Vol. 117, No. 4, April 1970.

J-29. A Kusko, "Modeling of Electric Drive Systems for KEW (Flywheel) Vehicles," 1976 Intersociety Conference and Exhibition on Transportation, Los Angeles, 18-24 July 1976.

J-30. AiResearch Manufacturing Company, _Study of Aircraft Electrical Power Systems_, N72-28028.

J-31. Balagurov et al., _State of the Art and Prospects of Magnetoelectric Machines for Self-Contained Electrical Supply Systems and Controllable Electrical Drives_ (NTIS AD-773 893).

J-32. Louis Allis Company, _UHS Electric Drive System Report_, U.S. Army Mobility Equipment R&D Center Contract DA-44009-AMC-15D(T).

J-33. R. Moser et al., _High-Power Motors for Electric Motor Vehicles_, NASA TT F 16,662.

APPENDIX K

THRUSTERS FOR GROUND COMBAT VEHICLES

M. G. Bekker

CONTENTS

APPENDIX K

THRUSTERS FOR GROUND COMBAT VEHICLES
by
M.G. Bekker

A. INTRODUCTION

1. Types of Ground Thrusters Considered and Guidelines for Their Study

The ground-vehicle thrusters considered here are tracks and whe l: All the known and previously tried exotic ground thruste.., such as screws or walking devices, have been eliminated because of their limited application.

Thrusters for ground vehicles differ fundamentally from thrusters for air, sea, or space vehicles. While the latter are independent, structurally and functionally, from lift-providing vehicle components, ground-vehicle thrusters must propel and simultaneously carry the weight of the vehicle. Thus the lift-drag-thrust effects in a ground vehicle cumulatively depend solely on thrusters and their interface with the vehicle and the soil. Furthermore, while air, water, and the space environment are fairly uniform and well-determined media of locomotion, soil is one of the most variable and poorly determined media. This further emphasizes the uniqueness of ground-vehicle thrusters and warns against simplistic, over-generalized conclusions. This situation calls for:

1. Use of a physical definition of soil properties that is compatible with applied mechanics and statistical methods.

K-3

2. Pragmatic exploration of specific classes of soil-vehicle systems, as opposed to treatment of ground locomotion as a subject for generalized, over-computerized solutions.

The present study follows these two guidelines and attempts to show a methodology rather than to solve the problem in its entirety.

2. Objective of the Study

The objective of the study is to quantify the present state of the art and the eventual advances needed to make improvements. An attempt has also been made to provide criteria against which new solutions for thrusters can be evaluated.

3. Method of the Study

To achieve the stated objective, the current technological trends and design practices are expressed in general terms of physical and geometrical parameters. The state of the art is quantified by means of well-established mathematical models which have been exposed to scrutiny in the national and international professional literature for two decades.

These same models may provide insight into the present limitations inherent in soil-thruster systems and may indicate what could be done to achieve progress. They may also serve as criteria against which new thruster concepts can be broadly evaluated within the bounds of physical possibility. The discussion is held on a general, first-order-of-approximation level, as the goals to be achieved are those of major consequence and magnitude. The method is amenable to more refined analyses, however, should they be desired in further studies.

Attention is focused on Army tanks and armored vehicles operating in soft soil conditions, since the combination of heavy vehicles and soft soils is most difficult for ground thrusters.

4. Terminology and Notation

The method applied in the following analysis is based on theory and practice expounded ʼs. K-1 through K-3. Most recently, it was successfully u... the NASA-Boeing-General Motors team, among others, in R&D programs for lunar surface vehicles. The following denotations are used in the text:

Soil Parameters

c Coefficient of cohesion (psi)

ϕ Angle of soil friction (deg)

k_c "Cohesive" modulus of soil deformation $(lb/in.^{n+1})$

k_ϕ "Frictional" modulus of soil deformation $(lb/in.^{n+2})$

n Exponent of soil consistency (dimensionless)

j Soil deformation, in shear (in.)

z Soil deformation, sinkage (in.)

K Coefficient of soil shear (in.)

τ Soil shearing stress (psi)

p Soil vertical load, ground pressure (psi)

T_s Soil thrust developed by the vehicle's load and ground contact areas (lb)

R_c Soil drag, mainly produced by soil compaction (lb)

Vehicle Parameters

b Width of the ground contact area (in.); also denoted, in the case of tracks, by $(w-w')/2$ (see Fig. K-4)

ℓ Length of the ground contact area (in.), used in the text with various subscripts which denote track, elastic, or rigid tire

W	Weight of the vehicle (lb)
W_{pt}	Load per tire (lb)
a	Acceleration (ft/sec^2)
P	Unit power to be developed by the engine (hp/ton); various subscripts denote: total, slip, and net acceleration power, as defined in the text.
v_m	Vehicle speed (ft/sec) reached upon accelerating from zero. In the calculations, it was assumed that v_m = 10 mph $\equiv$ 14.6 ft/sec
η_v	Coefficient of power train efficiency (dimensionless)
i_o	Vehicle's slip at wheel, track-soil interface (dimensionless)
D	Vehicle's drag (lb), including "external" motion resistance at soil-ground contact area interface, and "internal" running gear losses, unless specified otherwise
z_r	Sinkage of rigid tire (in.)
z_e	Sinkage of elastic tire (in.)
p_1	Inflation pressure of tire (psi)
p_c	Carcass stiffness pressure of tire (psi)
F,k',A,B,G,C	Transient tire calculation parameters
δ	Tire deflection (in.)
$(p_1)_{crit}$	Tire inflation pressure (psi) above which tire is rigid, and below which it deflects elastically.

B. TRACKED VEHICLES

1. Size, Form, and Weight

Figure K-1 shows a plot of the length and width dimensions for various weights of tanks. The trend is seen in the extrapolated lines, which exhibit a nearly linear relationship of the $W(\ell)$ and $W(w)$ functions. Though lack of reliable data beyond a gross vehicle weight (GVW) of 60 tons prevents one from extending the lines, it is evident that, beyond that range, their slopes must flatten because of external constrictions such as bridges, railroad gauges, and aircraft sizes. Also, the trend to increased battlefield survivability is an important factor here in keeping vehicle sizes as small as possible.

Figure K-2 shows the relationship between the length of the ground contact area of the thruster with reference to vehicle weight. The "flattening" of the $W(\ell')$ curve is here strongly demonstrated. It indicates that heavier vehicles are penalized by relatively shorter load supporting thrusters. This obviously has a double detrimental effect: it reduces lift and increases drag, at the same time diminishing the thrust.

Figure K-3 shows a similar "flattening" trend of the vehicle-height-versus-weight curve $W(h)$. External constrictions and the desire for battlefield survivability mentioned before explain the trend. Unorthodox vehicles such as the Swedish "S" tank are much lower.

Figure K-4 displays the trend in track width $(w-w')/2$ and in the "average" height h' of the track-suspension assembly, measured in the middle of the ground contact area. It appears that wider tracks are still possible for vehicles heavier than 60 tons. The height h' of the thruster assembly is limited by the conditions described before, however.

Figure K-5 dramatizes the penalty paid by heavier vehicles because of the shortening of the ground contact area. It

K-7
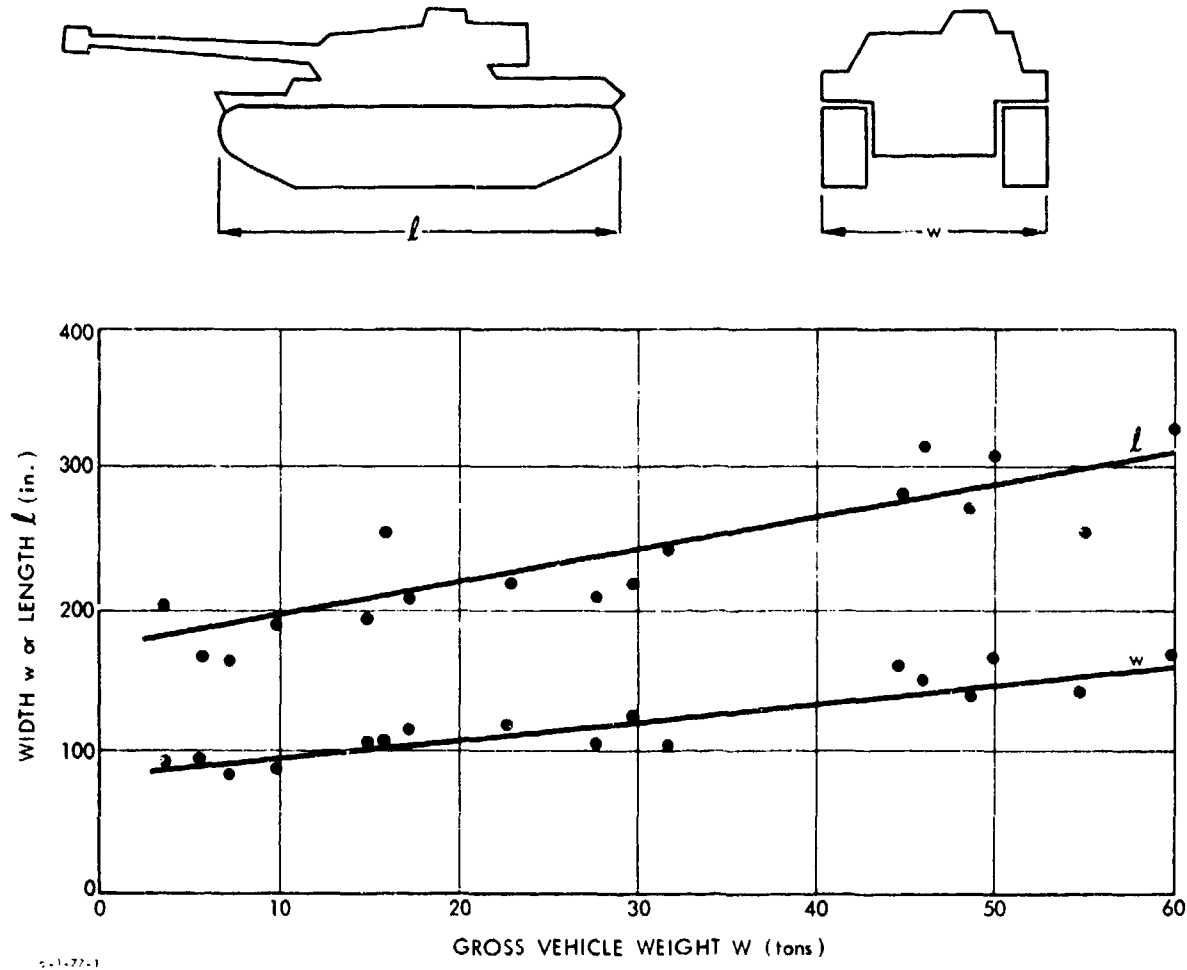
FIGURE K-1.   Tank length and width versus gross weight.
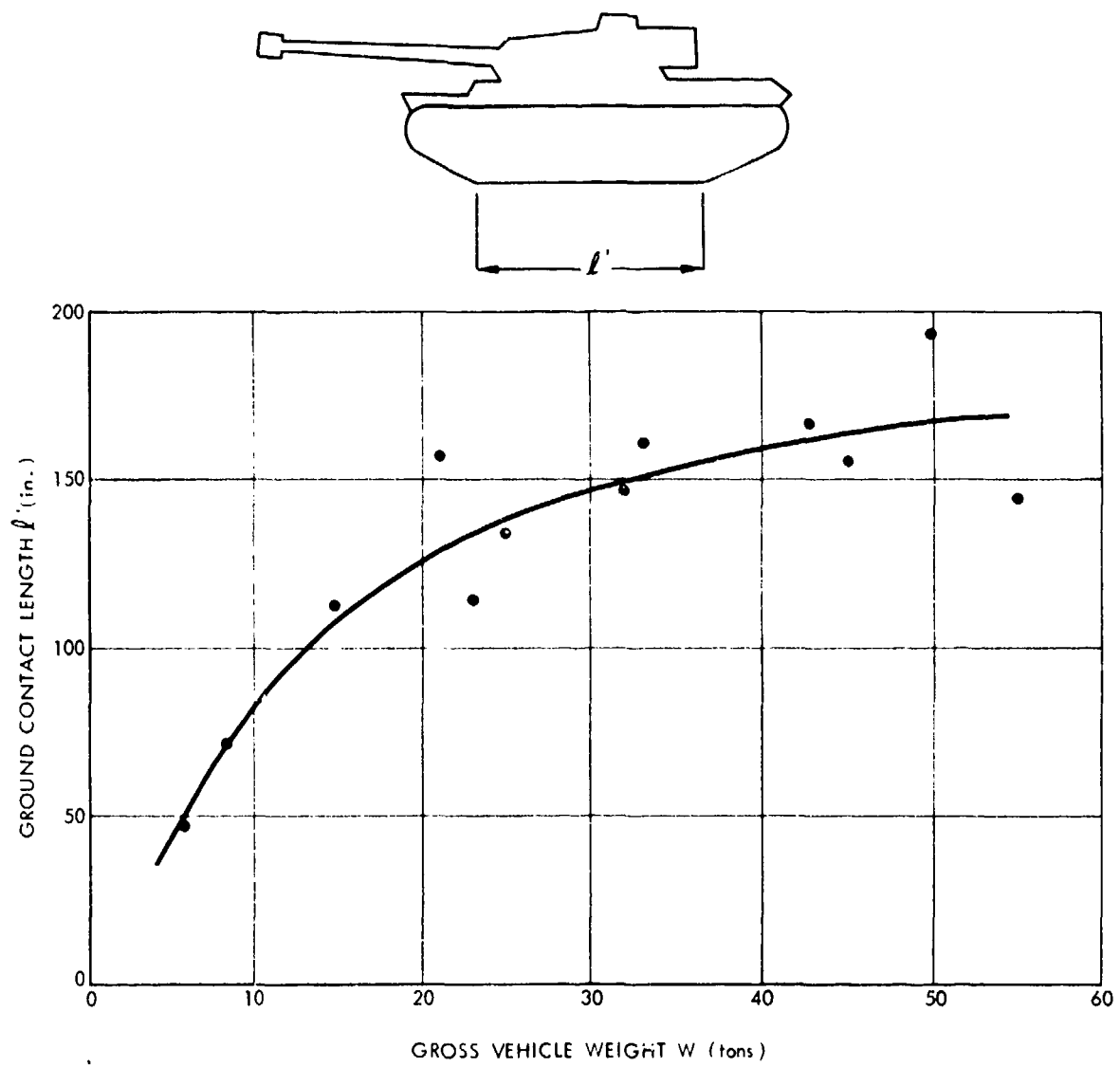
FIGURE K-2.   Length of ground contact area versus gross vehicle
              weight.
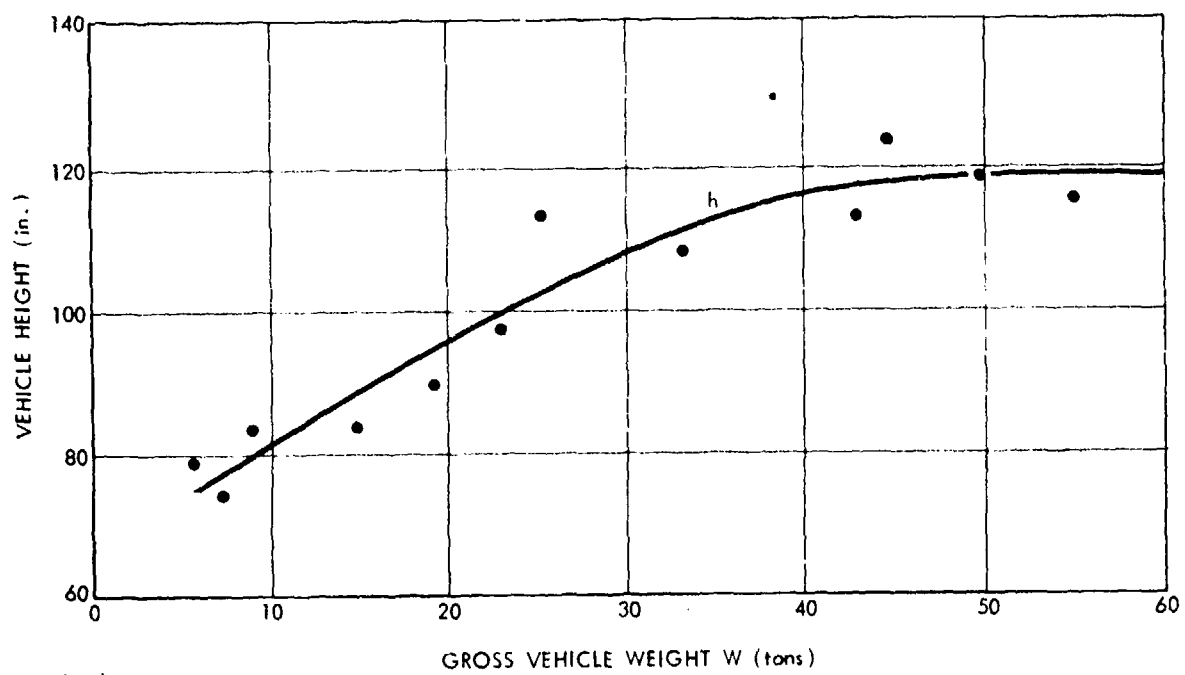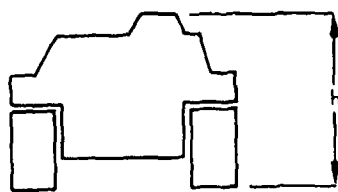
FIGURE K-3.   Vehicle height versus gross weight.
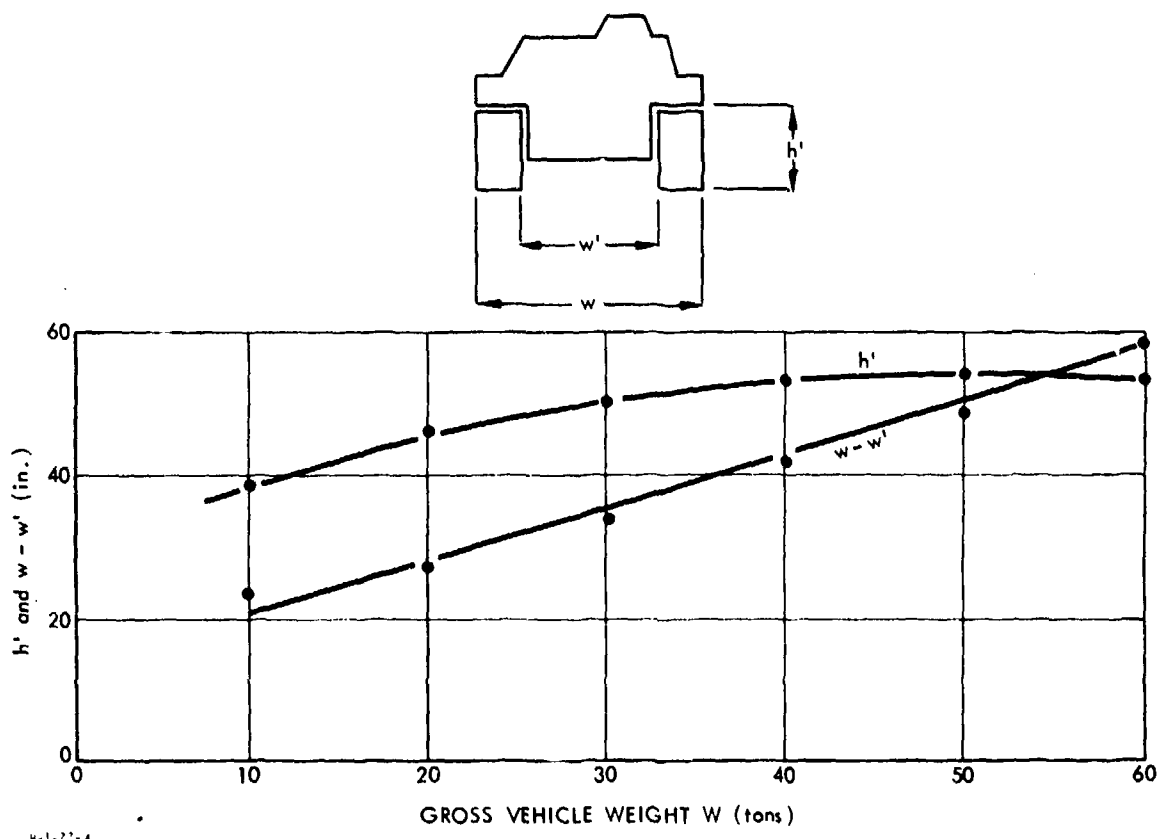
FIGURE K-4.   Track width w - w' and height h' of track-suspension assembly versus gross vehicle weight.

K-11
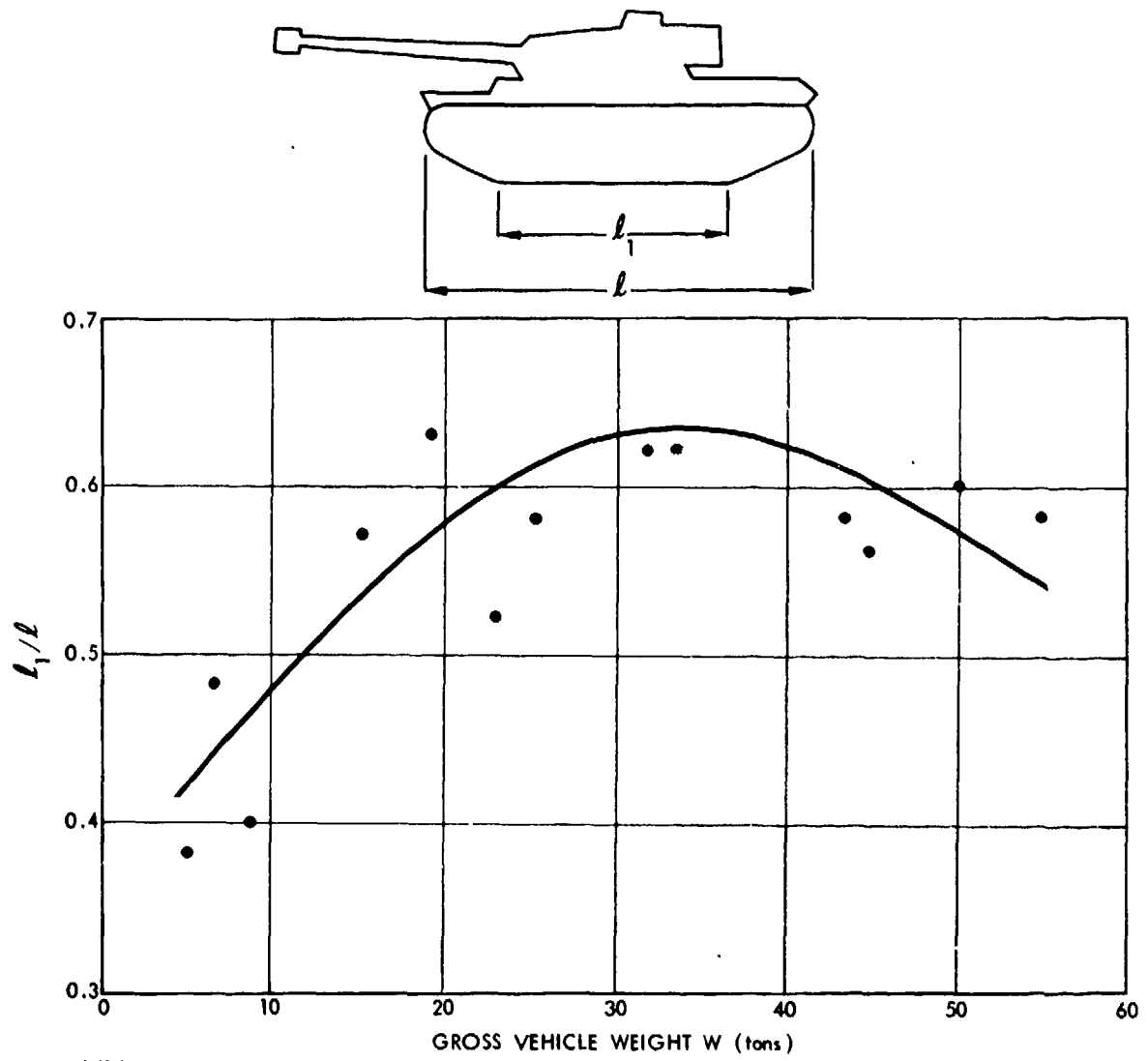
FIGURE K-5. Ratio ℓ_1/ℓ versus gross vehicle weight.

8-1-77-5

K-12

appears that the optimum relative length of the thruster in contact with the ground occurs at approximately 30-35 tons of vehicle weight. There seems to be no easy explanation for this trend, and the geometrical dissimilarity between 30- and 50-ton vehicles appears irrational, at this point.

Figure K-6 shows the same trend as Fig. K-4, i.e., that track width has more chance to increase with heavier vehicles than with lighter ones, though ultimate limits due to overall width limitation are unavoidable, as shown by the dotted line, which seems to fit the data points better. The trend may be explained by the fact that power-train component dimensions increase more slowly than the overall vehicle dimensions when the GVW is growing. This provides more space for wider tracks.

Figure K-7 confirms that conclusion, indicating the gradual increase of the volume provided for the thrusters, up to a GVW of about 50 tons. Beyond that limit, the growth of the thruster size and of the volume provided for its accommodation appears to stabilize because of general stabilization of vehicle dimensions.

Figure K-8 shows a rather surprising relative stability of thruster height, irrespective of vehicle weight. While this result is an example of the similitude law, it cannot be explained on purely technological grounds, for there is no reason why the height of the thruster should increase in the same proportion as the overall height of the vehicle. This is not only undesirable but also generally detrimental, as it unnecessarily reduces the volume of the vehicle body.

Figure K-9 demonstrates the trend to larger and larger track-suspension assemblies with increase of GVW. It appears evident that in the vicinity of GVW = 60 tons the W(V) curve gets so steep that it practically eliminates heavier vehicles.

Figure K-10 confirms this conclusion by showing the flattening of the ground contact area curve with reference to GVW.
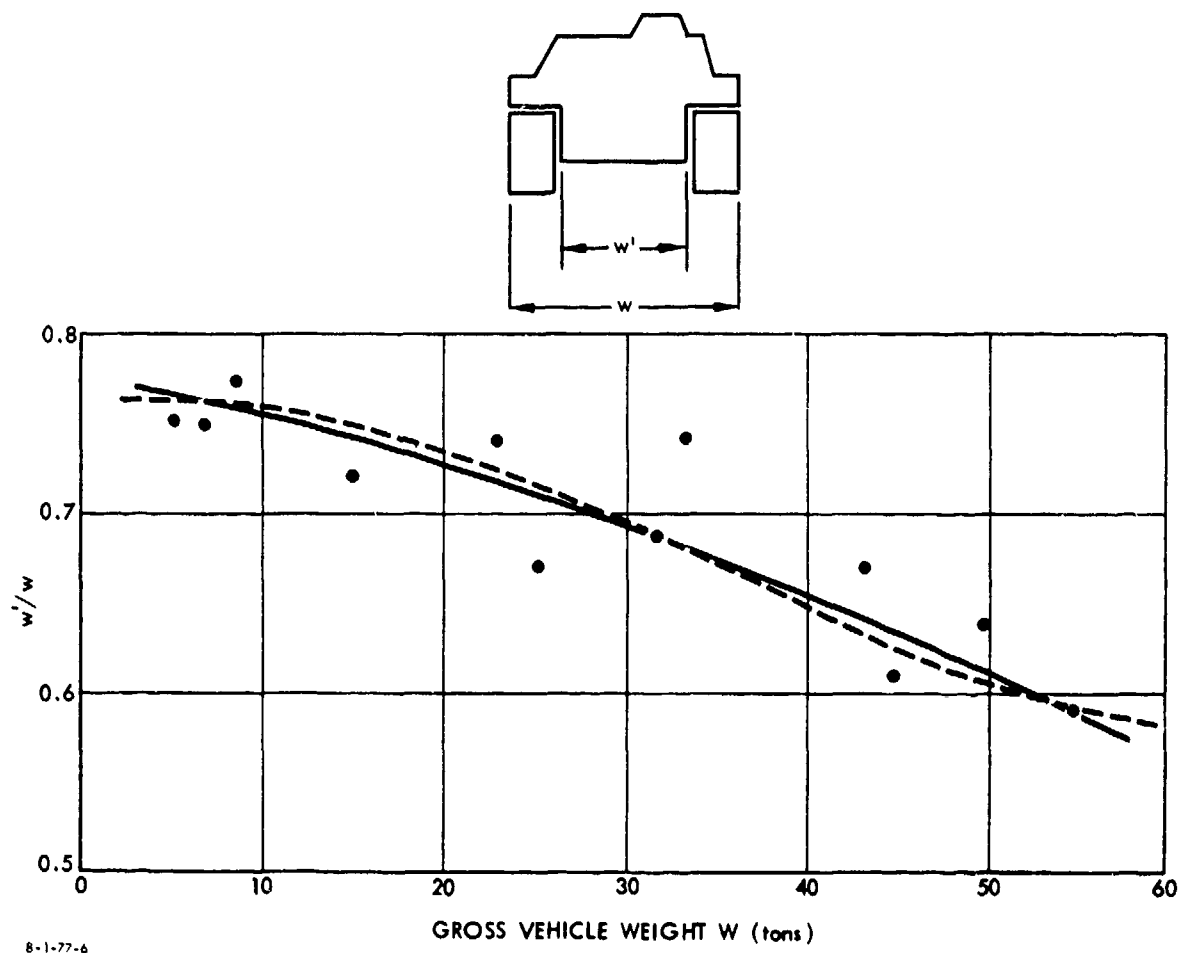
FIGURE K-6. Ratio w'/w versus gross vehicle weight.

VEHICLE ENVELOPE VOLUME: ℓhw

THRUSTER (TRACK) ENVELOPE VOLUME: $\ell h' (w - w')$

8-1-77-7
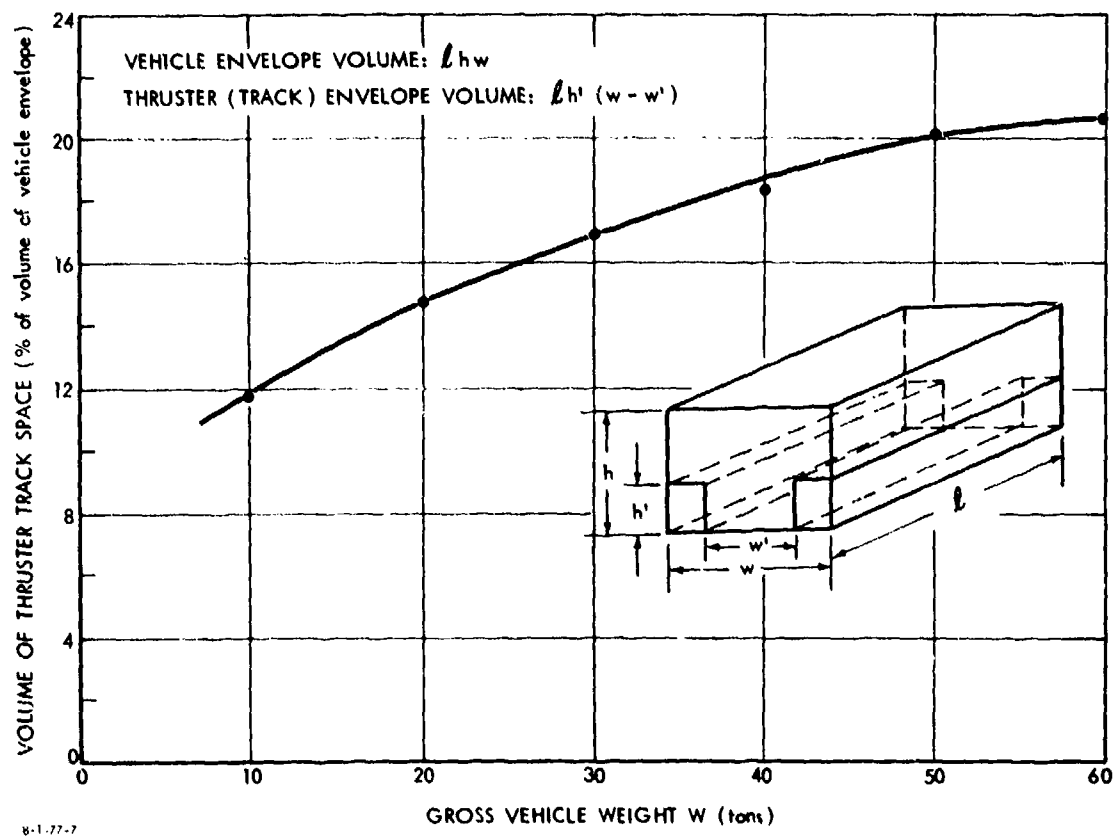
FIGURE K-7.   Thruster (track) envelope volume, expressed as percentage of vehicle envelope volume, versus gross vehicle weight.

K-15
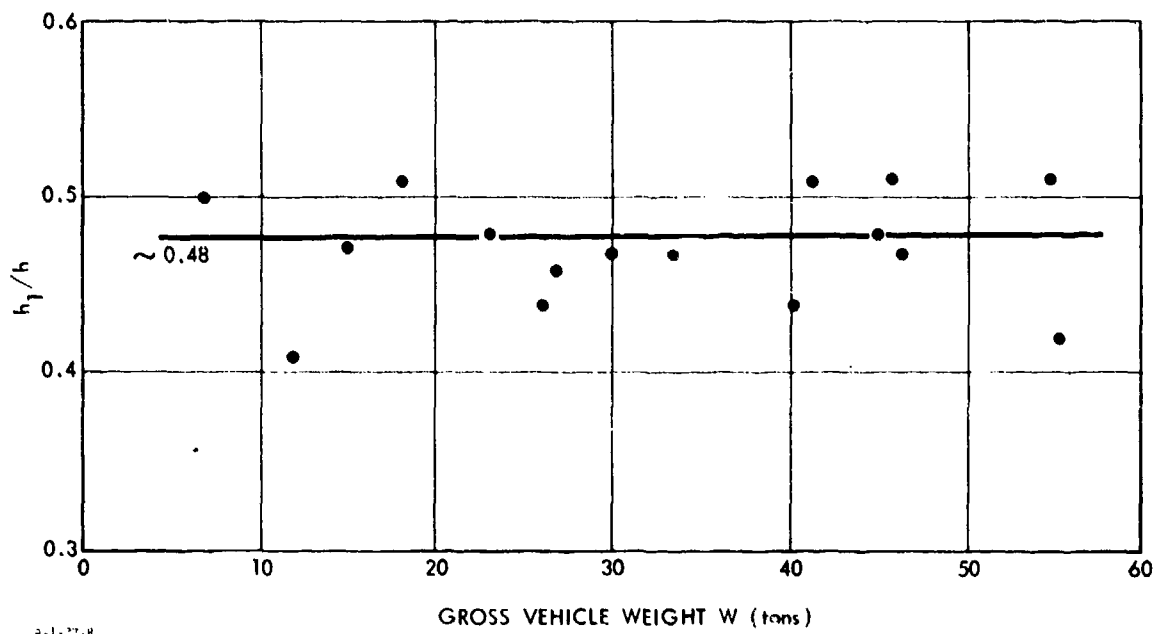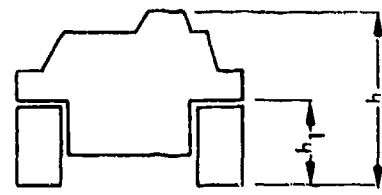
FIGURE K-8. Ratio h_1/h versus gross vehicle weight.
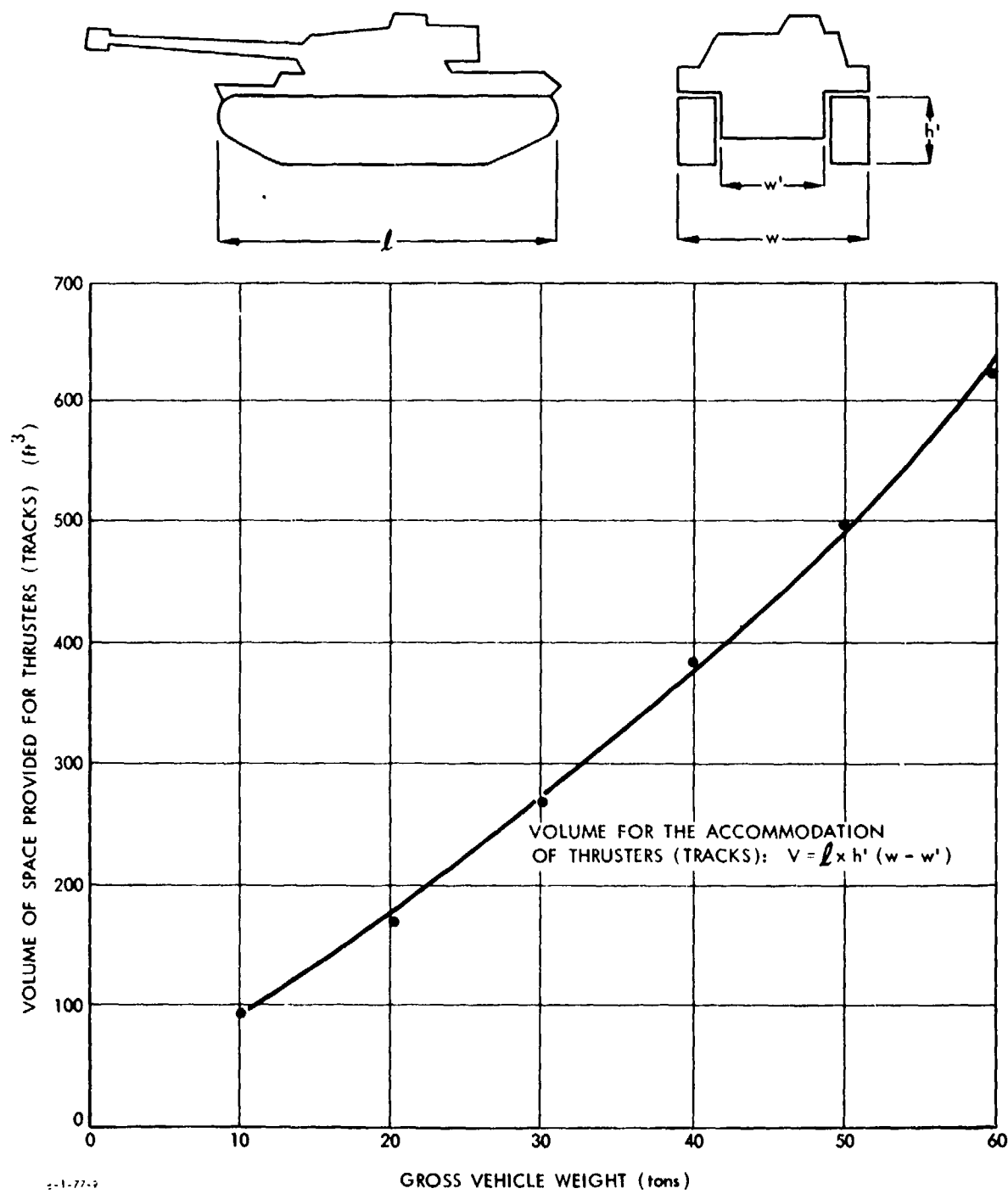
FIGURE K-9. Volume of space provided for thrusters versus gross vehicle weight.

The graph shows volume of space provided for thrusters (tracks) (ft^3) on the vertical axis versus gross vehicle weight (tons) on the horizontal axis.

VOLUME FOR THE ACCOMMODATION OF THRUSTERS (TRACKS): $V = \ell \times h' (w - w')$

K-17
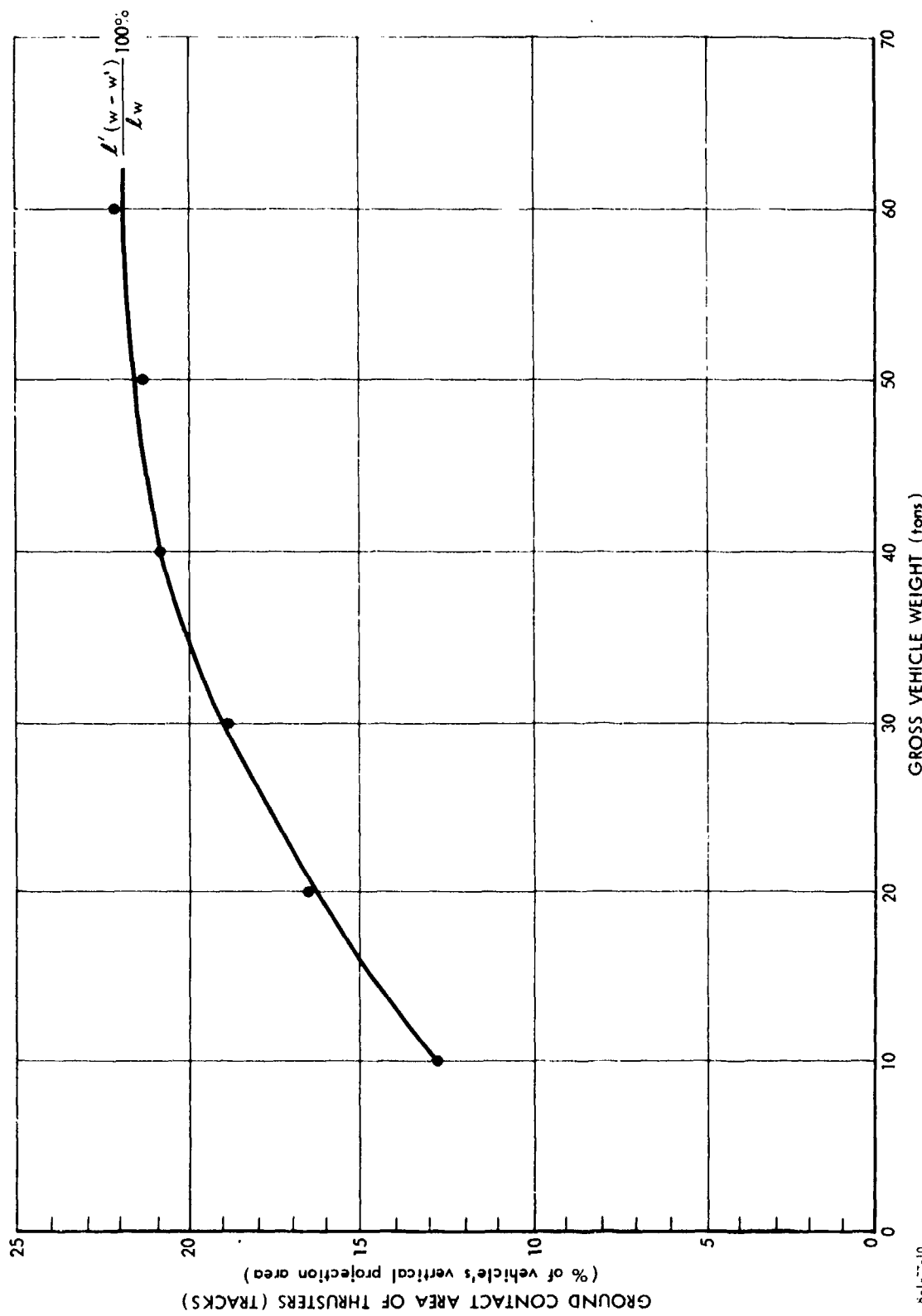
FIGURE K-10. Ground contact area of thrusters (tracks), expressed in percentage of vehicle's vertical projection area, versus gross vehicle weight.

K-18

If present performance levels of soft ground crossing are to be retained, vehicles heavier than 50-60 tons have no place in current tank concepts. New concepts must be sought.

Figure K-11 further supports this conclusion. It shows how the now acceptable maximum ground pressure of about 14 psi is reached at a GVW of about 30 tons. For heavier vehicles there is difficulty in keeping below this maximum, since contact area must increase linearly with GVW.

Figure K-12 dramatizes the problem by showing the rapid increase of thruster weight with the increase of GVW.

Figure K-13 shows the thruster weight as a percentage of GVW. The wide scatter of available data precludes exact trend extrapolation. It appears justifiable, however, to assume the upper dotted line is a trend indicator: percentagewise, heavy vehicles carry lighter thrusters than light vehicles. But the trend seems to slow down considerably in the vicinity of the 60-ton vehicle class. This again defines an upper limit for GVW, as discussed before.

2. Mathematical Models of Interactions at Soil-Track Interface

As reported in Ref. K-4, the following equations reflect the fundamental soil-vehicle relationship.

The maximum soil thrust potentially available at optimum slip for the given ground pressure of the vehicle is given by

$$\left(\frac{\tau}{p}\right)_{max} = \frac{c}{p} + \tan\phi \quad , \qquad (K-1)$$

where τ is the unit thrust (psi), p is the ground pressure (psi), c is soil "cohesion" (psi), and ϕ is the angle of soil friction. The same may be written in the following form by replacing the unit loads (psi) with gross vehicle weight W (lb), vehicle thrust T_s (lb), and the ground contact area, which for two tracks is $2\frac{w-w'}{2}\ell'$ (in.):

K-19

GROUND PRESSURE p (psi)

GROSS VEHICLE WEIGHT W (tons)

$$p = \frac{W \times 2200}{\ell'(w - w')} \text{ psi}$$
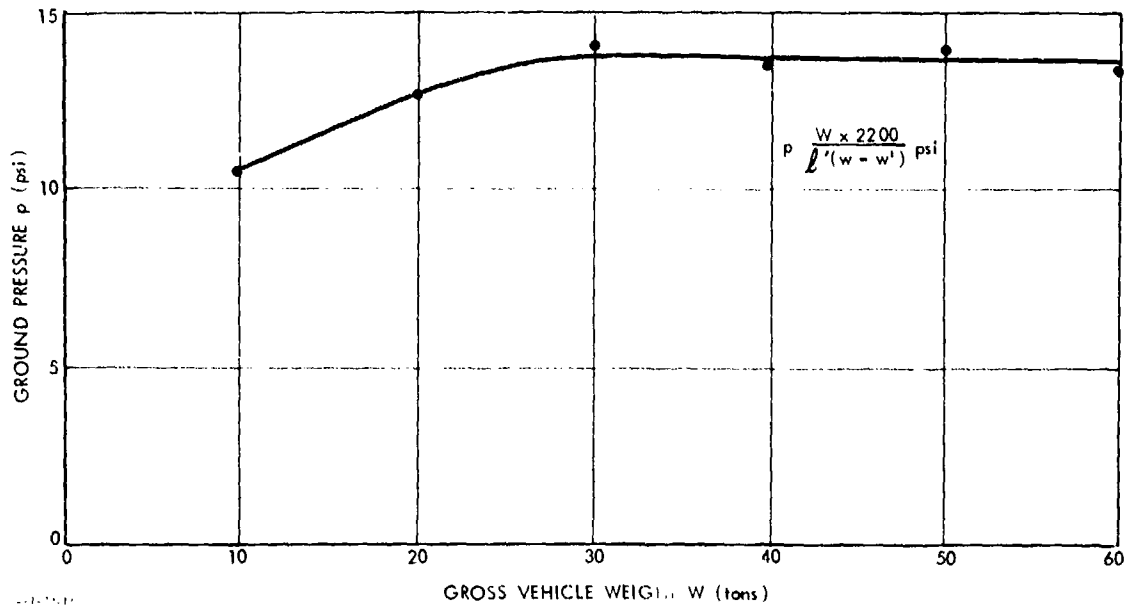
FIGURE K-11. Ground pressure versus gross vehicle weight.

GROSS VEHICLE WEIGHT W (tons)

WEIGHT OF THRUSTER (TRACK & SUSPENSION), COMPLETE (tons)
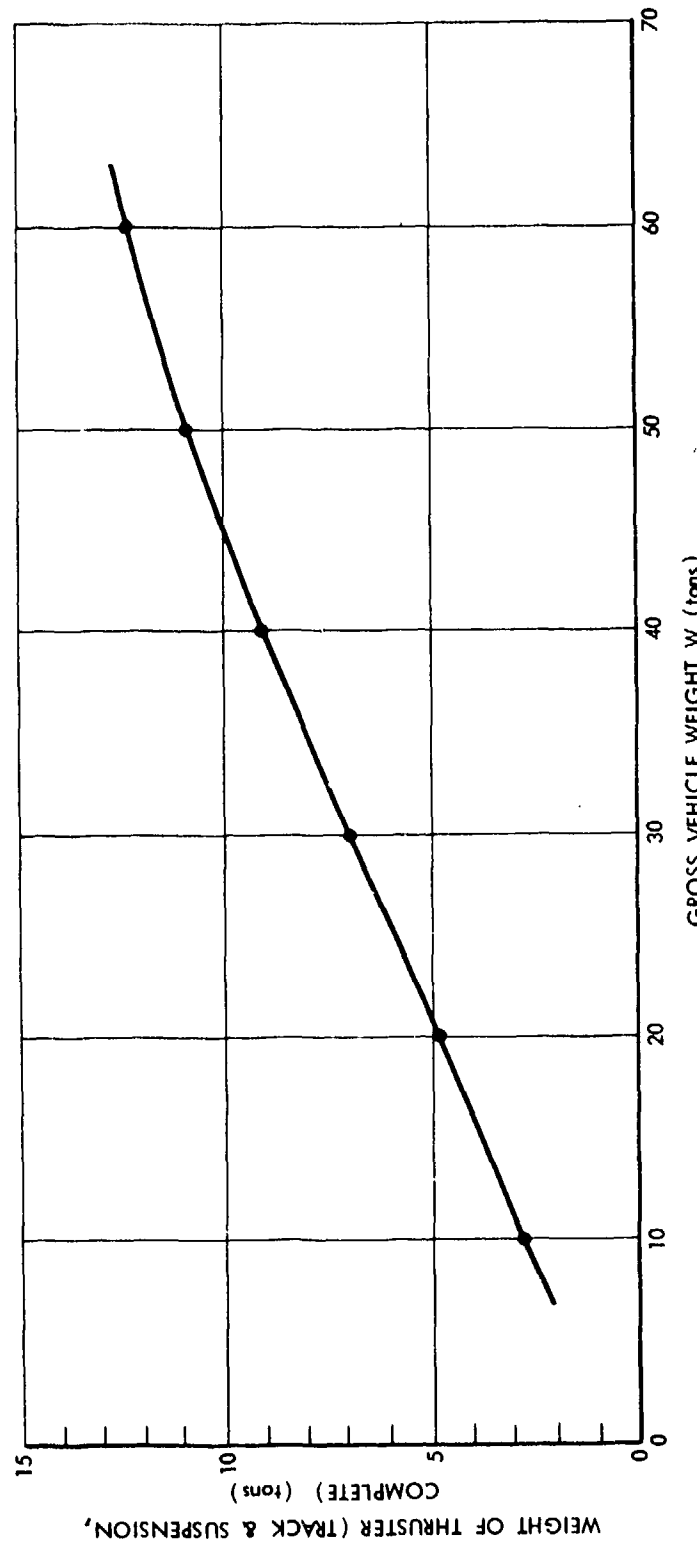
8-1-77-12

FIGURE K-12. Weight of thruster (track and suspension) versus gross vehicle weight.
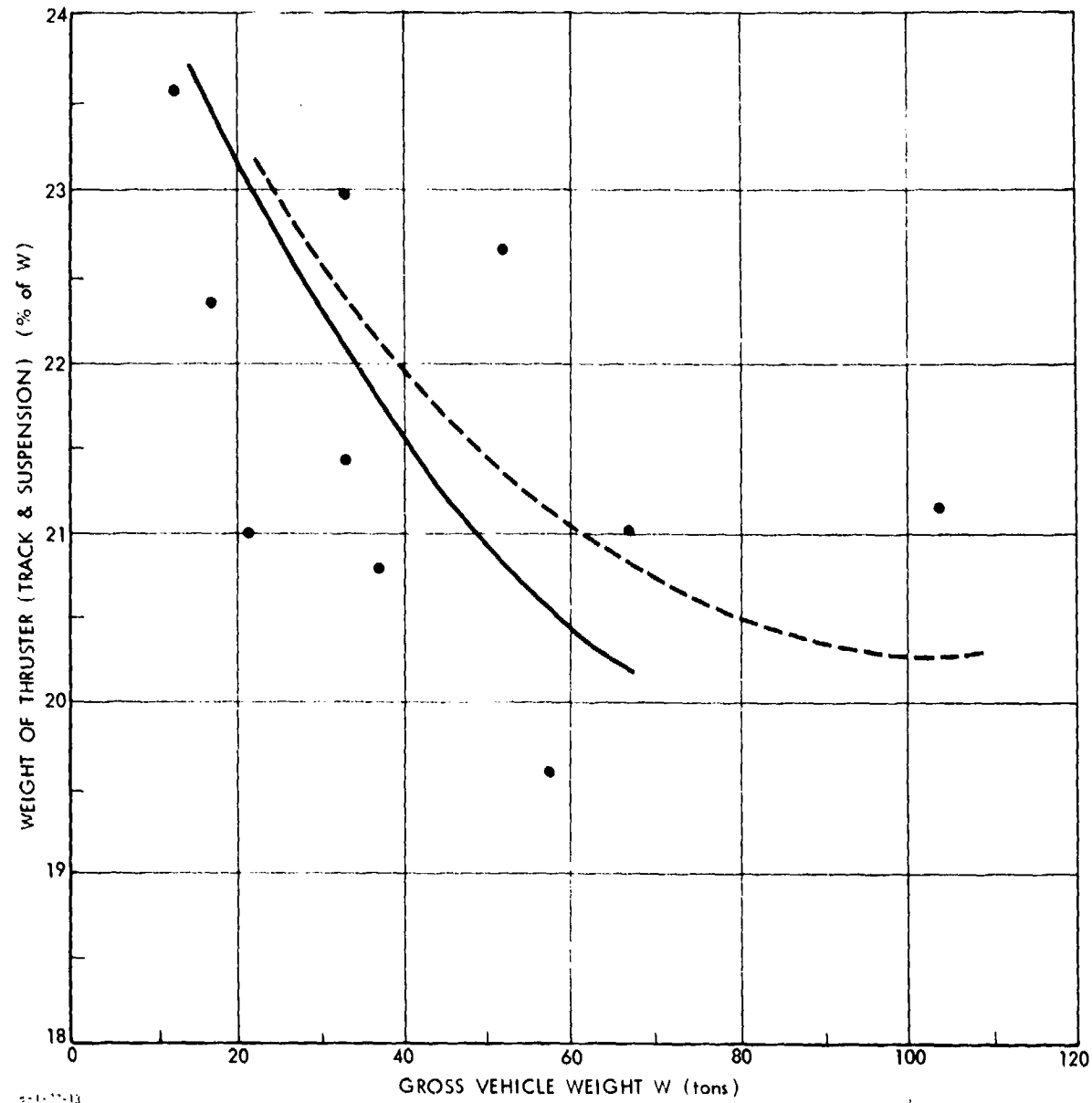
FIGURE K-13. Weight of thruster (track and suspension), expressed as percentage of gross vehicle weight, versus gross vehicle weight.

K-22

$$(T_s)_{max} = (w - w') \ell'c + W \tan\phi \quad . \qquad (K-2)$$

The intermediate thrust/weight ratio depends on the amount of track slip i_o:

$$\frac{T_s}{W} = \left(\frac{c}{p} + \tan\phi\right)\left[1 - \frac{K}{i_o\ell'}\left(1 - e^{-i_o\ell'/K}\right)\right] , \qquad (K-3)$$

where i_o is $1 - (v_{actual}/v_{theoretical})$, and K is the soil slip coefficient (in.).

The drag/lift ratio (D/W) is defined by the equation

$$\frac{D}{W} = \frac{a}{g}\left[1 + \frac{g}{W}\sum\frac{Ini_t}{r^2}\right] + \frac{(w - w')\ p^{n+1/n}}{W(n + 1)\left(\frac{2k_c}{w - w'} + k_\phi\right)^{1/n}} + f_{int} \ , \quad (K-4)$$

where a is vehicle acceleration. The expression between the brackets [] represents vehicle inertia plus the inertia of rotating masses, which can be assumed, according to the available technical literature, in the following manner:

- For heavy tanks, [] = 1.3
- For medium tanks, [] = 1.2
- For light tanks, [] = 1.15.

The quantities k_c, k_ϕ, and n are soil parameters; f_{int} is the co-efficient of internal resistance of tracks, usually assumed to be 0.05; $g = 32.2$ ft/sec^2; and $(w - w')/2$ is the track width (in.) (Fig. K-4).

The specific total power required for acceleration (a/g) from zero to speed v_m (ft/sec) at various track slips is

$$\frac{P_T}{W} = \frac{2}{\eta_v} \left(\frac{a}{g}\right) \frac{v_m}{1 - i_o} \quad , \qquad (K-5)$$

where W is in tons, P_T is in hp,* and η_v is the overall coefficient of power train efficiency (approximately 0.8).

The specific net power accelerating the vehicle is

$$\frac{P_N}{W} = \frac{2v_m}{\eta_v} \left(\frac{a}{g}\right) \quad . \qquad (K-6)$$

The specific power loss due to slip is

$$\frac{P_S}{W} = \frac{P_T}{W} - \frac{P_N}{W} \quad .$$

The coefficient of slip losses is

$$\eta_{i_o} = \frac{P_N}{P_T} = 1 - i_o \quad . \qquad (K-7)$$

The equation of equilibrium of forces acting upon the vehicle gives

$$\frac{T_s}{W} = \frac{D}{W} \quad , \qquad (K-8)$$

from which attainable accelerations may be obtained in conjunction with Eqs. K-3 and K-4.

---

*P_T is *net* engine power delivered to the transmission.

3. Power for Vehicle Acceleration and/or Hill Climbing*

From Eqs. K-8, K-4, and K-3, the values of attainable acceleration (a/g) may be calculated for a given slip i_o. This in turn gives, in conjunction with Eq. K-5, the power needed to accelerate from zero to v_m ft/sec. Since acceleration may be considered a measure of agility and maneuverability, it is important to know acceleration limitations imposed by the ability of the ground to absorb and dissipate the power imparted by the vehicle. Partial consideration of this question was given in Ref. K-4. The present examples focus on the question of tank power in general and on the eventual limits on vehicle powering.

Two types of soil are considered: purely frictional and cohesive-frictional soil, the latter being still on the friction side, as cohesion is relatively low (c = 0.1) when compared to friction (tanϕ = 0.7). One type represents a dry sand, the other a deep-plowed agricultural soil of sandy loam type. Their parameters are

> Sand: K = 1; k_c = 0; k_ϕ = 8; n = 0.8; c = 0; ϕ = 35°
>
> Ag. Soil: K = 1; k_c = 6; k_ϕ = 4; n = 0.5; c = 0.1; ϕ = 20°.

From Eqs. K-8, K-4, and K-3, and for p = 14.5 psi, w - w' = 57 in., W = 60 tons, and ℓ' = 160 in., one has:

$$\left(\frac{a}{g}\right)_{sand} = \frac{0.7}{1.3}\left[1 - \frac{1}{160i_o}\left(1 - e^{-160i_o}\right)\right]$$
$$- \frac{57 \times 14.5^{2.25}}{60 \times 2200 \times 1.8 \times 8^{1.25} \times 1.3} - \frac{0.05}{1.3} .$$

The result is shown in Fig. K-14. On the same figure the "slip efficiency" η_{i_o} is plotted. The curves clearly show that the

---

*Power available for acceleration may be spent for slope climbing, since the acceleration force equals approximately the vehicle's weight times the slope: a/g = slope (tangent).

K-25
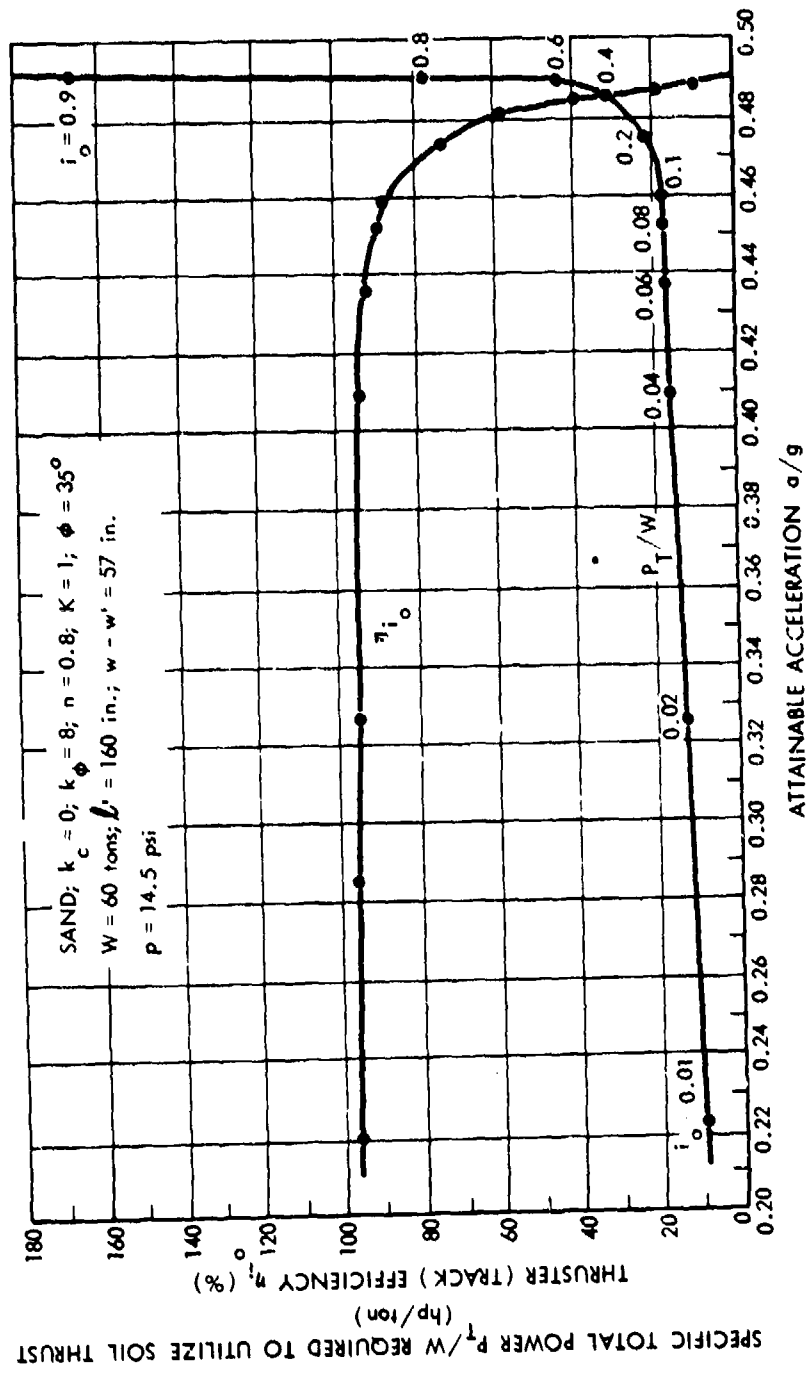
FIGURE K-14. Specific total power required to utilize soil thrust and track efficiency versus attainable acceleration.

K-26

acceleration power P_T/W which must be made available at the sprocket slowly increases for slips i_0 up to 10-20 %. Then it increases rapidly. The slip efficiency curve drops so rapidly above that slip that the main bulk of the power is spent on treading, shifting, and throwing away tons of sand instead of on thrust. Vehicle skid and stall practical end any thrust power increase at $a/g = 0.49$.

Although the figures are approximate because they are based on generalized and simplifying assumptions (for example, on the assumptions of a rigid track with a uniform load distribution such as those of a commercial Caterpillar tractor), the numerical values are basically correct and may serve as criteria of

1. The maximum economic engine power for sandy soils for the given vehicle class
2. The maximum attainable acceleration for the given available power.

Trial computations show that Fig. K-14 represents a first order of approximation in the evaluation of track thrusters in sandy soil. If we change thruster dimensions to those shown in Fig. K-15, the differences are small as far as maximum acceleration is concerned. However, note that the efficiency of the power used for acceleration increases with long, narrow thrusters when compared to the wide, short ones. For example, if sprocket power is not limiting, then a track with $\ell' = 240$ in. will achieve $a/g = 0.475$ theoretically under the considered conditions at 10% slip. A more "stubby" thruster with $\ell' = 160$ in. can make it at $i_0 = 20\%$. The larger slip, however, requires greater power. For $\eta_v = 0.8$ and $v_m = 10$ mph (14.667 ft/sec), one has

$$\frac{P_T}{W} = \frac{2}{0.8}\ 0.2\ \frac{14.667}{1-0.10} = 8.14 \text{ hp/ton} \quad \underline{\ell' = 160 \text{ in.};\ w - w' = 57 \text{ in.}}$$

$$\frac{P_T}{W} = \frac{2}{0.8}\ 0.2\ \frac{14.667}{1-0.20} \cong 9.17 \text{ hp/ton} \quad \underline{\ell' = 240 \text{ in.};\ w - w' = 38 \text{ in.}}$$

K-27
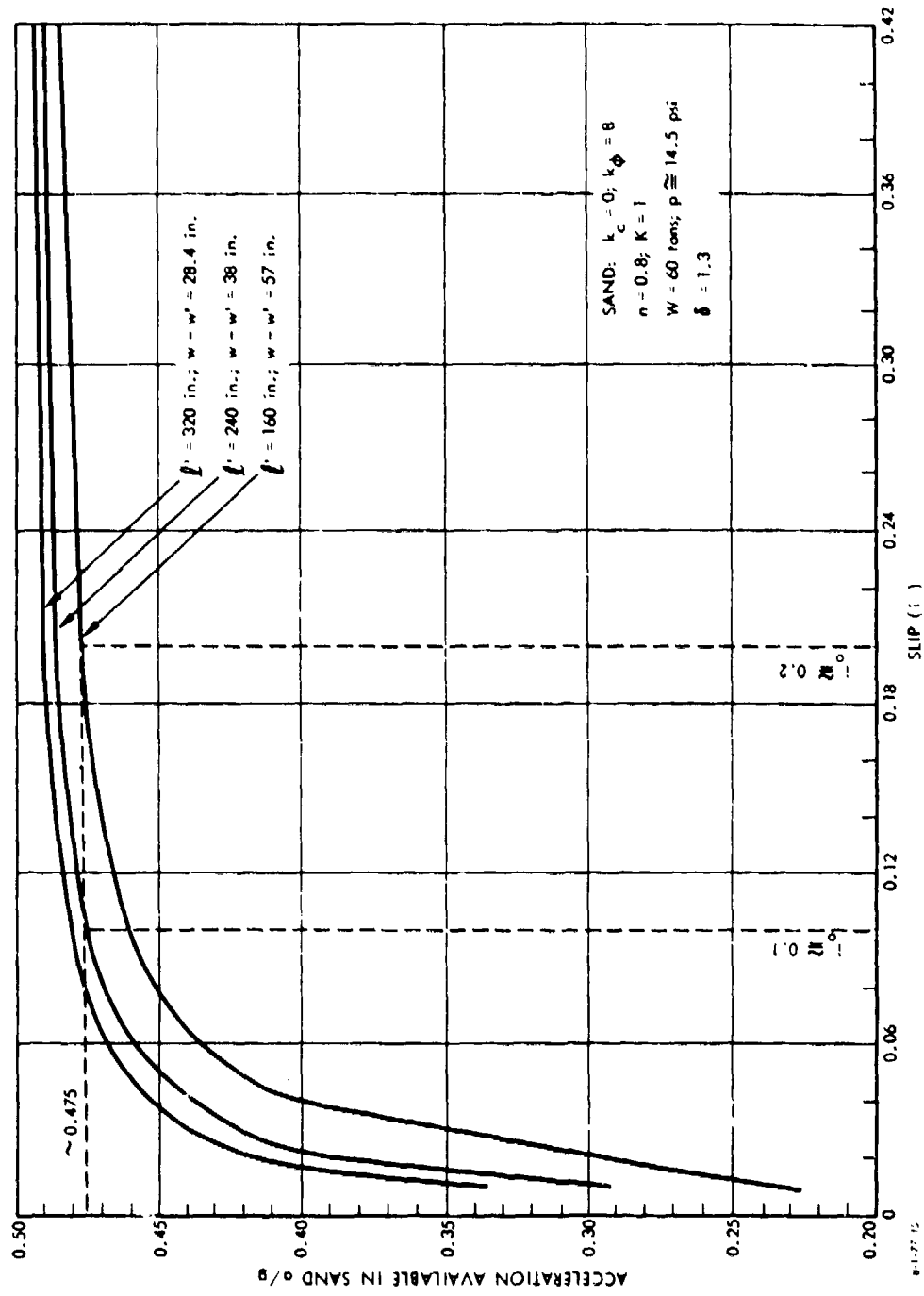
FIGURE K-15. Acceleration available in sand versus slip.

K-28

Longer, narrower tracks at higher acceleration ranges produce better results but are not easily utilized unless one contemplates articulated vehicles which represent a new species different from the established vehicle concepts.

Figure K-16 shows similar results in slightly cohesive, less frictional soils, of agricultural type. Since these soils are "weaker," the amount of acceleration achievable is much smaller (a/g ≅ 0.2, instead of a/g = 0.49 in dry sand). Otherwise, the situation is the same. Slip and hence acceleration power can be reduced if large-aspect-ratio tracks are used (Fig. K-17). This has been computed from the equation for soil acceleration and Eq. K-6:

$$\left(\frac{a}{g}\right)_{soil} = \frac{\frac{0.1}{14.5} + 0.364}{1.3}\left[1 - \frac{1}{160i_o}\left(1 - e^{-160i_o}\right)\right]$$

$$- \frac{57 \times 14.5^3}{60 \times 2200 \times 1.5 \left[\frac{6}{28.5} + 4\right]^2 \times 1.3} - \frac{0.05}{1.3} \quad .$$

Figures K-14 and K-16 show the rapid drop of thruster efficiency η_{i_o} upon reaching a critical amount of slip i_o. This happens in any soil, and the shapes of pertinent curves are similar, as shown in Fig. K-18. The only significant change is seen in the reduced attainable acceleration a/g, which diminishes with "weaker" soils. Important conclusions can be reached on the basis of the above observations:

- It is absolutely detrimental to skid and slip the vehicle in order to accelerate it beyond the point where thruster efficiency rapidly drops and the acceleration power dramatically increases.
- On the basis of the examples discussed (Figs. K-14 through K-17), the sensible slip limit $(i_o)_{opt}$ in most
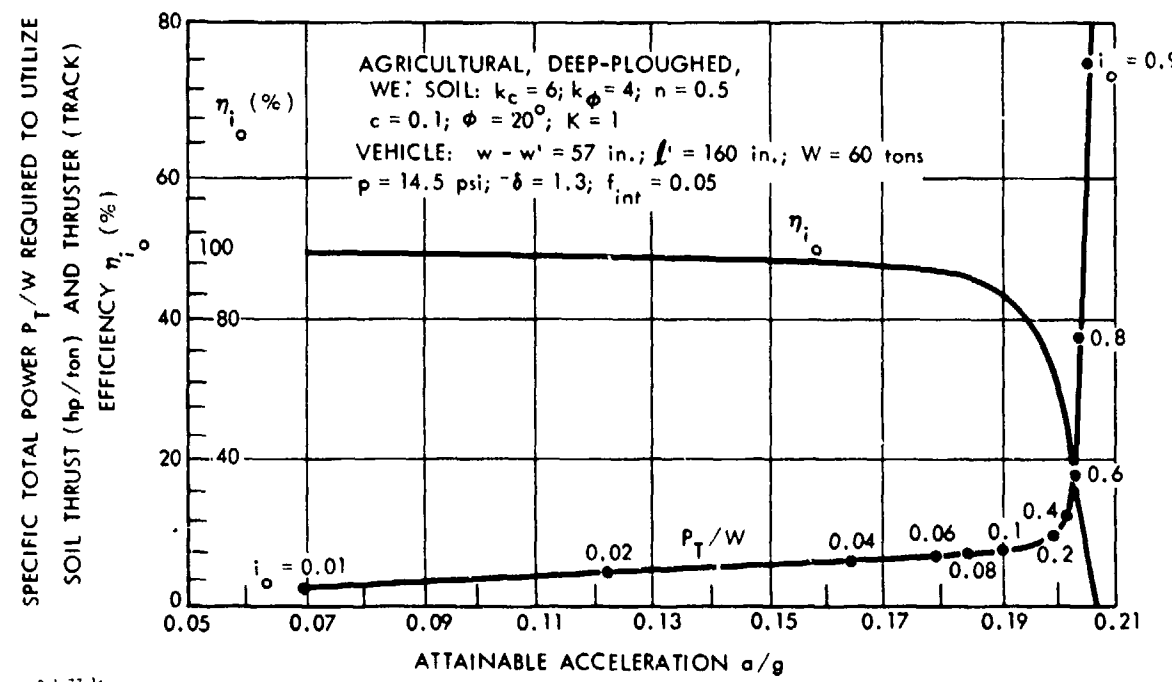
FIGURE K-16.   Specific total power required to utilize soil
thrust and thruster (track) efficiency versus
attainable acceleration.

K-30
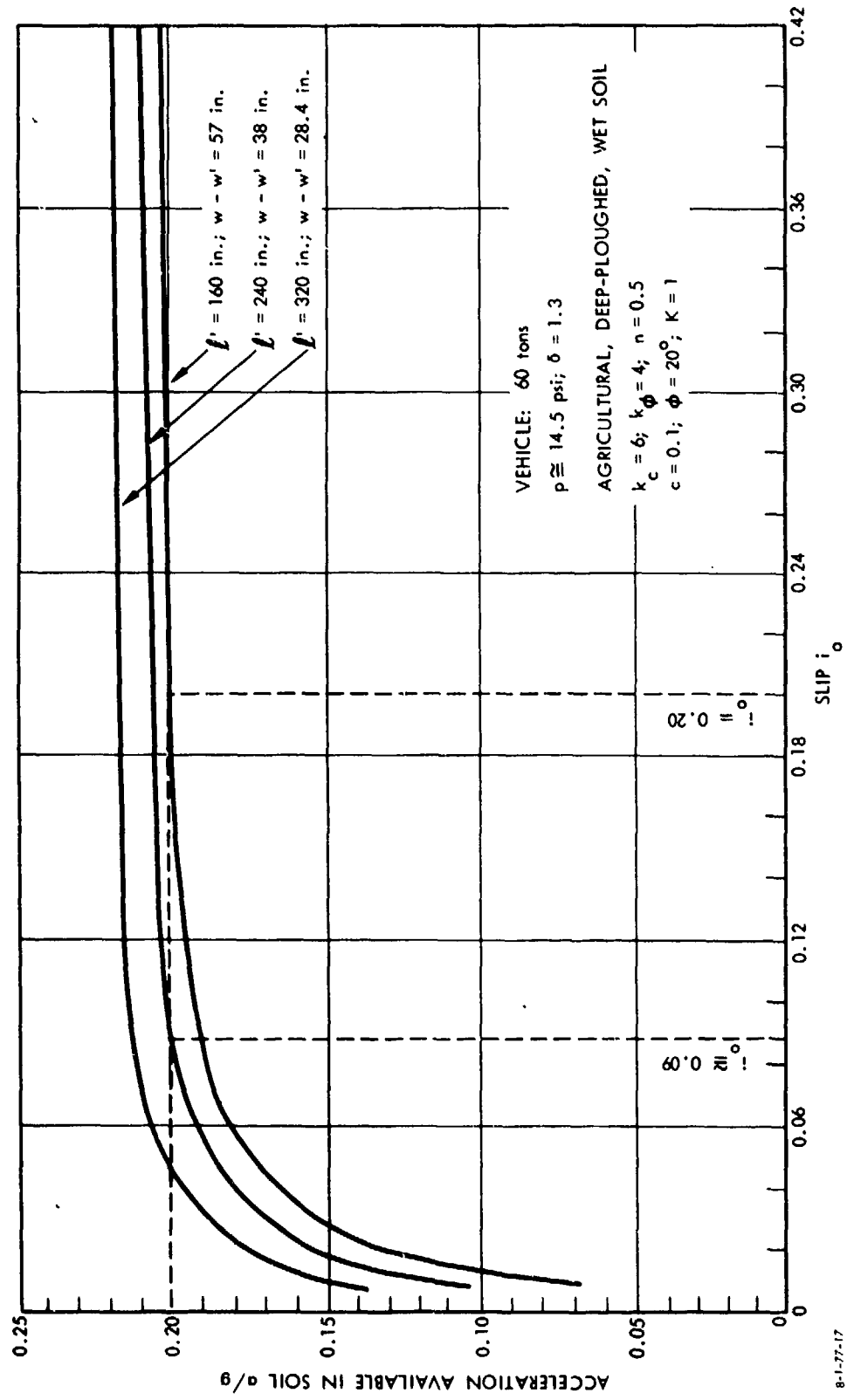
FIGURE K-17. Acceleration available in soil versus slip.

The figure shows a graph of ACCELERATION AVAILABLE IN SOIL a/g (vertical axis, from 0 to 0.25) versus SLIP i_o (horizontal axis, from 0 to 0.42).

Curves labeled:
$l' = 160$ in.; $w - w' = 57$ in.
$l' = 240$ in.; $w - w' = 38$ in.
$l' = 320$ in.; $w - w' = 28.4$ in.

VEHICLE: 60 tons
$p \cong 14.5$ psi; $\delta = 1.3$

AGRICULTURAL, DEEP-PLOUGHED, WET SOIL

$k_c = 6$; $k_\phi = 4$; $n = 0.5$
$c = 0.1$; $\phi = 20°$; $K = 1$

$i_o = 0.20$

$i_o \cong 0.09$

8-1-77-17

K-31
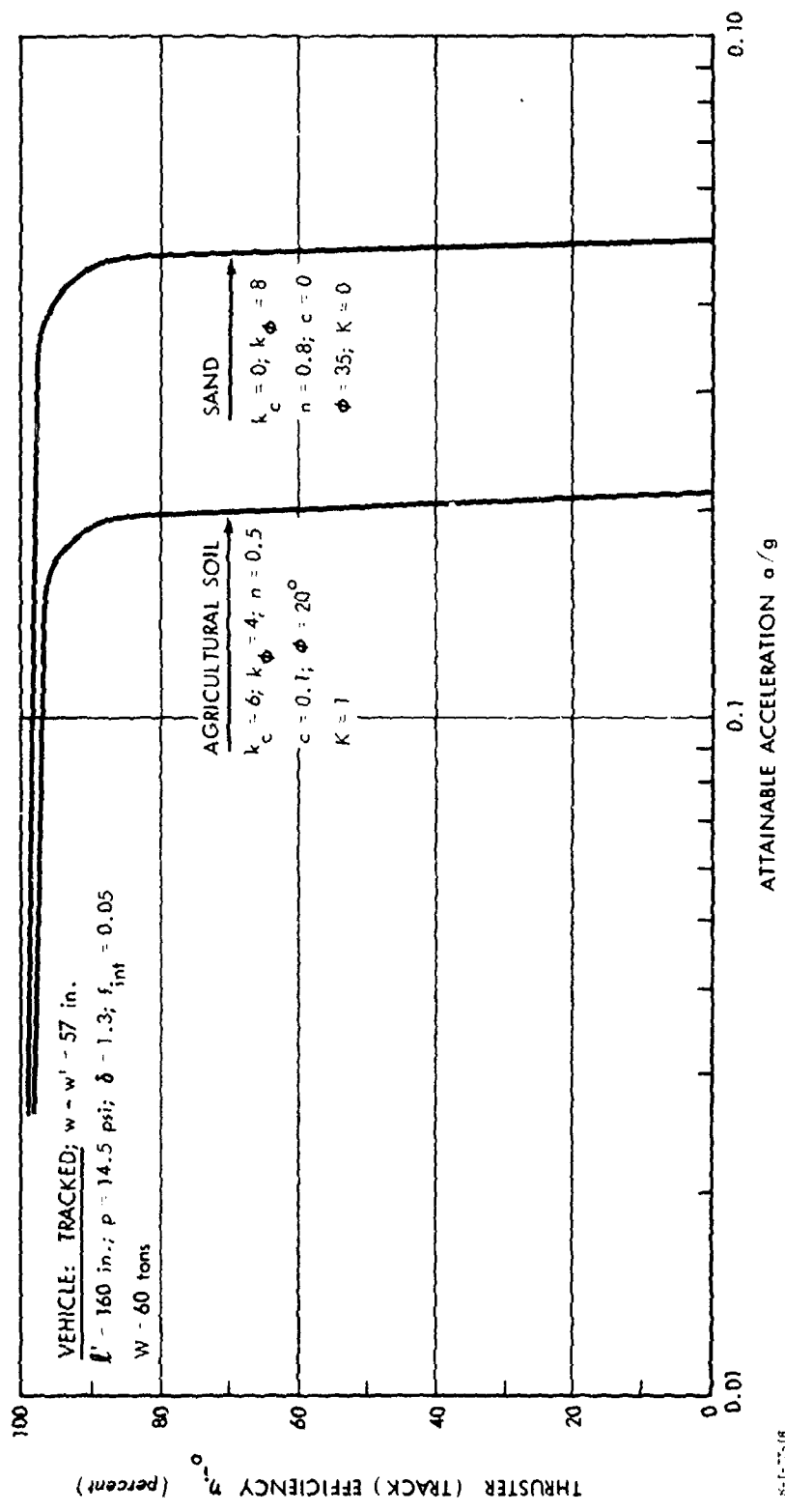
FIGURE K-18. Thruster (track) efficiency versus attainable acceleration.

K-32

common soils is of the order of 15-20%. Established in an empirical way with actual vehicles, $(i_o)_{opt} = 30\%$.

The analysis done here emphasizes the following points:

- To substantially reduce power consumption without unduly sacrificing acceleration capabilities available in the ground, slip control of the thrusters is a must. What is needed is an actual-speed sensor and a computer processor of that input which would calculate the rate-of-slip increase versus the acceleration and which would throttle the engine when n_{i_o} starts dropping too fast.

- Considering that sand is the "strongest" soil, vehicle power beyond some 30 hp/ton would be wasted on slip and skid rather than on vehicle acceleration. Similar limitations exist in agricultural soils, though apparently at a lower power level.

- Long, narrow thrusters save power, as compared to short, wide thrusters.

- Thrusters have to be matched with soils to achieve economy. Quantitative criteria can be obtained as shown in the discussion.

- This indicates need for a study of "accelerative capabilities" of various soil types in strategically important areas, along the lines discussed here. Such a study could evaluate the cost-effectiveness of a more or less radical departure from the vehicle concepts defined by Figs. K-1 through K-10.

C. WHEELED VEHICLES

1. Size, Form, and Weight

Figure K-19 shows length ℓ and width w of various 4-, 6-, and 8-wheeled vehicles plotted against their gross weight (GVW). The tendency of heavy, predominantly military vehicles towards displaying larger ℓ and w is quite evident. A similar tendency
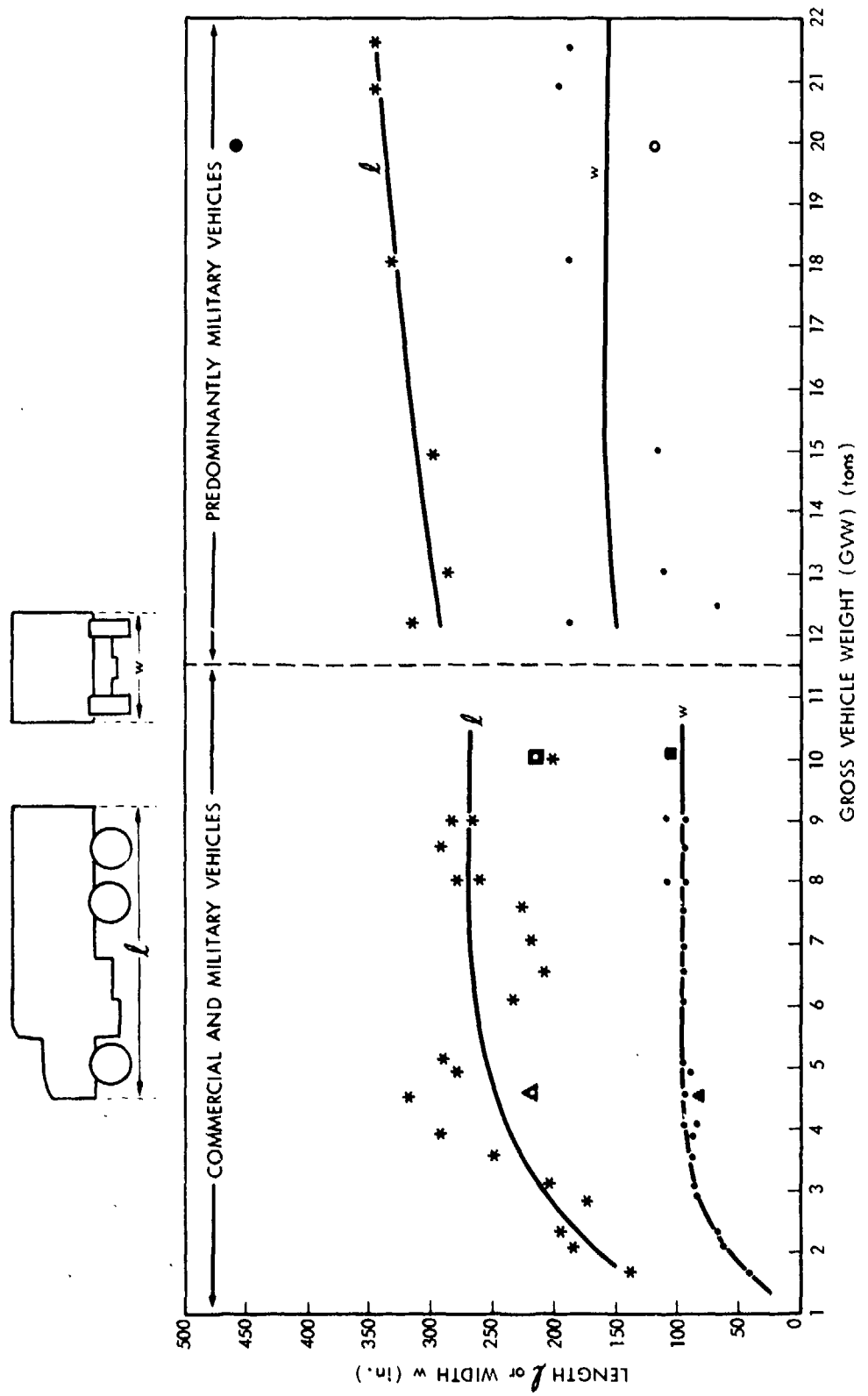
FIGURE K-19. Length and width of various 4-, 6-, and 8-wheeled vehicles versus gross vehicle weight.

K-34

does exist in heavy industrial, mining, and dump trucks which were not plotted in Fig. K-19. As in the case of tracked vehicles (Fig. K-1), the values of ℓ and w increase slowly with GVW. However, the increase is greater for lightweight wheeled vehicles, up to 5 tons GVW, than for heavier ones, a phenomenon nonexistent in the case of tracked vehicles. In general, the upper limits of ℓ and w are enforced by the external constraints. It is important to note, though, that the above limit for wheeled vehicles is of the order of $\ell \doteq 350$ in. and $w \cong 170$ in. at 20. tons GVW, while for tracked combat vehicles it amounts to $\ell \cong 225$ in. and $w \cong 100$ in. (Fig. K-1). The difference may be explained by the fact that the wheeled vehicles of the 20-ton class are transport vehicles for which battlefield survivability, and hence small size, is of secondary importance, if any. Also, the steering mode of tracks and wheels enters the picture. Note, however, that the ℓ-w values of the XM808 in the combat version (Fig. K-19) are identical with those of a 10-ton tank (Fig. K-1). The significance of this coincidence will be discussed later in conjunction with the study of thruster volume.

The concept of length of ground contact area for wheeled vehicles has a meaning different from that for tracked vehicles. Instead of the continuous length dimensions of tracks, four, six, or eight separate length dimensions of tires have to be considered. The tire's ground contact areas also may possess vertical deflection characteristics different from a track, which, as shown later, makes the pull-slip characteristics of a tire radically different from those of a track. Accordingly, "morphological" analysis of tires and tracks cannot be performed in a similar manner. This would be further complicated by the variation of ℓ with soil properties—an event unknown in track use, for any practical purposes.

However, a picture resembling Fig. K-2 may be obtained for a single tire, considering a hard ground (concrete) as shown in Fig K-20. Here, the length ℓ and the width b of the ground
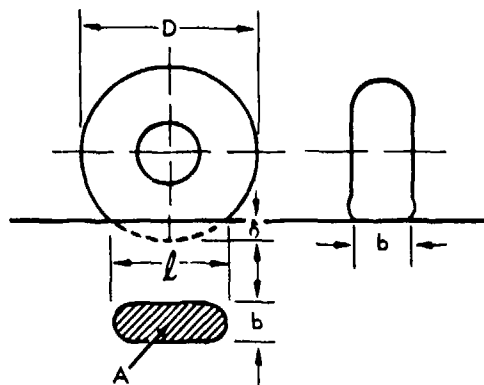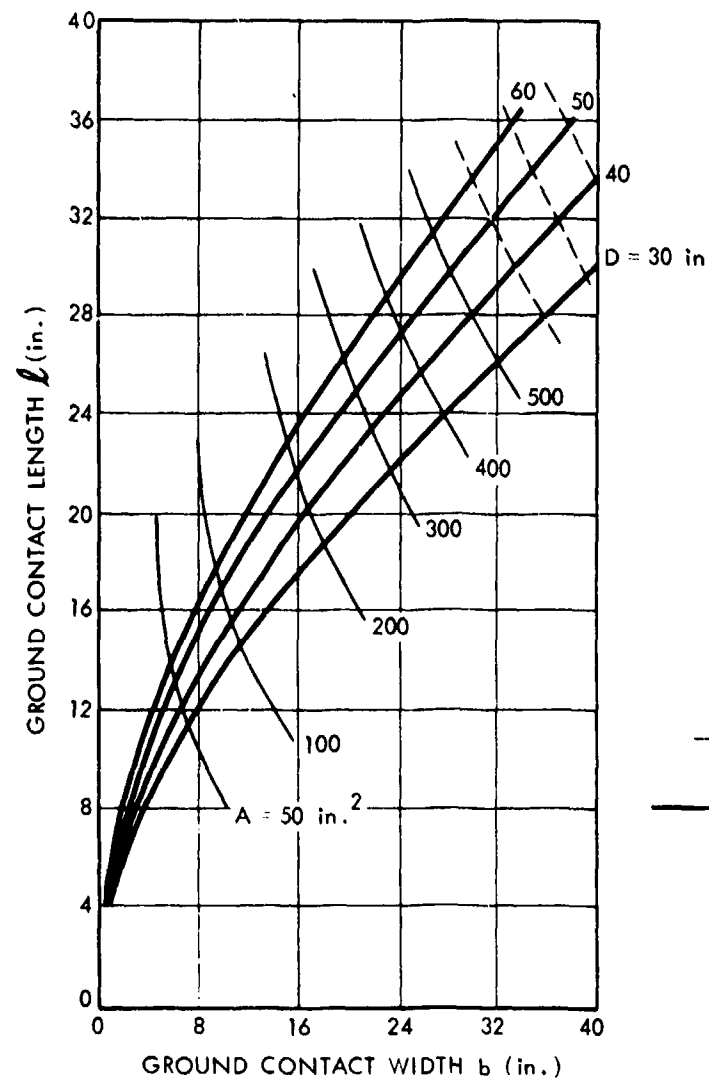
FIGURE K-20. Tire ground contact length versus tire ground contact width.

contact area A were plotted as a function of tire diameter D. Other tire parameters are implicit in the graph of Fig. K-20 on the basis of simple relationships:

$$A = 2b \sqrt{D\delta - \delta^2} \qquad \text{(K-9)}$$

$$W = Ap_i \quad , \qquad \text{(K-10)}$$

where W is tire load.

Figure K-20 leads to an otherwise obvious conclusion, providing a quantitative insight, however: in the case of a track, ℓ may reach 175-200 in.; in the case of a tire, ℓ may reach only approximately 40 in. However, the maximum track width $(w - w')/2$ and the maximum tire width b are fairly close: ~ 28 in. and ~ 35 in., respectively.

One may thus conclude that from the viewpoint of equal ground pressure, all other conditions being the same, about 3 to 5 regular tires may be needed to produce a summary length of ground contact area equal to that of one track. This indicates a rather severe vehicle envelope problem for heavier wheeled vehicles, as will be discussed later.

To pinpoint that problem more precisely, though still in a general comparative manner, the thrusters considered here must be brought under a common denominator. To this end, assume the conservative tire inflation pressure (p_i = 15 psi) of a "Goer" which almost coincides with the ground pressures of tracked vehicles close to the same vehicle class (GVW $\geq$ 20 tons) as shown in Fig. K-11. Assume further that the maximum tire deflection δ under load W is limited by hysteresis, dangerous heat generation, and so on, to $\delta = 0.25b$. The value of b equals approximately the tire width. Then, from Eqs. K-9 and K-10 one has

$$W_{\text{per tire}} \cong 15A = 30b\sqrt{0.25Db - (0.25b)^2} \quad . \qquad (K-11)$$

Catalog data indicate that for regular tires $b \cong 0.25D$, and hence Eq. K-11 yields

$$W_{\text{per tire}} = 1.8155D^2 \text{ lb} \qquad (K-12)$$

under the assumed conditions ($p_1 = 15$ psi, $\delta = 0.25b$, $b = 0.25D$). Equation K-12 enables one to plot a first-order approximation of tire diameter D versus load-carrying capacity W (i.e., a portion of GVW). Assuming 4-, 6-, and 8-wheel vehicles, the figures listed in Table K-1 were obtained.

TABLE K-1.   ESTIMATED LOAD-CARRYING CAPACITY ACCORDING
TO TIRE DIAMETER AND NUMBER

Tire Diameter, in.	Gross Vehicle Weight, tons		
	4 Tires	6 Tires	8 Tires
40	5.3	7.9	10.6
50	8.2	12.4	16.5
60	11.9	17.8	23.8
70	16.2	24.3	32.3

Table K-1 is plotted in Fig. K-21. By cross-plotting, Table K-2 is established.

TABLE K-2.   TIRE DIAMETER AND GROUND CONTACT (TIRE) WIDTH
REQUIRED ACCORDING TO GROSS VEHICLE WEIGHT AND
NUMBER OF TIRES

| Gross Vehicle Weight, tons	Tire Diameter D, in. [Ground Contact (Tire) Width b, in.]		
	4 Tires	6 Tires	8 Tires
5	39 (9.8)	--	--
10	55 (13.7)	45 (11.2)	39 (9.7)
15	68 (17)	55 (13.7)	47.5 (11.9)
20	79 (19.2)	63.5 (15.9)	55 (13.7)
25	--	71 (17.8)	61.5 (15.4)
30	--	78 (19.5)	67.5 (16.9)
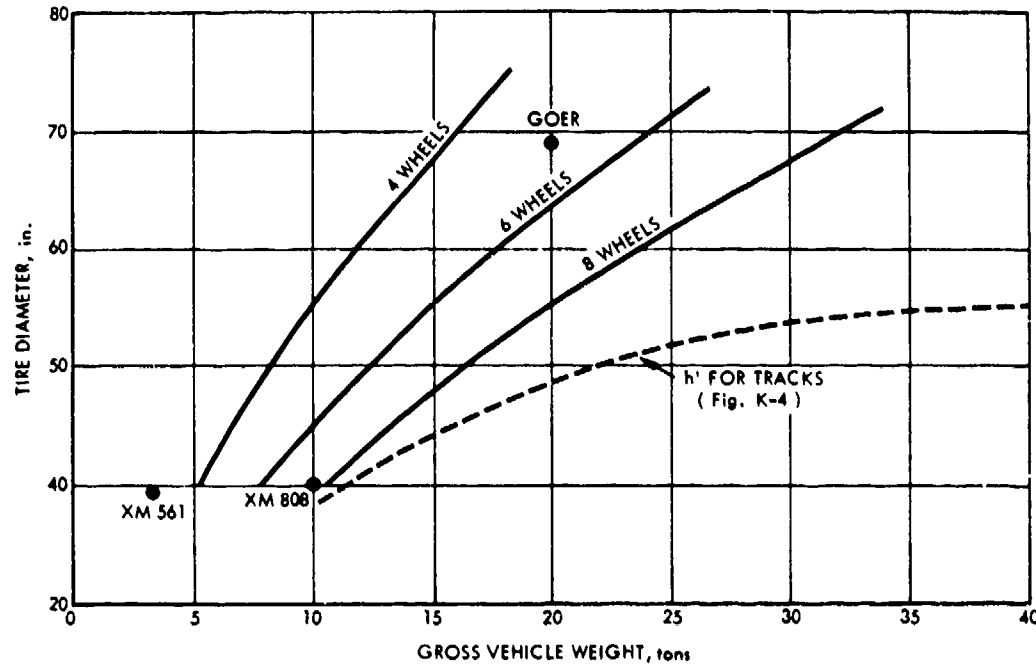
FIGURE K-21.   Estimated tire diameter as a function of gross
vehicle weight and number of tires.

The figures in parentheses () denote ground contact (tire) width b, in confirmity with the relationship b ≅ 0.25D.

Assume optimistically that the wheelbases are equal to wheel diameters. Thus, the length ℓ_{th} of the envelope of space required to accommodate the given number of thrusters may be tabulated as shown in Table K-3.

TABLE K-3. LENGTH OF ENVELOPE NEEDED TO ACCOMMODATE 4, 6, AND 8 TIRES (2, 3, AND 4 PER SIDE), ACCORDING TO GROSS VEHICLE WEIGHT

Gross Vehicle Weight, tons	Envelope Length ℓ_{th}, in.		
	4 Tires	6 Tires	8 Tires
5	78	--	--
10	110	135	156
15	138	165	190
20	158	190	220
25	--	213	246
30	--	234	270
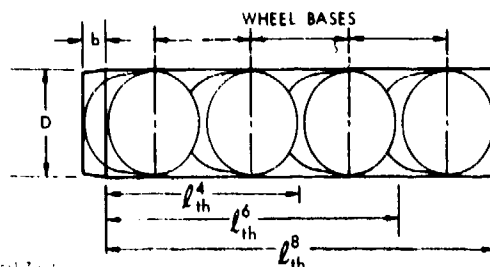
Tire thruster lengths ℓ_{th} are plotted in Fig. K-22. In the same figure similar values for track thrusters are replotted from Figs. K-1 and K-2.

An important conclusion is obvious: the length of the thruster increases faster with GVW for tires than for tracks. This again stresses the envelope problem for large wheeled vehicles, unless one may break away from environmental and "survivability" constraints.

The product of $2Db\ell_{th}$ gives a conservative volume of the envelope needed to install all the thrusters. Actually, more room is needed, as the space required for sprung motions of the tires and ti.c-wall clearances was not considered. Calculation of the $2Db\ell_{th}$ product yields Table K-4.
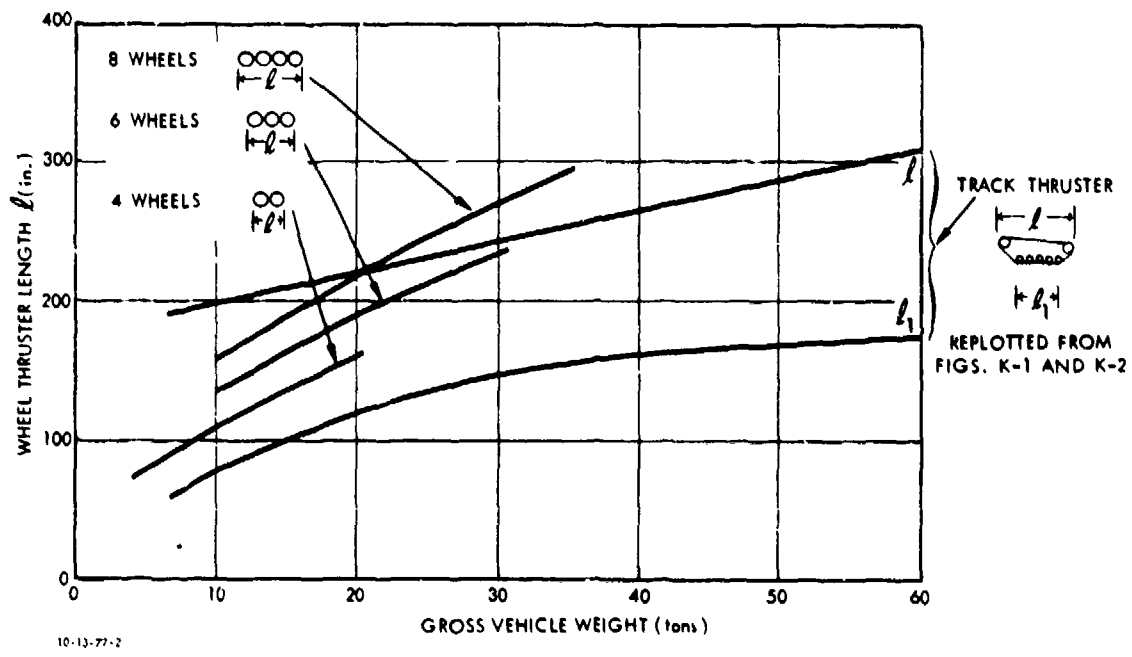
FIGURE K-22. Length of thrusters for 4-, 6-, and 8-wheel ve-
hicles versus gross vehicle weight. (Comparable
data for tracked vehicles are also shown.)

TABLE K-4. VOLUME OF THRUSTER ENVELOPE NEEDED FOR 4-, 6-,
AND 8-TIRE VEHICLES, ACCORDING TO GROSS VEHICLE WEIGHT

Gross Vehicle Weight, tons	Thruster Envelope Volume, ft^3		
	4 Tires	6 Tires	8 Tires
5	35	--	--
10	96	79	68
15	185	144	124
20	264	222	191
25	--	312	270
30	--	412	356

Table K-4 is plotted in Fig. K-23. Also, the volume of
track thrusters is replotted from Fig. K-9. The intuitively
known fact that tracks occupy less volume of the vehicle envelope
than wheels of comparable performance, as GVW is increased, is
thus demonstrated numerically. Notice that wheels may be traded
off for tracks for GVWs up to about 20 tons. For heavier vehi-
cles, the tradeoff becomes more and more difficult until it be-
comes unacceptable.

The "volume" disadvantage of tires as compared to tracks
may be explained by noting that tire diameter D increases as the
required length ℓ of the ground contact area increases, all other
conditions being equal. This may be deduced from the equation

$$\ell = 2\sqrt{D\delta - \delta^2} \, , \qquad\qquad (K-13)$$

so we obtain ℓ ~ D if we assume δ ~ D. On the other hand, ℓ for
a track can be increased without a proportionate increase in h'.
Figure K-21 also shows directly the rapid increase of wheel di-
ameter with the increase of GVW, which leads to the discussed
disadvantage of the wheeled thruster as compared to the tracked
one.

Weight analysis of tire thrusters based on catalog data can
hardly be generalized because of the great variety of tire
structures and inflation pressures for similar or identical load-
carrying capacities. This results in some discontinuities, as

K-42

10-13-77-3
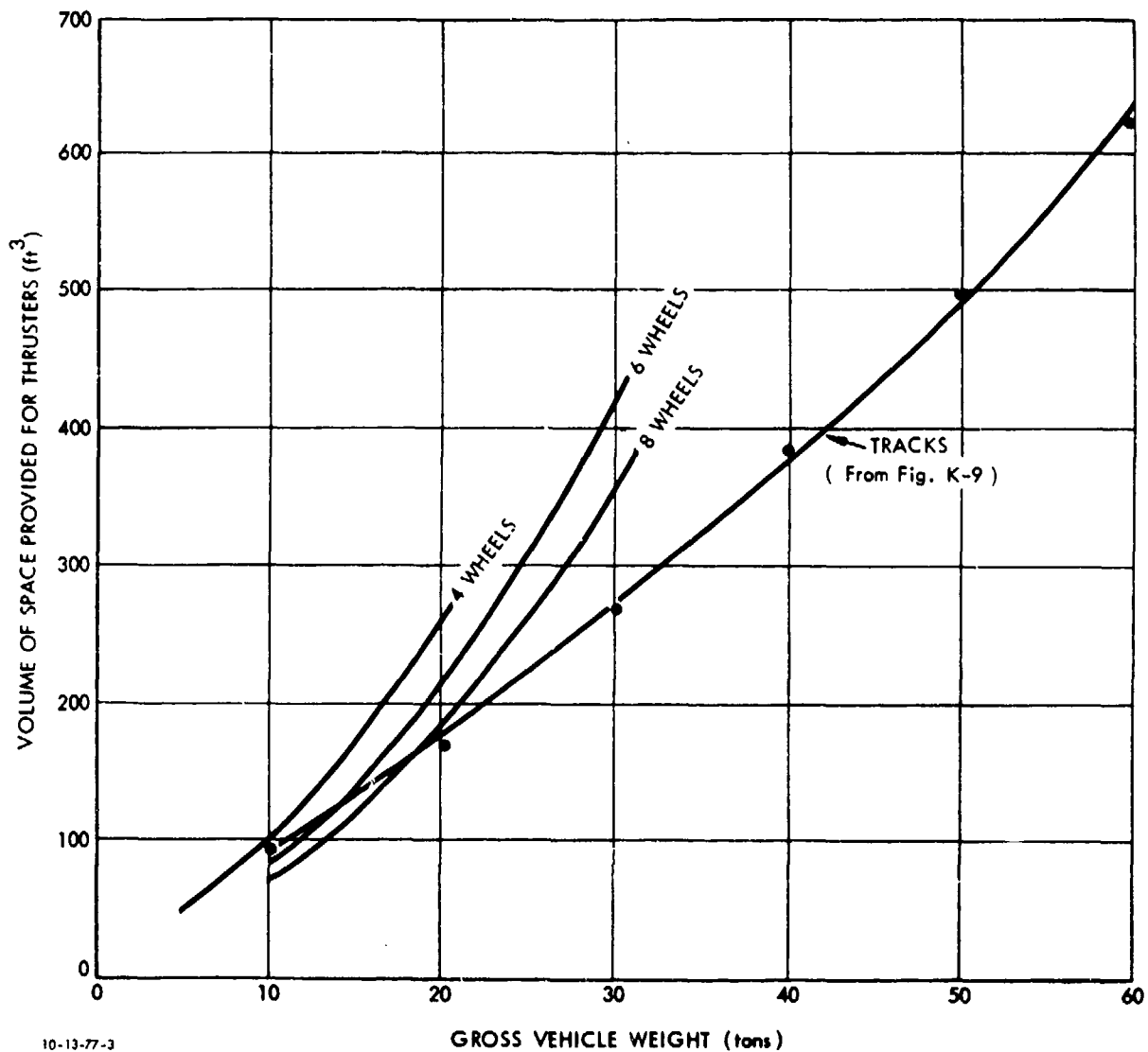
FIGURE K-23. Thruster envelope volume for 4-, 6-, and 8-wheel
vehicles versus gross vehicle weight. (Compa-
rable data for tracked vehicles are also shown.

shown in Fig. K-24, which leads to the variable scales of gross vehicle weights that may be supported by given tire dimensions, even if the data are averaged and smoothed.

To determine the rim and tire weight for the given class of vehicles, one may try to use the smoothed curve (Fig. K-24) and Table K-2. The D-values of that table, together with the averaged curve (Fig. K-24), yield the rim and tire weights for the given vehicle class as shown in Table K-5.

TABLE K-5. RIM AND TIRE WEIGHTS FOR 4-, 6-, AND 8-WHEEL
            VEHICLES, ACCORDING TO GROSS VEHICLE WEIGHT

Gross Vehicle	Rim & Tire Weights, tons		
Weight, tons	4 Wheels	6 Wheels	8 Wheels
10	0.25 x 4 = 1.0	0.15 x 6 = 0.9	0.1 x 8 = 0.8
15	0.6 x 4 = 2.4	0.25 x 6 = 1.5	0.15 x 8 = 1.2
20	0.85 x 4 = 3.4	0.5 x 6 = 3.0	0.25 x 8 = 2.0

As expected, the result shows some nonuniformity (Fig. K-25), although the trend is clear. The trend indicates the previously detected trend to the effect that wheeled thrusters become unmanageable beyond some 25-30 tons GVW, because the *tires and rims* become heavier than tracks. This again points to a limit to wheel thruster application for heavier vehicles, a conclusion based on experience and backed by consideration of thruster volume.

To check this and possibly to obtain more uniform quantitative data with respect to thruster weight versus GVW, a different input was analyzed, as shown in Fig. K-26. The input was based on a more detailed analysis of *tires, rims, and wheels* for an almost geometrically similar family of tires, showing a rather monotonic increase of load-carrying capacity with diameter increase. Using Table K-2 again and the graph in Fig. K-26, the result in Table K-6 is obtained.
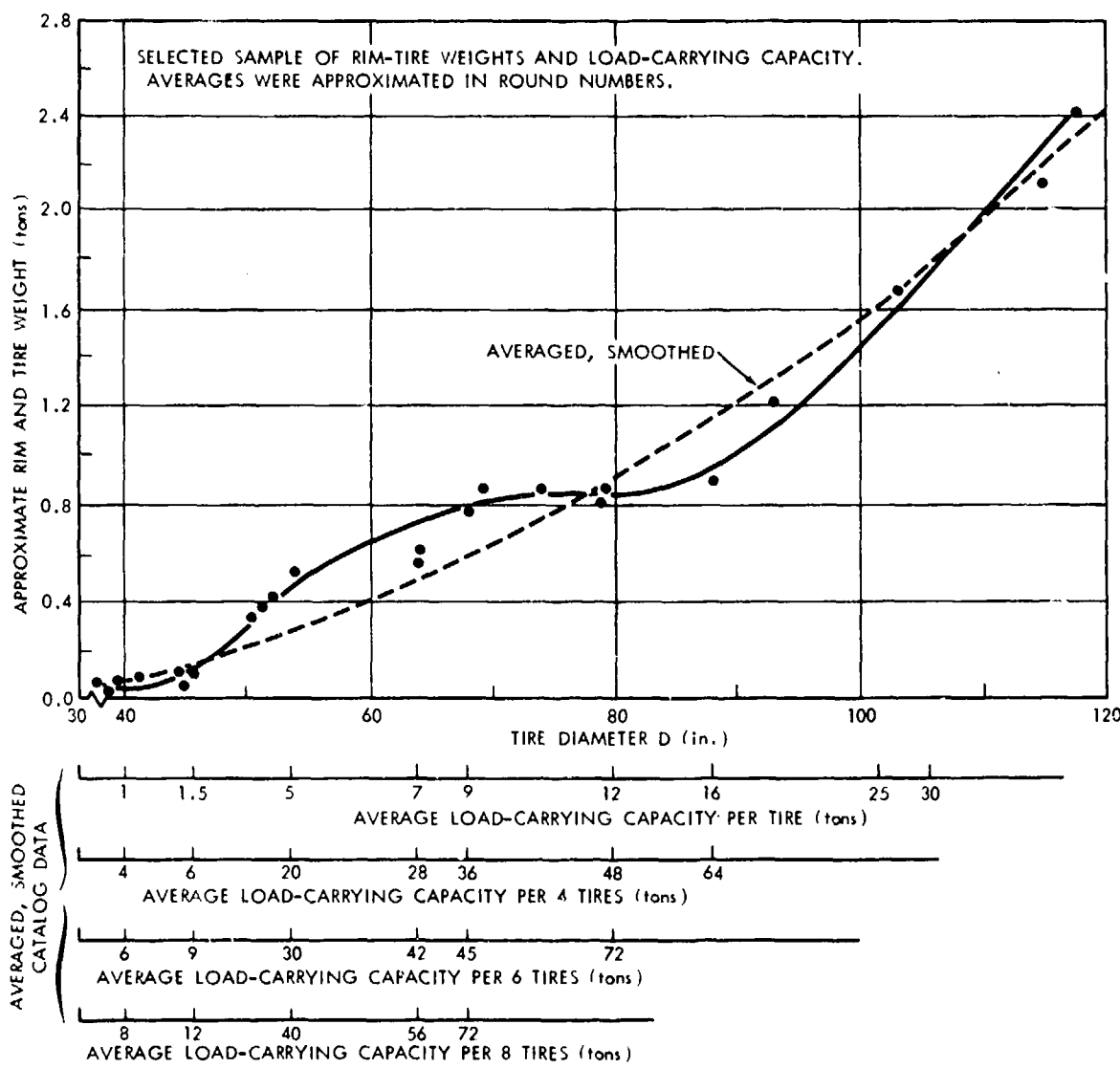
FIGURE K-24. Approximate rim and tire weight and load-carrying capacity versus tire diameter.
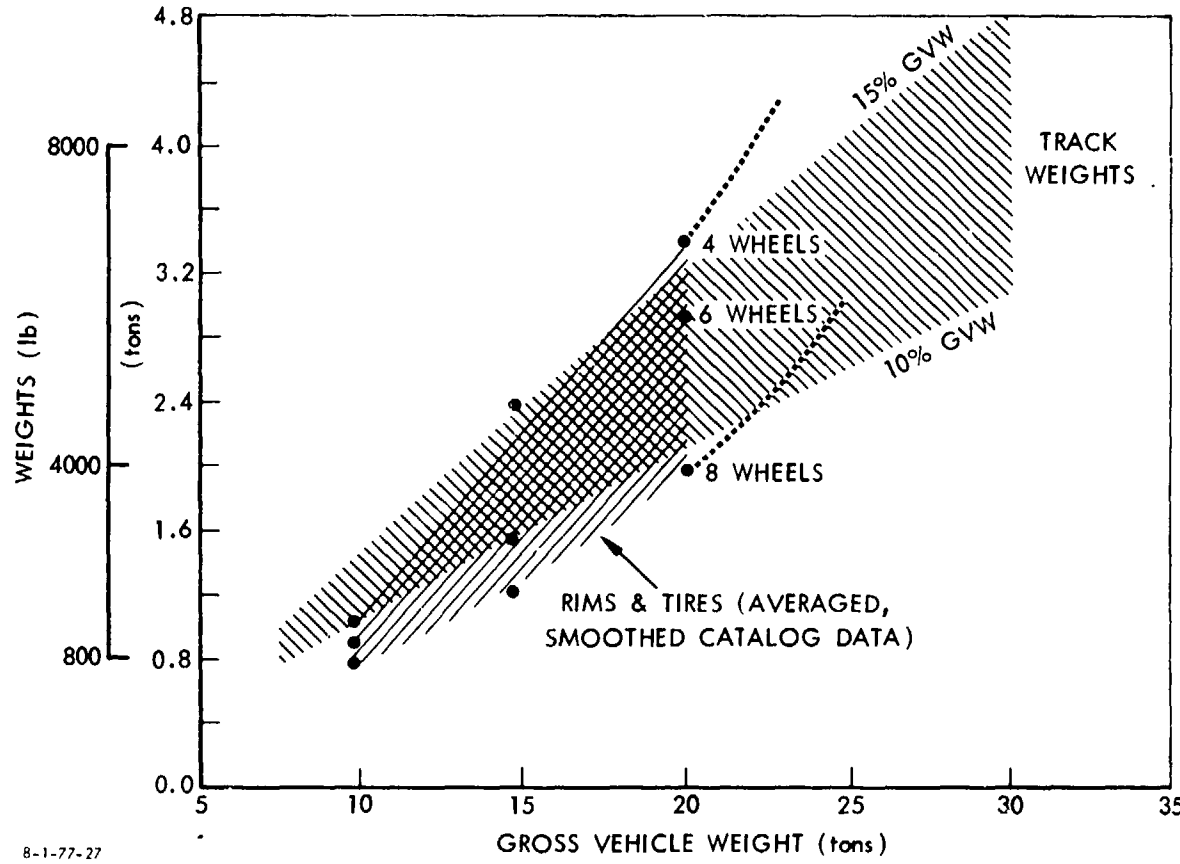
FIGURE K-25. Weights of rims and tires for wheeled vehicles and track weights versus gross vehicle weight.

K-46
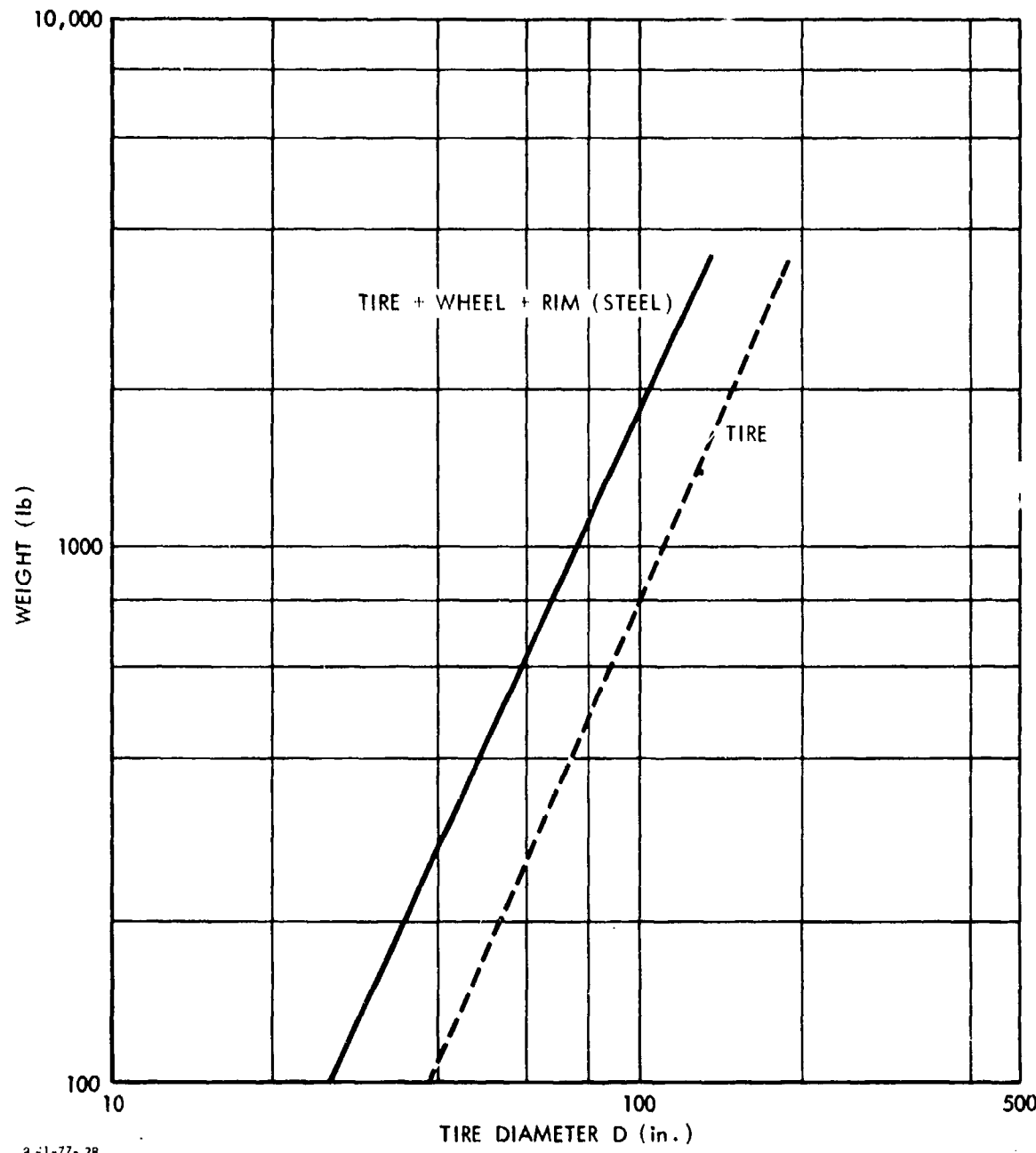
FIGURE K-26. Tire, wheel, and rim weight and tire weight versus tire diameter.

K-47

TABLE K-6. WHEEL, RIM, AND TIRE WEIGHTS FOR 4-, 6-, AND
8-WHEEL VEHICLES, ACCORDING TO GROSS VEHICLE WEIGHT

Gross Vehicle Weight, tons	Wheel, Rim, and Tire Weight, lb		
	4 Wheels	6 Wheels	8 Wheels
10	2000	2100	2160
15	3600	3000	2800
20	5600	4800	4000

This result is plotted in Fig. K-27. Here, the track and
roadwheel weights were plotted, assuming, in accordance with
prevailing experience, that the weight of the latter amounts to
some 3% of the GVW. Hence the track-roadwheel weight boundaries
were enclosed between 13% and 18% of GVW. The boundaries of the
track weight alone were assumed to be between 10% and 15% (Fig.
K-25). Note some inconsistency between Figs. K-27 and K-25,
because they show that the wheel-rim-tire assembly is somewhat
lighter than the wheel-rim assembly. But the overlapping of
pertinent graphs shows a relatively small difference (Fig. K-28),
a small penalty to pay for the differences in inputs on which
Figs. K-25 and K-27 were based.
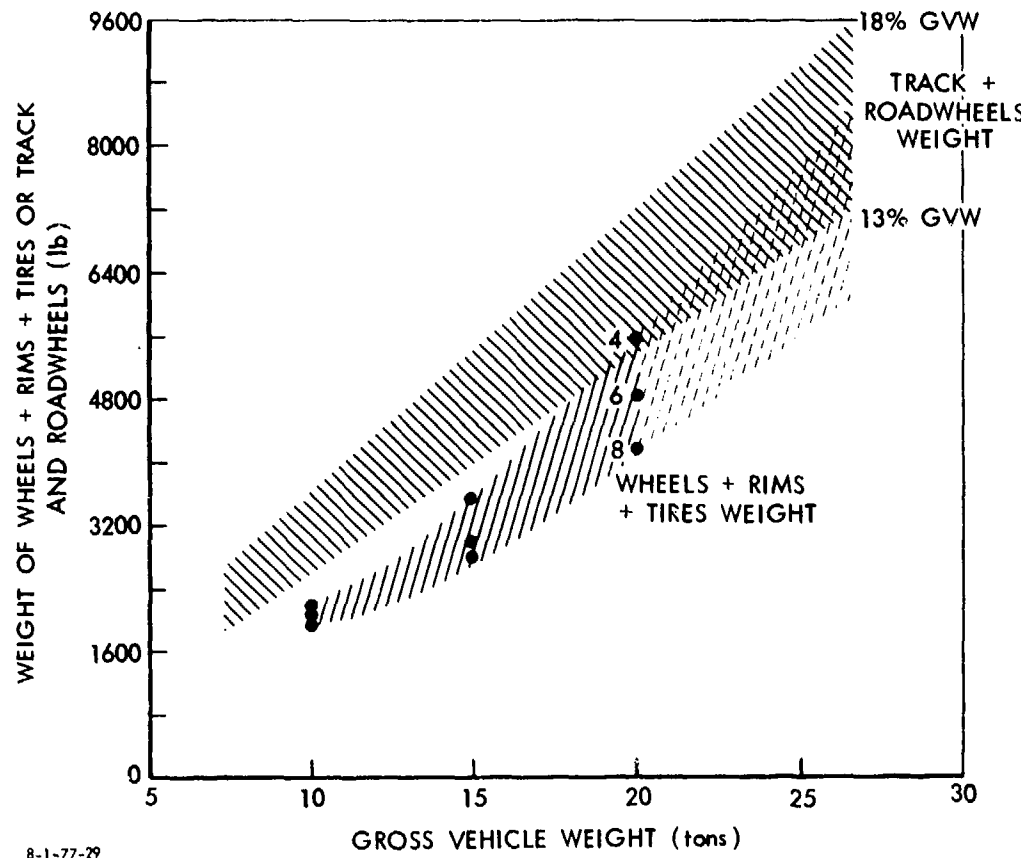
FIGURE K-27. Weights of wheels, rims, and tires and of tracks and roadwheels versus gross vehicle weight.
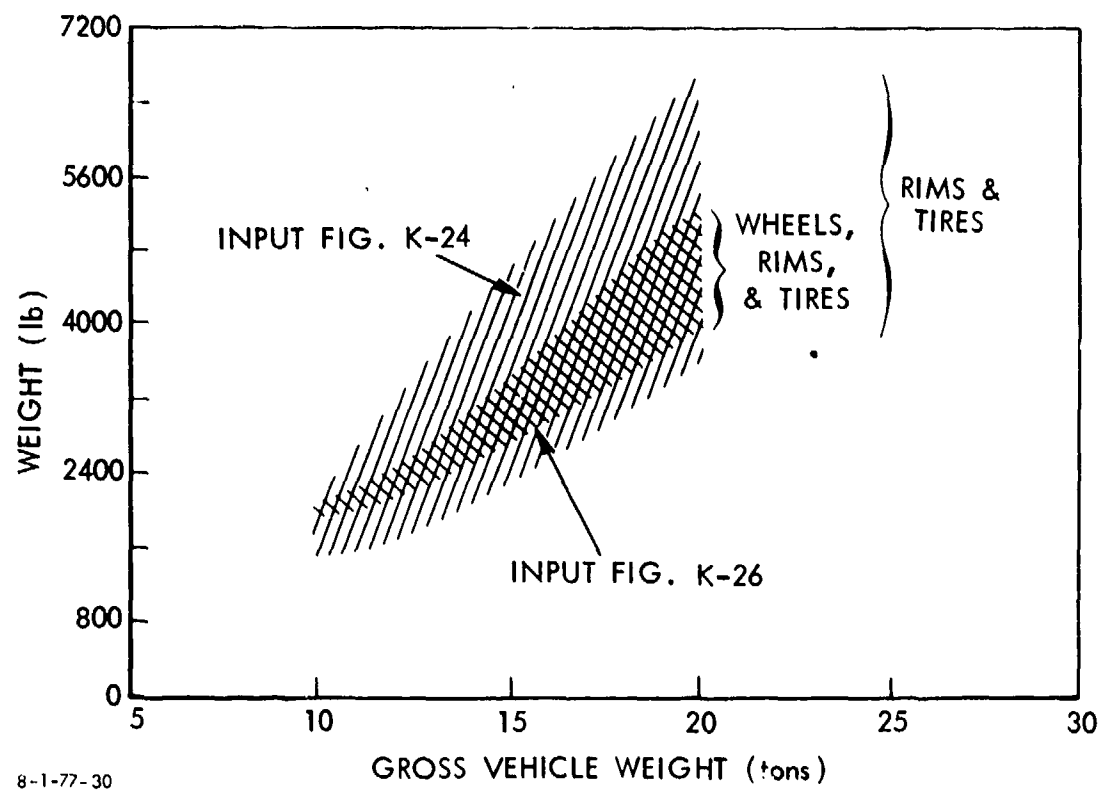
FIGURE K-28. Wheeled thruster weights for two sets of input data.

8-1-77-30

K-50

What is most important is that *the trend remains identical*. Consequently, the previously reached conclusion re undesirable growth of wheel thruster weight with GVW may be considered as corroborated. When one considers that the weight of the drive axles for all the tires of a wheel thruster may exceed the weight of the sprocket-idler drive for the track, the conclusion is further strengthened.

2. Interaction at the Soil-Wheel Interface

As reported in Ref. K-4, the fundamental equations reflecting the soil-vehicle relationship are the same for tires and tracks:

$$\left(\frac{\tau}{p}\right)_{max} = \frac{c}{p} + \tan\phi \quad , \tag{K-14}$$

where τ = thrust per unit area (psi)

$\quad$ p = ground pressure (psi)

$\quad$ c = coefficient of soil cohesion (deg)

$\quad$ ϕ = angle of soil friction (deg).

However, the tire-soil interaction is more complex, as the same inflation pressure may produce a rigid or elastic wheel, depending on the soil consistency, all other conditions being equal. Hence the soil thrust T_s for elastic tires which deflect in the given ground is approximated in the following general form:

$$\left(T_s\right)_{max} = 0.85\ell_1 b\left[c + (p_i + p_c)\tan\phi\right] \tag{K-15}$$

or for any values smaller than $(T_s)_{max}$:

$$T_s = 0.85\ell_1 b\left[c + (p_i + p_c)\tan\phi\right]\left[1 - \frac{K}{I_o\ell_1}\left(1 - e^{-I_o\ell_1/K}\right)\right]. \tag{K-16}$$

Denotations are shown in Fig. K-29: ℓ_1 and b are length and width of the ground contact area, respectively; p_i is inflation pressure and p_c is carcass stiffness pressure; d is tire diameter; δ is tire deflection under tire load W_{pt}; 0.85 is an average coefficient which corrects the rectangular ground contact area ℓ_1 x b for its ellipticity; value ℓ_2 may be neglected for low-pressure pneumatics.

From Fig. K-30, the ground contact area of a rigid tire may be assumed as

$$A = \ell_1' b$$

or

$$A = b\sqrt{dz_r - z_r^2} \qquad (K-17)$$

and T_s is expressed in terms of the above value as in Eq. K-16.

The method for determining ℓ_1 and other pertinent parameters of a tire is based on equations published a long time ago in Ref. K-2. These are repeated below in their basic form and in their operational sequence as follows:

$$F = \frac{1}{n + 1}$$

$$K' = \frac{F}{n + 2}$$

$$A = b(p_i + p_c)\left[\frac{F^2}{2} - K'\right]$$

$$B = \frac{W_{pt}F}{2}$$

$$z_e = \left[\frac{p_i + p_c}{k_c/b + k_\phi}\right]^{1/\eta}$$

$$(K-18)$$

8-1-77-31
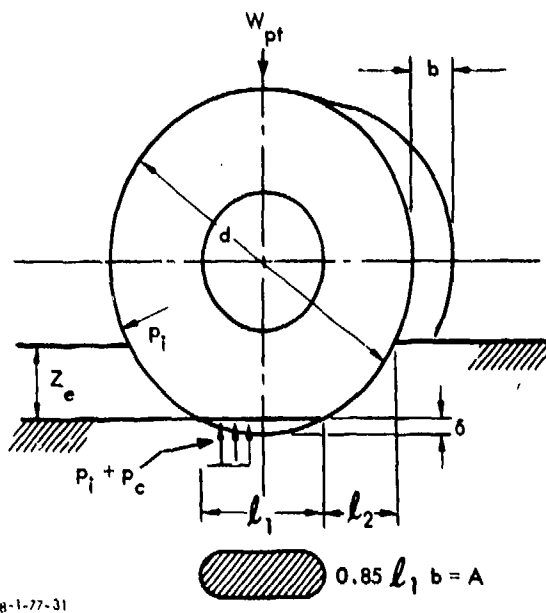
FIGURE K-29. Explanatory diagram for notation of Eq. K-16.

8-1-77-32
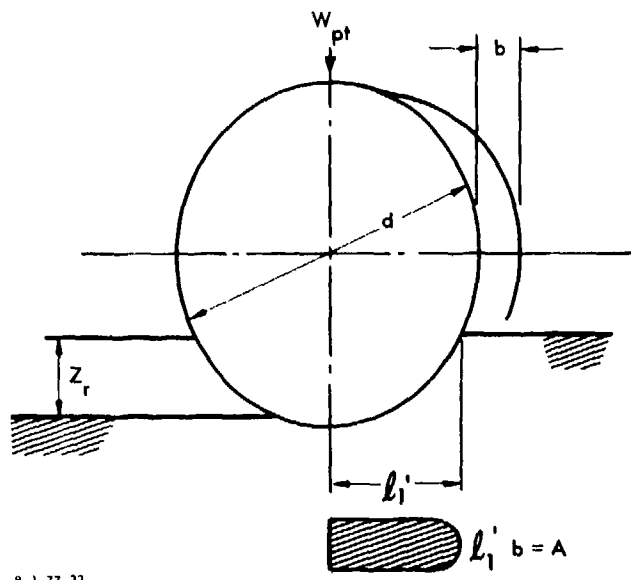
FIGURE K-30. Explanatory diagram for notation of Eq. K-17.

K-53

$$G = \frac{bz_e(p_1 + p_c)}{n + 1}$$

$$C = G(0.5d - 0.3333z_e)$$

$$\ell_2 = \frac{B - \sqrt{B^2 - 4AC}}{2A}$$

$$\ell_1 = \frac{W_{pt}}{b(p_1 + p_c)} - F\ell_2$$

$$\delta = 0.5d - \sqrt{(0.5d)^2 - (0.5\ell_1)^2}$$

(K-18 cont'd)

Considering Eqs. K-15 and K-17, the thrust of a rigid tire is, in a first approximation,

$$\left(T_s\right)_{max} = b\ell_1' c + \frac{W_{pt}}{b\ell_1'} \tan\phi \quad , \tag{K-19}$$

where

$$\ell_1' = \sqrt{dz_r - z_r^2} \quad , \tag{K-20}$$

as mentioned before. Rigid tire sinkage is:

$$z_r = \left[\frac{3W_{pt}}{(3 - n)\left[\dfrac{k_c}{\sqrt{dz_r - z_r^2}} + k_\phi\right] b \sqrt{d}} \right]^{\frac{2}{2n+1}} \tag{K-21}$$

Note that if $b < \sqrt{dz_r - z_r^2}$ the soil value k_c must be divided by the smaller ground contact dimension. Then, Eq. K-21 takes the form

K-54

$$z_r = \left[\frac{3W_{pt}}{(3-n)\left(\frac{k_c}{b}+k_\phi\right)b\sqrt{d}}\right]^{\frac{2}{2n+1}} \qquad . \qquad (K\text{-}22)$$

Sinkage of an elastic tire, as quoted in the group of Eqs. K-18, is:

$$z_e = \left[\frac{p_1 + p_c}{\frac{k_c}{b}+k_\phi}\right]^{\frac{1}{n}} \qquad .$$

Since it is not often known in advance whether a tire will behave like a rigid wheel or an elastic wheel, the critical inflation pressure $(p_1)_{crit}$ must be determined first:

$$(p_1)_{crit} = \frac{W_{pt}(n+1)}{b\sqrt{dz_r - z_r^2}} - p_c \qquad , \qquad (K\text{-}23)$$

where z_r is determined by Eq. K-21. For $(p_1)_{crit} < p_1$ the tire is rigid; for $(p_1)_{crit} > p_1$ the tire is elastic with deflection δ.

The compaction of motion resistance R_c (or drag D) may be expressed in accordance with the long-standing practice:

$$D \cong R_c = \frac{b\left(\frac{k_c}{b}+k_\phi\right)^{n+1}z_{e(or\ r)}}{n+1} \qquad . \qquad (K\text{-}24)$$

Actually, drag as considered here should include motion resistance due to carcass flexing and horizontal soil deformation (previously called bulldozing). However, computations show, and it will be referred to later in these pages, that the error

K-55

due to neglecting these values is not significant and does not change the basic conclusions. Accordingly, the drag/lift ratio D/W for a tire is assumed as follows:

$$\left(\frac{D}{W}\right)_{elastic} = \frac{a}{g}\left[1.05\right] + \frac{b\left(\frac{k_c}{b} + k_\phi\right)z_e^{n+1}}{W_{pt}(n+1)}$$

(K-25)

$$\left(\frac{D}{W}\right)_{rigid} = \frac{a}{g}\left[1.05\right] + \frac{b\left(\frac{k_c}{b} + k_\phi\right)z_r^{n+1}}{W_{pt}(n+1)}$$

where the figure 1.05 is an empirical coefficient that takes care of inertial effects of rotating masses of medium-weight trucks.

3. Power for Vehicle Acceleration and/or Hill Climbing

The power-acceleration-slip curves for tires are similar to those for tracks analyzed in conjunction with Eqs. K-5 through K-7.

The equations quoted heretofore thus enable one to make a direct comparison between tracks and tires under similar, if not identical, conditions. This is explained in the following numerical examples. As in Section B-3, assume two soil types:

Sand: $K = 1$, $k_c = 0$, $k_\phi = 2$, $n = 0.8$, $c = 0$, $\phi = 35°$.

Agricultural Soil: $K = 1$, $k_c = 6$, $k_\phi = 4$, $n = 0.5$, $c = 0.1$, $\phi = 20°$.

Also assume a Goer-type vehicle of GVW = 20 tons with *four driven tires*, at $p_i + p_c = 14.5$ psi. Tire diameter is 79.5 in., and tire width b is 25 in. The corresponding tracked vehicle has GVW = 20 tons, an assumed track width b = 20 in., and p = 14.5 i, and the length ℓ of the ground contact area is

$$\ell = \frac{20 \times 2200}{20 \times 14.5 \times 2} \cong 76 \text{ in.}$$

As shown in Section B-3, for the *track*

$$\left(\frac{a}{g}\right)_{\text{sand}}^{\text{track}} = \frac{\tan 35}{1.3} \left[1 - \frac{1}{76 i_o} \left(1 - e^{-76 i_o} \right) \right]$$

$$- \frac{2 \times 20 \times 14.5^{2.25}}{20 \times 2200 \times 1.8 \times 8^{1.25} \times 13} - \frac{0.05}{1.3} \ .$$

(K-26)

Combining Eqs. K-16 and K-25 for an elastic* tire, one obtains

$$\frac{4 \times 0.85 \ell_1 b (p_i + p_c) \tan \phi}{W} \left[1 - \frac{K}{i_o \ell_1} \left(1 - e^{-i_o \ell_1 / K} \right) \right]$$

$$- \frac{a}{g} \left[1.05 \right] - \frac{4 b \left(\frac{k_c}{b} + k_\phi \right)^{n+1} z_e}{W(n+1)} = 0 \ .$$

But $4 \times 0.85 \ell_1 b (p_i + p_c) = W$, and hence

$$\left(\frac{a}{g}\right)_{\text{sand}}^{\text{tire, elastic}} = \frac{\tan 35}{1.05} \left[1 - \frac{1}{i_o \ell_1} \left(1 - e^{-i_o \ell_1} \right) \right]$$

$$- \frac{4 \times 25 \times 8 \times z_e^{1.8}}{1.05 \times 20 \times 2200 \times 1.8} \ .$$

(K-27)

In this case, length ℓ_1 of the tire-ground contact area has to be determined first. To this end Eqs. K-18 are processed as shown, in their sequence:

---

*It is known from experience that a tire at 14.5 psi and with a 5-ton load is elastic in sand.

$$F = \frac{1}{1.8} = 0.5555$$

$$K = \frac{0.5555}{2.8} = 0.1984$$

$$A = 25 \times 14.5 \left(\frac{0.5555^2}{2} - 0.1984 \right) = 15.9898$$

$$B = \frac{20 \times 2200}{4} \times \frac{0.5555}{2} = 3055.25$$

$$z_e = \left(\frac{14.5}{8} \right)^{1.25} \cong 2.1 \text{ in.}$$

$$G = \frac{25 \times 2.1 \times 14.5}{1.8} = 422.92$$

$$C = 422.92 \left(\frac{79.5}{2} - 0.3333 \times 2.1 \right) = 16515.05$$

$$\ell_2 = \frac{3055.25 - \sqrt{3055.25^2 + 4 \times 15.9898 \times 16515.05}}{-2 \times 15.9898} = 5.26$$

$$\ell_1 = \frac{20 \times 2200}{4 \times 25 \times 14.5} - 0.5555 \times 5.26 \cong 28 \text{ in.}$$

Accordingly, Eq. K-27 for the tired vehicle takes the following form:

$$\left(\frac{a}{g} \right)_{sand}^{tire,elastic} = 0.6666 \left[1 - \frac{1}{28\ell_o} \left(1 - e^{-28\ell_o} \right) \right] - 0.0366 \quad .$$

(K-28)

For the corresponding tracked vehicle:

$$\left(\frac{a}{g}\right)^{\text{track}}_{\text{sand}} = 0.5385 \left[1 - \frac{1}{761_o}\left(1 - e^{-761_o}\right)\right] - 0.0503 . \qquad \text{(K-29)}$$

The interaction of Goer tires with sand is plotted in Fig. K-31 against the power required to produce the given acceleration (a/g), utilizing the total sand thrust (Eq. K-5).

For a wheel-versus-track comparison, a similar curve is plotted in Fig. K-31 for the *corresponding* tracked vehicle (Eqs. K-5 and K-29).

In a similar manner, the maximum attainable acceleration in sand is plotted versus slip in Fig. K-32. The higher values for the tired Goer vehicle, though paradoxical, should not be considered unreal. The intersecting curves in Fig. K-32 are mainly due to the assumption of different coefficients of inertia of rotating masses for tracks and wheels: 1.3 and 1.05, respectively. In addition, tire carcass stiffness resistance and bulldozing resistance were not considered, though "internal" track rolling resistance was (Eq. K-26, value 0.05). However, the outcome is not much affected by the inaccuracies considered here. Trial computations are also plotted as dashed lines in Fig. K-32 to show the influence of tire stiffness and horizontal sand deformation. The influence is small, and it appears fair to assume that in sand both a tire and an equivalent track will pull the same and will accelerate in the same fashion. The small discrepancy in their behavior, visible in Fig. K-32, is probably due more to the error involved in the method, as discussed in the literature, than to the actual performance of the vehicles. This theoretically explains why the oil industry does not use tracks in the desert, as tires are less expensive than tracks in overall cost, and yet they do the same job.
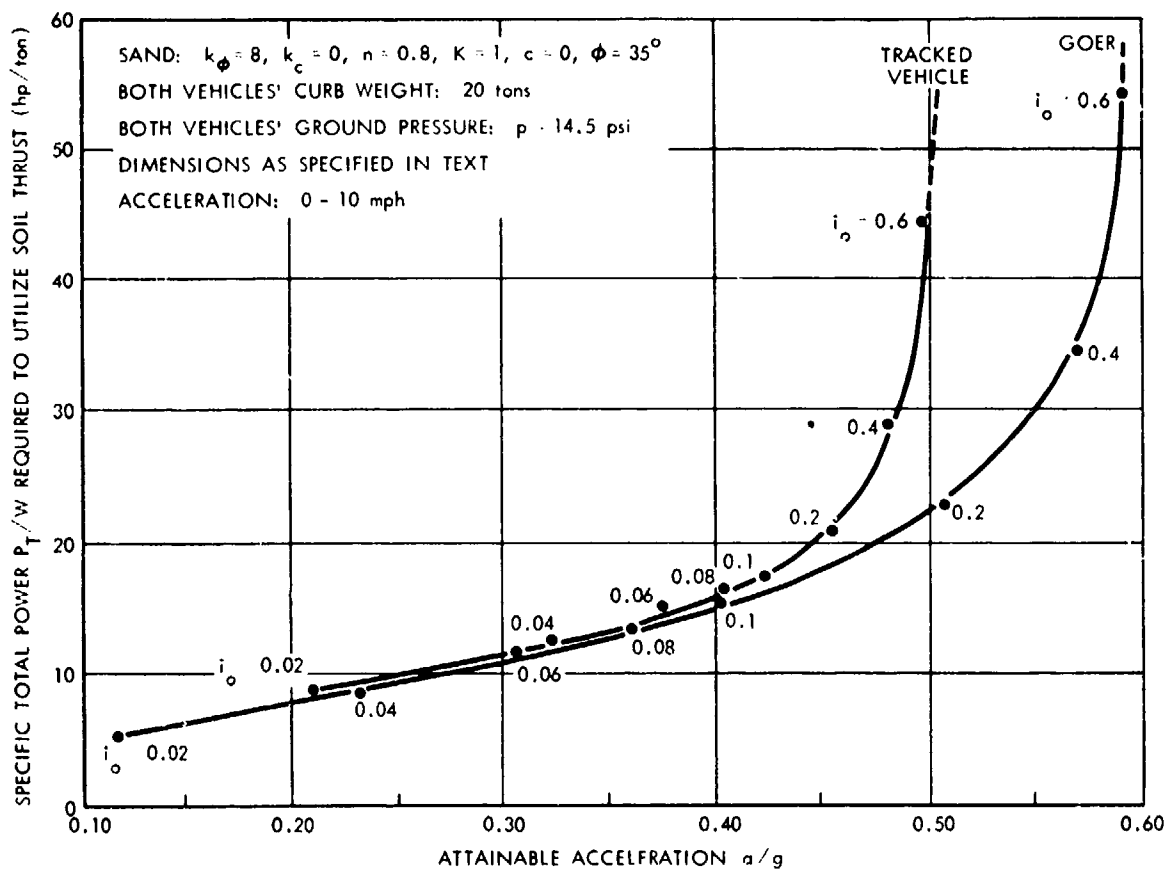
FIGURE K-31. Specific total power required to utilize soil thrust versus attainable acceleration, tracked vehicle and Goer.

K-60
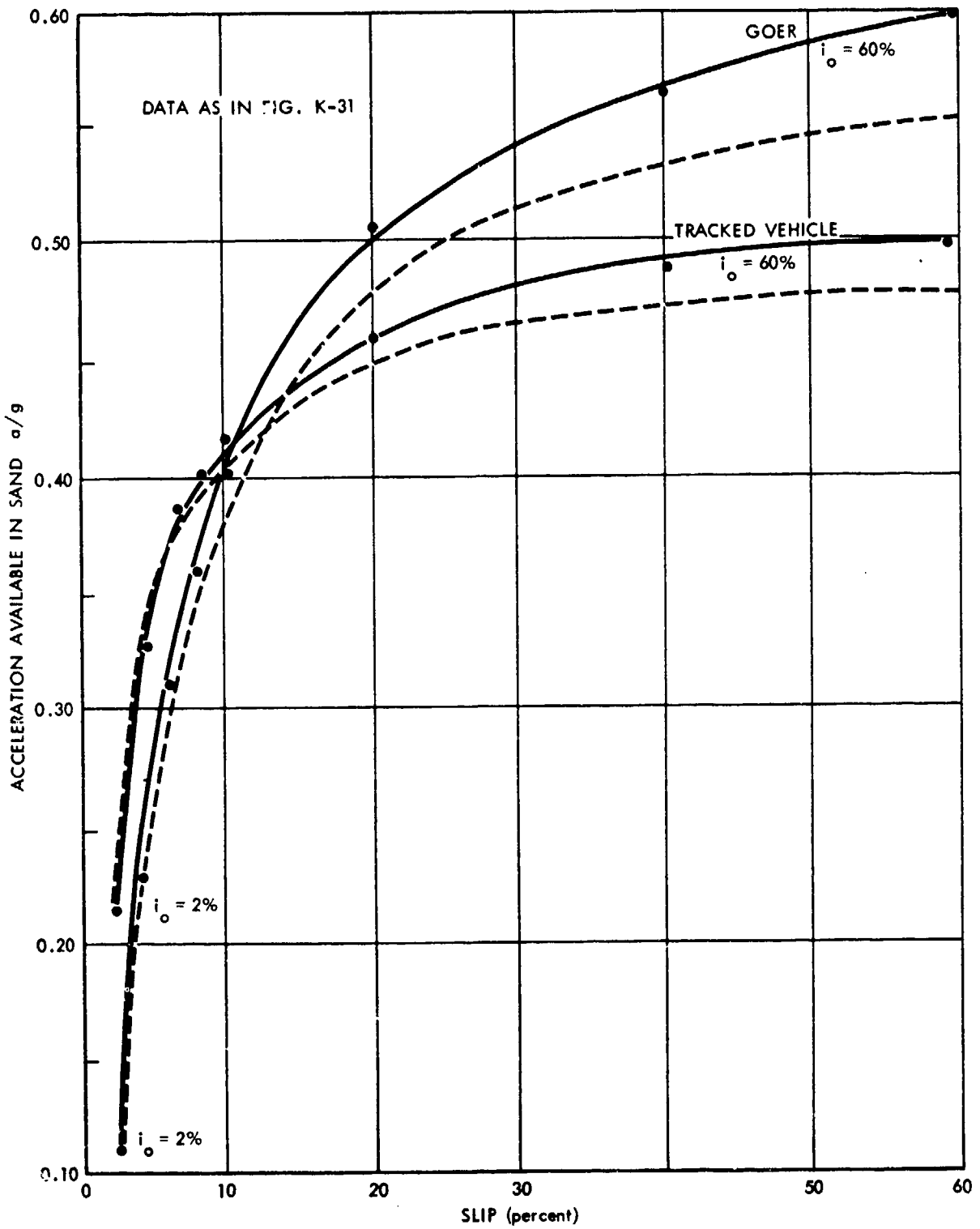
FIGURE K-32. Acceleration available in sand versus slip, tracked vehicle and Goer. (Dashed lines reflect influence of tire stiffness and horizontal sand deformation.)

K-61

Using the same method, one may evaluate tracks and tires in a soft agricultural soil. Accordingly, for the *track* (Eqs. K-3, K-4) one has:

$$\left(\frac{a}{g}\right)^{track}_{ag.soil} = \frac{\frac{c}{p} + \tan\phi}{1.3}\left[1 - \frac{K}{i_o\ell}\left(1 - e^{-i_o\ell}\right)\right]$$
$$- \frac{2bp^{\frac{n+1}{n}}}{1.3W(n+1)\left(\frac{k_c}{b} + k_\phi\right)^{1/n}} - \frac{0.05}{1.3}$$

or, upon substituting the soil values from the first paragraph of Section C-3,

$$\left(\frac{a}{g}\right)^{track}_{ag.soil} = 0.2853\left[1 - \frac{1}{76i_o}\left(1 - e^{-76i_o}\right)\right] - 0.1922 . \quad (K-30)$$

Now it is safer to check whether the tire behaves like a rigid or an elastic wheel. Thus, from Eq. K-22 one has:

$$z_r = \left[\frac{3 \times 20 \times 2200}{4 \times 2.5\left(\frac{6}{25} + 4\right) \times 25 \sqrt{795}}\right]^{\frac{2}{0.5\times2+1}} \cong 13.97 \text{ in.}$$

The length of the ground contact area ℓ'_1 (Fig. K-32) is:

$$\ell'_1 = \sqrt{79.5 \times 13.97 - 13.97^2} \cong 30.26 \text{ in.}$$

Since $b = 25$ in., as assumed in the equation for z_r smaller than ℓ'_1, the z_r calculation is valid. Otherwise, it would have to be reiterated for ℓ'_1, i.e., for k_c/ℓ'_1 instead of k_c/b. Hence, from Eq. K-23 one has:

$$\left(p_1\right)_{crit} = \frac{20 \times 2200}{4 \times 25 \times 30.26} - 3^* = 18.81 \text{ psi} \quad .$$

Since $p_1 = 14.5 - 3 = 11.5$ psi is smaller than $(p_1)_{crit} = 18.81$ psi, the tire is *elastic*. Accordingly, from Eq. K-18 one has:

$$F = \frac{1}{0.5 + 1} = 0.6666$$

$$K_1' = \frac{0.6666}{0.5 + 2} = 0.2666$$

$$A = 25 \times 14.5 \left(\frac{0.6666^2}{2} - 0.2666\right) = -16.1030$$

$$B = \frac{20 \times 2200 \times 0.6666}{4 \times 2} \cong 3666.3$$

$$z_e = \left[\frac{14.5}{\frac{6}{25} + 4}\right]^{1/0.5} \cong 11.7 \text{ in.}$$

$$G = \frac{25 \times 11.7 \times 14.5}{1.5} \cong 2827.5$$

$$C = 2827.5(0.5 \times 79.5 - 0.3333 \times 11.7) \cong 101366.98$$

$$\ell_2 = \frac{3666.3 - \sqrt{3666.3^2 + 4 \times 16.103 \times 101366.98}}{-2 \times 16.103} \cong 25 \text{ in.}$$

$$\ell_1 = \frac{20 \times 2200}{4 \times 25 \times 14.5} - 0.6666 \times 25 \cong 13 \text{ in.}$$

Considering Eq. K-28 and including the soil values, one obtains:

$$\left(\frac{a}{g}\right)_{ag.\ soil}^{tire,elastic} = \frac{\frac{0.1}{14.5} + \tan 20}{1.05}\left[1 - \frac{1}{13i_o}\left(1 - e^{-13i_o}\right)\right]$$
$$- \frac{4 \times 25\left(\frac{6}{25} + 4\right) \times 11.7^{1.5}}{1.5 \times 1.05 \times 20 \times 2200}$$

---

*The value of 3 psi is the approximate carcass stiffness, adapted from manufacturers' catalogs.

or

$$\left(\frac{a}{g}\right)^{\text{tire,elastic}}_{\text{ag.soil}} = 0.3532\left[1 - \frac{1}{131_o}\left(1 - e^{-131_o}\right)\right] - 0.2448 \ . \ (K-31)$$

Both Eqs. K-30 and K-31 are plotted in Figs. K-33 and K-34.
Here, the tire is definitely inferior to the track, as one may
expect intuitively. It is obvious, then, that a comparison
between a track and the corresponding configuration of wheels
is inevitably affected by the soil values K, k_c, k_ϕ, c, ϕ, and
n. Thus, comparisons that do not consider soil parameters may
be totally misleading, as exemplified in Figs. K-31 through
K-34.

Note that an increase of Goer inflation pressure to approxi-
mately 18.8 psi would immobilize the vehicle in agricultural
soils since the tires would behave as *rigid wheels*. Hence,
tire pressure control without considering soil values may be more
damaging than helpful.

D. GENERAL CONCLUSIONS

Equations K-1, K-2, and K-3 show that the soil thrust
which may be utilized by the thruster is composed of two parts:

    1. The "frictional" portion containing "$\tan\phi$"

    2. The "cohesive" portion which incorporates "c."

Note that the magnitude of available thrust depends on ground
pressure P (Eq. K-1) and/or on ground contact area $(w - w')\ell'$
and vehicle weight W. These values quantify thruster-soil
interaction. In the case of purely frictional soils (dry sand,
sandy loam, etc.), one has c = 0, and hence

$$\left(\frac{\tau}{P}\right)_{\text{max}} = \tan\phi \quad \text{or} \quad \left(T_S\right)_{\text{max}} = W\tan\phi \ ,$$
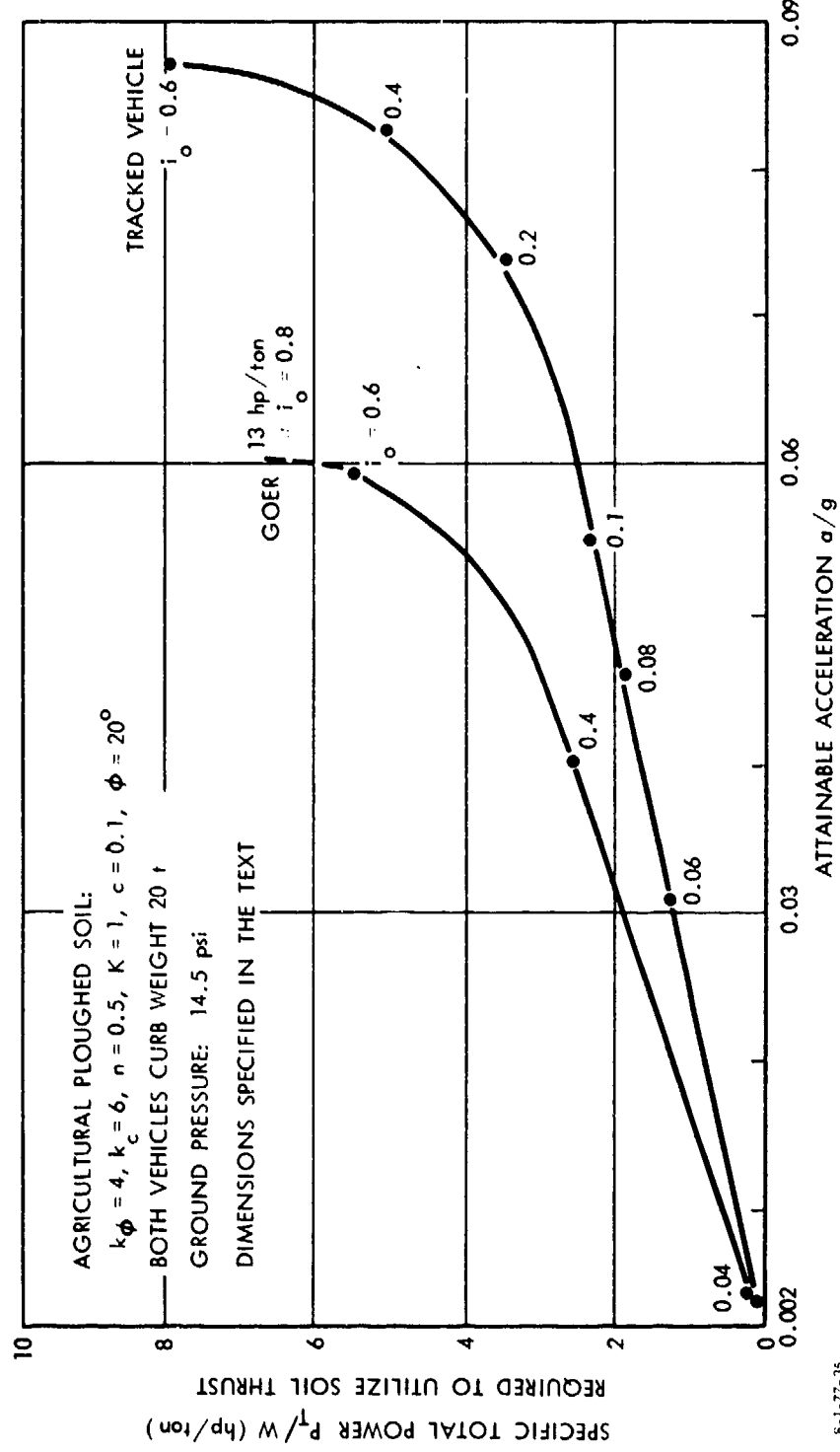
FIGURE K-33. Specific total power P_T/W required to utilize soil thrust versus attainable acceleration.

8-1-77-35
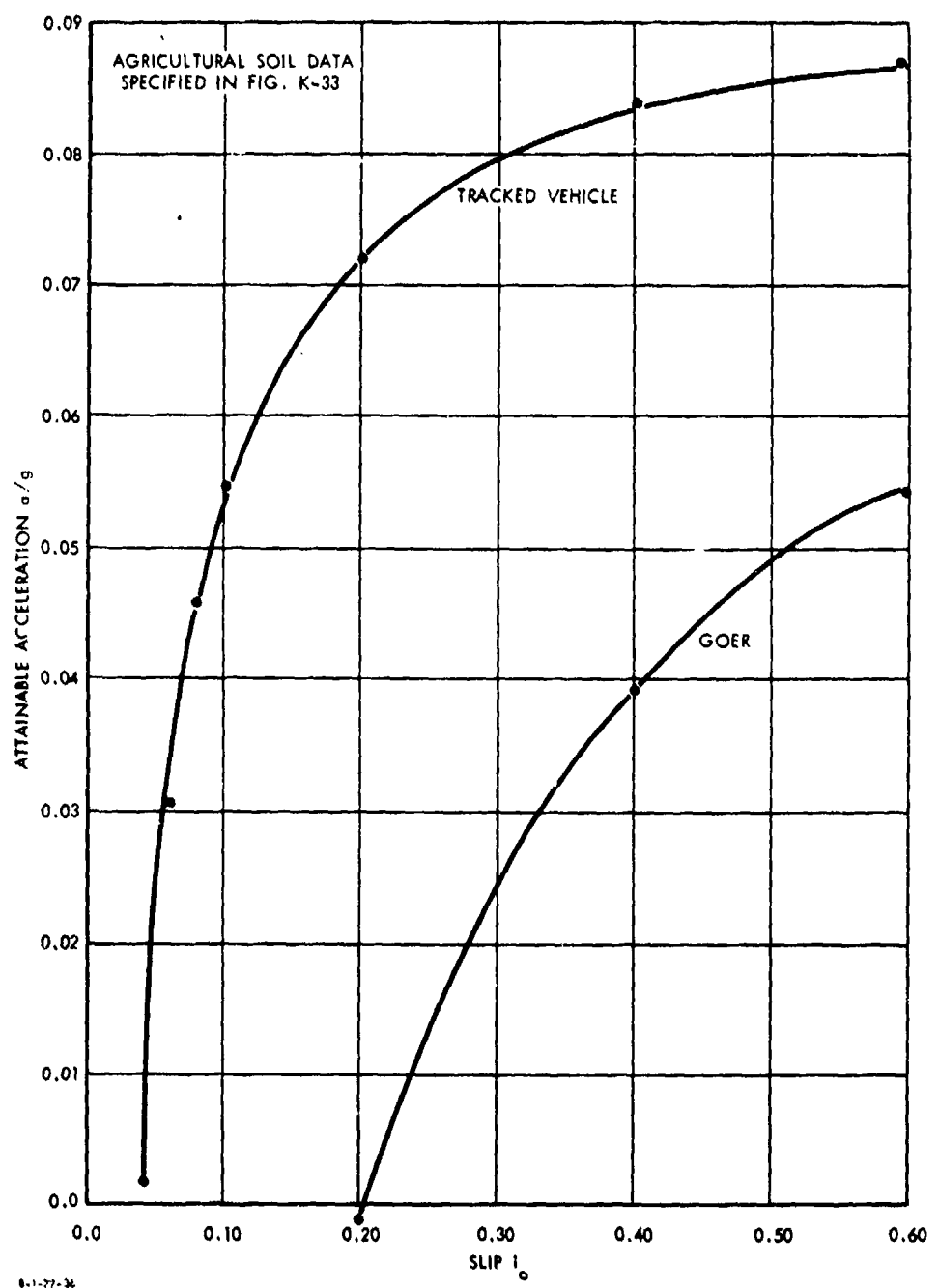
FIGURE K-34. Attainable acceleration versus slip.

K-66

i.e., the size of the ground contact area of the thruster does not enter this relationship. However, the drag/lift ratio is affected by ground contact area through (w − w') and/or ℓ', inasmuch as they affect the motion resistance

$$\frac{(w - w')\ P^{n+1/n}}{W(n + 1)\left(\dfrac{2k_c}{w - w'} + k_\phi\right)^{1/n}}\ .$$

In general, k_c is very small. The effect of motion resistance is not strong upon obtaining high accelerations in sandy soils provided that there is enough power in the engines. However, in purely cohesive soils (wet clay, clayey loam, etc.), $\phi = 0$, the acceleration attainable depends solely on low ground pressure, i.e., on large ground contact areas [ℓ' (w − w')] of the thrusters or on low vehicle weight.

We have thus two mutually conflicting trends, whereby drag/lift and accelerating thrust depend on the one hand primarily on vehicle weight alone (i.e., the frictional portion), and on the other hand primarily on ground pressure (the cohesive part). This appears to make a case for two types of vehicles: one for highly frictional soils (desert, dry sandy loams, etc.) and the other for highly cohesive soils (wet clayey loams). Thus it may be possible in some cases to build "desert vehicles" on wheels, since the size of the thruster has a relatively small effect, while "jungle vehicles" would have to be equipped with tracks, since large thrusters are required to get low ground pressure. Mixes of these two types could possibly improve cost-effectiveness as compared to the present trend, where one type of a thruster is expected to operate in all soils at all times.

This brief discussion appears to indicate that any future technological "breakthroughs" should aim at better adaptation of the thruster to terrain conditions following the quantitative criteria discussed above.

K-67

The importance of the problem cannot be overlooked when tires are considered versus tracks. As emphasized again by a numerical example for two "equivalent" (i.e., the same gross weight and ground pressure) vehicles, the tire and track performances in sand are practically identical. Since tires are more economic than tracks in the desert, tires should be used unless prohibitive loads that enter performance predictions dictate otherwise. In a soft ground such as moist ploughed agricultural soil (soft layer depth larger than 11-12 in.) tracks perform much better than tires.

Between sand and the above-mentioned soil there is an array of terrain conditions in which tracks and wheels may behave differently.

It has also been shown that without soil measurements as indicated in the text, the selection of the optimum of vehicle parameters, including in particular the right inflation pressure for tires, is almost totally impossible.

Similarly, the absolutely necessary slip control which would save fuel and energy cannot be properly adjusted unless the shear-slip properties of the ground are determined.

In sum, one may conclude that the optimization of vehicles depends on the availability of soil parameters.

It is up to the user, not the designer, to quantitatively measure the terrain, and to specify in those terms, where, when, and how a vehicle is expected to operate.

To optimize vehicle design such terrain and mission definitions are essential.

REFERENCES, APPENDIX K

K-1. M.G. Bekker, <u>Theory of Land Locomotion</u>, University of Michigan Press, Ann Arbor, 1956.

K-2. M.G. Bekker, <u>Off-the-Road Locomotion</u>, University of Michigan Press, Ann Arbor, 1960.

K-3. M.G. Bekker, <u>Introduction to Terrain-Vehicle Systems</u>, University of Michigan Press, Ann Arbor, 1969.

K-4. Institute for Defense Analyses, <u>Survey of Advanced Propulsion Systems for Surface Vehicles</u>, IDA Paper P-1073 F.R. Riddell, January 1975. (AD A011848)

APPENDIX L

THRUSTERS FOR HIGH-SPEED OCEANGOING SHIPS

A. Douglas Carmichael

CONTENTS

APPENDIX L
THRUSTERS FOR HIGH-SPEED OCEANGOING SHIPS
A. Douglas Carmichael

A. INTRODUCTION

At high forward speeds conventional propellers are subject to cavitation, which results in performance deterioration and blade damage. It was observed that performance could be enhanced and damage could be eliminated by utilizing special propeller blade shapes. At high speeds, with these special designs, a controlled cavity would be formed which did not collapse on the blade surface. The supercavitating blades are wedge shaped with sharp leading edges to encourage the cavity formation. These propellers have been widely investigated both theoretically and experimentally and have been used on various high-speed vehicles.

The other type of thruster that has found acceptance for high-speed ships is the waterjet system in which the water is taken on board via a special inlet and then pumped out at high velocity through a jet nozzle, usually placed above the water surface. The waterjet system could be used at any speed, but for ships of ocean-going size it is appreciably less efficient than a conventional propeller at speeds below where cavitation occurs. It is competitive, however, with the propulsion efficiency that has been reached with supercavitating propellers.

There have been investigations of other types of thrusters which use air or air/water mixtures as the propulsion medium. At speeds below 80 to 100 knots, however, it is difficult for such devices to meet the mass flow/ejector velocity requirements for competitive propulsive efficiency. It would appear that

L-3

using water as the propulsion medium has an inherent advantage in this speed regime. The characteristics of supercavitating propellers and waterjet systems are described in this appendix as typical of such thrusters.

B. SUPERCAVITATING PROPELLERS

1. Performance Prediction

Design procedures have been developed for supercavitating propellers, although the accuracy of methods of predicting supercavitating propeller performance are not as well established as the methods for conventional propellers. However, approximate methods may be utilized to provide acceptable performance pre- dictions, which include the influence of stress levels in the propeller blades on propulsion efficiency.

From momentum considerations the ideal propulsive efficiency of any propeller (conventional or supercavitating) can be ex- pressed as

$$\eta = \frac{2}{1 + (C_T + 1)^{1/2}} \ , \qquad (L-1)$$

where C_T = thrust coefficient = $\text{thrust}/\frac{1}{2}\rho V_A^2 \ \pi/4 \ D^2$

ρ = density

V_A = velocity of advance

D = propeller diameter.

The propulsive efficiency of supercavitating propellers is lower than this ideal efficiency because of the presence of the cavity flow on the blade surface and because of fluid friction. Since the size of the cavity springing from the blade leading edge must be minimized for good efficiency, yet the blade surface must not pierce the cavity, the thickness of the blade (and hence bending stress in the blade) is an important parameter.

Performance predictions have been provided in Ref. L-1 for supercavitating propellers. The method shows propulsive efficiency may be represented as

$$\eta_P = f(C_T, \lambda, \bar{\sigma}) \ ,$$

where C_T = thrust coefficient, thrust$/\frac{1}{2}\rho V_A^2 \ \pi/4 \ D^2$

$\quad \lambda$ = advance ratio, $V_A/\pi \ n \ D$

$\quad n$ = rotational speed, rps

$\quad \bar{\sigma}$ = stress coefficient, design stress$/\frac{1}{2}\rho V_A^2$

The maximum efficiency points for the predictions given in Ref. L-1 for well-designed four-bladed propellers are presented in Table L-1.

TABLE L-1. PREDICTED PERFORMANCE FOR SUPERCAVITATING PROPELLER*

$\bar{\sigma}$		C_T		
		0.05	0.1	0.2
100	η_P	0.66	0.61	0.525
100	λ	0.5	0.45	0.34
200	η_P	0.71	0.66	0.58
200	λ	0.5	0.45	0.36
500	η_P	0.75	0.705	0.63
500	λ	0.48	0.42	0.34

*From Ref. L-1.

By using these data, the propulsive efficiency, dimensions, and revolutions per minute of supercavitating propellers can be predicted for prescribed values of propeller input power and allowable stress.

L-5

2. Weight Estimation

The weight of high-performance propellers in titanium has been presented in Ref. L-2 as:

$$W_P = 6.5 \, D^3, \text{ lb} \quad , \tag{L-2}$$

where D is the propeller diameter.

The weight, propulsive efficiency, and revolutions per minute for supercavitating propellers are presented in Table L-2 for a propeller power of 20,000 hp and a 25,000-lbf/in.^{2} stress level.

TABLE L-2. PREDICTED CHARACTERISTICS FOR
SUPERCAVITATING PROPELLERS
(20,000 hp, 25,000 lbf/in.^{2})

Velocity V_A, knots		C_T		
		0.05	0.1	0.2
50	η_P	0.75	0.705	0.63
	Weight/hp	2.06	0.665	0.197
	rpm	183	305	564
80	η_P	0.71	0.66	0.58
	Weight/hp	0.242	0.076	0.022
	rpm	567	925	1744
110	η_P	0.66	0.61	0.525
	Weight/hp	0.05	0.016	0.0044
	rpm	1317	2153	4344

The propulsive efficiencies are expected to be independent of power level, except perhaps at very low powers weight/hp is proportional to $(\text{hp})^{1/2}$ and rpm is proportional to $(\text{hp})^{-1/2}$.

The data in Table L-2 is presented graphically in Fig. L-1.

The velocity of advance V_A for propeller designs is slower than the vehicle speed because of the boundary layer growth on the vehicle and the propeller boss. Furthermore, the efficiency of the propeller may be changed (increased or decreased) by the retarded flow. The corrections to speed of advance and propulsive efficiency depend on the details of the ship design. Such corrections can be predicted for conventional ships but there is uncertainty with high-speed or unconventional ships.

## C. WATERJET PROPULSION SYSTEMS

1. System Description

In a waterjet system the water is taken on board via a special inlet and ejected at high velocity from a jet nozzle. Two types of inlets have been used:

1. Ram or pitot inlet, where the water is taken into a streamlined nacelle that is suspended on a strut from the vehicle

2. Flush inlet, where the water passes into an opening in the side or the bottom of the vehicle.

The ram inlet has been used for hydrofoil ships, and the flush inlet has been applied to surface-effect ships and planing boats. The flush inlet system is more attractive at high speeds because the drag of the flush system is smaller than the drag of the nacelle of the ram inlet.

A diagrammatic view of the flush inlet is shown in Fig. L-2. The propulsion system consists of the inlet, with variable geometry ramp, a diffuser leading to pump, and a jet nozzle downstream of the pump. The pump is driven by an engine via a gear box.

In most applications the design of the system is a compromise between design and off-design limitations. In particular, the

L-7

9-8-77-1
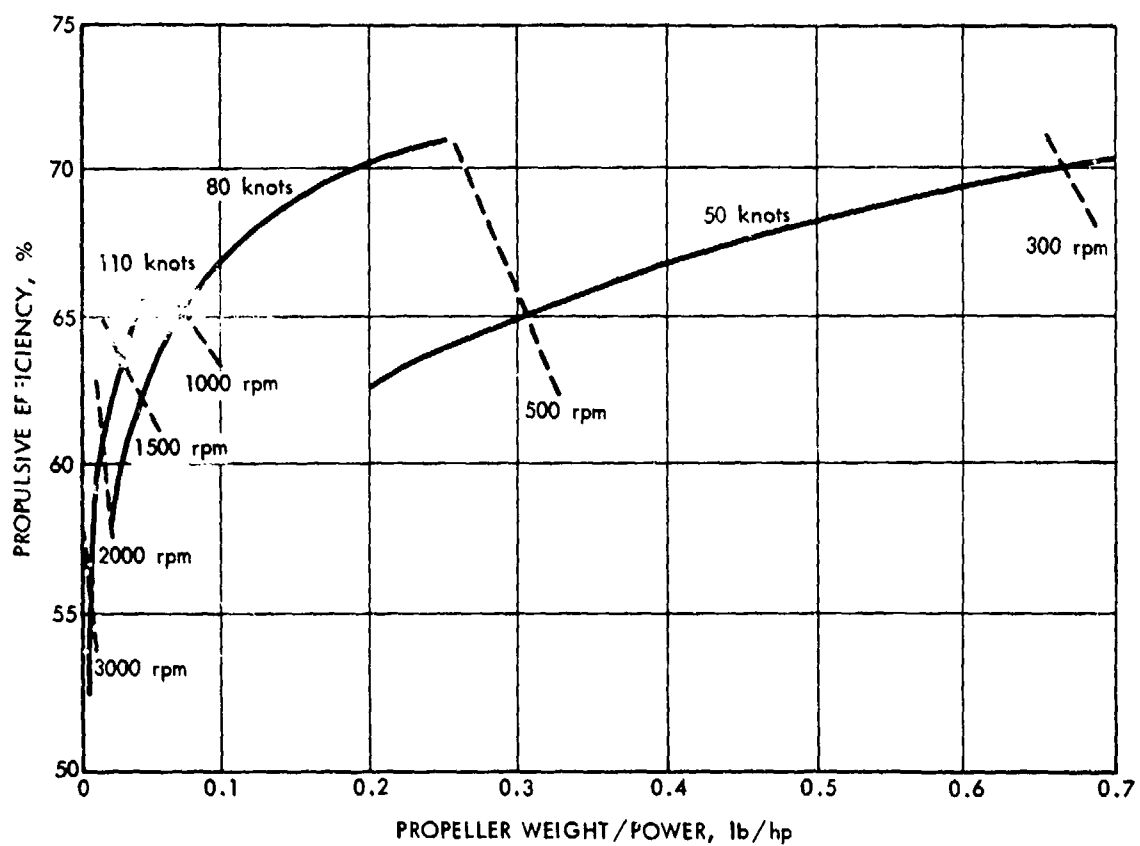
FIGURE L-1. Propulsive efficiency, weight, and revolutions per
minute of supercavitating propellers (20,000 hp).

L-8

most serious cavitation conditions normally occur at a speed much lower than the high-speed cruise condition. The pump of the waterjet system is normally designed at the most serious cavitation condition and hence operates slightly off peak efficiency at the high-speed cruise. However, in a system study this feature of detailed design may be neglected.
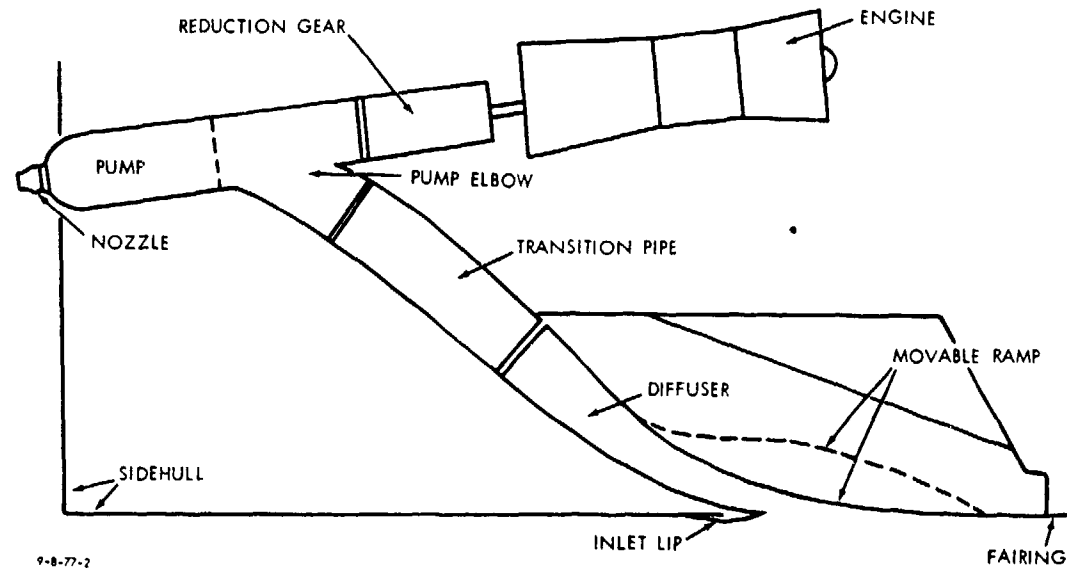

FIGURE L-2. Waterjet system, flush inlet.

In this study the propulsive coefficient and the weight per unit power of the waterjet propulsion system with a flush inlet is determined for a range of design conditions. The propulsive coefficient is calculated for very low internal losses and external drag values while the weights of the various components are based on best estimates for the components.

2. **Momentum and Energy Considerations**

In a waterjet system thrust is produced by increasing the momentum of the water passing through the unit. The thrust is given by

$$T = \rho Q(V_j - V_m) \quad , \tag{L-3}$$

where V_j is the velocity of the jet

V_m is the velocity of the water entering the unit

ρ is the density

Q is the volume flow rate.

The velocity of the water entering the unit V_m should be measured at a station where the local pressure is that corresponding to the depth. For a ram inlet the velocity V_m is the velocity of the ship V_o, while for the flush inlet the velocity V_m is reduced by the loss of momentum of flow entering the inlet from the boundary layer of the ship. In general $V_m = CV_o$, where C is close to unity for most applications. The thrust of the unit may be written as

$$T = \rho Q(V_j/V_o - C) \, V_o \quad . \tag{L-4}$$

In steady-state operation the thrust is equal to the total resistance of the vehicle. The total resistance has two components: the resistance R of the ship and the drag D due to the waterjet system. The resistance of the ship is therefore the thrust minus the inlet drag:

$$R = T - D \quad . \tag{L-5}$$

The drag of a body is usually expressed in terms of the drag coefficient as

$$\text{Drag} = C_D \, \frac{1}{2} \, \rho \, V_o^2 \, A \quad ,$$

where C_D is the drag coefficient

A is a representative area.

L-10

However, it is convenient for waterjet systems to introduce a modified form of this equation:

$$\text{Drag} = D = C_D \frac{1}{2} \rho Q V_o \ . \tag{L-6}$$

This is an acceptable form of the equation because the volume flow Q is equivalent to a velocity times an area.

Equations L-4 through L-6 may be combined to give

$$R = \rho Q V_o [V_j / V_o - C - 1/2 \ C_D] \ . \tag{L-7}$$

The power required to drive the pump of the waterjet system is

$$P = \rho Q g \Delta H / \eta_P \ ,$$

where P is power

Q is the volume flow

ΔH is the pump head rise

η_P is the pump efficiency.

The pump head rise ΔH has three components:

1. The jet velocity head
2. The pressure recovery in the inlet and internal ducting, $\Delta H_{recovery}$
3. The height of the jet above sea level, h_j.

The head recovery of the inlet and internal ducting is largely associated with reducing the velocity of the water from the inlet value V_m to that required at inlet to the pump (about 20 ft/sec). It is convenient to express this recovery as a form of diffuser efficiency:

L-11

$$\Delta H_{recovery} = \eta_D \frac{V_m^2}{2g} \; .$$

Hence, the head rise in the pump is

$$\Delta H = \frac{V_j^2}{2g} - \eta_D \frac{V_m^2}{2g} + h_j = \frac{V_o^2}{2g}\left[\left(\frac{V_j}{V_o}\right)^2 - \eta_D C^2 + \frac{2gh_j}{V_o^2}\right] \; . \qquad (L-8)$$

The propulsive coefficient for the complete waterjet system is defined as

$$PC = \frac{\text{Effective power}}{\text{Engine power}} = \frac{RV_o}{\text{Pump power}/\eta_g} \; , \qquad (L-9)$$

where η_g is the mechanical efficiency of the gears:

$$PC = \frac{RV_o}{\rho Qg\Delta H/\eta_g \eta_P} = \eta_g \eta_P \frac{RV_o}{\rho Qg\Delta H} \; . \qquad (L-10)$$

The expressions for R and ΔH may be substituted from Eqs. L-7 and L-8, respectively, into Eq. L-10 to give

$$PC = \frac{2\eta_g \eta_P \left(\frac{V_j}{V_o} - C - \frac{1}{2} C_D\right)}{\left[\left(\frac{V_j}{V_o}\right)^2 - \eta_D C^2 + \frac{2gh_j}{V_o^2}\right]} \; . \qquad (L-11)$$

The values of propulsive coefficient have been calculated for a range of values of jet velocity/ship velocity V_j/V_o. The published values of drag coefficients for flush inlets are in the range 0.08-0.15. The value assumed for this study was

L-12

0.07. The internal efficiency of the flush inlet systems varies between 0.75 at low speed to 0.5 at high speed. The value selected here was the pressure recovery of a good diffuser, 0.75. The elevation of nozzle above the water line, h_j, has a very small influence on PC and was neglected. The product of pump efficiency and gear efficiency was taken to be 0.92.

The calculated values of PC using the design assumptions are presented in Table L-3.

TABLE L-3. CALCULATED VALUES OF PROPULSIVE COEFFICIENT

V_j/V_o	1.3	1.55	1.7	1.9	2.1
PC	0.519	0.570	0.572	0.556	0.535

There is a maximum value of propulsive coefficient occurring in the region of $V_j/V_o = 1.7$. This value can be predicted by differentiating Eq. L-11 with respect to V_j/V_o and equating to zero. At the present time, well-designed waterjet systems are believed to have a PC value of about 0.5.

3. Waterjet System Weight

The components of the system are:

- Inlet and ducting
- Pump
- Reduction gear
- Engine.

The flush inlet has been assumed for this study. The weight of the inlet, including the water up to the pump, has been given as

$$W_I = K_I Q^{1.5} \ . \tag{L-12}$$

L-13

The constant K_I varies between 4 and 10. The value of 4 was selected for K_I. The pumps for waterjet systems are usually axial-flow with an inducer stage. The expression for pump weight is

$$W_P = K_P \, D^{2.3} \quad .$$

(L-13)

where D is the pump diameter

K_P is a constant depending on the number of pump stages.

The diameter was determined assuming that the approach velocity was 20 ft/sec. The number of stages was determined by the value of overall pump head. It was assumed that the inducer had a head limitation of 500 ft and the following stages each could produce a head rise of 360 ft.

The values of K_P are given in the following table:

Number of Stages	1	2	3	4	5
K_P	346	392	438	484	530

The gearbox weight was predicted by the well-known Dudley expression for lightweight planetary gears:

$$W_G = 9500 \, F/K \quad ,$$

(L-14)

where K is the gear loading factor

F is the torque factor.

F is given by

$$F = hp(mg + 1)^3 / N_P \, mg \quad ,$$

(L-15)

L-14

where hp is the shaft horsepower

mg is the gear ratio

N_P is the pinion rpm.

A value of K factor of 500 was selected for this study. The
gear ratio mg was estimated from the assumption that the tip
speed of the inducer was 200 ft/sec when the inducer head was
500 ft. The engine weight was assumed to be given by the
expression

$$W_E = 0.4 \text{ shp} . \qquad\qquad (L\text{-}16)$$

The component weights were calculated by the expressions L-12
through L-16 for the range of jet velocity ratios (V_j/V_o) 1.3-2.1
and for ship speeds of 50, 80, and 110 knots. The estimated
weights and propulsive coefficients are presented in Fig. L-3.

To estimate the size and origin of the losses in this type
of system the propulsive coefficients for zero internal loss,
zero drag, and ideal pumps were calculated. The results are
indicated in Fig. L-4 using the same conditions as in Fig. L-3,
i.e., the solid lines in Fig. L-4 represent the estimated
practically attainable values of Fig. L-3.
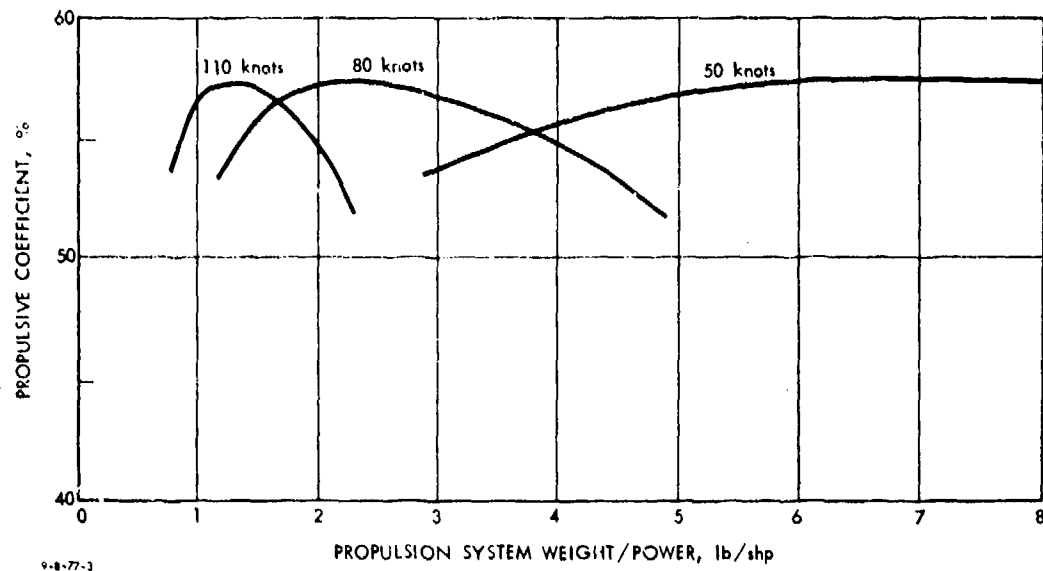
FIGURE L-3. Propulsive coefficient and system weight for flush
inlet waterjet systems (20,000 hp).
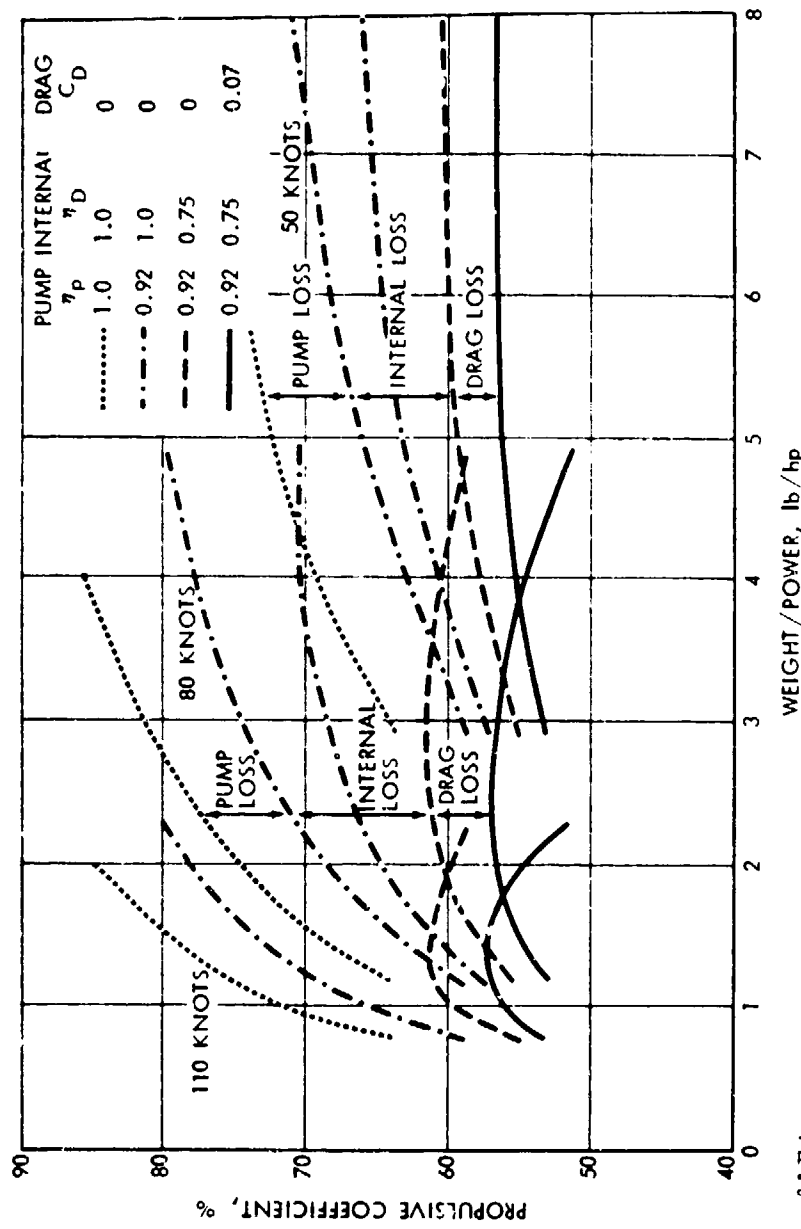
FIGURE L-4. Propulsive coefficient and system weight for flush inlet waterjet systems (20,000 hp).

L-17

REFERENCES, APPENDIX L

L-1.   R.A. Barr, "Supercavitating and Superventilated Propellers,"
       Transactions of SNAME, Vol. 78, 1970.

L-2.   R.A. Barr and R.J. Etter, "Selection of Propulsion Systems
       for High-Speed Advanced Marine Vehicles," Marine Technology,
       Vol. 12, No. 1, January 1975.

APPENDIX M

TASK STATEMENT

DEFENSE ADVANCED RESEARCH PROJECTS AGENCY
1400 WILSON BOULEVARD
ARLINGTON, VIRGINIA 22209

ASSIGNMENT FOR WORK TO BE PERFORMED
BY
INSTITUTE FOR DEFENSE ANALYSES

Project Assignment A-40   Date _____

You are hereby requested to undertake the following task:

1. **TITLE**: Technology Assessment of Advanced Military
        Propulsion Concepts

2. **BACKGROUND**: Previous advances in propulsion system tech-
nology have had a significant military impact, not only on
high-speed aircraft, but also on other high-power military
vehicles -- surface combat vehicles and helicopters. The
potential impact of further advances in this technology, if
achievable, also remains high for these latter vehicles.
Thus, in addition to the evolutionary developments pursued
by the Services, ARPA should encourage effort aimed at
potentially more significant advances in propulsion system
technology for these vehicles, if such potential advances
can be identified.

    To this end, ARPA organized an Advanced Propulsion Concepts
Technical Working Group to identify propulsion technology
advances that had potentially large payoffs for military surface
vehicles and to make recommendations as to the program which
ARPA should pursue. A major recommendation of this group was
that, in view of the wide variety of vehicle applications,
propulsion system types, and constituent propulsion system
technologies, ARPA should undertake a thorough technology
assessment of the area. Such a technology assessment, in
addition to identifying the present state-of-the-art, should
identify (1) the overall propulsion system characteristics which,
if achieved, would constitute a major technical advance for
various classes of vehicles, (2) the propulsion system forms
most appropriate to various classes of vehicles and (3) needed
advances in constituent propulsion system technologies.

3. **OBJECTIVE**: The objective is to quantify the technological
advances needed to make major improvements in military pro-
pulsion systems, and to provide criteria against which new
concepts in propulsion system components can be evaluated.

M-3

4. TECHNICAL SCOPE:

Task 1 -- Define Military Propulsion Characteristics

A study will be made of the range of values of total
power, specific weight, specific volume, specific fuel con-
sumption and the acquisition and O&M costs that are consistent
with proven design practice for military propulsion systems
in each of these classes of vehicles:

> High-speed Ocean-going Ships
> Main Battle Tanks
> Light Tracked Combat Vehicles
> High Mobility Combat Vehicles

From this data the improvements in the values of these
design parameters that are needed to produce a significant
impact on the performance or acquisition and O&M costs of
these classes of vehicles will be established.

Task 2 -- Establish Basic Physical Limitations

A study will be made of the physical parameters that
govern the different propulsion system components. For this
purpose the propulsion system will be considered as consisting
of three components: a device for producing power from a
fuel (an engine), a means for distributing the power (a trans-
mission system), and a means for producing propulsive force
(a thruster). The relationships between the significant
physical parameters will be defined and limits on component
performance established.

Task 3 -- Determine the Impact of Advances in Component
Technology

This task will be to establish the current state of tech-
nology by reference to existing design practice in each
component area. The state of technology will be expressed in
terms that can be related to the design parameters used in
Task 1 and the physical parameters used in Task 2.

Task 4 -- Synthesis of Results

The final task will be to combine the results of the above
tasks to show the impact of technological advances on the
classes of vehicles considered. The results will then be
analyzed to show where advances in technology could make major
impacts on the performance or acquisition and O&M costs of
these vehicles.